



Structure-Based Design of Artificial Metalloenzymes and Beyond

Inauguraldissertation

zur

Erlangung der Würde eines Doktors der Philosophie

Vorgelegt der

Philosophisch-Naturwissenschaftlichen Fakultät

der Universität Basel

von

Max Tillmann Heinisch

aus Leipzig

Basel, 2013

Genehmigt von der Philosophisch-Naturwissenschaftlichen Fakultät auf Antrag von

Prof. Dr. Thomas R. Ward

Prof. Dr. Tilman Schirmer

Basel, den 11.12.2012

Prof. Dr. Jörg Schibler

Dekan

This thesis includes results of a collaboration between the groups of Prof. Dr. Thomas R. Ward and Prof. Dr. Tilman Schirmer of the Chemistry Department and the Biozentrum of the University of Basel, respectively. It contains excerpts or the full versions of the following publications:

Monnard, F. W., Nogueira, E. S., Heinisch, T., Schirmer, T., Ward, T. R. Human Carbonic Anhydrase II as Host Protein for the Creation of Artificial Metalloenzymes: the Asymmetric Transfer Hydrogenation of Imines, *Chem. Sci.* (2013), 4, 3269.

Zimbron, J. M., Heinisch, T., Schmid, M., Hamels, D., Meuwly, M., Schirmer, T. and Ward, T. R., A dual anchoring strategy for the localization and activation of artificial metalloenzymes based on the biotin-streptavidin technolog. *J. Am. Chem. Soc.* (2013) 135, 5384.

Heinisch, T. Langovska, K., Tanner, P., Reymond, J.-L., Meier, W., Palivan, C. and Ward, T. R. Fluorescence-based assay for the optimization of artificial transfer hydrogenase activity within a biocompatible compartment. *ChemCatChem* (2013), 5, 720.

Köhler, V.*, Mao, J.*, Heinisch, T.*, Pordea, A., Sardo, A., Wilson, Y. M., Knörr, L., Creus, M., Prost, J.-C., Schirmer, T. and Ward, T. R., OsO₄·Streptavidin: A tunable hybrid catalyst for the enantioselective *cis*-dihydroxylation of olefins. *Angew. Chem. Int. Ed.* (2011) 50, 10863.

(* = shared first authorship)

Monnard, F. W., Heinisch, T., Nogueira, E., Schirmer, T. and Ward, T. R., Human carbonic anhydrase II as a host for piano-stool complexes bearing a sulfonamide anchor. *Chem. Commun.* (2011) 47, 8238.

Dürrenberger, M.* Heinisch, T.*, Wilson, Y. M.*, Rossel, T., Nogueira, E., Knörr, L., Mutschler, A., Kersten, K., Zimbron, J. M., Pierron, J., Schirmer, T. and Ward, T. R., Artificial transfer hydrogenases for the enantioselective reduction of cyclic imines. *Angew. Chem. Int. Ed.* (2011) 50, 3026. (* = shared first authorship)

Zimbron, J. M., Sardo, A., Heinisch, T., Wohlschlager, T., Gardinaru, J., Massa, C., Schirmer, T. and Ward, T. R., Chemo-genetic optimization of DNA recognition by metallodrugs using a presenter-protein strategy. *Chem. Eur. J.* (2010) 16, 12883.

Heinisch, T., Ward, T. R., Design strategies for the creation of artificial metalloenzymes. *Cur. Opin. Chem. Biol.* (2010) 14, 184.

Declaration:

I declare that I wrote this thesis, **Structure-Based Design of Artificial Metalloenzymes and Beyond**, with the help indicated and only handed it in to the faculty of science of the University of Basel and to no other faculty and no other university.

Acknowledgements:

My special thanks go to my PhD supervisors Prof. Thomas R. Ward and Prof. Tilman Schirmer who gave me the opportunity to work in the fascinating, interdisciplinary research area of artificial metalloenzymes, to learn protein crystallography and critical thinking.

I am grateful to Dr. Valentin Köhler and Dr. Yvonne Wilson for all the help in correcting this thesis, the scientific discussions and all the funny moments.

Dr. Marc Creus I would like to thank very much for the stimulating and motivating discussions and the lessons in creative thinking.

I wish to thank Dr. Alessia Sardo and Dr. Claudia Massa for their kind help introducing me into protein crystallography and for their friendship. I am grateful to all past and present members of the Schirmer group, Franziska, Paul, Christophe, Arnaud, Frederic, Cedric, Amit, Camille, Nisha, Chi-Seng, Caroline, Zora, Aline, Stephanie, Dietrich and Marlise.

Prof. Jincheng Mao and Beat Amrein I would like to thank for their collaboration in creating the artificial dihydroxylase.

My special thanks go to all the past and present members of the artificial metalloenzyme team and the molecular evolution team, Maurus, Marc D., Jeremy, Fabien, Thibaud, Cheikh, Sabina, Ewa, Didier, Anna, Anamitra, Praneth, Marc R., Rafael, Narasimha, Tomasso, Stefan, Gaetano, Aping, Todd, John, Maxim and Julian.

For all their great support I would like to thank the biologists in the group, especially Livia and Elisa.

For an insightful collaboration, fascinating discussions and a great atmosphere I am very grateful to Prof. Jean-Louis Reymond and his coworkers Justus Bürgi and Dr. Lise Brethous.

I learned a lot also through the great collaboration with Prof. Wolfgang Meier and Dr. Cornelia Palivan. Especially, I would like to thank Karolina Langowska and Pascal Tanner for the fascinating excursions in the world of synthetic polymers and fluorescence microscopy.

Prof. Hans-Beat Bürgi I am grateful for his fascinating comments on problems in crystallography and science in general.

The Marie-Curie training network BioChemLig I want to thank for the opportunity to meet so many great people, for all the interesting discussions and a great atmosphere.

Finally I would like to express my deep feelings for all my family and friends who followed me during this PhD thesis.

And thank you, Natalia, for all your support and the wonderful time we spent together...

Abstract:

Optically active molecules play a fundamental role in the functions of life. The enantioselective synthesis of chiral building blocks is crucial for the production of high value compounds such as pharmaceuticals or pesticides. Besides homogenous transition metal and enzymatic catalysts, artificial metalloenzymes - that consist of metal cofactors anchored within protein scaffolds - have been developed in the past decade to access optically pure compounds. The creation and optimization of these hybrid systems requires structural information. The asymmetric transfer hydrogenation of functional carbonyl, imine or enone groups to obtain the corresponding alcohols, amines or alkanes in high optical purity is achieved by transition metal piano stool complexes as well as by a number of different enzymes. In this thesis, two artificial transfer hydrogenases based on the streptavidin-biotin system for the asymmetric reduction of cyclic imines are structurally characterized. Potential substrate binding modes are proposed and the origins of the enantioselectivities are discussed. The Sharpless osmium-catalyzed asymmetric dihydroxylation of olefins is a powerful method to obtain chiral vicinal diols from variously substituted substrate molecules. The enantioselectivity of the reaction is governed by the interactions between the substrate olefins and the bulky chiral ligands bound to the catalytic osmium tetroxide center. In this thesis, an artificial olefin dihydroxylase is structurally characterized which is based on the embedding of an osmium tetroxide catalyst within streptavidin. Although none of the four osmium-binding sites located in the crystal structures was bound to the biotin-binding pocket, the activity pattern of various streptavidin mutants suggests that the active site is located in proximity to this position. During the processing of the diffraction data of one of the streptavidin-osmium crystals, an ambiguous packing disorder was diagnosed for which a quantitative model is proposed in the final chapter of this thesis.

Human carbonic anhydrase II is a well-characterized monomeric protein and numerous arylsulfonamide inhibitors with nanomolar and subnanomolar affinities for this enzyme are described in the literature. The potential of this protein to act as a host for the creation of an artificial transfer hydrogenase is evaluated by the structural characterization of an arylsulfonamide-tethered transition metal piano stool complex bound to human carbonic anhydrase II. This study is also investigating the structural origins of the high affinities of piano stool arylsulfonamide complexes for human carbonic anhydrase II and the implications for future metallodrug design.

A number of ruthenium-arene piano stool complexes have been demonstrated to strongly inhibit the growth of human cancer cell lines by unspecific interactions with nucleobases. To introduce DNA-specificity via second coordination sphere interactions, two ruthenium arene complexes have been biotinylated and bound to streptavidin. The structural basis of the DNA-specificity governed by the streptavidin-ruthenium arene complex is investigated.

The *in vivo* activity of artificial metalloenzymes is a prerequisite for their genetic optimization by directed evolution. Moreover, hybrid enzymes have the potential to be used *in vivo* to complement metabolic pathways or to act as bioorthogonal catalyst in the activation of prodrugs. The strategy of enzyme-encapsulation into cell-penetrating nanoreactors is investigated which allows the shuttling of artificial metalloenzymes into cells.

Keywords:

Artificial Metalloenzyme, Protein Crystallography, Piano Stool Transition Metal Complex, Streptavidin-Biotin, Human Carbonic Anhydrase II, Arylsulfonamide Inhibitors, Asymmetric Transfer Hydrogenation of Cyclic Imines, Asymmetric Olefin Dihydroxylation, Metallodrug, Nanoreactor, Fluorescence Assay, Crystal Packing Disorder

Abbreviations:

2-MPN	2-Methyl-pyrroline
AME	Artificial metalloenzyme
ATH	Asymmetric transfer hydrogenation
ATHase	Artificial transfer hydrogenase
AU	Asymmetric unit
CA	Carbonic anhydrase
CCD	Charged-coupled device
CHBE	(<i>R</i>)-4-Chloro-3-hydroxybutyrate
COBE	4-Chloroacetoacetate
Cp*	Pentamethylcyclopentadienyl
DDS	Drug delivery system
<i>Dl</i>	Dextrorotatory and levorotatory
<i>Ee</i>	Enantiomeric excess
EMSA	Electromobility shift assay
FADH ₂	Flavin adenine dinucleotide hydride
FDH	Formate dehydrogenase
hCAII	Human carbonic anhydrase II
IDA	Iminodiacetate
ITC	Isothermal titration calorimetry
MC	Metallocofactor
MR	Molecular replacement
NAD(P)H	Nicotinamide adeninedinucleotide (phosphate) hydride
PDB	Protein database
PEG	Polyethyleneglycol
Sav	Streptavidin
TOF	Turnover frequency
TON	Turnover number
TosEN	Tosylethylenediamine
TosDPEN	Tosyldiphenylethylenediamine

Nomenclature:

Schemes, figures, tables and compounds that are not part of a journal publication are labeled with a capital M. In contrast, schemes, figures, tables and compounds mentioned in the text with a two-number label refer to a journal publication. The first number refers to the position of the corresponding journal publication in the text and the second number to the position of the item in the publication.

Table of Content

I	Preamble	4
II	Aim of the Thesis	6
III	Artificial Metalloenzymes in Asymmetric Catalysis	8
1.	Introduction	8
1.1.	Asymmetric Homogenous Transition Metal Catalysis	8
1.2.	Asymmetric Biocatalysis	8
1.3.	Strategies for Artificial Metalloenzyme Design	9
1.4.	Streptavidin-Biotin Technology in Artificial Metalloenzyme Design	11
1.5.	Carbonic Anhydrase-Arylsulfonamide System in Artificial Metalloenzyme Design	12
2.	Artificial Transfer Hydrogenases Based on the Streptavidin-Biotin Technology for the Reduction of Cyclic Imines	15
2.1.	Author Contributions	27
2.2.	Comment on Publication	28
2.2.1.	Asymmetric Imine Transfer Hydrogenation Catalysts: Organometallic Complexes, Enzymes and Artificial Metalloenzymes	28
3.	A Dual Anchoring Strategy for the Localization and Activation of Artificial Metalloenzymes based on the Streptavidin-Biotin Technology	38
3.1.	Author Contributions	56
3.2.	Comment on Publication	57
3.2.1.	Towards the Directed Evolution of Artificial Transfer Hydrogenases	57
3.2.2.	Substrate Binding Models and Potential Influence of the 1 st and 2 nd Coordination Sphere on Catalysis	58
3.2.3.	Comparison of a Mono- and a Bis-Anchored Metallocofactor-Streptavidin Complex for Artificial Transfer Hydrogenation	59
3.2.4.	Compatibility of a Dual-Anchor Artificial Transfer Hydrogenase with in Vivo Screening	61
3.2.5.	Further Applications of Arene-Biotinylated Piano Stool-Streptavidin Complexes	62

4.	OsO ₄ -Streptavidin: A Tunable Hybrid Catalyst for the Enantioselective <i>cis</i> -Dihydroxylation of Olefins	63
4.1.	Author Contributions	77
4.2.	Comment on Publication	78
4.2.1.	Sharpless- vs. Enzymatic Asymmetric Olefin Dihydroxylation	78
4.2.2.	Potential Reaction Mechanisms of the Artificial Olefin Dihydroxylase	80
5.	Human Carbonic Anhydrase II as a Host for Piano-Stool Complexes Bearing a Sulfonamide Anchor	82
5.1.	Author Contributions	92
5.2.	Comment on Publication	93
5.2.1.	Structural Aspects of the Design of an Artificial Transfer Hydrogenase Based on Human Carbonic Anhydrase II	93
5.2.2.	Future Structure-Based Computational Design of Artificial Metalloenzymes Based on Human Carbonic Anhydrase II	94
IV	Structural Analysis of Piano Stool Ruthenium Complexes Bound to hCAII and Streptavidin: Implications for Future Metallodrug Design	96
6.	Introduction	96
7.	Human Carbonic Anhydrase II as a Host for Piano-Stool Complexes Bearing a Sulfonamide Anchor	97
7.1.	Comment on Publication	97
7.1.1.	Structure-Based Design of Metallodrugs for Human Carbonic Anhydrase II	97
7.1.2.	Piano Stool Complexes as Secondary Recognition Elements for the Inhibition of Human Carbonic Anhydrase II	98
8.	Chemo-Genetic Optimization of DNA Recognition by Metallodrugs Using a Presenter-Protein Strategy	100
8.1.	Author Contributions	121
V	Towards in Vivo Catalysis with Artificial Metalloenzymes	122
9.	Introduction	122
9.1.	Directed Evolution of Artificial Metalloenzymes	122
9.2.	Artificial Metalloenzymes in Metabolic Engineering	122
9.3.	Artificial Metalloenzymes in the Prodrug Strategy	123

9.4. Vesicular Delivery Systems for the Cellular Uptake of Enzymes	123
10. Fluorescence-Based Assay for the Optimization of Artificial Transfer Hydrogenase Activity within a Biocompatible Compartment	126
10.1. Author Contributions	145
10.2. Comment on Publication	146
10.2.1. Compatibility of the Fluorescence Assay with in Vivo Conditions	146
10.2.2. Outlook	146
VI Quantitative Model of a Streptavidin-K₂[OsO₂(OH)₄] Crystal with an Ambiguous Packing Disorder	148
11. Introduction	148
12. Experimental Part	148
13. Results and Discussion	149
14. Summary	160
VII Bibliography	161
VIII Curriculum Vitae	167

I Preamble

Chiral molecules such as amino acids or nucleotides are involved in fundamental processes of life. At the same time, our society relies on a great amount of high-value chiral compounds including pharmaceuticals, pesticides, aroma and flavor compounds, dyes and pigments, liquid crystals and others. Homogenous transition metal- and enzymatic catalysis are crucial technologies for the synthesis of optically pure building blocks. In the past, these two disciplines inspired one another to develop efficient catalytic processes, which are characterized by a high substrate specificity, a high activity, a long catalyst lifetime, a low reaction temperature and the employment of environmentally benign reactants and solvents. Due to the availability of scientific techniques such as site-directed protein mutagenesis and synthetic chemistry it is possible to engineer hybrid catalysts, which consist of an active metallocofactor anchored within a rigid protein scaffold. These artificial metalloenzymes (AME hereafter) combine principles of transition metal- and enzymatic catalysis. It is important to know the structure of an artificial metalloenzyme to understand its reaction mechanism and to optimize its function.

In this thesis, hybrid catalysts are structurally characterized, which are based on the well-characterized streptavidin-biotin complex. The structural information will be used to elucidate the reaction mechanism and to propose amino acid mutations for the improvement of the catalyst's activity and selectivity. The investigation concerns hybrid catalysts for two important reactions, the asymmetric transfer hydrogenation of cyclic imines and the asymmetric *cis*-dihydroxylation of olefins.

In addition to streptavidin-biotin, the potential of a second protein-ligand complex, the human carbonic anhydrase II-arylsulfonamide system, is explored by protein crystallography to be engineered into an artificial metalloenzyme. The strategy is based on the tethering of a number of catalytically active ruthenium-arene piano stool complexes to an arylsulfonamide anchor, which has a nanomolar affinity for human carbonic anhydrase II (hCAII hereafter). Since hCAII is an important drug target, the structural characterization of hCAII-ruthenium arene arylsulfonamide complexes is valuable for the design of novel metallodrugs. The ruthenium-arene piano stool functionalities of the complexes tested for catalysis and as inhibitors of hCAII were reported to inhibit the growth of human ovarian cancer cell lines. The goal of another chapter of this thesis is to increase the specificity of these ruthenium complexes for different DNA-targets. In the context of a presenter-protein strategy,

biotinylated ruthenium-arene complexes are attached to different streptavidin (Sav hereafter) mutants and the DNA-binding selectivity of the complexes is rationalized by crystal structure analysis.

For the optimization of AMEs by the high-throughput *in vivo* screening of genetic diversity or for the application of AMEs in metabolic engineering, strategies have to be developed to create hybrid catalysts that are robust, reactive and selective under physiological conditions. Towards this end, an artificial transfer hydrogenase is encapsulated into a cell-permeable nanoreactor. The activity of the catalyst inside the nanoreactor is tested by a fluorescence assay developed specifically to detect transfer hydrogenation activity.

The final chapter of the thesis discusses an ambiguous packing disorder, which was observed in a streptavidin crystal soaked with $K_2[OsO_2(OH)_4]$. A quantitative model for the packing anomalies is proposed.

II Aim of the Thesis

1. Artificial Metalloenzymes for Asymmetric Catalysis

To reveal the mechanism and determine amino acid residues crucial for the optimization of artificial metalloenzymes for the asymmetric transfer hydrogenation of cyclic imines and the asymmetric *cis*-dihydroxylation of olefins, the crystal structures are to be solved of complexes of:

- i. streptavidin mutants with biotinylated transition metal piano stool complexes,
- ii. streptavidin with $K_2[OsO_2(OH)_4]$
- iii. human carbonic anhydrase II with benzene sulfonamide-anchored transition metal piano stool complexes.

2. Structural Analysis of Piano Stool Ruthenium Complexes Bound to Streptavidin and Human Carbonic Anhydrase II: Implications for Future Metallodrug Design

The potential of benzene sulfonamide transition metal piano stool complexes as inhibitors of human carbonic anhydrase II has to be evaluated by crystal structure analysis.

For the structural and mechanistic elucidation of the specific DNA-binding properties of a biotinylated ruthenium-*p*-cymene piano stool complex bound to streptavidin the crystal structure of the complex needs to be solved.

3. Towards *in Vivo* Catalysis with Artificial Metalloenzymes

For future *in vivo* applications of streptavidin-biotin-based artificial metalloenzymes, an artificial transfer hydrogenase has to be encapsulated in a cell-permeable vesicle. To investigate the enzymatic activity inside the vesicle, a colorimetric transfer hydrogenation assay will be developed.

4. Quantitative Model of a Streptavidin-K₂[OsO₂(OH)₄] Crystal with an Ambiguous Packing Disorder

Crystal packing disorder is a common problem in crystallography. Upon soaking apo-streptavidin crystals with K₂[OsO₂(OH)₄] and processing of the collected diffraction data, a crystal packing disorder was detected. A quantitative model has to be generated to describe the disorder and to solve the structure.

III Artificial Metalloenzymes in Asymmetric Catalysis

1. Introduction

1.1. Asymmetric Homogenous Transition Metal Catalysis

A molecule is chiral when it can not be superimposed with its mirror image. The image and the mirror image of the chiral molecule are two enantiomers. Due to their different stereochemistry, opposite enantiomers of a small molecule can have very different biological effects.¹ The production of optically active (chiral) fine chemicals is relevant for the synthesis of more complex compounds such as pharmaceuticals, pesticides, aroma and flavor compounds, dyes and pigments, liquid crystals and others.

In asymmetric transition metal catalysis, optically pure metal complexes are employed to produce chiral building blocks from achiral precursors (**Scheme M1**).² Thereby, chirality is induced from the catalyst to the product molecule. In case both catalyst and substrate are part of one reaction phase (e.g. a solution), one refers to homogeneous catalysis. Many transition metal catalyzed reactions have a maximum performance in organic solvents and at elevated temperatures. Limitations in the enantioselectivity of the catalyst can be circumvented by the step-wise enrichment of one enantiomer through selective recrystallization or (dynamic) kinetic resolution.² However, highly enantioselective catalysts are desired to produce chiral building blocks with close to 100 % optical purity in one step.

1.2. Asymmetric Biocatalysis

Enzymes differ from homogenous small molecule catalysts in structural and functional terms.³ Most enzymes have evolved to catalyze a specific transformation in an aqueous environment at physiological conditions (e.g. pH about 7.5 and 37 °C) within a complex matrix of molecules. These special reaction conditions account for a complex biopolymeric architecture composed of recyclable amino acid units, which is optimized by evolution. The environmentally benign reaction conditions and the high selectivity of an enzyme are attractive features and responsible for a great amount of research in the area of biocatalysis. Enzymes consist of a substrate-specific active site pocket to bind the transition state of a reaction with high affinity. The selective substrate binding to the enzyme allows a strong

asymmetric induction with close to 100 % optical purity in the product molecule. Metals play often a pivotal role in asymmetric enzyme catalysis.^{4,5} They guide function in many different ways: e.g. by stabilizing the protein structure, by arranging the substrate in a reactive conformation in the active site, by acting as a Lewis acid to increase the electrophilicity of a reaction partner or another amino acid (**Figure M7**), by compensating negative charges in transition states or by donating or accepting electrons from substrates or cofactors. However, enzymes are not always suitable to catalyze reactions of interest since they may not bind the substrate molecule or because they denature in organic solvent and at elevated temperatures.

1.3. Strategies for Artificial Metalloenzyme Design

An alternative approach to find a highly selective enzyme for an important chemical transformation is the creation of artificial metalloenzymes. The hybrid asymmetric catalysts can be created by the incorporation of a transition metal into a rigid protein scaffold. Thereby, the high activity of the metal catalyst is combined with the enantioselectivity of an enzymatic substrate binding pocket.

In the past decades, numerous techniques have emerged, which can be employed for the engineering of artificial metalloenzymes: e.g. the synthesis of metallocofactors (MC hereafter), heterologous protein expression, site-directed and random mutagenesis, synthesis of monoclonal antibodies, protein crystal structure analysis and computational modeling. Given a chemical transformation of interest, three major strategies have been described in literature for the formation of AMEs: i) the redesign of a natural biomolecular scaffold employing an active MC,⁶⁻¹⁰ ii) the design of an AME based on the transition state of a reaction^{11,12} and iii) the directed evolution of existing metalloenzymes to acquire novel functions.¹³ The focus of this thesis is on the first concept.

Redesign of Biomolecular Scaffolds Using Active Metallocofactors:

The first examples of AMEs were based on the covalent and non-covalent chemical modification of existing protein scaffolds with MCs.^{14,15} The general concept is to use a readily available biomolecular scaffold, either protein or DNA/RNA, to define the reaction environment of an incorporated active MC. Thereby, the activity and selectivity of the hybrid catalyst can be improved for a given substrate by modulation of the 1st (including atoms covalently attached to metal) and 2nd (including atoms non-bonded to the metal) coordination

sphere of the metal (**Figure M1**). The individual steps towards the achievement of such a hybrid catalyst are described in the following paragraphs.

Search for Biomolecular Scaffold:

The choice of an appropriate biochemical scaffold is typically guided by the following criteria: i) availability of structural information from X-ray crystallography or NMR, ii) presence of a cavity of sufficient size to accommodate the MC and the substrate, iii) the possibility to tightly anchor the MC inside the cavity, iv) the cavity should be part of a rigid fold to constrain structural and functional unidirectionality, v) the biomolecule should be readily available in big amounts and high purity from a natural source, through synthesis or by heterologous expression (e.g. in *E. coli*), which allows screening of the functional effects of amino acid exchanges, vi) the biomolecule should ideally be stable at temperatures above room temperature, tolerate organic solvents, high ion concentrations and different pH values and vii) the biomolecule-MC complex should be easy to crystallize to get structural information of the catalyst by X-ray crystallography, which can be used to optimize the AME by chemical and genetic means.

Anchoring of the MC:

The MC can be anchored to the biomolecule: i) in a covalent fashion by ligation to a reactive amino acid (e.g. Cys, Lys, Ser) or nucleotide,^{16–20} ii) in a supramolecular fashion by ligation of a natural affinity tag (e.g. biotin, heme or acridine) to an active metal function (**Figure M1**),^{8,9,14,21,22} iii) in a dative fashion by direct coordination of the active metal to amino acid side chains or nucleotides in the cavity of the biomolecule^{23–29} or iv) by genetic encoding of a non-natural amino acid well suited for metal coordination.³⁰

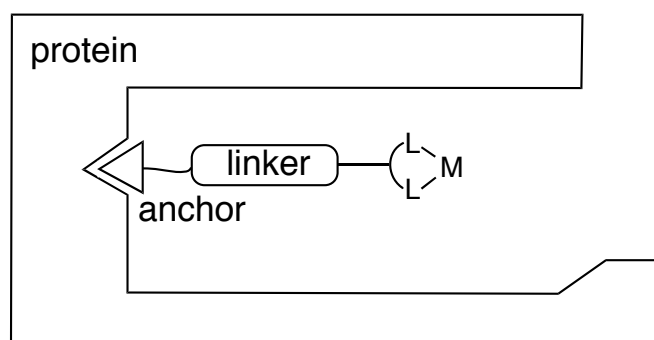


Figure M1: Supramolecular anchoring of metallofactor within a protein scaffold. Letters M and L indicate metal and ligand, respectively.

Chemical Optimization of the AME:

The advantage of using MCs in AME design as compared to transition state-based design methods is a relatively easy access to an initial activity of the hybrid catalyst. Furthermore, it holds the potential to screen chemical diversity for its impact on the activity and selectivity of a chemical transformation. It should be considered in the design process of the MC to have a facile access to a broad cofactor diversity compatible with the biomolecular scaffold by using reliable reactions with little side products, easy product purification and by avoiding residual reactive groups in the MC that can undergo undesired reactions with the biomolecule.

Genetic Optimization of the AME:

Integral part of AME design is the possibility to employ the transcription and translation machinery of bacteria to generate chemical diversity (amino acid substitutions) from genetic diversity (DNA) and, thus, to simulate natural evolution in a laboratory. Linkage of genotype and phenotype allows the application of genetic algorithms in AME design such as: 1) 1st generation diversification, 2) 1st generation activity screening and selection of fittest members, 3) characterization and diversification of fittest 1st generation members, 4) 2nd generation activity screening and selection of fittest members, and so on.³¹ The velocity of evolution of AMEs varies depending on the rate of the diversification techniques and the product screening method.

1.4. Streptavidin-Biotin Technology in Artificial Metalloenzyme Design

A suitable system for the engineering of a supramolecular AME is the streptavidin-biotin complex. The affinity of the cofactor biotin (vitamin H) for the bacterial protein streptavidin is very high ($K_D = 10^{-14}$ - 10^{-15} M) and the strongest non-covalent interaction known in Nature.³² Sav, which is a close structural homolog of the chicken protein avidin, is a 222-symmetrical homotetrameric protein (~ 66 kDa), the monomers of which consist of a rigid beta-barrel fold (**Figure M2**).³³ Each beta-barrel can bind one biotin molecule within its core. No cooperativity was observed for the individual biotin binding events.³⁴ There are two types of relatedness between biotin binding sites in a Sav tetramer: *cis* (small distance between two biotin molecules) and *trans* (long distance between two biotin molecules). Each biotin molecule is located within a deep binding pocket. The valeric acid chain of biotin faces towards a vestibule, which can accommodate a functional group tethered to the carboxylic acid of biotin. Depending on the size of the functional group, biotinylated ligands bound to

cis-related Sav monomers can influence one another.³⁵ The affinity of many functionalized biotin molecules for Sav is still in the nanomolar or subnanomolar range.³² Sav is stable up to a temperature of 110 °C,³⁶ in organic solvent (45 % DMSO)³⁷ and at high and low pH (pH 3 - 11). Sav can be obtained in high quantities (200 mg/L) by heterologous expression in *E. coli*. Complexes of Sav and functionalized biotin can be crystalized and characterized by X-ray protein crystallography, which allows structure-based intuitive and computational design and the assessment of hybrid catalysts.

Wilson and Whitesides were the first to use the avidin-biotin system to incorporate a rhodium diphosphine complex for the catalytic asymmetric hydrogenation of an olefin.¹⁴ Follow-up research by Ward and Reetz has demonstrated that Sav can be engineered into a highly enantioselective hybrid catalyst for C-H activation,³⁸ hydrogenation,^{22,39-42} transfer hydrogenation,⁴³⁻⁴⁵ allylic alkylation,⁴⁶ sulfoxidation²⁷ and ring-closing metathesis.⁴⁷

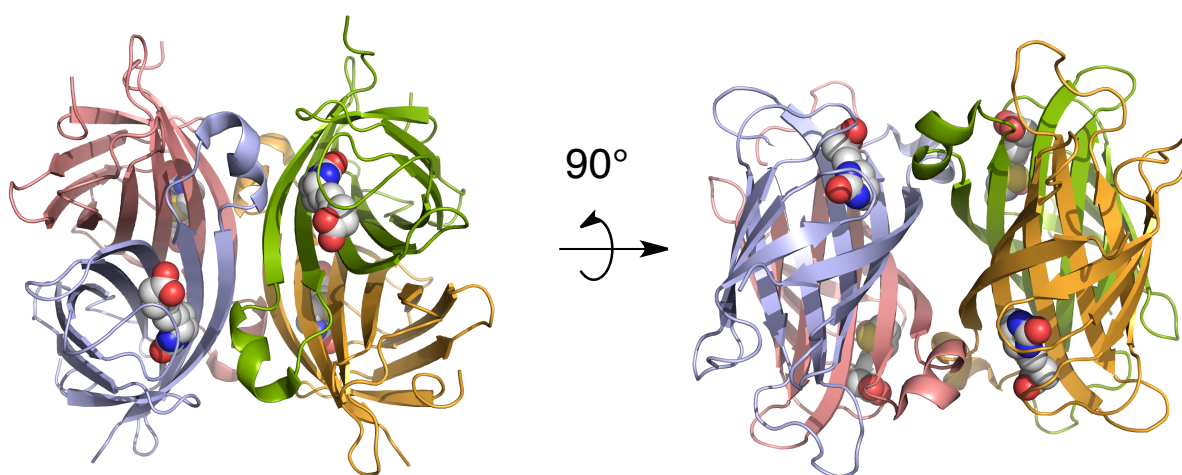


Figure M2: 222-symmetric streptavidin homotetramer (ribbon model) in complex with biotin (sphere model, PDB 3RY2). The left panel shows a top-view on two *cis*-related biotin binding pockets and the right panel a side view indicating the positions of two *trans*-related biotin-binding sites.

1.5. Carbonic Anhydrase-Arylsulfonamide System in Artificial Metalloenzyme Design

The numerous impressive hybrid catalysts afforded so far by engineering of the Sav-biotin complex encourages the adaptation of the concept to expand the scope of catalysts and reactions. This motivation is reinforced by the fact that due to the interference of *cis*-related cofactors in the Sav-biotin-based AME, structure-based design is difficult.³⁵ Engineering of

asymmetric *cis*-related Sav monomers (e.g. to bind the cofactor in one monomer and the substrate selectively in the *cis*-related monomer) is very difficult to achieve.^{48,49} Furthermore, *in vivo* screening to optimize the activity and selectivity of the Sav-MC complexes in *E. coli* is hampered by competitive biotin present in the cell.⁵⁰

Carbonic anhydrases (CA hereafter) exist in all organisms and are responsible mainly for i) the fixation and release of carbon dioxide (respiration, gas-exchange), ii) Na⁺ transport (signal transduction and intracellular pressure) and iii) pH regulation.⁵¹ The reaction of water and carbon dioxide into bicarbonate by CA is one of the fastest reactions in Nature ($k_{\text{cat}}/K_{\text{M}}^{\text{CO}_2} \approx 10^8 \text{ M}^{-1}\text{s}^{-1}$). In humans, 16 isoforms of CA exist which are located in the cytosol, in mitochondria, bound to the cell membrane and in saliva. The structurally (a total of 429 structures including 304 ligand-bound structures in the PDB, as of October 2012) and functionally best studied isoform is human carbonic anhydrase II. The monomeric enzyme consists of a central beta-sheet surrounded by numerous alpha-helices and loops that form a deep cone-shaped cavity with a catalytic Zn(II)His₃ motive at the bottom (**Figure M3**). In the enzymatic reaction, a water molecule is activated by binding to the Lewis acid Zn(II). A closely-bound carbon dioxide is attacked by the activated water to form bicarbonate.

A wealth of arylsulfonamide derivatives (some of which are in clinical use) have been described to inhibit hCAII and bind with up to picomolar affinity.^{51,52} Arylsulfonamides can be engineered to bind to hCAII in a multivalent fashion, meaning by i) mimicking the transition state of the native reaction (the sulfonamide group), ii) by hydrophobic interactions (aryl group) and iii) by further interactions (e.g. hydrophobic or ionic). Studies of hCAII ligand design have confirmed the more general ligand design principles that i) a good ligand often resembles the transition state of the native reaction, ii) hydrophobic protein-ligand interactions are far simpler to engineer than ionic or electrostatic interactions and iii) multivalency is an effective design principle; i.e. to append a high-affinity secondary component (hydrophobic protein-ligand interaction) to a low-affinity primary component (e.g. ionic protein-ligand interaction).⁵¹

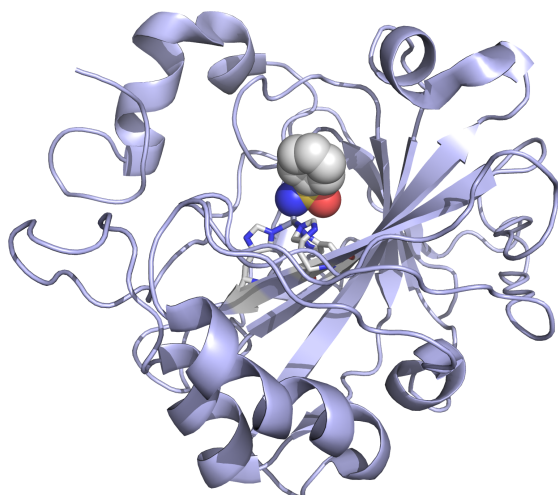


Figure M3: Human carbonic anhydrase (ribbon model) in complex with benzenesulfonamide (sphere model, PDB 2WEJ). Histidines and Zn(II) of the Zn(II)His₃ motif are depicted in stick representation.

In summary, the following aspects render hCAII to be an interesting candidate for AME design:

- it is monomeric, stable and of intermediate molecular weight (~29 kDa)
- numerous sulfonamide-based ligands are known with nanomolar and subnanomolar affinity
- it can be easily expressed in high yield in *E. coli* and purified by affinity chromatography
- it is structurally well-defined
- a number of straightforward assays are available (e.g. dansyl amide assay) to examine ligand binding
- its structure does not change drastically when it binds ligands
- a range of ligand motifs is easily synthetically accessible
- ligand design can be improved/guided by computational methods (e.g. *in silico* affinity screening of metallocofactors)

2. Artificial Transfer Hydrogenases Based on the Streptavidin-Biotin Technology for the Reduction of Cyclic Imines

Artificial Metalloenzyme

Artificial Transfer Hydrogenases for the Enantioselective Reduction of Cyclic Imines**

Marc Dürrenberger, Tillmann Heinisch, Yvonne M. Wilson, Thibaud Rossel, Elisa Nogueira, Livia Knörr, Annette Mutschler, Karoline Kersten, Malcolm Jeremy Zimbron, Julien Pierron, Tilman Schirmer, and Thomas R. Ward*

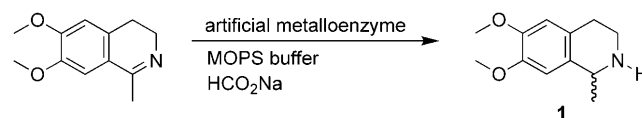
Enantiopure amines are privileged compounds which find wide use in the pharmaceutical, agrochemical, and flavor and fragrance industries. In this context, enzymatic,^[1] homogeneous,^[2] and chemoenzymatic^[3] approaches offer complementary means for the preparation of these targets.

The asymmetric transfer hydrogenation (ATH) of ketones using d⁶ piano stool complexes as catalyst has been the subject of numerous studies,^[4] leading to a unified picture of the reaction mechanism.^[5] The ATH of imines, however, has received less attention.^[6] Interestingly, the reaction proceeds through a different enantioselection mechanism: for a given aminosulfonamide ligand configuration, the opposite enantiomers (alcohol vs amine) are produced.^[7] In addition, it has been argued that the imine must be protonated for the reaction to proceed.^[8]

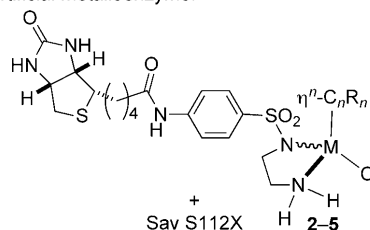
In recent years, artificial metalloenzymes, resulting from the introduction of a catalyst within a protein environment, have attracted attention as potential alternatives to traditional catalysts.^[9] Based on our experience in artificial ATHs for the reduction of ketones,^[10] we set out to test these systems toward the enantioselective reduction of imines and to compare their salient features with related homogeneous systems.

As a starting point, we screened d⁵ and d⁶ piano stool complexes bearing the biotinylated aminosulfonamide ligand (abbreviated Biot-*p*-L) combined with wild-type streptavidin (Sav) for the production of salsolidine **1** (Scheme 1).^[11]

This screening led to the identification of [Cp*Ir(Biot-*p*-L)Cl] (**5**⊂Sav) as the most promising catalyst. This contrasts with ATH of ketones for which [(η⁶-arene)Ru(Biot-*p*-L)Cl] **2** and **3** proved superior (Table 1).^[12] In all but one case, both amine **1** and 1-phenylethanol **6** were produced with the same configuration for a given artificial metalloenzyme.



artificial metalloenzyme:



M	η ⁿ -C _n R _n	Abbreviation
Ru	η ⁶ - <i>p</i> -cymene	[(<i>p</i> -cymene)Ru(Biot- <i>p</i> -L)Cl] 2
Ru	η ⁶ -benzene	[(benzene)Ru(Biot- <i>p</i> -L)Cl] 3
Rh	η ⁵ -C ₅ Me ₅	[Cp*Rh(Biot- <i>p</i> -L)Cl] 4
Ir	η ⁵ -C ₅ Me ₅	[Cp*Ir(Biot- <i>p</i> -L)Cl] 5

Scheme 1. Artificial metalloenzymes based on the biotin-streptavidin technology for the ATH of imines. MOPS = 3-morpholinopropanesulfonic acid.

Next, we screened complex **5** with the saturation mutagenesis library S112X (Table 2 and Supporting Information, Table S1). Noteworthy features include:

- 1) Incorporation of [Cp*Ir(Biot-*p*-L)Cl] (**5**) into Sav S112X produces predominantly (*R*)-**1**.
- 2) The best (*R*)-selectivities are obtained for the smallest amino acids at position 112 (S112G, S112A). The optimal pH is 6.50, affording the product in 85% *ee* at 55 °C (Table 2, entries 3 and 14).
- 3) The active biotinylated catalyst resides in the biotin-binding vestibule: addition of four equivalents of biotin to

[*] M. Dürrenberger,^[†] T. Heinisch,^[†] Y. M. Wilson,^[†] T. Rossel, E. Nogueira, L. Knörr, A. Mutschler, K. Kersten, M. J. Zimbron, J. Pierron, T. Schirmer, Prof. Dr. T. R. Ward
 Institut für Anorganische Chemie, Universität Basel
 Spitalstrasse 51, 4056 Basel (Switzerland)
 Fax: (+41) 61-267-1005
 E-mail: thomas.ward@unibas.ch

[†] These authors contributed equally to this work.

[**] This research was supported by the Swiss National Science Foundation (Grant 200020-126366), the Cantons of Basel, and Marie Curie Training Networks (FP7-ITN-238531, FP7-ITN-238434). We thank Prof. C. R. Cantor for the Sav gene.

Supporting information for this article is available on the WWW under <http://dx.doi.org/10.1002/anie.201007820>.

Table 1: Results for the chemical optimization of artificial transfer hydrogenases.

Entry	Complex	<i>ee</i> [%] [conv.] 1 ^[a]	<i>ee</i> [%] [conv.] 6 ^[b]
1	2	22 (<i>R</i>) [97]	70 (<i>R</i>) [84]
2	3	12 (<i>R</i>) [76]	45 (<i>S</i>) [56]
3	4	52 (<i>R</i>) [94]	15 (<i>R</i>) [26]
4	5	57 (<i>R</i>) [quant.]	13 (<i>R</i>) [47]

[a] The reaction was carried out at 55 °C for 15 h using 1 mol % complex **2–5** (690 μM final concentration) and 0.33 mol % tetrameric WT Sav at pH 8.0 (MOPS buffer 2.9 M) containing 3.65 M HCO₂Na (see Supporting Information for experimental details). [b] Data from Ref. [12].

Table 2: Selected results for the genetic optimization of artificial transfer hydrogenases for the production of Salsolidine **1**.^[a]

Entry	Sav mutant	T [°C]	t [h]	pH	Conv. [%]	ee [%]
1	no prot.	25	5	7.25	quant.	rac.
2	WT Sav	55	2	7.25	quant.	57 (R)
3	S112G	55	2	7.25	quant.	60 (R)
4	S112R	55	2	7.25	quant.	19 (S)
5	S112K	55	2	7.50	94	35 (S)
6	S112K	55	64	7.25	30 ^[b]	6 (S)
7	S112K	5	48	7.50	quant.	78 (S)
8	S112K	25	24	7.25	39 ^[c]	44 (S)
9	S112K ^[d]	25	24	7.25	30 ^[c]	42 (S)
10	empty plasmid	25	24	7.25	43 ^[c]	1 (S)
11	S112A	55	2	7.25	quant.	79 (R)
12	S112A	55	64	7.25	69 ^[b]	27 (R)
13	S112A	55	2	7.25	59 ^[e]	14 (R)
14	S112A	55	2	6.50	quant.	85 (R)
15	S112A	5	24	6.50	quant.	91 (R)
16	S112A	5	24	6.50	quant. ^[f]	93 (R)
17	S112A	5	24	6.50	quant. ^[g]	88 (R)
18	S112A	5	96	6.50	quant. ^[h]	96 (R)
19	S112A	5	115	6.50	86 ^[h,i]	96 (R)
20	S112A	25	24	7.25	77 ^[j]	64 (R)
21	S112A ^[d]	25	24	7.25	65 ^[j]	61 (R)
22	H87A	55	2	7.25	quant.	48 (R)
23	H127A	55	2	7.25	quant.	54 (R)
24	S112AK121T	5	24	6.50	90	54 (R)

[a] See Table 1 and Supporting Information for full experimental details; S112P was expressed as inclusion bodies and thus was not tested. [b] Acetophenone reduction yielding 1-phenylethanol **6**. [c] 50 μM $[\text{Cp}^*\text{Ir}(\text{Biot-}p\text{-L})\text{Cl}]$ (**5**; i.e. 1 mol% vs **1**) and 25 μM S112K (tetramer). [d] Precipitated protein from cell free extracts (Supporting Information). [e] Four equivalents (vs tetrameric Sav) biotin added. [f] 0.25 mol% complex **5** and 0.25 mol% S112A tetramer. [g] 1 mol% complex **5** and 0.25 mol% S112A tetramer. [h] 0.025 mol% complex **5** and 0.025 mol% S112A tetramer. [i] 86% yield of isolated product on 100 mg scale. [j] 39 μM $[\text{Cp}^*\text{Ir}(\text{Biot-}p\text{-L})\text{Cl}]$ (**5**; i.e. 1 mol% vs **1**) and 20 μM S112A (tetramer).

$[\text{Cp}^*\text{Ir}(\text{Biot-}p\text{-L})\text{Cl}]\text{C}S112A$ affords (*R*)-**1** in low *ee* (Table 2, entry 13).

- (*S*)-selectivities result from the presence of a cationic residue at position S112 (e.g. S112K and S112R, Table 2, entries 4 and 5).
- Decreasing the temperature to 5 °C allows improvement of the enantioselectivity to 91% (*R*) for **5**C112A and 78% (*S*) for **5**C112K (Table 2, entries 7 and 15). Importantly, these reactions are not sensitive to traces of oxygen: no degassing is required prior to catalysis.
- Up to 4000 turnovers can be achieved with no erosion of selectivity (Table 2, entry 18). On a preparative scale (100 mg substrate, 0.025 mol% catalyst), the *ee* could be further increased to 96%, with an isolated yield of 86% (Table 2, entry 19).
- $[\text{Cp}^*\text{Ir}(\text{Biot-}p\text{-L})\text{Cl}]\text{C}S112A$ produces the same preferred enantiomer for alcohol (*R*)-**6** and amine (*R*)-**1**. Similarly, $[\text{Cp}^*\text{Ir}(\text{Biot-}p\text{-L})\text{Cl}]\text{C}S112K$ affords (*S*)-**6** and amine (*S*)-**1**, respectively (Table 2, entries 6 and 12). This suggests that both imine and ketone reduction proceed through the same enantioselection mechanism. We thus conclude that the second coordination sphere interactions provided by

the host protein outweigh the preference of the related homogeneous catalyst.

- Increasing the ratio of $[\text{Cp}^*\text{Ir}(\text{Biot-}p\text{-L})\text{Cl}]$ vs Sav tetramer from one to four leads to a gradual erosion of enantioselectivity (93 to 88% *ee*, Table 2, entries 16 and 17). This suggests that an empty biotin binding site adjacent to a $[\text{Cp}^*\text{Ir}(\text{Biot-}p\text{-L})\text{Cl}]$ moiety within Sav may be favorable for selectivity.
- Performing catalysis with Sav mutants obtained from an ethanol precipitation step on a dialyzed protein extract yields results very similar to those obtained with dilute samples of pure protein for both S112K and S112A (Table 2, compare entries 8–10 and 20–21). This finding demonstrates that $[\text{Cp}^*\text{Ir}(\text{Biot-}p\text{-L})\text{Cl}]$ (**5**) tolerates cellular components.^[13] This opens fascinating perspectives for parallel screening as it significantly shortens the protein purification effort (from 12 to 3 days).

To gain structural insight into the best (*R*)-selective artificial metalloenzyme, crystals of S112A Sav were soaked with a solution containing an excess of cofactor **5**. The X-ray crystal structure was solved to 1.9 Å resolution. Strong residual density in the $F_o - F_c$ map indicated that all biotin-binding sites are fully occupied by ligand Biot-*p*-L (Figure 1 a,

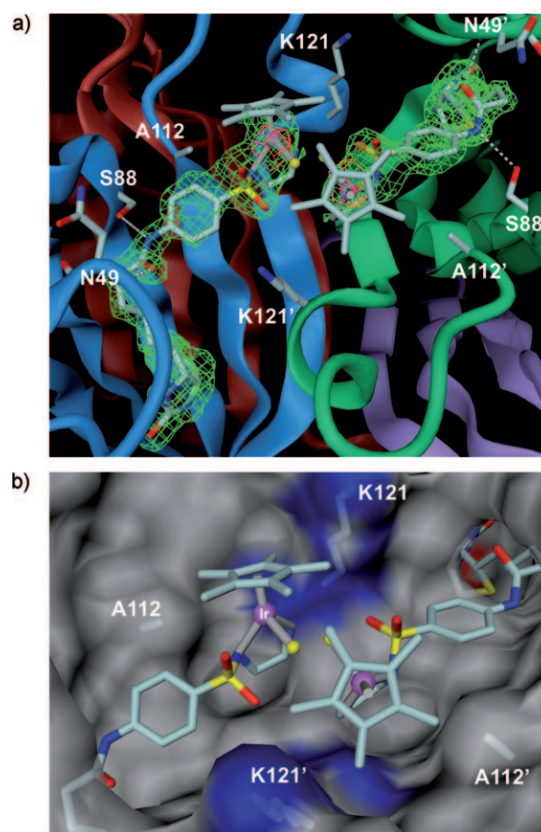


Figure 1. Close-up view of the X-ray crystal structure (PDB: 3pk2) of complex **5**C112A Sav showing two symmetry-related cofactors in the biotin-binding pocket of the protein tetramer. $F_o - F_c$ omit map colored in green (contoured at 3 σ) and anomalous difference density map (5 σ) in red (a). Surface representation with basic residues in blue, acidic in red, polar and apolar in gray (b); (chloride: yellow sphere).

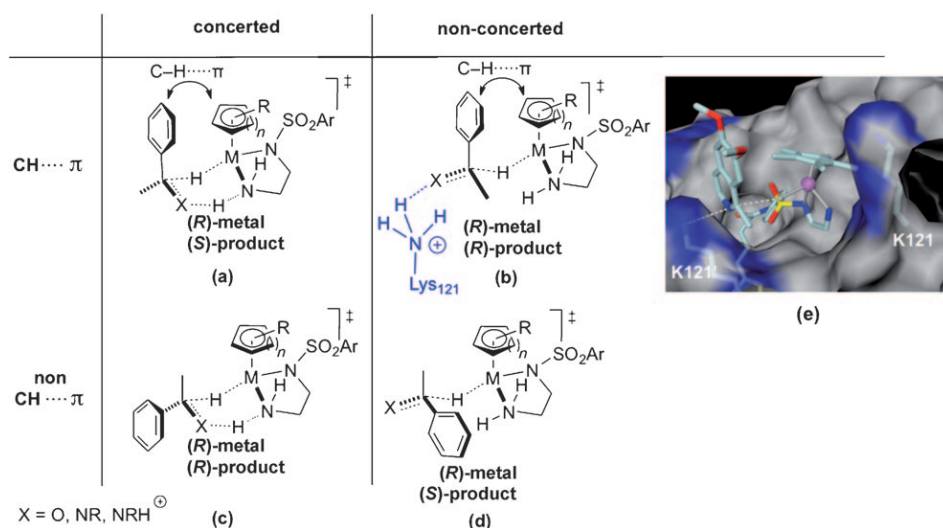


Figure 2. Possible transition states for the d^6 piano stool catalyzed asymmetric transfer hydrogenation of ketones and imines a–d. a) $\text{CH}\cdots\pi$ interaction combined with a contact between the imine N and K121 affords (*R*)-products (b and e; latter viewed from the empty biotin-binding pocket).

note that due to crystallographic symmetry all Sav monomers are identical). Adjacent to the ethylenediamine moiety of Biot-*p*-L a strong peak (15σ) in the anomalous difference map suggested the position of iridium. To avoid negative $F_o - F_c$ density the iridium atom occupancy was set to 50%. This most likely indicates partial dissociation of the $\{\text{IrCp}^*\text{Cl}\}$ fragment upon soaking, since alternative conformations appear sterically not possible. The iridium atoms of two symmetry-related cofactors (face-to-face) are separated by 5.2 Å. Despite the purity of the complex used for soaking, no $F_o - F_c$ density was found for Cp^* and chloride ligands. To prevent steric clashes between symmetry-related Cp^* groups, this bulky moiety was modeled with a dihedral angle $\text{S-N-Ir-Cp}^*_{\text{centroid}} = 98.3^\circ$ (and $\text{S-N-Ir-Cl} = -34.2^\circ$). This sets the configuration at Ir in the structure to (*S*)- $[\text{Cp}^*\text{Ir}(\text{Biot-}p\text{-L})\text{Cl}]$ (and correspondingly (*R*)- $[\text{Cp}^*\text{Ir}(\text{Biot-}p\text{-L})\text{H}]$).

Compared to the recently characterized $[(\eta^6\text{-benzene})\text{Ru}(\text{Biot-}p\text{-L})\text{Cl}]$ (**3**; S112K; PDB: 2qcb, an (*S*)-selective ATH),^[10] the absolute configuration at the metal is (*S*) in both cases, but the metal fragment is rotated along the aryl–S bond by about 150° . This prevents steric clashes between the benzene moiety and K121 of the adjacent monomer B (Figure S2b).

Additional anomalous difference density indicating iridium was found in the vicinity of the N_ϵ atoms of H87 and H127 (Figure S2c,d). These species, however, are not involved in catalysis, as demonstrated by the results obtained with the H87A and H127A mutants which are nearly identical to those obtained with WT Sav (Table 2, entries 22 and 23).

Assuming that the absolute configuration revealed in the X-ray structure is catalytically active, two transition states leading to the observed (*R*)-products (alcohol or amine) can be envisaged: non-concerted + $\text{CH}\cdots\pi$ or concerted + non- $\text{CH}\cdots\pi$, respectively (Figure 2b,c). Qualitative modeling of the imine substrate into a vacated neighboring biotin site was carried out for both possible transition states leading to (*R*)-**1**. For the concerted + non- $\text{CH}\cdots\pi$ mechanism, steric clashes

between the substrate's aromatic group and the protein project the imine moiety into the Cp^* fragment (Figure S2e). In contrast, for the non-concerted + $\text{CH}\cdots\pi$ interaction, no steric clashes with the protein are apparent (Figure 2e). Interestingly, the imine functionality lies close to the ammonium group of K121 (of the adjacent monomer). This contact may replace the amine group of the ligand for the delivery of a proton to the substrate (Figure 2b,e). To test this possibility, the double mutant S112AK121T was tested in catalysis (Table 2, entry 24). The erosion in enantioselectivity suggests that the non-concerted + $\text{CH}\cdots\pi$ mechanism is operative both for the ATH of ketones and imines.

anism is operative both for the ATH of ketones and imines.

In summary, introduction of a biotinylated iridium piano stool complex $[(\eta^5\text{-Cp}^*)\text{Ir}(\text{Biot-}p\text{-L})\text{Cl}]$ (**5**) within streptavidin affords an artificial imine reductase. Both (*R*)-**1** (96% *ee*) and (*S*)-**1** (78% *ee*) are accessible with the same organometallic moiety. This corresponds to a $\Delta\Delta G^\ddagger$ of $3.3 \text{ kcal mol}^{-1}$ for a single-point mutation. With the implementation of laboratory evolution protocols for the optimization of artificial metalloenzymes for the reduction of more challenging imines in mind,^[1,14] we have shown that the screening can be performed in air with up to 4000 TON and, most importantly, on precipitated protein rather than on rigorously purified Sav samples used thus far. Based on X-ray structural data, we suggest that the reaction proceeds, both for the imine and the ketone reduction, through a non-concerted + $\text{CH}\cdots\pi$ interaction,^[7b,15] whereby the residue K121 may be involved in the protonation step.

Received: December 12, 2010

Published online: February 24, 2011

Keywords: artificial metalloenzymes · asymmetric catalysis · imine reduction · piano stool complexes · transfer hydrogenation

[1] N. J. Turner, *Nat. Chem. Biol.* **2009**, *5*, 567–573.

[2] a) T. C. Nugent, M. El-Shazly, *Adv. Synth. Catal.* **2010**, *352*, 753–819; b) N. Fleury-Brégeot, V. de La Fuente, S. Castillon, C. Claver, *ChemCatChem* **2010**, *2*, 1346–1371.

[3] L. K. Thalén, D. Zhao, J.-B. Sortais, J. Paetzold, C. Hoben, J.-E. Backvall, *Chem. Eur. J.* **2009**, *15*, 3403–3410.

[4] R. Noyori, S. Hashiguchi, *Acc. Chem. Res.* **1997**, *30*, 97–102.

[5] a) M. Yamakawa, I. Yamada, R. Noyori, *Angew. Chem.* **2001**, *113*, 2900–2903; *Angew. Chem. Int. Ed.* **2001**, *40*, 2818–2821; b) M. Yamakawa, I. Yamada, R. Noyori, *Angew. Chem.* **2001**, *113*, 2900–2903; c) S. E. Clapham, A. Hadzovic, R. H. Morris, *Coord. Chem. Rev.* **2004**, *248*, 2201–2237; d) T. Ikariya, A. J. Blacker, *Acc. Chem. Res.* **2007**, *40*, 1300–1308.

- [6] a) N. Uematsu, A. Fujii, S. Hashiguchi, T. Ikariya, R. Noyori, *J. Am. Chem. Soc.* **1996**, *118*, 4916–4917; b) C. Li, J. Xiao, *J. Am. Chem. Soc.* **2008**, *130*, 13208–13209; c) L. Evanno, J. Ormala, P. M. Pihko, *Chem. Eur. J.* **2009**, *15*, 12963–12967; d) C. Wang, C. Li, X. Wu, A. Pettman, J. Xiao, *Angew. Chem.* **2009**, *121*, 6646–6650; *Angew. Chem. Int. Ed.* **2009**, *48*, 6524–6528; e) C. Wang, C. Li, X. Wu, A. Pettman, J. Xiao, *Angew. Chem.* **2009**, *121*, 6646–6650; *Angew. Chem. Int. Ed.* **2009**, *48*, 6524–6528; f) J. Wu, F. Wang, Y. Ma, X. Cui, L. Cun, J. Zhu, J. Deng, B. Yu, *Chem. Commun.* **2006**, 1766–1768.
- [7] a) J. Mao, D. C. Baker, *Org. Lett.* **1999**, *1*, 841–843; b) J. E. D. Martins, G. J. Clarkson, M. Wills, *Org. Lett.* **2009**, *11*, 847–850.
- [8] a) J. B. Aberg, J. S. M. Samec, J. Bäckvall, *Chem. Commun.* **2006**, 2771–2773; b) D. G. Blackmond, M. Ropic, M. Stefinovic, *Org. Process Res. Dev.* **2006**, *10*, 457–463.
- [9] a) Y. Lu, N. Yeung, N. Sieracki, N. M. Marshall, *Nature* **2009**, *460*, 855–862; b) F. Rosati, G. Roelfes, *ChemCatChem* **2010**, *2*, 916–927; c) M. T. Reetz, *Top. Organomet. Chem.* **2009**, *25*, 63–92; d) S. Abe, T. Ueno, Y. Watanabe, *Top. Organomet. Chem.* **2009**, *25*, 25–43; e) Q. Jing, R. J. Kazlauskas, *ChemCatChem* **2010**, *2*, 953–957; f) P. J. Deuss, G. Popa, C. H. Botting, W. Laan, P. C. Kamer, *Angew. Chem.* **2010**, *122*, 5443–5445; *Angew. Chem. Int. Ed.* **2010**, *49*, 5315–5317; g) P. J. Deuss, G. Popa, C. H. Botting, W. Laan, P. C. Kamer, *Angew. Chem.* **2010**, *122*, 5443–5445; *Angew. Chem. Int. Ed.* **2010**, *49*, 5315–5317; h) J. Podtetenieff, A. Taglieber, E. Bill, E. J. Reijerse, M. T. Reetz, *Angew. Chem.* **2010**, *122*, 5277–5281; *Angew. Chem. Int. Ed.* **2010**, *49*, 5151–5155; i) J. Podtetenieff, A. Taglieber, E. Bill, E. J. Reijerse, M. T. Reetz, *Angew. Chem.* **2010**, *122*, 5277–5281; *Angew. Chem. Int. Ed.* **2010**, *49*, 5151–5155; j) T. Heinisch, T. R. Ward, *Curr. Opin. Chem. Biol.* **2010**, *14*, 184–199; k) P. Fournier, R. Fiammengo, A. Jäschke, *Angew. Chem.* **2009**, *121*, 4490–4493; *Angew. Chem. Int. Ed.* **2009**, *48*, 4426–4429; l) P. Fournier, R. Fiammengo, A. Jäschke, *Angew. Chem.* **2009**, *121*, 4490–4493; *Angew. Chem. Int. Ed.* **2009**, *48*, 4426–4429.
- [10] a) M. Creus, A. Pordea, T. Rossel, A. Sardo, C. Letondor, A. Ivanova, I. LeTrong, R. E. Stenkamp, T. R. Ward, *Angew. Chem.* **2008**, *120*, 1422–1426; *Angew. Chem. Int. Ed.* **2008**, *47*, 1400–1404; b) M. Creus, A. Pordea, T. Rossel, A. Sardo, C. Letondor, A. Ivanova, I. LeTrong, R. E. Stenkamp, T. R. Ward, *Angew. Chem.* **2008**, *120*, 1422–1426; *Angew. Chem. Int. Ed.* **2008**, *47*, 1400–1404.
- [11] T. S. Kaufman, *Tetrahedron: Asymmetry* **2004**, *15*, 1203–1237.
- [12] C. Letondor, A. Pordea, N. Humbert, A. Ivanova, S. Mazurek, M. Novic, T. R. Ward, *J. Am. Chem. Soc.* **2006**, *128*, 8320–8328.
- [13] a) C. Streu, E. Meggers, *Angew. Chem.* **2006**, *118*, 5773–5776; *Angew. Chem. Int. Ed.* **2006**, *45*, 5645–5648; b) C. Streu, E. Meggers, *Angew. Chem.* **2006**, *118*, 5773–5776; *Angew. Chem. Int. Ed.* **2006**, *45*, 5645–5648; c) V. Köhler, Y. M. Wilson, C. Lo, A. Sardo, T. R. Ward, *Curr. Opin. Biotechnol.* **2010**, *21*, 744–752.
- [14] M. T. Reetz, J. J.-P. Peyerlans, A. Maichele, Y. Fu, M. Maywald, *Chem. Commun.* **2006**, 4318–4320.
- [15] J. E. D. Martins, M. A. C. Redondo, M. Wills, *Tetrahedron: Asymmetry* **2010**, *21*, 2258–2264.

Supporting Information

© Wiley-VCH 2011

69451 Weinheim, Germany

Artificial Transfer Hydrogenases for the Enantioselective Reduction of Cyclic Imines**

*Marc Dürrenberger, Tillmann Heinisch, Yvonne M. Wilson, Thibaud Rossel, Elisa Nogueira, Livia Knörr, Annette Mutschler, Karoline Kersten, Malcolm Jeremy Zimbron, Julien Pierron, Tilman Schirmer, and Thomas R. Ward**

X-RAY CRYSTAL STRUCTURE OF [Cp*Ir(Biot-*p*-L)Cl] \subset S112A SAV

Crystallization

Mutant S112A of the Sav fragment 13-159 with a N-terminal T7-tag was expressed and crystallized within 3 days by the hanging drop vapor diffusion technique upon mixing 6.5 μ L protein solution (26 mg/mL in water) and 3.5 μ L precipitation buffer (2.0 M ammonium sulfate, 0.1 M sodium acetate, pH 4.0), followed by equilibration against 500 μ L precipitation buffer. Single S112A Sav crystals were transferred into 10 μ L of 10 mM [Cp*Ir(Biot-*p*-L)Cl] **5** in precipitation buffer (10 % final DMF concentration). After 3 h, the crystals were transferred into cryobuffer containing 30 % glycerol in precipitation buffer. Finally, crystals were shock-frozen and stored in liquid nitrogen.

Data Collection and Structure Solution

X-ray diffraction data of a **5** \subset S112A Sav crystal were collected at the Swiss Light Source

(beam line PX3) at a wavelength of 0.9793 Å. Data indexing, integration and scaling were carried out with programs MOSFLM and SCALA of the CCP4-Suite⁵ (**Supporting Table 2**). The structure was solved by molecular replacement with program MOLREP⁶ using as search model the structure with PDB code 2qcb,⁷ lacking ligand and water molecules. Rigid body and full restraint refinement, including TLS and individual B-factor refinement, was carried out with program REFMAC-5.⁸ Electron and anomalous scattering density visualization as well as model building was performed with programs O⁹ and COOT.¹⁰ Ligand-protein interactions were analyzed using program LIGPLOT¹¹ and structure validation using MOLPROBITY*. Structural figures were drawn with program DINO⁺.

Supporting Table 2

Data Processing

Resolution (Å)	46.0 - 1.9
Space Group	I4 ₁ 22
Cell dimensions (Å)	a = 57.6, b = 57.6, c = 184.0 $\alpha, \beta, \gamma = 90^\circ$
R _{merge} (%)	10.9 (20.1)*
No. unique reflections	11601
Multiplicity	5.5 (4.0)
Completeness	91.2 (87.4)
I/sig(I)	9.7 (4.5)

Structure Refinement

Resolution (Å)	46.0 - 1.9
R _{work} /R _{free}	18.5/20.4
B-factors (Å ²)	
Protein	9.5
BIR	23.1
BI1	29.1
BI2	43.4

* <http://molprobity.biochem.duke.edu/>

+ <http://www.dino3d.org/>

Water	18.4
R.m.s deviations from ideal values	
Bond lengths (Å)	0.011
Bond angles (°)	2.162

* values in parenthesis are for the highest resolution bin (2.0 - 1.9 Å). Please find ligands BIR, BI1 And BI2 described in the text.

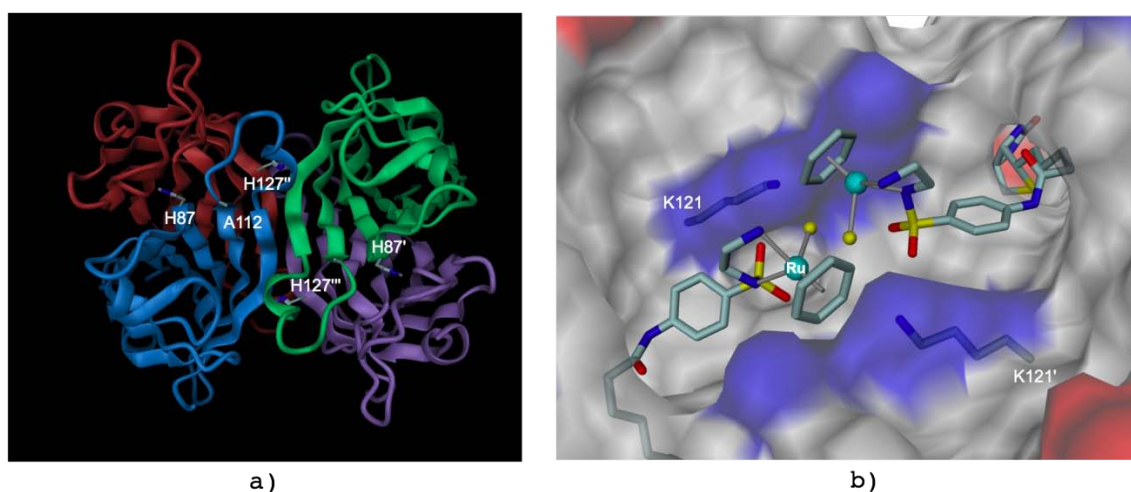
Structure Description

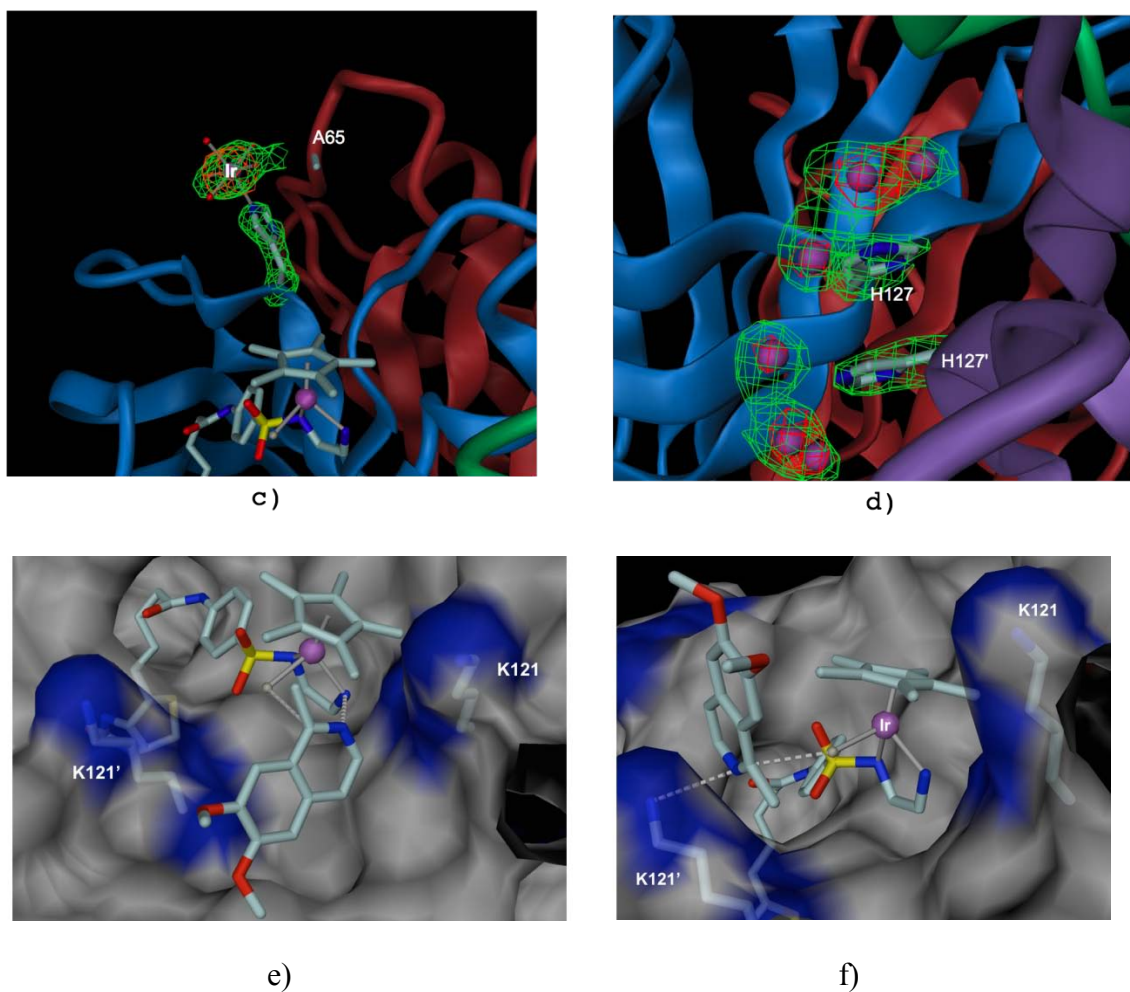
Overall structure: The asymmetric unit contains one S112A Sav monomer. Application of crystal symmetry yields the 222-symmetrical (D₂) tetramer (**Supporting Figure 2a**). The final model comprises residues 13-134 with 95.8 % of the residues found in the most-favored regions of a Ramachandran plot, and no Ramachandran outliers. As observed before,⁷ both the N-terminal T7 tag (residues 1-12) and 25 residues at the C-terminus are not resolved, probably due to disorder. The flexible loop comprising residues 45-53 was found in the open conformation, as described elsewhere.¹² In addition, the structure comprises three ligands (BIR, BI1 and BI2) and 71 water molecules.

[Cp*Ir(Biot-*p*-L)Cl] in the biotin-binding site: Residual positive electron density was detected in the biotin-binding pocket and in the vestibule surrounded by loops 112-122 and 45-53 (**Figure 2a**). As expected from the large f'' (8.3 e⁻) of Ir at the measured wavelength, a strong peak (15 σ) in the anomalous difference map was found in the vestibule close to residue A112 and next to a molecular 2-fold symmetry axis. Coordinates for **5** (ligand PDB identifier BIR) were generated from ligand [η^6 -(benzene)Ru(Biot-*p*-L)Cl] of structure 2qcb. The Ru and the benzene group in 2qcb were replaced by Ir and Cp*, respectively. Parameters of bond lengths and angles between Ir and N4, N5, Cp* as well as Cl for structure refinement were adapted from complex [Cp*Ir(en)Cl] (en: ethylenediamine) from the Cambridge Structural Database (CSD code CICFEA). The interactions of the biotin moiety of **5** and

S112A Sav are the same as described elsewhere for wild type Sav (**Figure 2a**).¹³ The valeric acid carbonyl and amide of **5** form H-bonds to N49-N (2.8 Å) and S88-O γ (2.9 Å), respectively. Nitrogen N5 of the ethylenediamine group of **5** lies within H-bonding distance to the carbonyl oxygen of K121 (2.8 Å).

Iridium binding to H87 and H127: Further anomalous difference density peaks were found close to H87 and H127 (24 and 7-10 σ , respectively, **Supporting Figure 2a, c and d**). The density next to the H87 imidazole was fitted with $[\text{Ir}(\text{OH}_2)_5]^{3+}$ and an occupancy of 70 % (ligand PDB identifier BI1). Thereby, the axial position of the octahedral complex is saturated by H87-N ϵ (**Supporting Figure 2c**). Residue H127 is located in a cavity formed between two symmetry-related Sav monomers. The imidazole side chains of two symmetry-related H127 interact by π -stacking. Anomalous difference density peaks in the vicinity to the H127 imidazole were modeled with three iridium atoms of varying occupancy according to the peak strength (ligand PDB identifier BI2, **Supporting Figure 2d**). The positions of these atoms relative to the orientation of the H127-N ϵ lone-pair orbital does not suggest coordinative interactions. Due to a lack of experimental data no further ligands to the iridium atoms were modeled.





Supporting Figure 2: Cofactor binding in Sav mutants. S112A Sav tetramer, view along molecular 2-fold axis, showing residues in vicinity to anomalous difference peaks (a, PDB code 3pk2). Close-up view of cofactor in complex $[\eta^6\text{-(benzene)Ru(Biot-}p\text{-L)}] \subset$ S112K Sav (b, PDB code 2qcb, basic residues in blue, acidic in red, polar and apolar in grey). Ligand $[\text{Ir}(\text{OH}_2)_5]^{3+}$ bound to H87-N ϵ (c) and Ir atoms in vicinity to H127 (d, Fo-Fc omit map in green contoured at 3σ and anomalous difference density in red contoured at 5σ). Substrate-catalyst complex for proposed concerted & non-CH $\cdots\pi$ transition state (e) and non-concerted & CH $\cdots\pi$ transition state (f), viewed from the empty neighboring biotin-binding pocket.

REFERENCES

- (1) C. Letondor, A. Pordea, N. Humbert, A. Ivanova, S. Mazurek, M. Novic, T. R. Ward, *J. Am. Chem. Soc.* **2006**, *128*, 8320-8328.
- (2) N. Humbert, A. Zocchi, T. R. Ward, *Electrophoresis* **2005**, *26*, 47-52.
- (3) G. Klein, N. Humbert, J. Gradinaru, A. Ivanova, F. Gilardoni, U. E. Rusbandi, T. R. Ward, *Angew. Chem. Int. Ed.* **2005**, *44*, 7764-7767; G. Klein, N. Humbert, J. Gradinaru, A. Ivanova, F. Gilardoni, U. E. Rusbandi, T. R. Ward, *Angew. Chem.* **2005**, *117*, 7942-7945.
- (4) M. Skander, N. Humbert, J. Collot, J. Gradinaru, G. Klein, A. Loosli, J. Sauser, A. Zocchi, F. Gilardoni, T. R. Ward, *J. Am. Chem. Soc.* **2004**, *126*, 14411-14418.
- (5) *Acta Crystallogr., Sect. D: Biol. Crystallogr.* **1994**, *50*, 760-763.
- (6) G. N. Murshudov, A. A. Vagin, E. J. Dodson, *Acta Crystallogr., Sect. D: Biol. Crystallogr.* **1997**, *53*, 240-255.
- (7) M. Creus, A. Pordea, T. Rossel, A. Sardo, C. Letondor, A. Ivanova, I. LeTrong, R. E. Stenkamp, T. R. Ward, *Angew. Chem. Int. Ed.* **2008**, *47*, 1400-1404; M. Creus, A. Pordea, T. Rossel, A. Sardo, C. Letondor, A. Ivanova, I. LeTrong, R. E. Stenkamp, T. R. Ward, *Angew. Chem.* **2008**, *120*, 1422-1426.
- (8) A. T. Brünger, *Acta Crystallogr., Sect. D: Biol. Crystallogr.* **1993**, *49*, 24-36.
- (9) T. A. Jones, J.-Y. Zou, S. W. Cowan, M. Kjeldgaard, *Acta Crystallogr., Sect. A: Found. Crystallogr.* **1991**, *47*, 110-119.
- (10) P. Emsley, K. Cowtan, *Acta Crystallogr., Sect. D: Biol. Crystallogr.* **2004**, *60*, 2126-2132.
- (11) A. C. Wallace, R. A. Laskowski, J. M. Thornton, *Protein Eng.* **1995**, *8*, 127-134.
- (12) S. Freitag, I. LeTrong, L. Klumb, P. S. Stayton, R. E. Stenkamp, *Protein Sci.* **1997**, *6*, 1157-1166.

2.1. Author Contributions

General idea:

Thomas R. Ward

Synthesis of biotinylated piano stool metal complexes:

Marc Dürrenberger, Christophe Letondor, Annette Mutschler, Thibaud Rossel, Julien Pierron, Jeremy M. Zimbron

Production of streptavidin variants:

Yvonne M. Wilson, Elisa Nogueira, Livia Knörr, Karoline Kersten

Screening of streptavidin mutants and biotinylated metal complexes for transfer hydrogenation of salsolidine precursor:

Marc Dürrenberger, Yvonne Wilson, Annette Mutschler, Thibaud Rossel, Julien Pierron, Jeremy M. Zimbron

Crystal structure analysis of the best (*R*)-enantioselective ATHase:

Tillmann Heinisch, Tilman Schirmer

Manuscript writing:

Thomas R. Ward and all other authors

2.2. Comment on Publication

2.2.1. Asymmetric Imine Transfer Hydrogenation Catalysts: Organometallic Complexes, Enzymes and Artificial Metalloenzymes

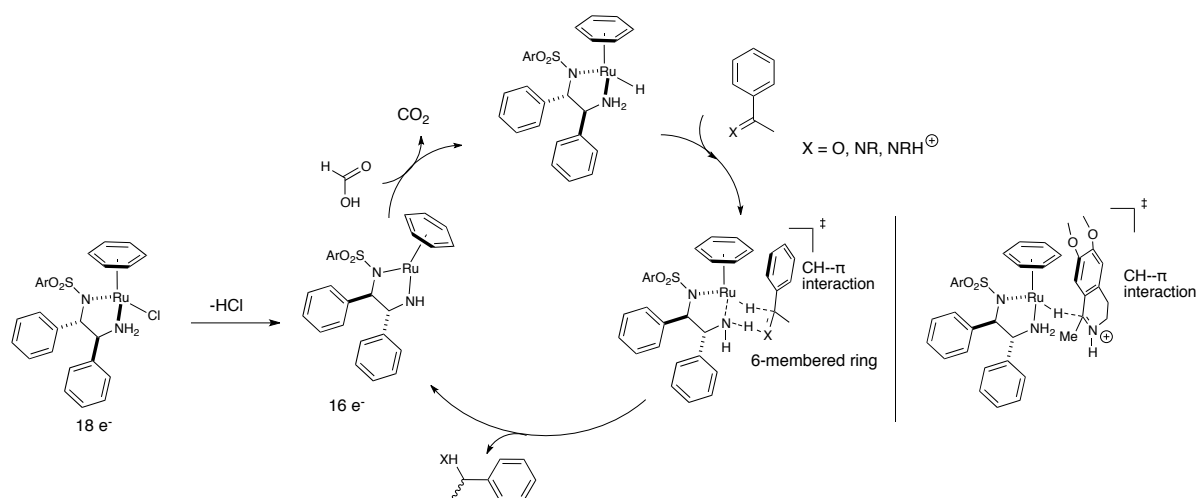
As an alternative to the powerful asymmetric hydrogenation, the asymmetric transfer hydrogenation (ATH) of C=O, C=N or activated C=C double bonds into chiral alcohols, amines and alkanes gained much interest in the last two decades for the production of fine chemicals and pharmaceuticals. The formal hydride transfer between a donor and an acceptor molecule is catalyzed in Nature by the family of oxidoreductases,⁵³ while in the laboratory mainly d⁶ piano stool transition metal complexes, and to a smaller extent, organocatalysts are used. While homogenous catalysts for the ATH of many ketones have been described, the efficient enantioselective and “green” reduction of imines is still a challenge.⁵⁴ The asymmetric transfer hydrogenation of ketones and imines is a valuable reaction to test the scope and limitations of AME design based on the (strept)avidin-biotin technology and other protein-ligand complexes. Novel asymmetric transfer hydrogenation hybrid catalysts can contribute in the production of high-value optically active amines.

Organometallic Complexes for Asymmetric Transfer Hydrogenation of Imines:

d⁶ piano stool-shaped transition metal complexes have been proven versatile for the asymmetric transfer hydrogenation of ketones, enones and imines.^{2,54,55} Named habitually after the Japanese chemist and Nobel Prize laureate, these Noyori-type catalysts consist of a central transition metal (Ru(II), Ir(III) and Rh(III)), an arene cap (e.g. benzene, *p*-cymene or pentamethylcyclopentadienyl, Cp*) and three “leg”-substituents (**Scheme M1**).⁵⁶ The presence of bidentate ligands such as aminoethylalcohol or tosylthylenediamine (TosEN hereafter) has an accelerating effect on the reaction rate.⁵⁶ Chiral derivatives of TosEN (e.g. tosyldiphenylethylenediamine, (*R,R*)- or (*S,S*)-TosDPEN hereafter) allow for the enantioselective hydride transfer from the catalyst to the substrate. As a hydride source, isopropanol, an azeotropic mixture of formic acid and triethylamine (5:2) or sodium formate are commonly used. The reaction performs best in polar solvents such as acetonitrile, dichloromethane, isopropanol or water.

The catalytic cycle is initiated by hydrogen chloride abstraction of the 18 electron metal chloro-complex to yield a planar 16-electron complex (**Scheme M1**). Hydride transfer from formate to the 16-electron complex yields the activated metal hydrido complex. Depending on the substrate, the substrate-catalyst transition state can be stabilized i) by CH••• π interactions

between the catalyst's arene cap and an aromatic group of the substrate and ii) by the formation of a 6-membered-ring arrangement between catalyst and substrate. No direct substrate-metal coordination is involved in the reaction mechanism (outer sphere mechanism). The chirality at the metal determines the chirality of the product. Besides the beneficial interactions between catalyst and substrate via the CH••• π bond and the cyclic intermediate, the origins of the enantioselection stem from the repulsion of the substrate by the phenyl groups of the ligand. Release of the product yields the 16-electron species, which can undergo the next catalytic cycle.



Scheme M1: Catalytic cycle of asymmetric transfer hydrogenation of ketone and imines with $[(\eta^6\text{-benzene})\text{Ru}(\text{S,S-TosDPEN})\text{Cl}]$ catalyst. The proposed transition state of the analogous reaction with the salsolidine precursor is depicted on the right side.⁵⁷

In the last two decades, numerous piano stool transition metal complexes with various chiral ligands have been described for the effective enantioselective reduction of many different ketones into the corresponding alcohols, including sterically demanding aliphatic and aromatic, unfunctionalized and functionalized ketones (**Figure M4**).⁵⁴

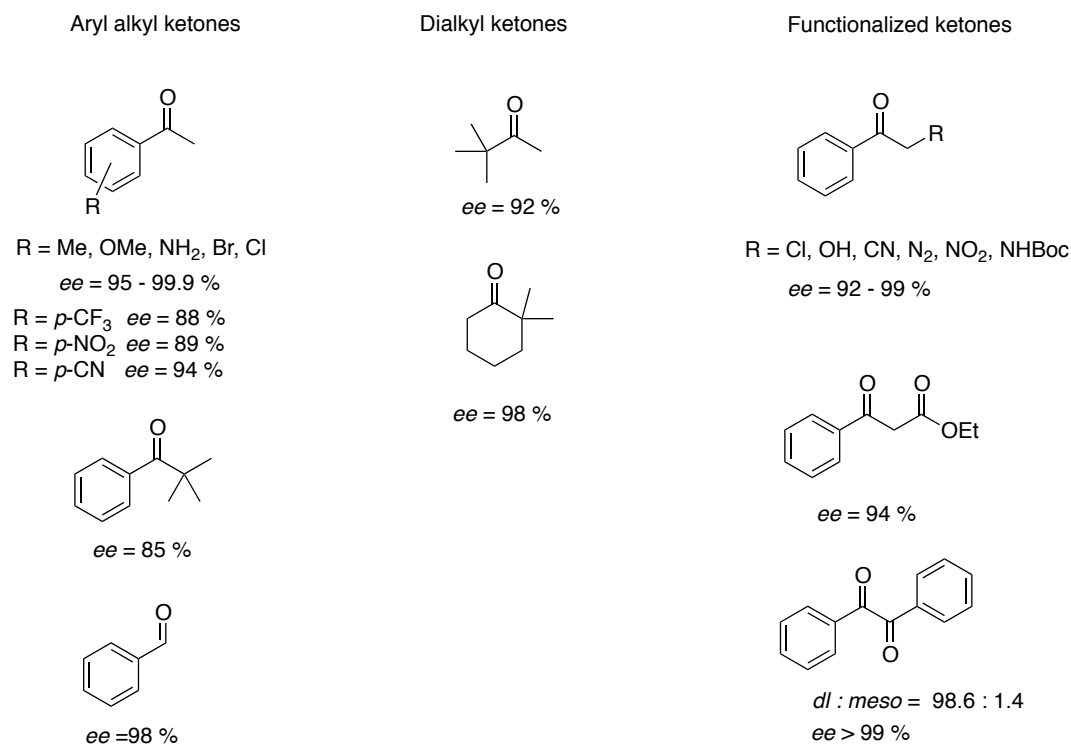


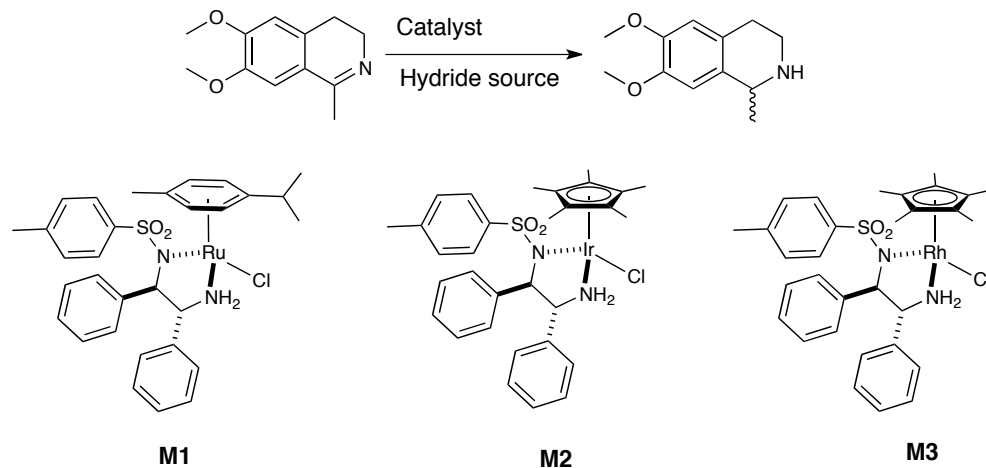
Figure M4: Scope of homogenous asymmetric transfer hydrogenation of ketones with piano stool transition metal complexes.^{2,54,55}

In contrast, examples of organometallic catalysts for the ATH of imines to obtain chiral primary and secondary amines are rarer (**Figure M5 and Table M1**). Chiral terminal alkyl and aryl amines can be obtained by transition metal-catalyzed reductive amination⁵⁸ or via formation of the *N*-diphenylphosphinylimines from the corresponding ketones and subsequent transfer hydrogenation.⁵⁹ Generally, cyclic imines yield higher *ees* and react faster than linear ones.⁶⁰ The homogeneous ATH of the cyclic imine salsolidine precursor in water compared to organic solvents is possible but requires longer reaction times (**Table M1**).

Substrate	Catalyst	Ligand	Reaction condition	Yield	<i>Ee</i>
	$[(p\text{-cymene})\text{RuCl}_2]_2$ (1 mol%)		0.1 M <i>i</i> PrOH, <i>i</i> PrOK (5 mol%) rt 2 min	80 %	70 % (<i>S</i>)
	$[\text{Cp}^*\text{RhCl}_2]_2$		$\text{HCO}_2\text{H}:\text{NEt}_3$ DCM 40 min	93 %	68 %
	$[\text{Cp}^*\text{RhCl}_2]_2$		$\text{HCO}_2\text{H}:\text{NEt}_3$		99 %
R = naphthyl					
		see Table M1		95 - 99.9 %	

Figure M5: Scope of homogenous asymmetric transfer hydrogenation of imines with piano stool transition metal complexes.^{59,61,62}

Table M1: Homogenous asymmetric transfer hydrogenation of salsolidine precursor.^{56,63–65}



Catalyst	Catalyst loading vs. substrate (mol%)	Solvent	Hydride source	Time (h)	Conv. (%)	<i>Ee</i> (%)
M1	0.5	CH ₂ Cl ₂	HCO ₂ H/ Et ₃ N	3	99	95 (<i>S</i>)
M1	0.6	H ₂ O	NaCO ₂ H	16	90	99 (<i>S</i>)
M2	1	H ₂ O	NaCO ₂ H	24	88	92 (<i>S</i>)
M3	0.5	CH ₃ CN	HCO ₂ H / Et ₃ N	0.2	96	89 (<i>S</i>)

Enzymes for Asymmetric Transfer Hydrogenation of Imines:

Hydrolases, amine oxidases, transaminases, decarboxylases and imine reductases have been used to obtain chiral amines i) from racemic amines or amides, ii) from ketones or iii) from imines (**Figure M6**).⁵⁹ Product formation is achieved by i) kinetic resolution, ii) dynamic kinetic resolution or deracemization, and iii) asymmetric synthesis.⁶⁰ Using hydrolases, oxidases and transaminases, numerous chiral aliphatic and aromatic primary and secondary amines have been synthesized for academic and industrial use.

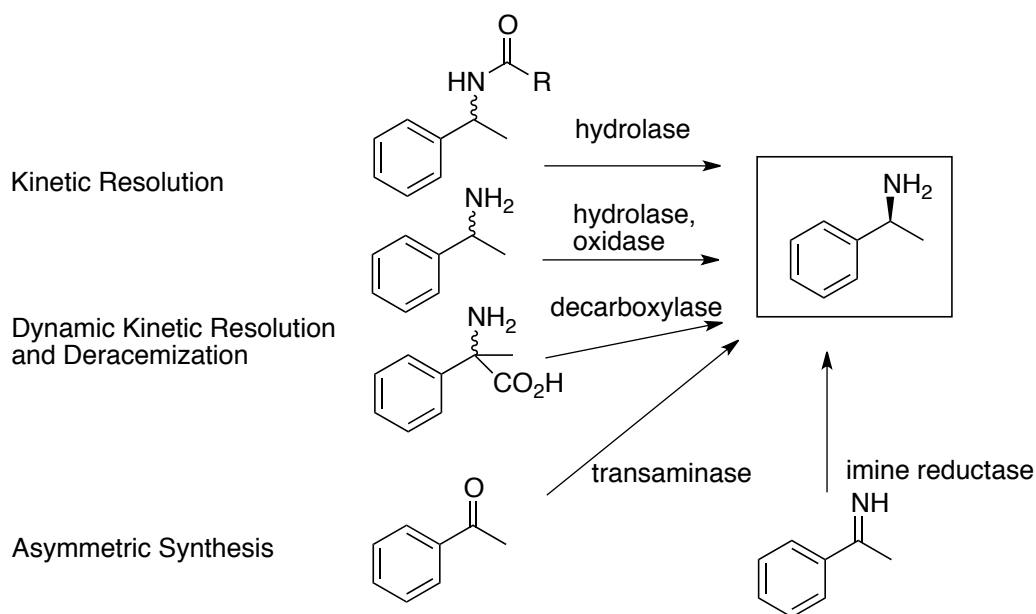


Figure M6: Biocatalytic routes to chiral terminal amines.

In Nature, hydrogen transfer reactions are carried out by oxidoreductases. During enzymatic ATH, cofactors such as NADH, NADPH, FADH₂ or tetrahydrofolate act as hydride sources. The H⁻ charged cofactor binds to the apo-enzyme followed by binding of the substrate in

close proximity to the cofactor (**Figure M7**).⁶⁶ In the holoenzyme, metals (e.g. Zn(II)) and/or amino acids act as general acids to increase the electrophilicity of the substrate's C=O, C=N or C=C double bond by hydrogen bonding. This facilitates the transfer of the coenzyme's reactive hydride, which is located in close proximity to the reactive double bond. Very high enantioselectivities (>99 % *ee*) are induced by the tight interaction between holoenzyme and substrate (**Figure M7**). The enantioselection is guided by the interactions of the substrate with the 1st and the 2nd coordination sphere around the reactive hydride. Once product and cofactor have been released from the enzyme, latter can be recharged with a H⁻ by different enzymes such as formate-, glucose- and alcohol dehydrogenase or NDAPH-reductase, which use formate, sugars or electrons from water (via photosystem II and I) as electron source.⁵³

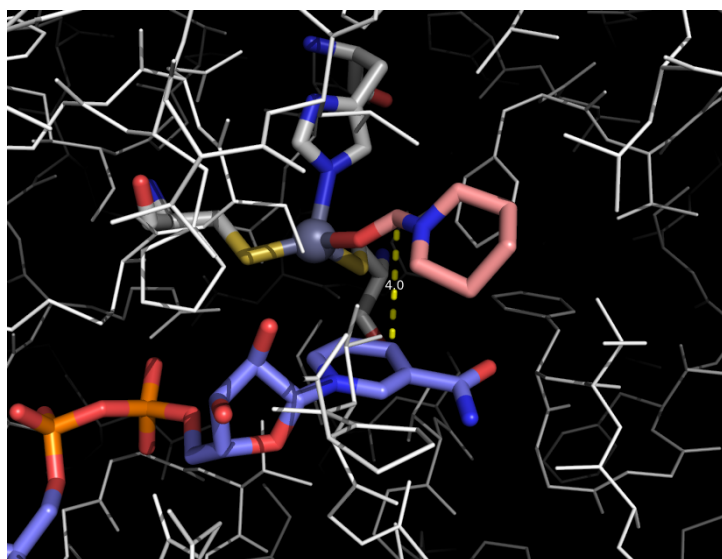


Figure M7: Crystal structure (PDB 1LDE) of the active site of horse liver alcohol dehydrogenase in complex with inhibitor *N*-formyl piperidine (orange). The hydride-donating NADPH is shown in blue, the Zn(II)Cys₂His motif in grey and the inhibitor- and coenzyme-binding residues in white.

The spectrum of ketoreductases that allow asymmetric reduction of numerous aliphatic and aromatic ketones of commercial relevance is broad.⁵⁹ The investigation of novel ketoreductases is achieved by i) the activity screening of microorganisms, ii) the expression and activity screening of reductases from metagenomes and iii) the adaptation of characterized ketoreductases by saturation mutagenesis or directed evolution. Common features of established ketoreductases are the use of cofactors NADH or NADPH, the application in whole cells or in purified form, the tolerance to some organic solvents and

elevated temperatures. Glucose dehydrogenase or formate dehydrogenase are often used to recycle the cofactor (**Figure M8**).

For example, Hasagawa and coworkers from the company Kaneka Cooperation screened 10 microorganisms for their activity to selectively reduce 4-chloroacetoacetate (COBE) into (*R*)-4-chloro-3-hydroxybutyrate (CHBE), a synthesis precursor of the ACE inhibitor captopril.⁵⁹ Highest activity and enantioselectivity was found for the strain *Candida magnolia*. The NADPH-dependent COBE-reductase of *Candida magnolia* was expressed in *E. coli* together with glucose dehydrogenase for cofactor recycling. This biocatalyst yielded >99 % *ee* in favor of the *R*-alcohol at 55 °C in a biphasic system of water and organic solvent, which was subsequently used to separate the product. Furthermore, a variant of the *Candida magnolia* COBE-reductase was engineered by structure-based rational design, which was functional in conjunction with the cofactor NADH instead of NADPH. This allowed the coexpression of a formate dehydrogenase (FDH) in *E. coli* to recycle the cofactor with formate instead of glucose (**Figure M8**).

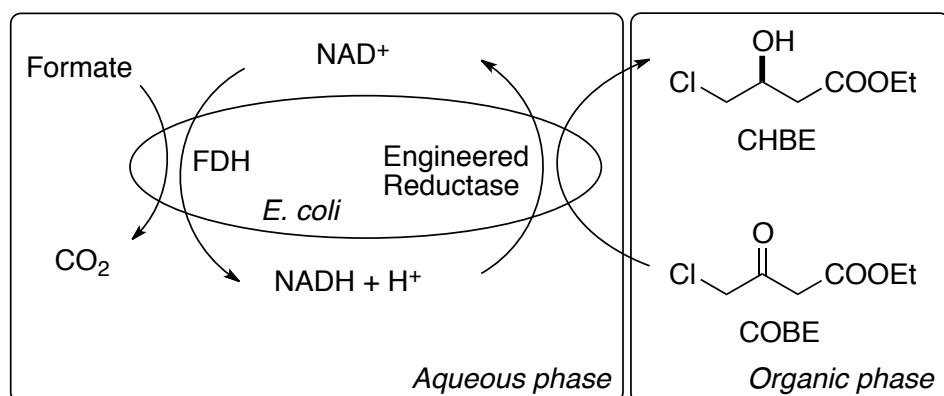
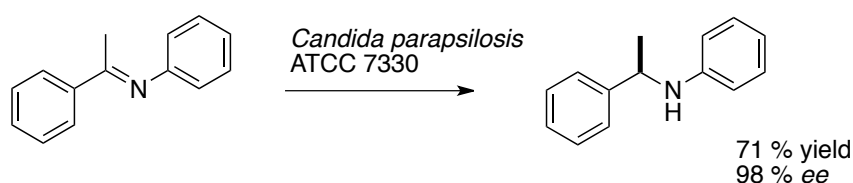


Figure M8: Biocatalytic transfer hydrogenation of a ketone using an engineered alcohol dehydrogenase.

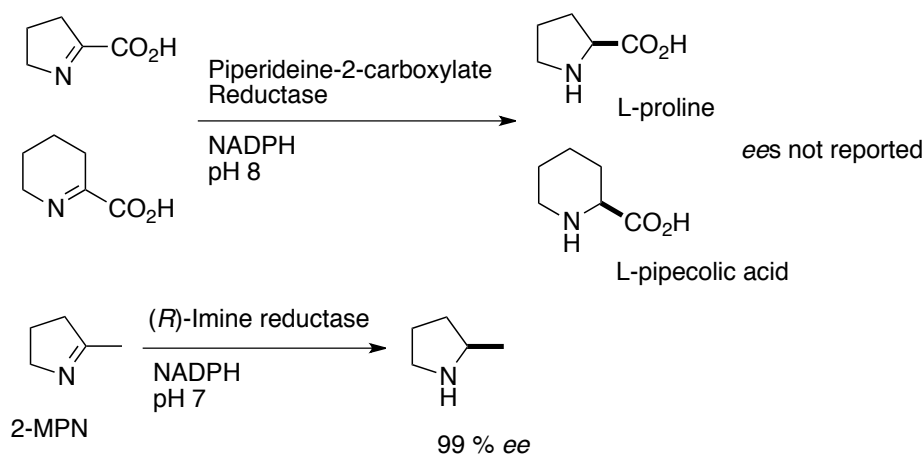
In contrast to ketoreductases, only few examples of the biocatalytic asymmetric transfer hydrogenation of imines are reported and none of these processes is yet of commercial relevance. In these reactions whole cells as well as purified enzymes are used as catalysts (**Figure M9**). Water hydrolysis of the imine substrate limits the screening of the catalyst and mainly cyclic imines are used. Nagasawa and coworkers screened hundreds of yeast, fungi and bacterial strains for the reduction of 2-methyl-pyrroline (2-MPN).⁶⁷ Only five *streptomyces sp.* strains were found to be active. An NADPH-dependent, *R*-selective imine reductase, that produces (*R*)-2-methyl-pyrrolidine with 99 % *ee*, could be isolated from the

cell extract by step-wise fractionation. In another example, based on the homology model of a leucine dehydrogenase from *Bacillus stereothermophilus* and the crystal structure of a phenylalanine dehydrogenase from *Rhodococcus sp.* M4, Bommarius and coworkers created libraries of active site mutants of the leucine dehydrogenase and tested them in the asymmetric reductive amination of various ketones.⁶⁸ While the wild type leucine dehydrogenase did not yield any conversion of methylisobutylketone, the corresponding *R*-amine was obtained in 99.8 % *ee* with mutant K68S-E114V-N261I-V291C (**Figure M9**).

Imine reduction with whole-cell biocatalysts



Imine reductions with purified enzymes



Imine reduction with purified engineered enzyme

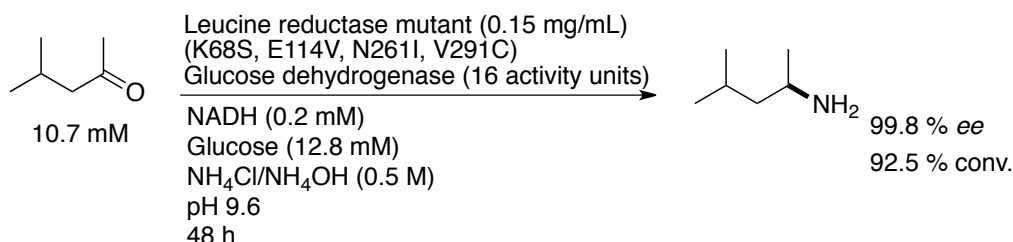


Figure M9: Asymmetric transfer hydrogenation of imines using whole cells and purified enzymes.^{67–71}

Artificial Metalloenzymes for Asymmetric Transfer Hydrogenation of Imines:

Artificial metalloenzymes can be useful to complement both organometallic- and biocatalysts for the asymmetric reduction of imines. Research in the Ward group has demonstrated that the streptavidin-biotin system can be used to create enantioselective artificial transfer hydrogenases (ATHase) for ketones. Based on the crystal structure of the streptavidin-biotin complex, different racemic biotinylated Noyori-type complexes, $[(\eta^6\text{-benzene})\text{Ru}(\text{Biot-L})\text{Cl}]$ and $[(\eta^6\text{-}p\text{-cymene})\text{Ru}(\text{Biot-L})\text{Cl}]$, with biotin located in *ortho*-, *meta*- and *para*-position of the phenylsulfonamide ligand, were designed and tested in the transfer hydrogenation of various arylalkylketones in water and in presence of the hydride source sodium formate (**Figure M10**). Various Sav mutants with mutations mainly in position 64, 112, 121 and 124 in proximity to the assumed metal location were screened in complex with the racemic complexes $[(\eta^6\text{-benzene})\text{Ru}(\text{Biot-}p\text{-L})\text{Cl}]$ and $[(\eta^6\text{-}p\text{-cymene})\text{Ru}(\text{Biot-}p\text{-L})\text{Cl}]$. While racemic product was formed in absence of Sav, once the cofactor was bound to Sav, the arene cap of the catalyst had the most dramatic effect on the enantioselectivity going from 87 % *ee* (*R*-alcohol) to 57 % *ee* (*S*-alcohol) using substrate 4-bromoacetophenone (**Figure M10**). Additionally, the enantioselectivity was effected by the amino acid mutations: The enantiomeric excess of the reaction improved from 57 % to 75 % when comparing SavWT to the double mutant Sav_{S112A-K121N}. The strong effect on the activity and the enantioselectivity of i) the variation of the catalyst's arene cap (benzene vs. *p*-cymene) and ii) the mutations in proximity to the active metal center demonstrated the contribution of the 1st and 2nd coordination sphere around the metal to control catalysis. The crystal structure of Sav_{S112K} in complex with $[(\eta^6\text{-benzene})\text{Ru}(\text{Biot-}p\text{-L})\text{Cl}]$ allowed for the rationalization of the influence of the arene cap and the Sav mutations.

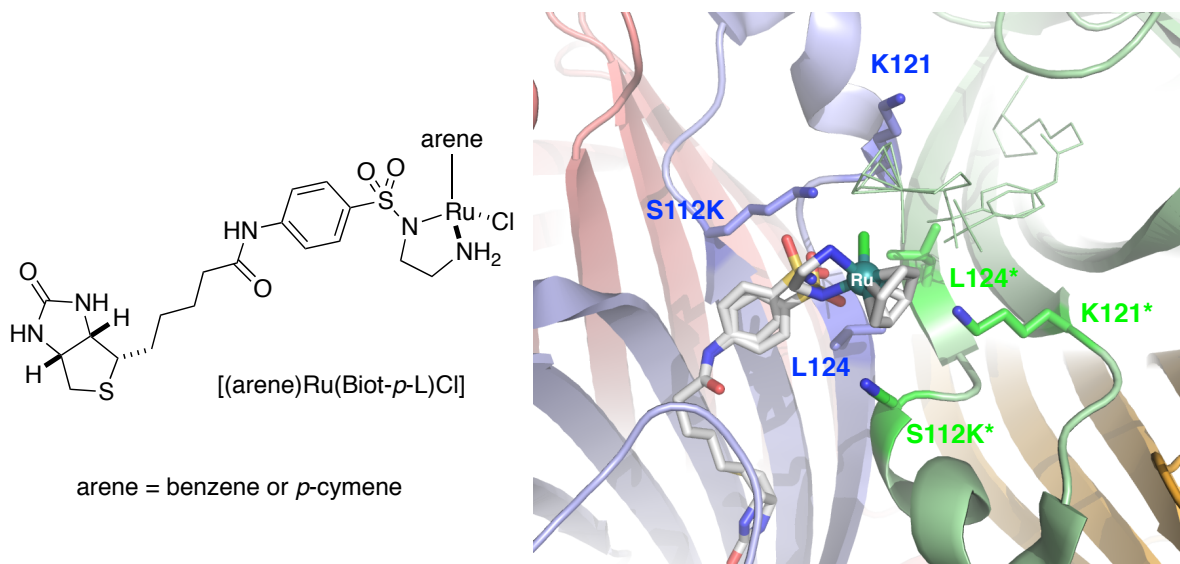
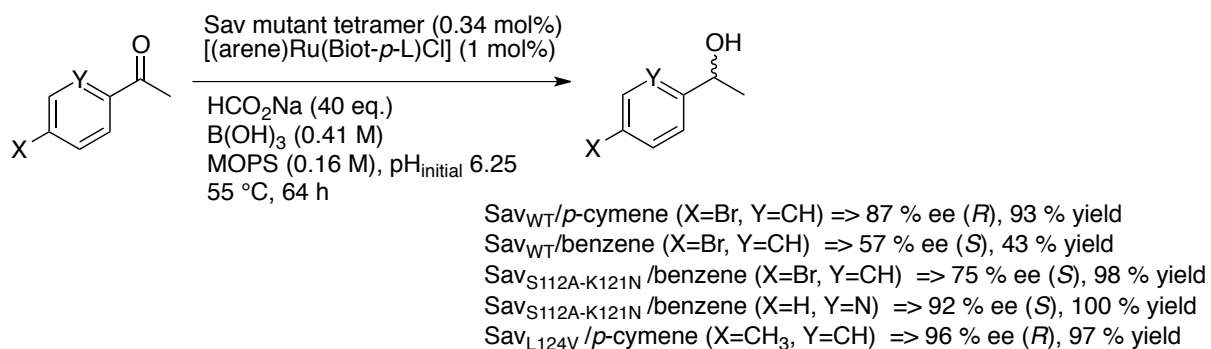


Figure M10: Artificial transfer hydrogenase (PDB 2QCB, protein depicted in ribbon and MC as well as amino acids in stick representation) for the reduction of arylalkylketones.

3. A Dual Anchoring Strategy for the Localization and Activation of Artificial Metalloenzymes based on the Streptavidin-Biotin Technology

A dual anchoring strategy for the localization and activation of artificial metalloenzymes based on the biotin-streptavidin technology

Jeremy M. Zimbron, Tillmann Heinisch, Maurus Schmid, Didier Hamels, Elisa Nogueira, Livia Knörr, Markus Meuwly, Tilman Schirmer and Thomas R. Ward*

Biozentrum and Department of Chemistry, University of Basel CH-4056 Basel, Switzerland

e-mail: thomas.ward@unibas.ch

Abstract

Artificial metalloenzymes result from anchoring an active catalyst within a protein environment. Towards this goal, various localization strategies have been pursued: covalent-, supramolecular- or dative anchoring. Herein we show that introduction of a suitably positioned histidine residue contributes to firmly anchor via a dative bond a biotinylated rhodium pincer complex within streptavidin. The *in silico* design of the artificial metalloenzyme was confirmed by X-ray crystallography. The resulting artificial metalloenzyme displays significantly improved catalytic performance, both in terms of activity and selectivity in the transfer hydrogenation of imines. Depending on the position of the histidine residue, both enantiomers of salsolidine can be obtained.

Introduction

In recent years, the field of artificial metalloenzymes has attracted increasing attention as alternative to the more traditional heterogeneous-, homogeneous- and enzymatic catalysts.¹⁻⁶ Artificial metalloenzymes result from incorporation of a catalytically competent organometallic moiety within a protein scaffold. Towards this goal, covalent-, dative- and supramolecular anchoring strategies have been pursued.

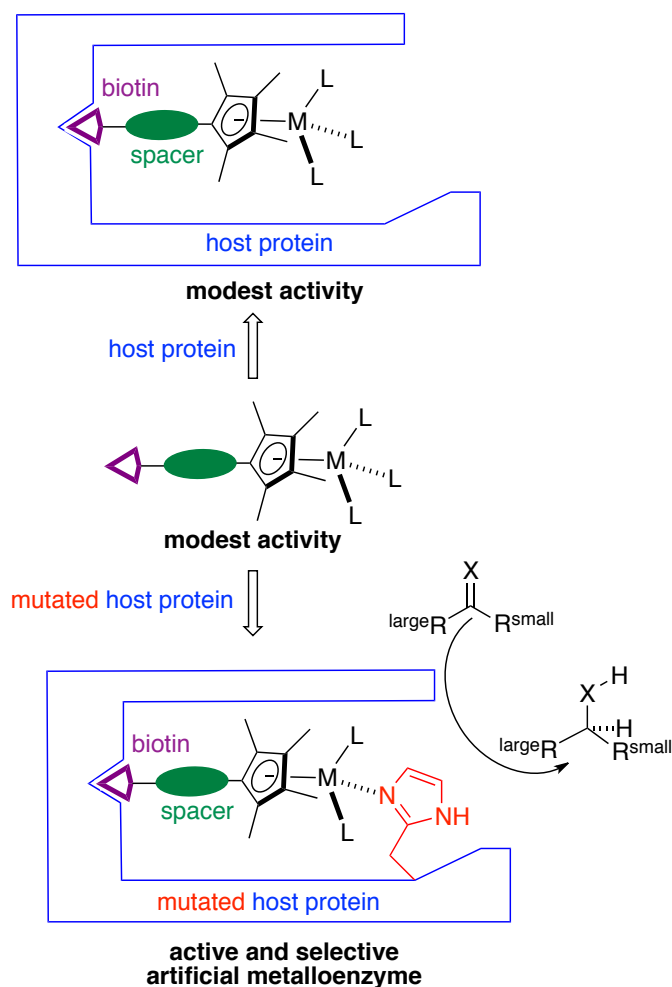
We and others have been relying on the biotin-(strept)avidin technology to create artificial metalloenzymes.⁷⁻¹⁰ The catalytic performance of these can be optimized relying on either chemical- or genetic- means.¹¹ Recent structural and kinetic data of artificial metalloenzymes based on the biotin-streptavidin technology highlighted that: i) the metal is located in a shallow energy minimum resulting in poorly localized metal

moieties (as reflected by low occupancy in the X-ray structure); ii) the presence of second coordination sphere provided by streptavidin significantly influences the selectivity of the resulting artificial metalloenzymes.¹² In contrast, the activity (TOF, TON) is only moderately affected upon incorporation in streptavidin. This presents a serious limitation towards the implementation of directed evolution protocols of artificial metalloenzymes. Indeed, it requires the precise quantification of the protein as any non-protein bound metal would lead to an erosion of enantioselectivity.¹⁰ We speculated that, in addition to the biotin anchor, a properly positioned histidine residue provided by streptavidin may contribute to firmly localize the metal-containing biotinylated cofactor and to activate the precatalyst, Scheme 1. Herein we present our efforts towards the design and application of a dually anchored artificial metalloenzyme for the reduction of prochiral imines.

Results and Discussion

Ligand Design With the aim of generating a widely applicable d⁶-pianostool complex for a variety of catalytic applications upon introduction in streptavidin (Sav hereafter), we set out to link the biotin anchor to the cyclopentadienyl moiety. This strategy leaves three coordination sites available for catalysis and/or activation via additional ligands (Scheme 1).

In order to gain a semi-quantitative insight on the position of the biotinylated pianostool complex **5** upon incorporation within Sav and which amino acid position may be amenable to bind to the metal upon mutation to a histidine, docking simulations were performed.



Scheme 1 Dual anchoring strategy to localize and activate a biotinylated piano-stool catalyst precursor upon incorporation into streptavidin.

Docking Simulations All X-ray crystal structures containing a biotinylated metal complex obtained within the Ward group indicate that the position of the biotin moiety and the C_{α} of the protein is essentially invariant, irrespective of the nature of the metal complex bound to biotin.¹²⁻¹⁵ Therefore, the DFT-optimized structure of the monomeric biotinylated complex $[\eta^5\text{-(Biot-2)RhCl}_2(\text{H}_2\text{O})]$ was manually positioned into the WT Sav (PDB code 1MK5) by superimposing the biotin anchor of the complex to the native biotin present in the crystal structure. Having properly positioned the biotin moiety, the native biotin was deleted. Simulations were performed in NAMD¹⁶ using the CHARMM27 force-field¹⁷ with parameters developed in our group¹⁸ or elsewhere¹⁹ (See SI for details).

The system was subsequently minimized for 1000 Conjugate Gradient steps, followed by a short molecular dynamics simulation (Langevin NVT ensemble) of 500 ps. The structure in the final snapshot was minimized again for 1000 steps to yield the docked

structure. Only the aquo complex $[\eta^5\text{-(Biot-2)RhCl}_2(\text{H}_2\text{O})]$ and atoms within 5 Å of the complex were allowed to relax during the simulation, the rest of the protein was kept frozen. The resulting structure is depicted in Figure 1 a. With respect to the rhodium-center, the two closest lying C_β atoms are provided by S112 (5.62 Å), K121 (6.09 Å of the adjacent monomer). Next, mutations were introduced at either positions S112H or K121H. The rhodium-bound water was replaced by a bond to the N_ϵ histidine and the procedure described above was applied yielding $[(\eta^5\text{-Biot-2)RhCl}_2] \mathbf{5} \subset \text{S112H Sav}$ and $[(\eta^5\text{-Biot-2)RhCl}_2] \mathbf{5} \subset \text{K121H Sav}$, Figure 1 b and 1 c respectively.

These simulations thus suggest that an ethylene spacer between the Cp^* - and the biotin moieties positions the metal center in an environment, suitable for additional dative anchoring to a histidine side chain upon mutation of either S112H or K121H.

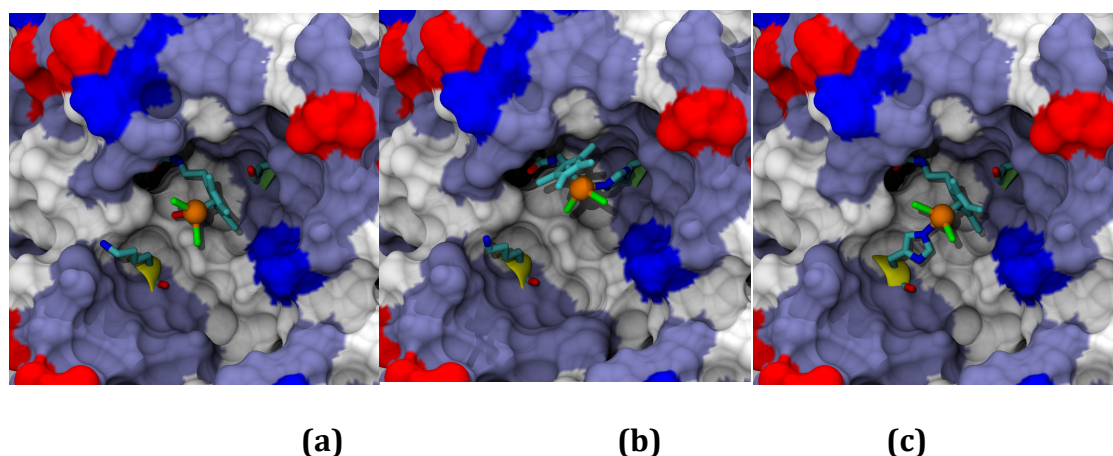
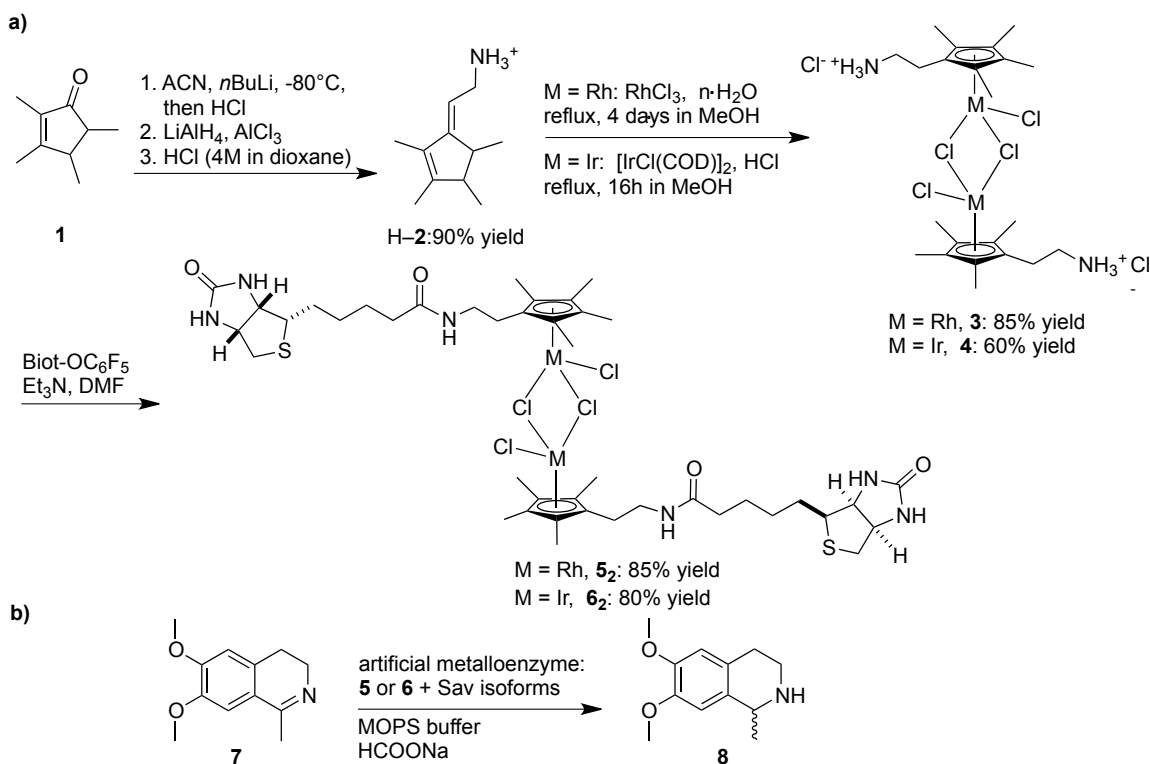


Figure 1 Docked structure of $[\eta^5\text{-(Biot-2)RhCl}_2(\text{H}_2\text{O})] \subset \text{WT Sav}$ (a); $[(\eta^5\text{-Biot-2)RhCl}_2] \mathbf{5} \subset \text{S112H Sav}$ (b) and $[(\eta^5\text{-Biot-2)RhCl}_2] \mathbf{5} \subset \text{K121H Sav}$ (the His is provided by the adjacent Sav monomer of the homotetrameric structure)(c). The piano stool complex and streptavidin's side-chains at positions 112 and 121 are displayed as stick representation, Sav as solvent accessible surface (red anionic-, blue cationic- white apolar and grey polar residues).

Synthesis Having identified a suitable spacer between the biotin anchor and the Cp^* moiety, the corresponding d^6 -piano stool complexes were synthesized. For this purpose, tetramethylcyclopentenone **1** was used as starting material for the synthesis of the cyclopentadienyl precursor H-2 according to a slightly modified protocol of Teuben and coworkers.²⁰ Reaction with $\text{RhCl}_3 \cdot (\text{H}_2\text{O})_n$ or with $[\text{Ir}(\text{COD})\text{Cl}]_2$, followed by an *in-situ* oxidation with HCl yielded the dinuclear piano stool complexes $[\eta^5\text{-(2)RhCl}_2]_2^{2+}$ **3** and

$[\eta^5\text{-}(\mathbf{2})\text{IrCl}_2]_2^{2+}$ **4** respectively.^{21,22} Subsequent biotinylation using the pentafluorophenylester of biotin, allowed the isolation of the analytically pure, dimeric, $[\eta^5\text{-}(\text{Biot-}\mathbf{2})\text{RhCl}_2]_2$ **5** and $[\eta^5\text{-}(\text{biot-}\mathbf{2})\text{IrCl}_2]_2$ **6** respectively (See SI for details).



Scheme 2 Synthesis of biotinylated piano-stool complexes (a) and asymmetric transfer hydrogenation conditions used towards the production of salsolidine **8** (b).

Catalysis As model reaction we selected the asymmetric transfer hydrogenation (ATH) of the prochiral imine **7** using biotinylated dimeric catalyst precursors **5** and **6**. This reaction is frequently used as a benchmark as it offers a straightforward access to the alkaloid salsolidine **8** (Scheme 2c).²³ Selected results are collected in Table 1 and can be summarized as follows:

1) The iridium catalyst precursor $[\eta^5\text{-}(\text{Biot-}\mathbf{2})\text{IrCl}_2]_2$ **6** leads to higher conversions than the rhodium congener $[\eta^5\text{-}(\text{Biot-}\mathbf{2})\text{RhCl}_2]_2$ **5**. The same trend applies upon incorporation in WT Sav albeit with reduced conversions (Entries 1-4).

2) The presence of a histidine residue at position S112 Sav has a dramatic effect on the activity and the selectivity of the ATH. Salsolidine **8** is produced in 95 % conversion and 41 % ee (*S*) using $[\eta^5\text{-}(\text{Biot-}\mathbf{2})\text{RhCl}_2]_2$ **5** \subset S112H at 55°C and pH 6.5. The activity and the selectivity can be further improved upon lowering the pH to 5.0 (quantitative

conversion with 1 mol % catalyst **5** and 55 % ee (*S*)) (Table 1, entries 5 and 6). In stark contrast, the presence of a histidine residue at position S112H has a detrimental effect on ATH with iridium (Table 1, entry 8).

3) Introduction of a histidine residue at position K121H Sav affords (*R*)-salsolidine **8** in up to 79 % ee using the rhodium catalyst at 55°C (Table 1, entries 9 and 10). Unexpectedly, lowering the temperature to 5°C leads in both hybrid catalysts to an erosion of enantioselectivity (Table 1, entries 7 and 11). Again here, *rac*-**8** is produced with the iridium catalyst in the presence of K121H Sav.

4) All point mutants tested devoid of a histidine at either position S112 or K121 afforded nearly racemic salsolidine **8** (ee < 20 %) (Table 1, entries 13-18). Interestingly, the double mutant S112H-K121H Sav gave very low levels of enantioselectivity, Table 1 entry 18.

5) Compared to $[\eta^5\text{-(Biot-2)RhCl}_2]$ **5** \subset WT Sav, both histidine bearing artificial metalloenzymes $[\eta^5\text{-(Biot-2)RhCl}_2]$ **5** \subset S112H Sav and $[\eta^5\text{-(Biot-2)RhCl}_2]$ **5** \subset K121H display increased turnover frequencies: 1 hour⁻¹ for the WT Sav compared to 6 hour⁻¹ for both S112H and K121H mutants.

Table 1 Selected results for the asymmetric transfer hydrogenation of prochiral imine **7** catalyzed by a dually anchored artificial metalloenzymes.

Entry	$[\eta^5\text{-Biot-L)MCl}_2]$	Sav isoform	Temp (°C)	pH	M loading	Conv. (%)	ee (%)
1	Rh	–	55	6.5 ^a	2%	26	rac.
2	Ir	–	55	6.5 ^a	2%	87	rac.
3	Rh	WT	55	6.5 ^a	2%	18	rac.
4	Ir	WT	55	6.5 ^a	2%	60	6 (<i>S</i>)
5	Rh	S112H	55	6.5 ^a	2%	95	41(<i>S</i>)
6	Rh	S112H	55	5.0 ^b	1%	quant.	55(<i>S</i>)
7	Rh	S112H	5	5.0 ^b	1%	5	45(<i>S</i>)
8	Ir	S112H	55	6.5 ^a	2%	27	11(<i>S</i>)
9	Rh	K121H	55	6.5 ^a	2%	95	50(<i>R</i>)
10	Rh	K121H	55	5.0 ^b	1%	quant.	79(<i>R</i>)
11	Rh	K121H	5	5.0 ^b	1%	5	50(<i>R</i>)
12	Ir	K121H	55	6.5 ^a	2%	37	rac.
13	Rh	S112C	55	6.5 ^a	2%	93	14(<i>S</i>)
14	Rh	S112E	55	6.5 ^a	2%	26	rac.

15	Rh	S112K	55	6.5 ^a	2%	40	13(<i>S</i>)
16	Rh	S112M	55	6.5 ^a	2%	98	19(<i>R</i>)
17	Rh	K121N	55	6.5 ^a	2%	44	rac.
18	Rh	S112H- 121H	55	6.5 ^a	2%	40	9 (<i>R</i>)

^aThe reaction was carried out in a MOPS buffer at pH 6.5 using HCOONa as hydride source: 2 mol% monomeric biotinylated catalyst **5** or **6** (458 μ M final metal concentration), 4 mol % biotin binding sites (916 μ M final concentration) and substrate **7** (22.9 mM final concentration, total reaction volume 200 μ L) (See SI). ^bThe reaction was carried out in a MOPS buffer at pH 5.0 using HCOONa as hydride source: 1 mol% monomeric biotinylated catalyst **5** or **6** (458 μ M final metal concentration), 2 mol % biotin binding sites (916 μ M final concentration) and substrate **7** (45.8 mM final concentration, total reaction volume 200 μ L) (See SI).

X-ray Characterization Next, X-ray crystal structure analyses were carried out with the most selective artificial metalloenzymes: $[(\eta^5\text{-Biot-2})\text{RhCl}_2] \subset \text{S112H}$ and $[\eta^5\text{-(Biot-2)}\text{RhCl}_2] \subset \text{K121H}$, respectively. Crystals of apo-streptavidin mutants S112H and K112H were soaked at pH 6 with an excess complex $[\eta^5\text{-(Biot-2)}\text{RhCl}_2]_2$ **5**₂. The crystal structures of **5** \subset S112H and **5** \subset K121H could be solved to 2.4 Å and 1.8 Å resolution, respectively. Both structures contain strong electron density in the Fo-Fc map in the biotin-binding pocket and in the proximity of the histidine residue either at position H112 or H121. The monomeric complexes $[\eta^5\text{-(Biot-2)}\text{Rh}]^{2+}$ and $[\eta^5\text{-(Biot-2)}\text{RhCl}]^+$ were modeled with full occupancy in the electron densities localized around H112 and H121' respectively (Figure 2 and SI Figure 1). As highlighted by the docking simulations, the H121' of an adjacent monomer in homotetrameric streptavidin lies closest to the Rh in the **5** \subset K121H structure, Figure 1 c and 2b. Dative bonds were modeled between rhodium and the corresponding histidine: Rh–N δ^{His112} 2.3 Å for **5** \subset S112H and Rh–N $\epsilon^{\text{His121'}}$ 2.3 Å for **5** \subset K121H. The Rh···Rh distances between two biotinylated molecules bound to neighboring symmetry-related Sav monomers are 9.5 Å and 9.2 Å for **5** \subset S112H and **5** \subset K121H, respectively. The position of the complexes in the S112H and K121H isoforms differs by an approximate 180° rotation of the Cp*Rh(Cl) group along an axis pointing towards the biotin binding pocket. For the complex bound to S112H, no additional electron density to complete the three-legged pianostool geometry could be detected whereas the presence of a chloride ligand was apparent for the K121H structure.

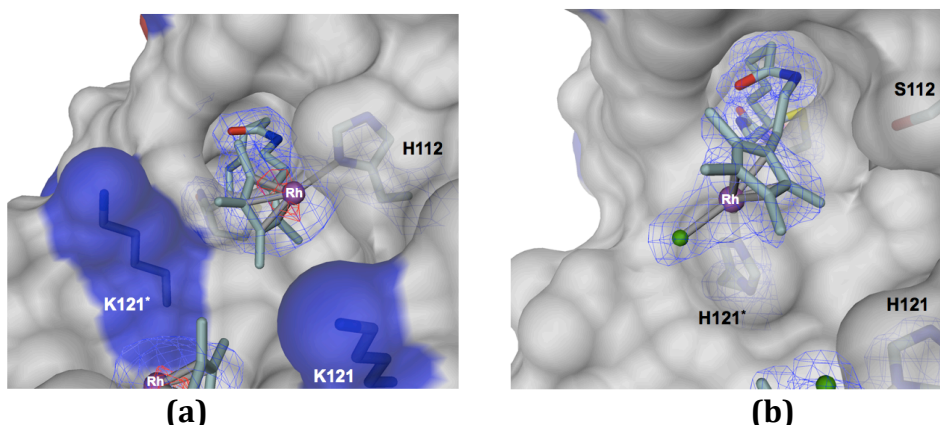


Figure 2. Close-up view of the X-ray crystal structure of $[(\eta^5\text{-Biot-2})\text{Rh}]^{2+} \subset \text{S112H Sav}$ (a); and $[(\eta^5\text{-Biot-2})\text{RhCl}]^+ \subset \text{K121H Sav}$ (b). The protein is displayed as surface representation and the ligand molecules as well as residues 112 and 121 in stick representation. The positions of ligand molecules are indicated by the 2Fo-Fc electron density (blue, contoured at 1.2σ) and anomalous difference density (red, contoured at 4σ , due to weak absorption at a wavelength of 1.00 \AA no anomalous density was observed in structure $[(\eta^5\text{-Biot-2})\text{RhCl}]^+ \subset \text{K121H Sav}$). Rhodium is colored in purple and chlorine in green. The primed residues (H121' and K121') are provided by the adjacent Sav monomer.

Outlook

Dual anchoring of a biotinylated three-legged rhodium piano stool complex affords an artificial transfer hydrogenase. It was shown that coordination of the catalyst precursor to a suitably positioned histidine residue has a significant impact on the catalyst's performance, both in terms of activity and of selectivity. The computational design towards the identification of the spacer-length and site of mutation was confirmed by X-ray crystallography for the most selective artificial metalloenzymes $[\eta^5\text{-(Biot-2)RhCl}_2] \mathbf{5} \subset \text{K121H}$ and $[\eta^5\text{-(Biot-2)RhCl}_2] \mathbf{5} \subset \text{S112H}$. Current efforts are aimed at computing the transition state to identify and engineer additional second coordination sphere interactions to improve the catalytic performance of these dually-anchored artificial metalloenzymes.

Acknowledgments. Generous support from the Canton of Basel, SNF (grant grants 200020_126366) as well as the Marie Curie training networks (BioChemLig FP7-ITN-238434 to TH and Biotrains FP7-ITN-238531 to EN) is gratefully acknowledged. TRW thanks Umicore for a precious metal loan as well as Prof. C. R. Cantor for the streptavidin gene.

Supporting Information Modelling, biotinylated complex synthesis and characterization, catalytic runs and X-ray data. This material is available free of charge via the Internet at <http://pubs.acs.org>.

Literature Cited

- (1) Ward, T. R. *Acc. Chem. Res.* **2011**, *44*, 47.
- (2) Rosati, F.; Roelfes, G. *ChemCatChem* **2010**, *2*, 916.
- (3) Deuss, P. J.; den Heeten, R.; Laan, W.; Kamer, P. C. *Chem. Eur. J.* **2011**, *17*, 4680.
- (4) Lu, Y.; Yeung, N.; Sieracki, N.; Marshall, N. M. *Nature* **2009**, *460*, 855.
- (5) Abe, S.; Ueno, T.; Reddy, P. A. N.; Okazaki, S.; Hikage, T.; Suzuki, A.; Yamane, T.; Nakajima, H.; Watanabe, Y. *Inorg. Chem.* **2007**, *46*, 5137.
- (6) Reetz, M. T. *Top. Organomet. Chem.* **2009**, *25*, 63.
- (7) Wilson, M. E.; Whitesides, G. M. *J. Am. Chem. Soc.* **1978**, *100*, 306.
- (8) Lin, C.-C.; Lin, C.-W.; Chan, A. S. C. *Tetrahedron Asymmetry* **1999**, *10*, 1887.
- (9) Collot, J.; Gradinaru, J.; Humbert, N.; Skander, M.; Zocchi, A.; Ward, T. R. *J. Am. Chem. Soc.* **2003**, *125*, 9030.
- (10) Reetz, M. T.; Peyeralans, J. J.-P.; Maichele, A.; Fu, Y.; Maywald, M. *Chem. Commun.* **2006**, 4318.
- (11) Klein, G.; Humbert, N.; Gradinaru, J.; Ivanova, A.; Gilardoni, F.; Rusbandi, U. E.; Ward, T. R. *Angew. Chem. Int. Ed.* **2005**, *44*, 7764.
- (12) Dürrenberger, M.; Heinisch, T.; Wilson, Y. M.; Rossel, T.; Nogueira, E.; Knörr, L.; Mutschler, A.; Kersten, K.; Zimbron, M. J.; Pierron, J.; Schirmer, T.; Ward, T. R. *Angew. Chem. Int. Ed.* **2011**, *50*, 3026.
- (13) Creus, M.; Pordea, A.; Rossel, T.; Sardo, A.; Letondor, C.; Ivanova, A.; LeTrong, I.; Stenkamp, R. E.; Ward, T. R. *Angew. Chem. Int. Ed.* **2008**, *47*, 1400.
- (14) Zimbron, J. M.; Sardo, A.; Heinisch, T.; Wohlschlager, T.; Gradinaru, J.; Massa, C.; Schirmer, T.; Creus, M.; Ward, T. R. *Chem. Eur. J.* **2010**, *16*, 12883.
- (15) Koehler, V.; Mao, J.; Heinisch, T.; Pordea, A.; Sardo, A.; Wilson, Y. M.; Knoerr, L.; Creus, M.; Prost, J.-C.; Schirmer, T.; Ward, T. R. *Angew. Chem., Int. Ed.* **2011**, *50*, 10863.
- (16) Phillips, J. C.; Braun, R.; Wang, W.; Gumbart, J.; Tajkhorshid, E.; Villa, E.; Chipot, C.; Skeel, R. D.; Kale, L.; Schulten, K. *J. Comput. Chem.* **2005**, *26*, 1781.

- (17) MacKerell Jr., A. D.; Brooks III, C. L.; Nilsson, L.; Roux, B.; Won, Y.; Karplus, M. *CHARMM: The Energy Function and Its Parameterization with an Overview of the Program*; John Wiley & Sons: Chichester, 1998; Vol. 1.
- (18) Schmid, M.; Nogueira, E. S.; Monnard, F. W.; Ward, T. R.; Meuwly, M. *Chem. Sci.* **2012**, *3*, 690.
- (19) Izrailev, S.; Stepaniants, S.; Balsera, M.; Oono, Y.; Schulten, K. *Biophys. J.* **1997**, *72*, 1568.
- (20) Van Leusen, D.; Beetstra, D. J.; Hessen, B.; Teuben, J. H. *Organometallics* **2000**, *19*, 4084.
- (21) Reiner, T.; Jantke, D.; Raba, A.; Marziale, A. N.; Eppinger, J. *J. Organomet. Chem.* **2009**, *694*, 1934.
- (22) Amouri, H. E.; Gruselle, M.; Jaouén, G. *Synth. React. Inorg. Met.-Org. Chem.* **2010**, *24*, 395.
- (23) Kaufman, T. *Tetrahedron Asymmetry* **2004**, *15*, 1203.

Supporting Information for

A dual anchoring strategy for the localization and activation of artificial metalloenzymes based on the biotin-streptavidin technology

Jeremy M. Zimbron, Tillmann Heinisch, Maurus Schmid, Didier Hamels, Elisa Nogueira, Livia Knörr, Markus Meuwly, Tilman Schirmer and Thomas R. Ward*

Biozentrum and Department of Chemistry, University of Basel CH-4056 Basel, Switzerland

e-mail: thomas.ward@unibas.ch

X-ray Crystal Structures

Protein Crystallization and Biotinylated Complex Soaking. Crystals of streptavidin mutants Sav K121H and Sav S112H (residues 13-159 of mature streptavidin fused N-terminally to the 12 residues of a T7-tag)¹⁵ were obtained within one month by hanging-drop vapor diffusion technique mixing 2 μ L crystallization buffer (0.1 M MES, 19 % PEG500, pH 6.0) and 3 μ L protein solution (20 mg/mL in water) prior to equilibration of the solution against a reservoir of 500 μ L crystallization buffer. Subsequently, single crystals of mutants Sav K121H and Sav S112H were soaked for 4 h at room temperature in a soaking buffer, which was prepared by mixing 1 μ L of a 10 mM stock solution of complex **5**₂ ($[\eta^5\text{-(Biot-2)RhCl}_2]_2$) in dimethyl formamide and 9 μ L crystallization buffer. After the soaking, crystals were shock-frozen in liquid nitrogen.

Data Processing and Refinement. X-ray diffraction data were collected at the Swiss Light Source beam line X06DA and processed with software XDS¹⁶ or MOSFLM (CCP4 Suite)¹⁷. The structures were solved by molecular replacement using program PHASER¹⁸ (CCP4 Suite) and the structure 2qcb from the PDB as model input with ligand and water molecules removed. For structure refinement PHENIX.REFINE¹⁹ was used. Crystallographic details are given in Supporting Table 1. Structural figures were drawn with software DINO. The structures were deposited in the pdb repository with the codes 4GJS and 4GJV for $[\eta^5\text{-(Biot-2)RhCl}]^+ \subset$ K121H and $[\eta^5\text{-(Biot-2)Rh}]^{2+} \subset$ S112H

respectively.

Supporting Table 1: Summary of data processing and refinement.

Data processing		
Complex	$[\eta^5\text{-(Biot-2)RhCl}]^+$ K121H	$[\eta^5\text{-(Biot-2)Rh}]^{2+}$ C S112H
Wavelength of X-ray experiment (Å)	1.00	1.55
Software	MOSFLM	XDS
Resolution (Å)	40.80 - 1.85	150.00 - 2.40
Space group	C2	I4 ₂ 2
Cell dimensions (Å)	a=81.7, b=81.3, c=47.0, β =104.8	a=57.6, b=57.6, c=183.8
R_{merge}	8.1 (18.5)	9.8 (79.2)
No unique reflections	24972	10085
Multiplicity	2.7	3.4
I/sig(I)	6.0 (2.3)	10.3 (1.6)
Completeness (%)	98.5 (96.3)	86.2 (73.2)
CC (1/2)	n/d	62.5
Refinement		
Resolution (Å)	28.32 - 1.85	19.88 - 2.40
$R_{\text{work}}/R_{\text{free}}$ (%)	20.3 (25.0)	18.5 (23.0)
RMSD _{bond} (Å)	0.007	0.032
RMSD _{angle} (deg)	1.365	1.121
Bfactor		
all atoms	23	36
solvent	33	33
$[\eta^5\text{-(Biot-2)RhCl}]^+$	32	44
/ $[\eta^5\text{-(Biot-2)Rh}]^{2+}$		

Values in brackets refer to the highest resolution shell

Structure of $[\eta^5\text{-(Biot-2)RhCl}]^+ \subset \text{Sav K121H}$

There are two streptavidin monomers in the asymmetric unit from which a tetramer can be formed by application of the crystallographic 2-fold symmetry axis parallel b (**Supporting Figure 1a**). The 12 N-terminal residues of the T7-tag and 25 residues at the C-terminus are not resolved, probably due to disorder. Strong residual electron density in the $F_o - F_c$ omit map was present in the biotin binding pocket and its vestibule reaching to residue His121' of the neighboring SAV monomer suggesting the cleavage of Rh-dimer **5**₂ upon binding to Sav K121H. The initial ligand model to be fit in the residual

electron density comprised a rhodium-bound pentamethylcyclopentadienyl ring (Cp**Rh* group), which was covalently attached to biotin via an ethylene spacer and an amide bond. The geometry of the $[\eta^5\text{-(Biot-2)Rh}]^{2+}$ moiety was derived from the X-ray structure of the closely related small molecule rhodium complex 1-(4-nitrophenyl)-1H-imidazol-3-yl)-dichloro-(η^5 -pentamethylcyclopentadienyl)-rhodium (CSD code FACHEY, **Supporting Figure 1e, right side**). Ligand restraints were adapted manually using software REEL (PHENIX package). The biotin moiety is bound to the streptavidin pocket as described by Weber *et al.*²⁰ An H-bond is formed between the ligand's carbonyl group and the backbone nitrogen of residue N49. Due to structural heterogeneity, the ethylene spacer and portions of the aromatic 5-membered ring of complex $[\eta^5\text{-(Biot-2)Rh}]^{2+}$ are not properly resolved in the electron density (**Supporting Figure 1b**). The position of the rhodium atom as bound to the Cp* ring is well defined by the strong residual positive electron density signal (12 σ) in bonding distance (2.3 Å) to the N ϵ of His121' of the neighboring SAV monomer. Close to the metal, residual density suggested the presence of an additional chloride ligand. There is no density at the third rhodium coordination site. In the refinement, bond angles Cp*_{centroid}-Rh-Cl, Cp*_{centroid}-Rh-N ϵ ^{His121'} and Cl-Rh-N ϵ ^{His121'} were restrained to the values given by the X-ray structure of the related small molecule pianostool complex with CSD code FACHEY (**Supporting Figure 1e**).

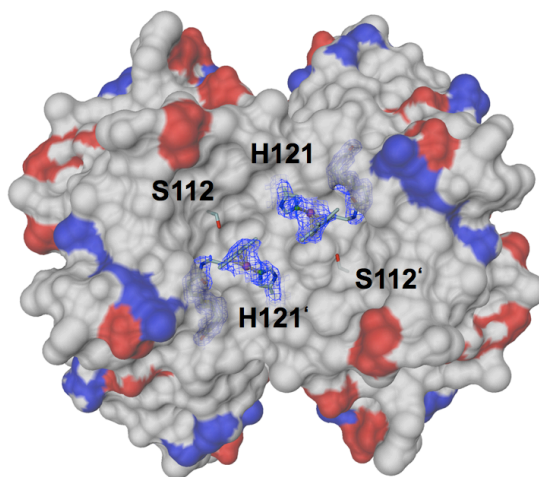
Strong density (11 σ) was found in the Fo-Fc map close to His127 and was modeled as a rhodium ion covalently attached to the histidine-N ϵ , suggesting the binding of an additional rhodium, due to the use of a large excess biotinylated complex **5₂** for soaking. Finally, the structure contains 328 water molecules.

Structure of $[\eta^5\text{-(Biot-2)Rh}]^{2+} \subset \text{Sav S112H}$

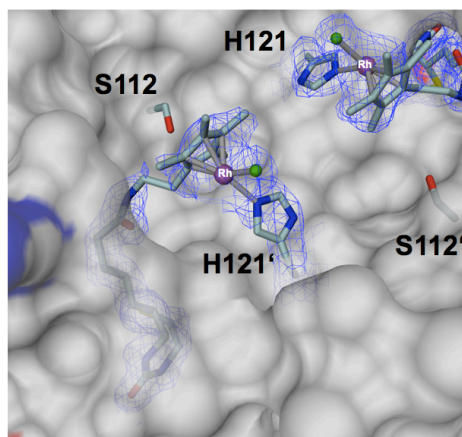
There is one streptavidin molecule in the asymmetric unit. The SAV tetramer is obtained by application of the crystallographic dyads parallel to *c* and along the *a*-*b* diagonal. As in the structure of complex $[\eta^5\text{-(Biot-2)RhCl}]^+ \subset \text{Sav K121H}$, 12 N-terminal and 25 C-terminal amino acids are not resolved. Strong residual electron density in the Fo-Fc omit map was evident in the biotin-binding pocket and its vestibule close to the imidazole ring of His112 of the same subunit (**Supporting Figure 2c**). As expected from the small f' (3.6 e⁻) of Rh at the employed wavelength, only a weak peak (5.3 σ) in the anomalous difference map was found in the vestibule in the same position close to residue H112. Complex $[\eta^5\text{-(Biot-2)Rh}]^{2+}$ was modeled in the densities (**Supporting Figure 2d**). As in

the structure of $[\eta^5\text{-(Biot-2)RhCl}]^+ \subset \text{Sav K121H}$, the ethylene spacer and the methyl-substituted 5-membered ring of complex $[\eta^5\text{-(Biot-2)Rh}]^{2+}$ are not resolved in the electron density. The distance between the Cp*-bound Rh and N δ_{H112} is 2.3 Å indicating a coordinative bond. No further electron density was detected in the coordination sphere of the rhodium. However, the positions are likely to be occupied by two water molecules, which would give rise to a piano-stool-type of ligand coordination sphere around the metal.

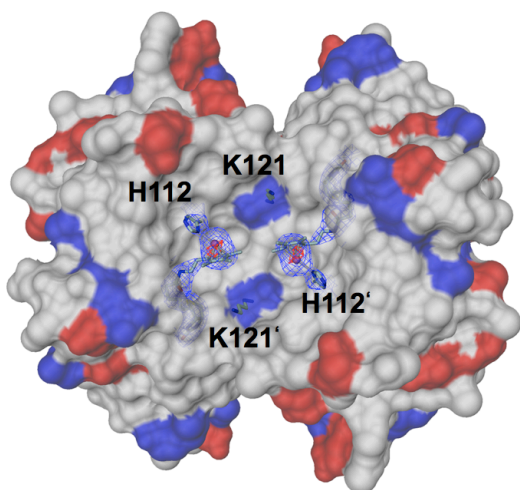
Additional strong electron density in the Fo-Fc omit map was found next to the following protein nitrogen atoms: backbone G48(N) (5 σ), K80(N ζ) (3 σ), R84(N η) (7 σ), H87(N ϵ) (7 σ) and H127(N ϵ) (14 σ , 4.6 σ peak in anomalous scattering density). A rhodium atom was modeled next to His127 and chloride in all other positions. Again here this is most probably due to the use of a large excess biotinylated complex **5**₂ for soaking purposes. Besides these ligands, the structure contains 23 water molecules.



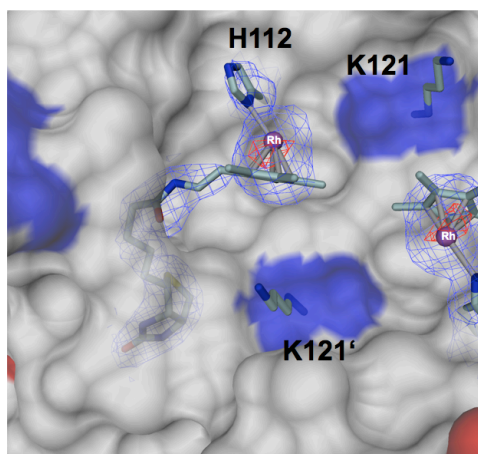
a



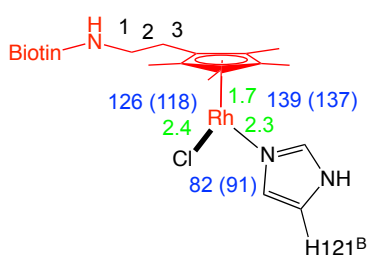
b



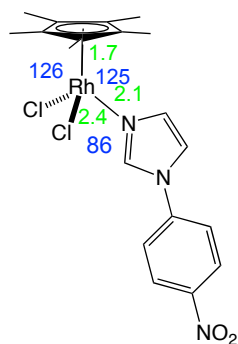
c



d



Ligand 9 (red lines)



CSD code FACHEY

e

Supporting Figure 1: X-ray structures of $[\eta^5\text{-(Biot-2)RhCl}]^+ \subset \text{K121H}$ and $[\eta^5\text{-(Biot-2)Rh}]^{2+} \subset \text{S112H}$. a) Top view of two cis-related biotin-binding pockets of tetrameric complex $[\eta^5\text{-(Biot-2)RhCl}]^+ \subset \text{K121H}$ in surface representation (red: acidic amino acids, blue: basic amino acids). The 2Fo-Fc map covering complex $[\eta^5\text{-(Biot-2)RhCl}]^+$ and His121 is contoured at 1.2σ . b) Close-up view of the ligand binding site of complex $[\eta^5\text{-(Biot-2)RhCl}]^+ \subset \text{K121H}$. c) $[\eta^5\text{-(Biot-2)Rh}]^{2+} \subset \text{S112H}$, view as in a). d) Close-up view of complex $[\eta^5\text{-(Biot-2)Rh}]^{2+} \subset \text{S112H}$. Significant anomalous scattering density (contoured at 4σ , red) indicates the position of the rhodium. e) Comparison of the piano stool structures of complex $[\eta^5\text{-(Biot-2)RhCl}]^+$ as bound to Sav K121H (left) and CSD ligand FACHEY (right). Green and blue colored numbers indicate bond distances and angles, respectively (numbers in parentheses refer to symmetry-related ligand $[\eta^5\text{-(Biot-2)RhCl}]^+$ in same asymmetric unit).

SI Literature Cited

- (1) Hohenberg, P.; Kohn, W. *Phys. Rev. B* **1964**, *136*, B864.
- (2) Frisch, M. J.; Trucks, G. W.; Schlegel, H. B.; et al. In *Gaussian 09, Revision B.01*, Gaussian, Inc., Wallingford CT Wallingford CT, 2009.
- (3) Stephens, P. J.; Devlin, F. J.; Chabalowski, C. F.; Frisch, M. J. *J. Phys. Chem.* **1994**, *98*, 11623.
- (4) Becke, A. D. *J. Chem. Phys.* **1993**, *98*, 5648.
- (5) Hay, P. J.; Wadt, W. R. *J. Chem. Phys.* **1985**, *82*, 270.
- (6) Humphrey, W.; Dalke, A.; Schulten, K. *J. Mol. Graphics Modell.* **1996**, *14*, 33.
- (7) Phillips, J. C.; Braun, R.; Wang, W.; Gumbart, J.; Tajkhorshid, E.; Villa, E.; Chipot, C.; Skeel, R. D.; Kale, L.; Schulten, K. *J. Comput. Chem.* **2005**, *26*, 1781.
- (8) MacKerell Jr., A. D.; Brooks III, C. L.; Nilsson, L.; Roux, B.; Won, Y.; Karplus, M. *CHARMM: The Energy Function and Its Parameterization with an Overview of the Program*; John Wiley & Sons: Chichester, 1998; Vol. 1.
- (9) Schmid, M.; Nogueira, E. S.; Monnard, F. W.; Ward, T. R.; Meuwly, M. *Chem. Sci.* **2012**, *3*, 690.
- (10) Izrailev, S.; Stepaniants, S.; Balsera, M.; Oono, Y.; Schulten, K. *Biophys. J.* **1997**, *72*, 1568.
- (11) Rappe, A. K.; Casewit, C. J.; Colwell, K. S.; Goddard, W. A.; Skiff, W. M. *J. Am. Chem. Soc.* **1992**, *114*, 10024.
- (12) Van Leusen, D.; Beetstra, D. J.; Hessen, B.; Teuben, J. H. *Organometallics* **2000**, *19*, 4084.

- (13) Reiner, T.; Jantke, D.; Raba, A.; Marziale, A. N.; Eppinger, J. *J. Organomet. Chem.* , 694, 1934.
- (14) Amouri, H. E.; Gruselle, M.; Jaouén, G. *Synth. React. Inorg. Met.-Org. Chem.* **2010**, , 395.
- (15) Humbert, N.; Schurmann, P.; Zocchi, A.; Neuhaus, J. M.; Ward, T. R. *Methods Mol Biol* **2008**, 418, 101.
- (16) Kabsch, W. *Acta Crystallogr D* **2010**, 66, 125.
- (17) Collaborative *Acta Crystallogr., Sect. D: Biol. Crystallogr.* **1994**, 50, 760.
- (18) McCoy, A. J.; Grosse-Kunstleve, R. W.; Adams, P. D.; Winn, M. D.; Storoni, L. C.; Read, R. J. *J. Appl. Cryst* **2007**, 40, 658.
- (19) Adams, P. D.; Afonine, P. V.; Bunkóczi, G.; Chen, V. B.; Davis, I. W.; Echols, N.; Headd, J. J.; Hung, L.-W.; Kapral, G. J.; Grosse-Kunstleve, R. W.; McCoy, A. J.; Moriarty, N. W.; Oeffner, R.; Read, R. J.; Richardson, D. C.; Richardson, J. S.; Terwilliger, T. C.; Zwart, P. H. *Acta Crystallogr. D Biol. Crystallogr.* **2010**, 66, 213.
- (20) Weber, P. C.; Ohlendorf, D. H.; Wendoloski, J. J.; Salemme, F. R. *Science* **1989**, 243, 85.

3.1. Author Contributions

General idea:

Thomas R. Ward

Computational design of biotinylated piano stool complexes and Sav_{His} mutants:

Maurus Schmid, Markus Meuwly

Synthesis of biotinylated piano stool complexes:

Jeremy M. Zimbron, Didier Hamels

Production of streptavidin variants:

Elisa Nogueira, Livia Knörr

Screening of streptavidin mutants and biotinylated metal complexes for transfer hydrogenation of salsolidine precursor:

Jeremy M. Zimbron, Didier Hamels, Elisa Nogueira

Crystal structure analysis of complexes (Sav_{K121H}-[η^5 -(Biot-**2_2**)RhClL₂]⁺) and (Sav_{S112H}-[η^5 -(Biot-**2_2**)RhL₃]²⁺):

Tillmann Heinisch, Tilman Schirmer

Manuscript writing:

Thomas R. Ward and all other authors

3.2. Comment on Publication

3.2.1. Towards the Directed Evolution of Artificial Transfer Hydrogenases

Artificial metalloenzymes are an emerging alternative to asymmetric homogenous- and biocatalysts to obtain chiral building blocks, although to date their use is limited to academic research. In the previous chapter an artificial transfer hydrogenase for the asymmetric reduction of a cyclic imine with very high enantioselectivity and turnover number (TON = 4000) was reported. To date, it has been shown in numerous examples that the chemical and genetic optimization of artificial metalloenzymes based on the streptavidin-biotin technology is possible. The scope of this technology can be further expanded by the use of high-throughput screening methods such as directed evolution.

The following requirements have to be fulfilled to do directed evolution with streptavidin mutants and biotinylated metal catalysts *in vivo*:

- the stability of the MC in a cellular matrix
- the binding of the MC to Sav in a cellular matrix
- a protein accelerated activity of Sav-MC complex
- a high-throughput screening method with high sensitivity, e.g. HPLC analysis of the products.

Many biotinylated metal complexes tested so far lose activity upon binding to Sav (a noteworthy exception is the C-H activating AME³⁸). This is a significant limitation to the application of directed evolution optimization protocols since the background activity of the free cofactor is high and Sav-bound MC would not be detectable by increased product formation.

One strategy to accelerate the activity of a Sav-bound biotinylated metal complex would be to engineer an amino acid side chain (e.g. histidine) in proximity to the metal, which can coordinate to the metal. Locking the catalyst may have a beneficial effect on the activity and selectivity due to i) improved interactions between a well-defined (as compared to a flexible) catalyst-1st and -2nd coordination sphere and the substrate and ii) by variation of the electronic properties of the metal (ligand-accelerated catalysis).

Different anchoring strategies of functional metal complexes in rigid protein scaffolds have been described to create artificial metalloenzymes: covalent, supramolecular and dative anchoring. So far the supramolecular strategy based on the streptavidin-biotin technology was

shown to give the most active and selective AMEs for asymmetric catalysis.⁶ This study will give interesting information about the compatibility and potential positive effects of a combination of supramolecular and dative anchoring.

Strong ligand accelerating effects have been demonstrated for a number of bidentate ligands (e.g. TosEN) in the transfer hydrogenation of ketones and imines with Noyori-type Ru-benzene, Ru-*p-cymene*, IrCp* or RhCp* catalysts.⁵⁶ The energy of the transition state seems to be lowered in presence of an acidic terminal aminoproton as of the TosEN ligand (**Scheme M1**). However, moderate ligand acceleration was also observed with monodentate tertiary amines and 2,2'-bipyridyl, which lack acidic protons.

A Noyori type IrCp* complex can be biotinylated at the arene cap. Upon anchoring of such a complex to Sav_{WT}, the IrCp* unit would have three vacant coordination sites and would be loosely positioned in the vestibule of the biotin binding pocket (**Scheme 2_1**). An engineered histidine in proximity to the metal can occupy one coordination site. A positive effect on the activity and enantioselectivity of the reaction may result through the high effective molarity of the imidazole ligand.

3.2.2. Substrate Binding Models and Potential Influence of the 1st and 2nd Coordination Sphere on Catalysis

Based on the crystal structures of complexes (Sav_{K121H}-[η^5 -(Biot-2_2)RhClL₂]⁺) and (Sav_{S112H}-[η^5 -(Biot-2_2)RhL₃]²⁺) and the information about the stereochemistry of the products preferentially formed by these hybrid catalysts, qualitative models for the substrate binding to the ATHases can be proposed (**Figure M11**).

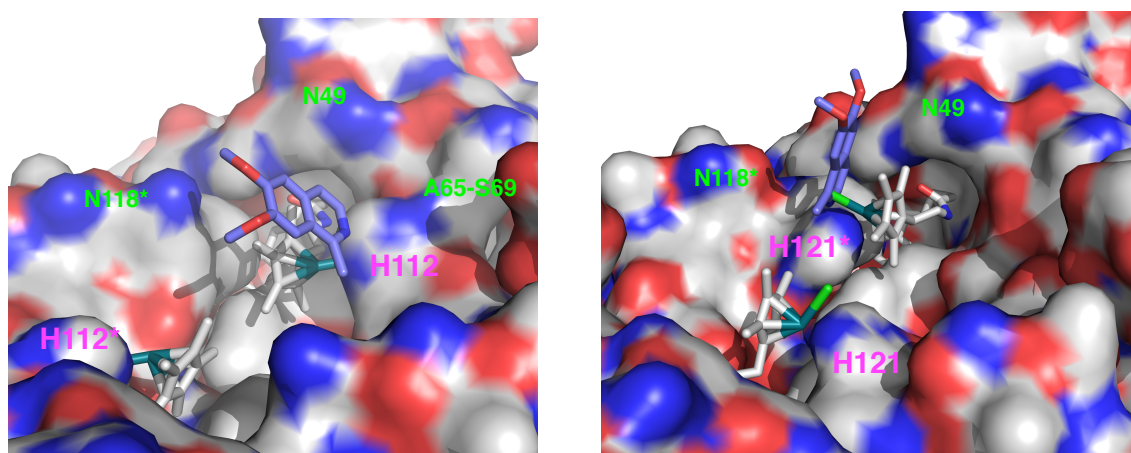


Figure M11: Model of salsolidine precursor binding to Sav_{S112H}-[η^5 -(Biot-2_2)RhL₃]²⁺ (left) and Sav_{K121H}-[η^5 -(Biot-2_2)RhClL₂]⁺ (right). The metallocofactor is represented in grey and

the salsolidine precursor in purple. Green numbers indicate residues, which are potentially interesting for mutagenesis.

In both structures the RhCp*-unit of the cofactor is located in the vestibule of the biotin-binding site close to the surface of the protein. Upon cofactor binding to both Sav mutants, shallow depressions are formed, which are defined by protein residues within loops 45-51, 64-71, 112-118 and the arene cap of the cofactors. From the substrate modeling we conclude that only few and unspecific interactions exist between substrate and protein, while the arene cap of the cofactor is likely to contribute strongly to design the pose of the substrate binding. Thus, we speculate that the 1st coordination sphere has a greater impact on activity and selectivity than the 2nd coordination sphere (although in the first place the protein defines the cofactor position). Further experiments are needed to support this hypothesis. Mutations in proximity to the assumed substrate-binding site (in addition to either S112H or K121H) can help to elucidate the influence of the 2nd coordination sphere. The following amino acid positions would be of special interest due to their close proximity to the presumed substrate binding sites (**Figure M11**):

- double or triple mutants of Sav_{K121H}: saturation mutagenesis in positions Asn49, Gly48 (part of loop 45-51) and Asn118 (part of loop 112-118)
- double or multiple mutants of Sav_{S112H}: Asn49 (part of loop 45-51), Ala65, Asp67, Ser69 (part of loop 64-71) and Asn118 (part of loop 112-118)

Additionally would the application of other piano stool complexes (e.g. biotinylation of benzene or *p*-cymene instead of Cp*) help to elucidate the impact of the 1st coordination sphere and the metal on catalysis. Computational docking studies may help to obtain a quantitative model of the substrate binding to the complexes and rationalize the different activities and enantioselectivities.

3.2.3. Comparison of a Mono- and a Bis-Anchored Metallocofactor-Streptavidin Complex for Artificial Transfer Hydrogenation

The activity and enantioselectivity of the best *R*-selective dual-anchor ATHase (Sav_{K121H}-[η^5 -(Biot-2_2)RhCIL₂]⁺) is lower than that of the best mono-anchor ATHase mentioned in the previous chapter, Sav_{S112A}-[Cp*Ir(Biot-*p*-L)Cl] (**Table M2**).

Table M2: Comparison of performance of Sav_{S112A}-[Cp*Ir(Biot-*p*-L)Cl], Sav_{K121H}-[η^5 -(Biot-**2_2**)RhCIL₂]⁺ and Sav_{S112H}-[η^5 -(Biot-**2_2**)RhL₃]²⁺.

Entry	1	2	3
ATHase	Sav _{S112A} -[Cp*Ir(Biot- <i>p</i> -L)Cl]	Sav _{K121H} -[η^5 -(Biot- 2_2)RhCIL ₂] ⁺	Sav _{S112H} -[η^5 -(Biot- 2_2)RhL ₃] ²⁺
Reaction conditions	- 1 mol% complex - 0.33 mol% Sav _{S112A} tetramer - 69.0 mM** substrate - 3.65 M HCO ₂ Na - 2.9 M MOPS - pH 6.5, 55 °C, 2 h	- 2 mol% complex - 1 mol% Sav _{S112A} tetramer - 22.9 mM substrate - 3.8 M HCO ₂ Na - 3.1 M MOPS - pH 6.5, 55 °C, 12 h	- 2 mol% complex - 1 mol% Sav _{S112A} tetramer - 22.9 mM substrate - 3.8 M HCO ₂ Na - 3.1 M MOPS - pH 6.5, 55 °C, 12 h
<i>Ee</i> (%)	85 (<i>R</i>)	50 (<i>R</i>)	Rac.
Convers.(%)	100	95	37
TON	100	48	19
Approx. TOF (h ⁻¹)*	50	4	2

*TON divided by number of hours reaction time

**Note, the substrate concentrations in entries 2 and 3 are 0.33x that of entry 1 and the catalyst concentrations are 0.66x that of entry 1

The most prominent differences between the two hybrids (entry 1 and 2 **Table M2**) concern i) the central metal (Ir vs. Rh), ii) the 1st coordination sphere around the functional metal (monodentate histidine vs. bidentate TosEN ligand) and iii) the 2nd coordination sphere (**Figure M12**).

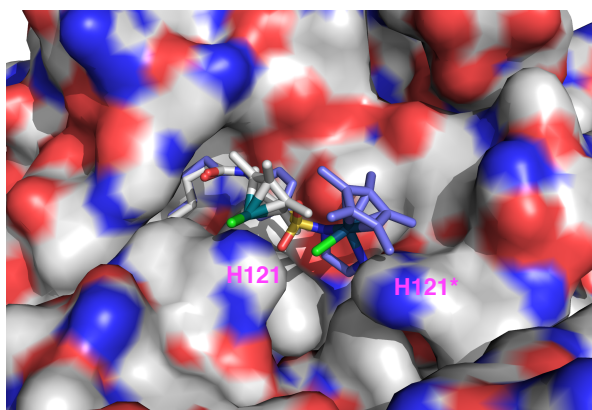


Figure M12: Superimposition of the crystal structures of the dual-anchor ATHase Sav_{K121H}-[η^5 -(Biot-**2_2**)RhCIL₂]⁺ (surface model and grey stick model) and the mono-anchor ATHase Sav_{S112A}-[Cp*Ir(Biot-*p*-L)Cl] (purple stick model).

Influence of Metal in the Artificial Transfer Hydrogenation:

Xiao and coworkers have investigated the influence of the metal by comparing the scope of the equivalent complexes $[\text{Cp}^*\text{Rh}(\text{TosDPEN})\text{Cl}]$ and $[\text{Cp}^*\text{Ir}(\text{TosDPEN})\text{Cl}]$ in the ATH of ketones and imines in aqueous conditions with sodium formate as hydrogen source. Although on average, the rhodium complex is the better catalyst with respect to the reaction rate, the turnover number and the enantioselectivity of the reduction of ketones,⁷² this can change in favor of the iridium catalyst when an imine instead of a ketone is employed as substrate.⁷³ In case of the dual-anchor ATHase, application of the iridium instead of the rhodium complex in Sav_{K121H} leads to an erosion of activity and selectivity (**Table 2_1**, entry 9 and 12). For the mono-anchored complex Sav_{S112A}- $[\text{Cp}^*\text{Ir}(\text{Biot-}p\text{-L})\text{Cl}]$, however, employment of the rhodium complex led to a slightly lower enantioselectivity and activity profile (**Table 1_1**, entry 3 and 4) and, thus, the Rh-cofactor was not tested with any further mutants. In conclusion, the effect of the metal, even though it can be very drastic, is hard to predict and, thus, testing different metals can be considered a good advice in artificial metalloenzyme design.

Influence of the 1st and the 2nd Coordination Sphere in Artificial Transfer Hydrogenation:

Noyori has reported a nearly 5 fold difference in reaction rate comparing complexes $[(\eta^6\text{-benzene})\text{Ru}(\text{TosEn})\text{Cl}]$ (TOF 86 h⁻¹) and $[(\eta^6\text{-benzene})\text{Ru}(2,2'\text{-bipyridyl})\text{Cl}]^+$ (TOF 18 h⁻¹). In complex with Sav, the two different biotinylated complexes Sav_{S112A}- $[\text{Cp}^*\text{Ir}(\text{Biot-}p\text{-L})\text{Cl}]$ and Sav_{K121H}- $[\eta^5\text{-(Biot-2_2)RhCl}_2]^+$ follow the same trend.

In summary, the bidentate biotinylated TosEN ligand, which contains a terminal acidic amine proton, is the better cofactor inside Sav compared to the monodentate arene-biotinylated cofactor.

3.2.4. Compatibility of a Dual-Anchor Artificial Transfer Hydrogenase with in Vivo Screening

Given that this concept meets one of the basic requirements to perform directed evolution – the cofactor activity is accelerated upon binding to Sav_{S112H}/Sav_{K121H} – initial experiments of the ATH of the salsolidine precursor in nearly physiological conditions were carried out by Elisa Nogueira and Yvonne Wilson. The following samples were used: i) Sav purified by selective precipitation from cell extracts, ii) Sav purified from cell extracts by filtration of Sav-bound biotin beads and iii) cell free extracts. Unfortunately, the high activity and

enantioselectivity obtained with Sav mutants purified by affinity chromatography could not be reproduced with any of the crude Sav preparations.

Three major problems have been pointed out that hamper the application of *in vivo* screening with the streptavidin-biotin technology:

- the inactivation of piano stool complexes by cellular thiol compounds (e.g. glutathione)
- the occupation of the biotin-binding sites of Sav expressed in *E. coli* with intrinsic biotin and
- the transportation of piano stool complex into the cytosol.

Currently, different strategies are followed in the Ward group to address these problems.

3.2.5. Further Applications of Arene-Biotinylated Piano Stool-Streptavidin Complexes

Upon binding to Sav_{WT}, a transition metal piano stool complex, which is biotinylated at the arene cap possesses three vacant coordination sites at the metal. Since in the ATH of ketones, imines and alkenes only one coordination site is required to form the active metal hydrido complex, the remaining two positions can be occupied by mono- or bidentate ligands. Instead of the tedious synthesis of biotinylated transition metal complexes, addition of a pool of commercially available ligands would be sufficient for the formation and screening of an ATHase library. Research towards this end is currently followed in the Ward group.

4. OsO₄·Streptavidin: A Tunable Hybrid Catalyst for the Enantioselective *cis*-Dihydroxylation of Olefins

Artificial Metalloenzymes

OsO₄-Streptavidin: A Tunable Hybrid Catalyst for the Enantioselective *cis*-Dihydroxylation of Olefins**

Valentin Köhler, Jincheng Mao, Tillmann Heinisch, Anca Pordea, Alessia Sardo, Yvonne M. Wilson, Livia Knörr, Marc Creus, Jean-Christophe Prost, Tilman Schirmer,* and Thomas R. Ward*

Enzymatic and homogeneous catalysis have evolved independently to address the challenges in the synthesis of enantiopure products. With the aim of complementing these fields, artificial metalloenzymes, which combine the structural diversity of biocatalysts with the wealth of metal-catalyzed reactions, have attracted increasing attention.^[1] In homogeneous catalysis the *cis*-selective, OsO₄-dependent asymmetric dihydroxylation (AD) of olefins ranks among the most powerful methods for the synthesis of vicinal diols. Ligands for homogeneous catalysis have been largely developed by Sharpless and co-workers, and are, with few exceptions, almost exclusively based on quinidine or quinine derivatives.^[2] Although most classes of prochiral olefins are dihydroxylated with good activity and selectivity, the *cis*-substituted olefins are problematic. Nature relies on non-heme iron dioxygenases such as naphthalene dioxygenase (NDO) to perform a related reaction. These enzymes display broad substrate scope.^[3] It is believed that both the OsO₄- and NDO-catalyzed dihydroxylations proceed by an outer sphere [3+2] mechanism in which the substrate is not bound to the metal in the transition state (Figure 1).^[2a,f,3c]

Considering a biomimetic approach, we hypothesized that anchoring a catalytically competent Os^{VIII} center within a protein might afford an artificial metalloenzyme for the AD of olefins. Encouraged by a report by Kokubo et al.,^[2d] we set out to screen various proteins and to test whether the

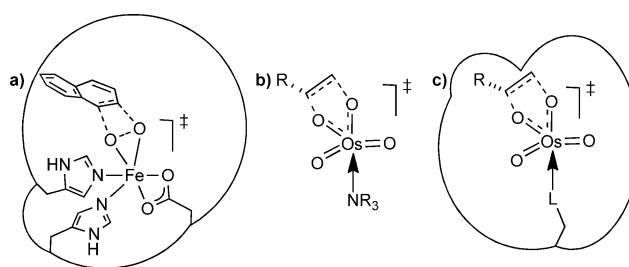


Figure 1. Postulated transition-state structure for the dihydroxylation of olefins: a) for the naphthalene dioxygenase; b) for the osmium-catalyzed AD of prochiral olefins; and c) for an artificial *cis*-dihydroxylase resulting from anchoring of OsO₄ within a host protein.

resulting dihydroxylases could be optimized by genetic means.

Five proteins were evaluated as hosts for the AD of α -methylstyrene: Wild-type streptavidin (SAV) clearly performed best. In contrast, bovine serum albumin (BSA) yielded the opposite enantiomer, albeit with a low turnover number (Table 1). In view of the size of the proteins (66 kDa for BSA and 16 kDa for the SAV monomer), the difficult recombinant production of BSA,^[4] and the number of

Table 1: Identification of a suitable host for the AD of α -methylstyrene in the presence of OsO₄.^[a]

Entry	Protein	<i>ee</i> [%] ^[b]	TON ^[c]
1 ^[d]	avidin	2 (R)	16
2	BSA	77 (S)	4
3 ^[e]	lysozyme	5 (S)	6
4 ^[f]	human carbonic anhydrase II	25 (S)	< 1
5 ^[g]	SAV	95 (R)	27

[a] Reactions were carried out with 6 μ mol substrate in a total reaction volume of 0.2 mL. [b] *ee* value determined by HPLC on a chiral stationary phase; absolute configuration assigned by comparison with literature data. [c] Determined by reverse-phase HPLC with internal standard. TON = mol product per mol K₂[OsO₂(OH)₄]. [d] Some precipitation was observed at the end of the run. [e] Immediate precipitation occurred upon addition of K₂CO₃/K₃[Fe(CN)₆]/K₂[OsO₂(OH)₄] stock solution to the protein stock solution. [f] Protein was not fully soluble. [g] Average of two independent runs.

[*] Dr. V. Köhler,^[4] Dr. J. Mao,^[4] T. Heinisch,^[4] Dr. A. Pordea, Dr. A. Sardo, Dr. Y. M. Wilson, L. Knörr, Dr. M. Creus, J.-C. Prost, Prof. Dr. T. R. Ward
Departement Chemie, Universität Basel
Spitalstrasse 51, 4056 Basel (Switzerland)
E-mail: thomas.ward@unibas.ch

T. Heinisch,^[4] Prof. Dr. T. Schirmer
Biozentrum, Universität Basel
Klingelbergstrasse 50/70, 4056 Basel (Switzerland)
E-mail: tilman.schirmer@unibas.ch

[†] These authors contributed equally to this work.

[**] We thank Prof. C. R. Cantor for the SAV gene, Chiral Technologies Europe for help with the method development for chiral-phase HPLC analysis, Beat Amrein for preliminary experiments, and Maurus Schmid for his contribution to the artwork. This research was funded by the Swiss National Science Foundation (Grant 200020-126366), the Cantons of Basel, and the Marie Curie Training Network (FP7-ITN-238434).

Supporting information for this article is available on the WWW under <http://dx.doi.org/10.1002/anie.201103632>.

histidine residues in BSA (17 His for BSA vs. 2 His per SAV monomer), SAV was selected as the host for further studies.

Next, a range of substrates was subjected to AD in the presence of SAV. With the exception of indene and precocene I, all the substrates produced the same enantiomer as with the quinidine scaffold in the Sharpless AD (i.e. AD-mix-β).^[2a,h-1] Although some substrates were converted with a low to moderate *ee* value, both *cis*-β-methylstyrene and α-methylstyrene were dihydroxylated with good selectivity (Table 2). The expected *syn* specificity of the reaction was demonstrated unambiguously (i.e. 1% or less *anti* product detected) by comparison of the dihydroxylation products of *cis*-β-methylstyrene and *trans*-β-methylstyrene (see Supporting Information).

To investigate the fate of SAV under the oxidizing conditions, the reaction mixture was subjected to SDS-PAGE after catalysis, and a remaining biotin-binding capability was revealed by biotin-4-fluorescein staining of the gel. As the *ee* value remained constant over the course of the reaction, we concluded that any decomposition pathway of the catalyst leads to species with strongly reduced activity (see Supporting Information).

Addition of 1.05 equivalents of biotin per SAV monomer afforded a nearly racemic product for the AD of α-methylstyrene. This finding suggests that the catalytically active Os moiety is located in the vicinity of the biotin-binding pocket (Figure 2b and 2c). As the carboxylate D128 ... HN_{urea} hydrogen bond of biotin is a key interaction for high biotin-SAV affinity,^[8] SAV D128A was tested in the AD. α-Methylstyrene was converted by the OsO₄-SAV D128A catalyst with significantly diminished selectivity.^[9] The AD of allyl phenyl ether in the presence of SAV D128A afforded the opposite enantiomer than with SAV and allyl phenyl sulfide was converted with remarkable selectivity. In contrast, the conservative mutation SAV D128E, which extends the side chain of residue 128 by a methylene group, led to less dramatic changes in the enantioselectivity (Table 2).

Further insight on the location of the catalytically active Os species was gathered by mutation of further residues located close to the biotin-binding site. Inspection of the SAV structure revealed that the L-7,8 loops (residues 113–121, Figure 2b) of two neighboring monomers line the biotin-binding pocket.^[10] Single point mutants at position S112, K121, and L124 were combined with various amounts of K₂[OsO₂(OH)₄] and tested in AD.^[11] Mutation at position SAV S112 proved most effective for fine-tuning purposes. Both SAV S112Y and SAV S112M led to an improvement of selectivity in many cases. α-Methylstyrene was converted with 75% *ee* (*R*) with SAV S112Y and 97% *ee* (*R*) with SAV S112M. Allyl phenyl sulfide, which gave nearly racemic product with SAV, was converted with 71% *ee* (*S*) with SAV S112Y. The best result for the AD of 1,2-dihydronaphthalene was obtained with SAV S112M (41% *ee*, 1*R*,2*S*). The conservative mutation SAV S112T, which introduces an additional methyl group to the amino acid side chain of residue 112, proved best for the dihydroxylation of precocene (68% *ee*, 3*R*,4*R*) and of *cis*-β-methylstyrene (92% *ee* 1*R*,2*S*), Table 2).

Table 2: Genetic optimization of the performance of artificial AD.^[a]
0.625 mol% SAVmutant (tetramer)
2.5 - 5 mol% K₂[OsO₂(OH)₄]
90 mM K₂CO₃
90 mM K₃[Fe(CN)₆]
H₂O, RT, 24h

Entry	Olefin	SAV mutant (mol% Os) ^[b]	<i>ee</i> [%] ^[c]	TON ^[d]	Ref. <i>ee</i> [%] [Ref.]
1		WT (2.5)	40 (<i>S</i>)	13	88 [2h]
2		S112Y (5.0)	82 (<i>S</i>)	14	
3		D128A (2.5)	77 (<i>R</i>)	21	
4		D128E (2.5)	0	9	
5		WT (2.5)	2 (<i>R</i>)	4	61 [2i]
6		S112Y (5.0)	71 (<i>S</i>)	7	
7		D128A (2.5)	71 (<i>R</i>)	10	
8		D128E (2.5)	12 (<i>R</i>)	5	
9		WT (2.5)	30 (1 <i>R</i> ,2 <i>S</i>)	13	56 [2j]
10		S112Y (5.0)	7 (1 <i>S</i> ,2 <i>R</i>)	12	
11		S112M (5.0)	41 (1 <i>R</i> ,2 <i>S</i>)	12	
12		WT (2.5)	90 (1 <i>R</i> ,2 <i>S</i>)	26	72 [2j]
13		S112Y (5.0)	45 (1 <i>R</i> ,2 <i>S</i>)	11	
14		S112T (2.5)	92 (1 <i>R</i> ,2 <i>S</i>)	16	
15 ^[e]		S112T (2.5)	91 (1 <i>R</i> ,2 <i>S</i>)	≥ 16	
16		WT (2.5)	5 (1 <i>S</i> ,2 <i>R</i>)	12	53 [2k]
17		S112Y (5.0)	16 (1 <i>R</i> ,2 <i>S</i>)	12	
18		D128A (2.5)	45 (1 <i>R</i> ,2 <i>S</i>)	13	
19		WT (2.5)	62 (3 <i>R</i> ,4 <i>R</i>)	6	67 [2l]
20		S112Y (5.0)	26 (3 <i>R</i> ,4 <i>R</i>)	5	
21		S112T (2.5)	68 (3 <i>R</i> ,4 <i>R</i>)	6	
22		WT (2.5)	95 (<i>R</i>)	27	99 [2n]
23		K121N (5.0)	24 (<i>R</i>)	8	
24		L124G (5.0)	16 (<i>R</i>)	11	
25		L124K (2.5)	89 (<i>R</i>)	18	
26		S112Y (5.0)	75 (<i>R</i>)	15	
27		S112M (5.0)	97 (<i>R</i>)	16	
28		D128A (2.5)	53 (<i>R</i>)	22	
29		D128E (2.5)	80 (<i>R</i>)	21	
30 ^[f]		WT (2.5) + biotin	9 (<i>R</i>)	13	

[a] Results are the average of two independent runs, see Table 1 and Supporting Information for experimental details. [b] The ideal osmate loading was determined for each mutant (see Supporting Information and Ref. [7]). [c] *ee* determined by HPLC on a chiral stationary phase; absolute configuration assigned by comparison with literature data. [d] Determined by reverse-phase HPLC with internal standard. TON = mol product/mol K₂[OsO₂(OH)₄]. [e] Carried out on a 120 μmol scale; TON is based on yield of isolated product. [f] 1.05 equivalents of D-biotin were added relative to protein monomer.

The system performed well on a range of challenging substrates. Noteworthy results were obtained for allyl phenyl sulfide (Table 2, entries 6, and 7) and *cis*-β-methylstyrene (Table 2, entry 14) and are the highest *ee* values ever reported for these substrates to the best of our knowledge.

For other demanding *cis*-substituted substrates, such as 1,2-dihydronaphthalene and indene, the enantioselectivities could be significantly improved by site-directed mutagenesis

(Table 2, entries 11 and 18). For the AD of precocene, the *ee* value obtained with SAV S112T matched the best result obtained with quinidine-derived systems.

Importantly, exchange of the lysine side chain at position 121 resulted in low levels of stereoselectivity: the highest *ee* value observed for any SAV K121 mutant/substrate combination was 24% (*R*) (α -methylstyrene; Table 2, entry 23). Mutating the leucine L124 had a less pronounced deleterious (or neutral in one case) effect on selectivity.

With the aim of gaining structural insight on the location of the Os center, SAV crystals were grown (at pH 4.0 or 7.3) and subsequently soaked in a solution of $K_2[OsO_2(OH)_4]$. The resulting crystals were subjected to X-ray analysis (see the Supporting Information).

Soaking crystals, obtained at pH 7.3, resulted in anomalous scattering density (modeled with an Os atom), which was detected in the proximity of four residues: N^ϵ of K80, N^ϵ of H87, N^ϵ of H127 and N^ϵ of K132 (Figure 2a). The intrinsic packing disorder, however, did not allow full refinement but yielded precious information on potential Os-binding sites. In contrast, the X-ray data of the crystals obtained at pH 4.0, yielded a well-behaved structure with a single Os binding site close to N^ϵ of the H127 side chain (see the Supporting Information).

The three osmium binding sites identified by X-ray crystallography located in the proximity of the biotin binding

site (e.g. H87, H127 and K80) were subjected to site-directed mutagenesis. Catalysis in the presence of single mutants SAV H87A, SAV H127A, and SAV K80G gave comparable results to SAV in the AD of α -methylstyrene, (lowest *ee* 89% (*R*) with H87A; see Table S1 in the Supporting Information).^[6] Although the structural data did not allow identification of the actual catalytic site, it suggests that not all of the osmium is catalytically active, which accounts for the modest TONs (up to 27 turnovers per added osmium).^[2m]

In summary, we have demonstrated that high selectivity for challenging substrates can be obtained with an artificial AD based on OsO_4 ·SAV. Importantly, it was shown that the hybrid catalyst offers vast opportunities for genetic optimization: Single point mutations can lead to a significant increase in enantioselectivity and even to an inversion of enantiopreference. As for several natural mono- and dioxygenases, this artificial metalloenzyme suffers from modest TONs combined with a high molecular weight. Current efforts are thus aimed at increasing the TON by identifying the location and the kinetic profile of the catalytically competent osmium species and testing other challenging substrates, including tri- and tetrasubstituted olefins. Finally, from a biomimetic perspective, combination with a flavin-coupled NMO-recycling system with H_2O_2 as the stoichiometric oxidant would be of great interest.^[2n,o]

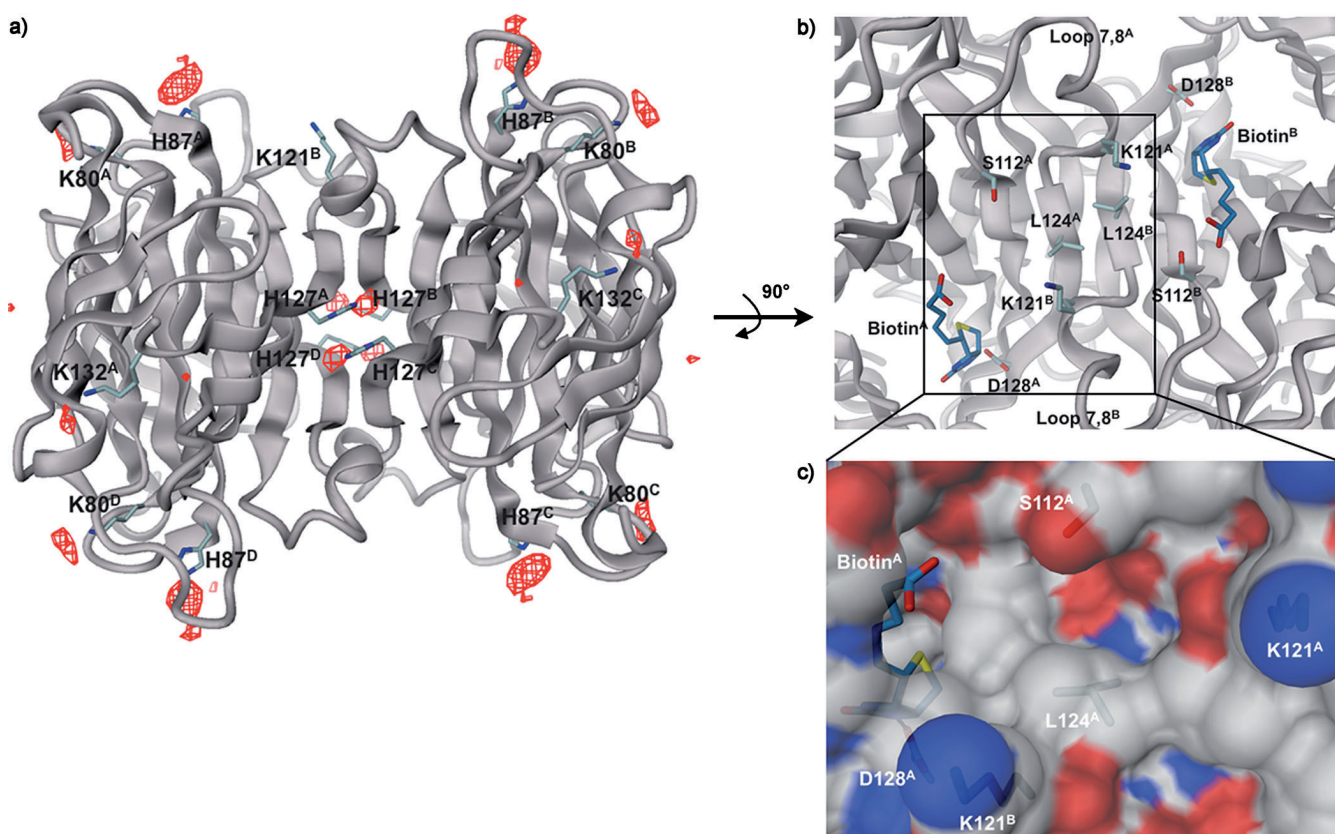


Figure 2. Crystal structure of SAV soaked in $K_2[OsO_2(OH)_4]$ at pH 7.3: a) ribbon representation of SAV tetramer highlighting positions of strong anomalous difference density (in red, contoured at 4σ); b) close-up view of the biotin-binding pocket (from PDB 1stp) highlighting the residues and biotin (stick representation) which strongly influence catalysis; c) surface representation of close-up view.

Received: May 27, 2011
 Revised: August 29, 2011
 Published online: September 21, 2011

Keywords: dihydroxylation · metalloenzymes · mutagenesis · osmium

- [1] a) Y. Lu, N. Yeung, N. Sieracki, N. M. Marshall, *Nature* **2009**, *460*, 855–862; b) F. Rosati, G. Roelfes, *ChemCatChem* **2010**, *2*, 916–927; c) M. T. Reetz, *Top. Organomet. Chem.* **2009**, *25*, 63–92; d) S. Abe, T. Ueno, Y. Watanabe, *Top. Organomet. Chem.* **2009**, *25*, 25–43; e) Q. Jing, R. J. Kazlauskas, *ChemCatChem* **2010**, *2*, 953–957; f) P. J. Deuss, G. Popa, C. H. Botting, W. Laan, P. C. Kamer, *Angew. Chem.* **2010**, *122*, 5443–5445; *Angew. Chem. Int. Ed.* **2010**, *49*, 5315–5317; g) J. Podtetenieff, A. Taglieber, E. Bill, E. J. Reijerse, M. T. Reetz, *Angew. Chem.* **2010**, *122*, 5277–5281; *Angew. Chem. Int. Ed.* **2010**, *49*, 5151–5155; h) T. Heinisch, T. R. Ward, *Curr. Opin. Chem. Biol.* **2010**, *14*, 184–199; i) P. Fournier, R. Fiammengio, A. Jäschke, *Angew. Chem.* **2009**, *121*, 4490–4493; *Angew. Chem. Int. Ed.* **2009**, *48*, 4426–4429.
- [2] a) H. C. Kolb, M. S. VanNieuwenhze, K. B. Sharpless, *Chem. Rev.* **1994**, *94*, 2483–2587; b) T. Oishi, M. Hirama, *Tetrahedron Lett.* **1992**, *33*, 639–642; c) Y. Imada, T. Saito, T. Kawakami, S.-I. Murahashi, *Tetrahedron Lett.* **1992**, *33*, 5081–5084; d) T. Kokubo, T. Sugimoto, T. Uchida, S. Tanimoto, M. Okano, *J. Chem. Soc. Chem. Commun.* **1983**, 769–770; e) M. A. Andersson, R. Epple, V. V. Fokin, K. B. Sharpless, *Angew. Chem.* **2002**, *114*, 490–493; *Angew. Chem. Int. Ed.* **2002**, *41*, 472–475; f) A. B. Zaitsev, H. Adolfsson, *Synthesis* **2006**, 1725–1756; g) K. B. Sharpless, *Angew. Chem.* **2002**, *114*, 2126–2135; *Angew. Chem. Int. Ed.* **2002**, *41*, 2024–2032; h) Z.-M. Wang, X.-L. Zhang, K. B. Sharpless, *Tetrahedron Lett.* **1993**, *34*, 2267–2270; i) P. J. Walsh, P. T. Ho, S. B. King, K. B. Sharpless, *Tetrahedron Lett.* **1994**, *35*, 5129–5132; j) H. Becker, S. B. King, M. Taniguchi, K. P. M. Vanhessche, K. B. Sharpless, *J. Org. Chem.* **1995**, *60*, 3940–3941; k) L. Wang, K. B. Sharpless, *J. Am. Chem. Soc.* **1992**, *114*, 7568–7570; l) Z.-M. Wang, K. Kakiuchi, K. B. Sharpless, *J. Org. Chem.* **1994**, *59*, 6895–6897; m) H. C. Kolb, P. G. Andersson, K. B. Sharpless, *J. Am. Chem. Soc.* **1994**, *116*, 1278–1291; n) S. Y. Jonsson, K. Färnegårdh, J.-E. Bäckvall, *J. Am. Chem. Soc.* **2001**, *123*, 1365–1371; o) K. Bergstad, S. Y. Jonsson, J.-E. Bäckvall, *J. Am. Chem. Soc.* **1999**, *121*, 10424–10425.
- [3] a) D. R. Boyd, G. N. Sheldrake, *Nat. Prod. Rep.* **1998**, *15*, 309–324; b) T. Hudlicky, D. Gonzalez, D. T. Gibson, *Aldrichimica Acta* **1999**, *32*, 35–62; c) A. Karlsson, J. V. Parales, R. E. Parales, D. T. Gibson, H. Eklund, S. Ramaswamy, *Science* **2003**, *299*, 1039–1042; d) T. Hudlicky, J. W. Reed, *Synlett* **2009**, 685–703.
- [4] P. A. Colussi, T. C. Evans, C. H. Taron (New England Biolabs, Inc.), WO2007123689, **2007**.
- [5] N. Humbert, A. Zocchi, T. R. Ward, *Electrophoresis* **2005**, *26*, 47–52.
- [6] Although the effect of mutating K132 has not yet been investigated, the results obtained with mutations at other sites (namely S112, K121, L124, and D128) render the involvement of this amino acid side chain unlikely.
- [7] The performance of mutants/batches used in this study was first evaluated with various ratios of osmate to protein to determine the loading that led to the highest HPLC yield without erosion of enantioselectivity; see the Supporting Information for details.
- [8] a) P. C. Weber, D. H. Ohlendorf, J. J. Wendoloski, F. R. Salemme, *Science* **1989**, *243*, 85–88; b) P. C. Weber, J. J. Wendoloski, M. W. Pantoliano, F. R. Salemme, *J. Am. Chem. Soc.* **1992**, *114*, 3197–3200; c) J. DeChancie, K. N. Houk, *J. Am. Chem. Soc.* **2007**, *129*, 5419–5429; d) S. Freitag, V. Chu, J. E. Penzotti, L. A. Klumb, R. To, D. Hyre, I. Le Trong, T. P. Lybrand, R. E. Stenkamp, P. S. Stayton, *Proc. Natl. Acad. Sci. USA* **1999**, *96*, 8384–8389.
- [9] A. Pordea, M. Creus, J. Panek, C. Duboc, D. Mathis, M. Novic, T. R. Ward, *J. Am. Chem. Soc.* **2008**, *130*, 8085–8088.
- [10] The residue K121 is significantly closer to residue D128 of the adjacent monomer in the tetrameric structure of SAV than to the D128 on the same oligopeptide chain (12.67 vs. 20.70 Å for C_α).
- [11] After an initial screening of a wider range of SAV mutants with styrene, five SAV S112X mutants (S112N, S112A, S112T, S112M, S112Y), four SAV K121X (K121A, K121F, K121N, K121H), and four SAV L124X mutants (L124G, L124K, L124N, L124Y) were selected for further study.

Supporting Information

© Wiley-VCH 2011

69451 Weinheim, Germany

OsO₄-Streptavidin: A Tunable Hybrid Catalyst for the Enantioselective *cis*-Dihydroxylation of Olefins**

Valentin Köhler, Jincheng Mao, Tillmann Heinisch, Anca Pordea, Alessia Sardo, Yvonne M. Wilson, Livia Knörr, Marc Creus, Jean-Christophe Prost, Tilman Schirmer, and Thomas R. Ward**

7. Crystal structures of two streptavidin-osmium complexes

7.1 Crystallization

Streptavidin used for crystallization comprised residues 13-159 of the native core streptavidin and an N-terminal T7-tag. Stable SAV crystals for osmium soaking were obtained in two different forms at pH 4.0 and 7.3 by hanging-drop vapor diffusion at room temperature (Table S3). For complex formation, single crystals were equilibrated against an excess of $K_2[OsO_2(OH)_4]$ and flash-frozen in liquid nitrogen.

Table S3: Crystallization of streptavidin and osmium soaking.

	Crystal Form I (pH 4.0)	Crystal Form II (pH 7.3)
Crystallization	2.5 μ L Sav (26 mg/mL lyophilized protein in H ₂ O) + 7.5 μ L precipitation buffer (2 M NH ₄ SO ₄ , 0.1 M Na acetate, pH 4.0) equilibrated against reservoir buffer; crystals within 24h	5 μ L Sav (15 mg/mL lyophilized protein in H ₂ O) + 5 μ L precipitation buffer (0.2 M Mg acetate, pH 7.3, 30 % PEG 3350) equilibrated against reservoir buffer; crystals within 1 week
Metal soaking	single Sav crystal was soaked in 10 μ L of 10 mM $K_2[OsO_2(OH)_4]$ in precipitation buffer and equilibrated 24 h	single Sav crystal was soaked in 10 μ L of 10 mM $K_2[OsO_2(OH)_4]$ in precipitation buffer and equilibrated 24 h
Cryo soaking	osmate-soaked crystal was cryo-protected by soaking in a solution of 20 % glycerol in precipitation buffer	-

7.2 X-ray diffraction experiment and structure determination

Diffraction data were collected at the Swiss Light Source (beamline X06DA) at a wavelength of 0.9793 Å, i.e. slightly below the L-II absorption edge of osmium (1.0010 Å). Crystal indexing and data processing was carried out with programs MOSFLM, POINTLESS and SCALA from the CCP4 Suite.^[6] The phase problem was solved by molecular replacement with MOLREP^[7] (crystal I) and PHASER^[8] (crystal II). Rigid body and restrained refinement

was carried out with REFMAC.^[9] COOT^[10] and O^[11] were used for model building and DINO¹ for figure drawing.

7.2.1 Crystal form I (pH 4.0)

Molecular Replacement and Structure Refinement. Molecular replacement was carried out using as a model the structure with PDB code 2qcb. The initial model was refined by rigid body refinement and subsequent restrained anisotropic refinement, including TLS tensors (**Table S4**). Ligand building and refinement was carried out using geometrical restraints as derived from a complex of glycol-osmate ester with a cinchona alkaloid ligand deposited in the CSD (CSD code ketkez).^[12]

Table S4: Data processing and refinement statistics.

	Crystal Form I	Crystal Form II
Data Processing		
Resolution (Å)	25 - 1.75 (1.84 - 1.75)	49 - 2.40 (2.53 - 2.40)
Space Group	I4 ₁ 22	C2
Cell dimensions (Å)	a = 57.5 b = 57.5 c = 172.0	a = 81.2 b = 81.6 c = 91.5 β = 90.3°
R _{merge} (%)	6.2 (27.6)	10.9 (33.3)
No. unique reflections	14995	19722
Multiplicity	7.9 (3.8)	2.7 (2.2)
Completeness	99.3 (96.9)	84.4 (71.2)
I/sig(I)	19.4 (4.0)	5.3 (2.1)
Structure refinement		
Resolution (Å)	30 - 1.75	49 - 2.4
R _{work} /R _{free}	16.5 (20.4)	28.6 (30.6)

¹ www.dino3d.org

	Crystal Form I	Crystal Form II
Overall B-factor (\AA^2)	12.4	3.4
R.m.s deviations		
Bond lengths (\AA)	0.0118	0.0048
Bond angles ($^\circ$)	1.396	0.813

values in parenthesis refer to the highest resolution bin

Overall Structure. Crystal form I is of space group $I4_122$ and contains one SAV molecule in the asymmetric unit. Application of a crystallographic dyad symmetry generates the functional SAV tetramer of 222-symmetry. The final protein model comprises residues 13-134 with 94.7 % of the residues found in the most-favored regions of a Ramachandran plot, and no Ramachandran outliers (**Figure S5a**). As observed before,^[13] both the N-terminal T7 tag (residues 1-12) as well as 25 residues at the C-terminus are not resolved, probably due to disorder. The residues of the flexible loop 45-53 are in the open, non-biotin binding conformation.^[14] As expected, no cofactor is present in the structure. Instead, the density observed in the biotin-binding cavity suggests the presence of two glycerol and five water molecules.

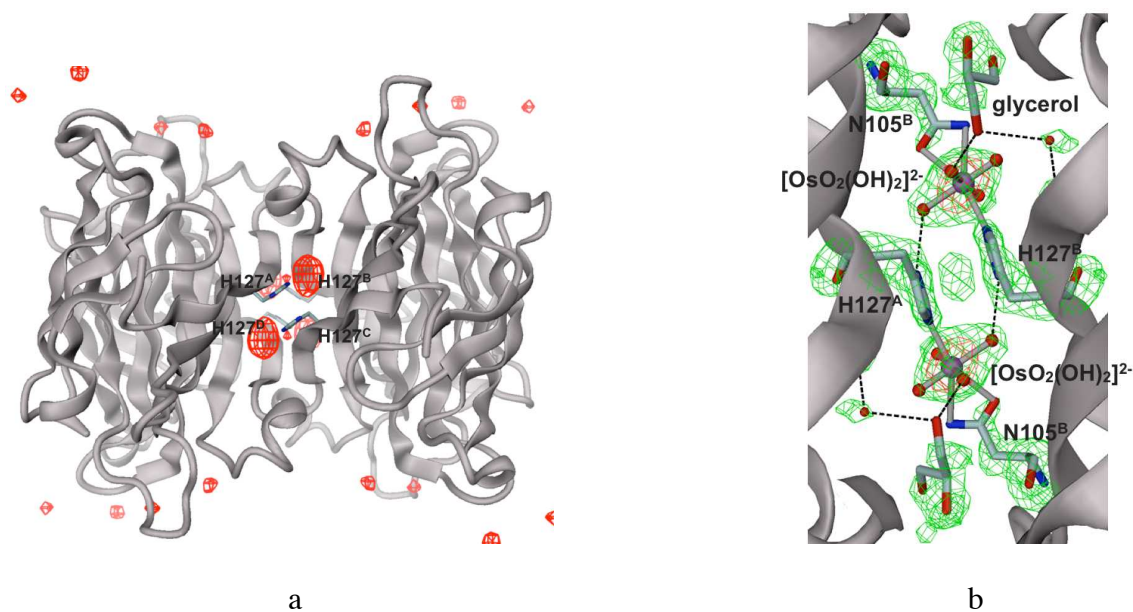


Figure S9: Crystal structure of crystal form I (pH 4.0), view along local 2-fold symmetry axis. (A) Ribbon representation of SAV tetramer indicating residues next to strong anomalous difference density (in red,

contoured at 4 σ), (B) Close-up view of $[\text{OsO}_2(\text{OH})_2]^{2-}$ binding site between two symmetry-related SAV monomers.

Osmium-Binding Sites. Strong Fo-Fc (39 σ) and anomalous difference density peaks (44 σ) were found next to N ϵ of H127 (**Figure S9a and Table S5**) and assigned to osmium atoms. The short Os-N ϵ (H127) distance of 2.2 Å suggests osmium coordination by the nitrogen lone electron pair. The Fo-Fc density of the osmium ligand has the shape of an ellipsoid with the equatorial plane at right angle to the imidazole plane of H127 (**Figure S9b**). Four oxygen atoms were modeled in equatorial position. The Os-O distances were set to 1.7 Å for one pair of *cis*-related oxygens and to 2.1 Å for the other pair. This is consistent with two Os=O double bonds and two Os-OH single bonds. The anisotropic shape of the density might be explained by a restricted rotation of the $\{\text{OsO}_2(\text{OH})_2\}$ moiety around the Os-N ϵ (H127) bond due to H-bonds between the equatorial oxygens and the neighboring N δ (H127') as well as a glycerol molecule (**Figure S9b**). The second axial position is not occupied. However, the side chain of residue N105, in vicinity to the osmium, is present in two conformations, in one of which the amide group is in proximity to coordinate osmium (**Figure S9b**). The $\{\text{OsO}_2(\text{OH})_2\}$ moiety appears not to be fully occupied. Best refinement results were obtained with an occupancy of 80 % for the $\{\text{OsO}_2(\text{OH})_2\}$ fragment.

Table S5: Positions of strong spots of anomalous scattering and Fo-Fc density.

	Peak height of anomalous density [σ]	Peak height of Fo-Fc map [σ]	Estimated osmium occupancy [%]	Modeled as
Crystal Form I (pH 4.0)				
His127	44	39	80	$\{\text{OsO}_2(\text{OH})_2\}$ moiety
Crystal Form II (pH 7.3)				
Lys80	5-7	9-10	80	Os atom
His87	14-17	21-24	80	$\{\text{OsO}_3\}$ moiety

	Peak height of anomalous density [σ]	Peak height of Fo-Fc map [σ]	Estimated osmium occupancy [%]	Modeled as
His127	6	9-10	0	due to unclear densities no ligand was modeled
Lys132	5	10-11	30	Os atom

7.2.2 Crystal form II (pH 7.3)

During structure determination of crystal form II, a crystal packing disorder became obvious. Probably, layers of Sav tetramers extending in the ab-plane are stacked with a stochastic 2-fold ambiguous displacement of ± 9.3 Å. A crystallographic report about these interesting packing defects will be published elsewhere (Heinisch and Schirmer, unpublished). Despite the disorder, the structure could be solved in space group C2 by molecular replacement using as a model the C2 form of the structure with PDB code 2bc3 (Table S4). Due to the incomplete crystal-packing model, however, rigid body and full restraint refinement yielded only a moderate R_{free} of 30.6 %.

Overall Structure. Although crystallized at a different pH, the overall SAV structure of crystal form II (pH 7.3) is virtually the same as that of crystal form I (pH 4.0). The only difference between the two crystal forms is the replacement of the H-bridge D61'-O δ - H85-N ϵ by the salt bridge D61'-O δ - H87-N δ in crystal II. The pH-dependent effect has been reported by Katz and co-workers.^[15] The salt bridge between D61' and H87 may have a positive effect on the osmium coordination to H87-N ϵ due to a possibly increased charge density at H87-N ϵ .

Osmium-Binding Sites. In contrast to crystal form I, weak density in the anomalous difference and the Fo-Fc map was found close to H127^{A/B} (Figure 2a and Table S5; the indices A and B indicate the two monomers of a SAV dimer within the asymmetric unit). A

stronger peak, however, was located in vicinity to H87^{A/B}. Additional weak density was found next to lysine residues K80^{A/B} and K132^{A/B}. The strong density at H87^{A/B}-N ϵ was modeled as an osmium atom surrounded by four equatorial and one axial oxygen. The H87^{A/B}-N ϵ -Os distance was set to 2.1 Å. Because of insufficient electron density, only one osmium atom was modeled next to the side-chain amino acid groups of K80 and K131 and no osmium next to the side chain of H127. The best refinement results were obtained with ligand occupancies between 80 % and 0 % (**Table S5**).

8. References

- [1] N. Humbert, A. Zocchi, T. R. Ward, *Electrophoresis* **2005**, *26*, 47-52.
- [2] M. Minato, K. Yamamoto, J. Tsuji, *J. Org. Chem.* **1990**, *55*, 766-768.
- [3] a) Preparative procedure used for all compounds and comparison for product from allylphenylether: Z.-M. Wang, X.-L. Zhang, K. B. Sharpless, *Tetrahedron Lett.* **1993**, *34*, 2267-2270; b) comparison for product from allylphenylsulfide (the assignment of the absolute configuration in the cited reference is based on the mnemonic device developed by Sharpless and coworkers): P. J. Walsh, P. T. Ho, S. B. King, K. B. Sharpless, *Tetrahedron Lett.* **1994**, *35*, 5129-5132; c) comparison for product from α -methylstyrene, *cis*- β -methylstyrene, dihydronaphthalene and indene: H. Becker, S. B. King, M. Taniguchi, K. P. M. Vanheesche, K. B. Sharpless, *J. Org. Chem.* **1995**, *60*, 3940-3941; d) comparison for product from precocene: Z.-M. Wang, K. Kakiuchi, K. B. Sharpless, *J. Org. Chem.* **1994**, *59*, 6895-6897.
- [4] L. Zheng, U. Baumann, J.-L. Reymond, *Nucleic Acids Res.* **2004**, *32*, e115.
- [5] www.basic.northwestern.edu/biotools/OligoCalc.html
- [6] *Acta Cryst. D*, **1994**, *50*, 760-763.
- [7] Murshudov, G. N., Vagin, A. A., Dodson, E. J., *Acta Cryst. D*, **1997**, *53*, 240-255.
- [8] McCoy, A. J., Kunstleve, R. W., Adams, P. D., Winn, M. D., Storono, L. C., Read, R. J., *J. Appl. Cryst.*, **2007**, *40*, 658-674.
- [9] Brunger, A. T., *Acta Cryst. D*, **1993**, *49*, 24-36.
- [10] Emsley, P., Cowtan, K., *Acta Cryst. D*, **2004**, *60*, 2126-2132.
- [11] Jones, T. A., Zou, J. Y., Cowan, S. W., Kjeldgaard, M., *Acta Cryst. A*, **1991**, *47*, 110-119.
- [12] Pearlstein, R. M., Blackburn, B. K., Davis, W. M., Sharpless, K. B., *Angew. Chem. Int. Ed.*, **1990**, *29*, 639 - 641.

- [13] Creus, M., Pordea, A., Rossel, T., Sardo, A., Letondor, C., Ivanova, A., Letrong, I., Stenkamp, R. E., Ward, T. R., *Angew. Chem. Int. Ed.*, **2008**, *47*, 1400-1404.
- [14] Freitag, S., LeTrong, I., Klumb, L., Stayton, P. S., Stenkamp, R. E., *Prot. Sci.*, **1997**, *6*, 1157-1166.
- [15] Katz, B. A., *J. Mol. Biol.*, **1997**, *274*, 776-800.

4.1. Author Contributions

General idea:

Thomas R. Ward

Catalyst screening and experiment design:

Valentin Köhler, Jinjeng Mao, Tillmann Heinisch, Anca Pordea, Jean-Christophe Prost

Production of streptavidin variants:

Alessia Sardo, Yvonne M. Wilson, Livia Knörr, Marc Creus,

Crystal structure analysis:

Tillmann Heinisch, Tilman Schirmer

Manuscript writing:

Thomas R. Ward, Valentin Köhler and all other authors

4.2. Comment on Publication

4.2.1. Sharpless- vs. Enzymatic Asymmetric Olefin Dihydroxylation

Sharpless Asymmetric Dihydroxylation:

It is known since the 1930s that osmium tetroxide can be used to dihydroxylate olefins in either a stoichiometric or a catalytic reaction using catalytic amounts of pyridine and a sacrificial oxidant.^{74,75} Sharpless and coworkers developed in the 1970s chiral auxiliaries based on cinchona alkaloids for the catalytic asymmetric dihydroxylation of olefins (**Figure M13**). Upon testing many different stoichiometric oxidants, $K_3[Fe(CN)_6]$ was identified as the most suitable for the dihydroxylation of a large number of olefins.⁷⁶ To improve the stereoselectivity of the reaction, a biphasic system of tBuOH and water was introduced.⁷⁷ The standard reactants for the efficient laboratory-scale asymmetric olefin dihydroxylation of many different olefins are commercially available premixed as AD-mixes α and β .

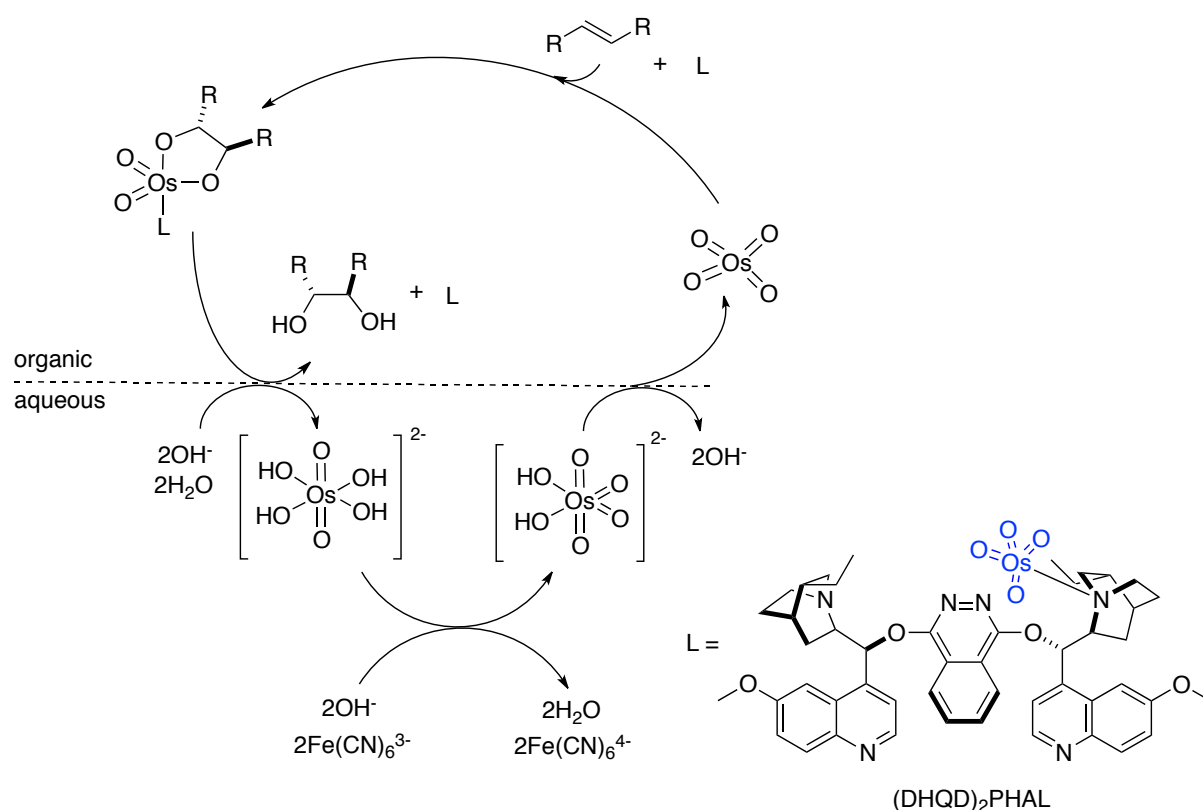


Figure M13: Catalytic cycle of Sharpless asymmetric olefin dihydroxylation in a biphasic system.

Although the Sharpless asymmetric olefin dihydroxylation has an impressive substrate scope, its application on industrial scale is limited due to the relatively high costs of osmium and

cinchona alkaloid ligands, the moderate turnover number, the large amounts of expensive oxidant ($K_3[Fe(CN)_6]$) needed and the toxicity of osmium tetroxide. Instead, alternative synthesis strategies to obtain chiral diols seem to be favored in industry (e.g. via catalytic asymmetric hydrogenation).

Several studies tried to address these problems using i) the oxidant *N*-morpholino-*N*-oxide (NMO, 5x cheaper than $K_3[Fe(CN)_6]$),⁷⁸ ii) a coupled NMO-flavin- H_2O_2 system⁷⁹ or iii) molecular oxygen/air⁸⁰ as sacrificial oxidants. Further improvement of the catalyst performance is needed to provide a system of wide acceptance on industrial scale as well as for the selective dihydroxylation of reluctant olefins (e.g. *cis*-disubstituted or tetrasubstituted olefins).

Mono- and Dioxygenases for Asymmetric Olefin Dihydroxylation:

In Nature, oxygenation reactions are catalyzed by heme-iron monooxygenases (cytochromes P450), by diiron monooxygenases (e.g. methane monooxygenase), α -ketoglutarate-dependent non-heme iron monooxygenase (e.g. prolyl hydroxylase) or Rieske non-heme iron dioxygenases. The biological functions of these enzymes are to metabolize cellular building blocks (e.g. tryptophan) and pollutants (e.g. benzol), to repair DNA or to build collagen (e.g. prolyl hydroxylase). Numerous attempts have been made to apply oxygenases in the (asymmetric) hydroxylation of small synthons.⁸¹

The asymmetric olefin dihydroxylation catalyzed by the bacterial enzyme naphthalene dihydroxylase can be compared to the Sharpless dihydroxylation. The enzyme consists of three domains for i) olefin dihydroxylation (catalytic domain), ii) electron transport (ferredoxin domain) and iii) an NAD(P)H-dependent reductase domain (**Figure M14**).^{81–83} Even though the exact mechanism is still a matter of debate, an outer sphere mechanism (as in the Sharpless dihydroxylation) has been proposed for the transfer of the two oxygens to the substrate's C=C double bond (**Figure 3_1**). The enzyme's substrate scope ranges from the *cis*-dihydroxylation of olefins and aromats to the monohydroxylation of methyl groups, sulfoxidations and dealkylation reactions. Very high enantiomeric excess and yield are observed in many cases.⁸¹

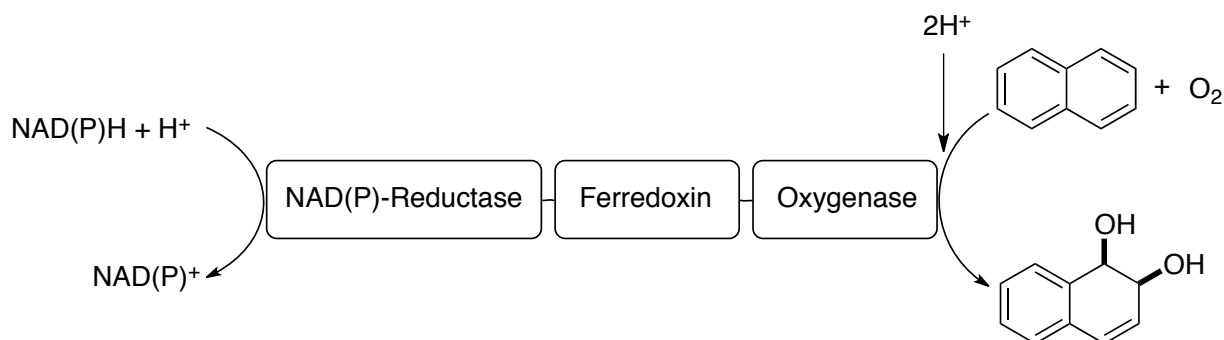


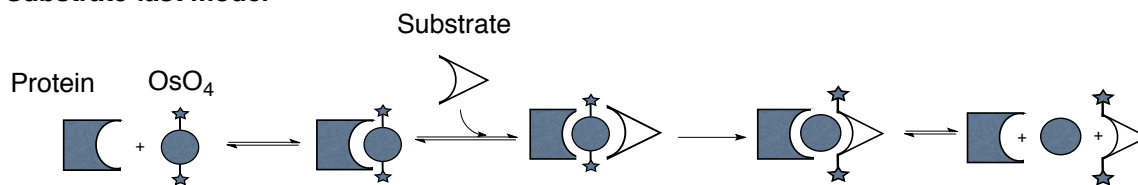
Figure M14: Domain organization of naphthalene dioxygenase.

4.2.2. Potential Reaction Mechanisms of the Artificial Olefin Dihydroxylase

Proposed Active Site and Reaction Mechanisms of the Artificial Olefin Dihydroxylase:

The crystal structures of complexes of Sav and K₂[OsO₂(OH)₄] solved at pH 4.0 and pH 7.5 revealed the osmium binding at His87 and His127 as well as Lys80 and Lys132. No osmium was detected in the biotin-binding pocket. This result suggests that the biotin-binding site has a low affinity for osmium as compared to the mentioned histidines and lysines. Unfortunately, CD-measurements of solutions with different Sav-OsO₄ stoichiometries did not allow to determine a K_d value. Further experiments (e.g. ITC) are needed to obtain a measure of cofactor affinity. The structure determination of an apo-Sav crystal soaked with K₂[OsO₂(OH)₄] and of α -methylstyrene did not yield any bound olefin molecule. Mutation of the amino acids involved in osmium binding in the two crystal structures did not change the catalytic results significantly. Moreover, the Sav mutant-activity pattern of the dihydroxylation α -methylstyrene hints for the importance of the biotin-binding pocket and particularly Lys121 in the reaction (**Figure 3_2**). In order to improve the catalytic performance of the Sav-OsO₄ system by site directed mutagenesis the knowledge of the active site is crucial. Towards this end, future attempts could aim at the synthesis of a stable reaction intermediate analogue α -methylstyrene osmate ester, which could be soaked into apo-Sav. Based on the results presented in the publication, two sequences of olefin dihydroxylation with the artificial dihydroxylase can be hypothesized: i) a substrate-last and ii) a sandwich model (**Figure M15**).

Substrate-last model



Sandwich model

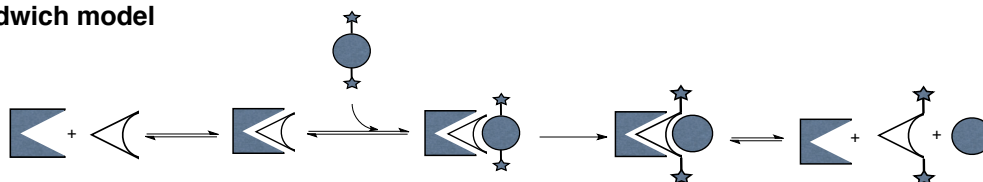


Figure M15: Two models of the reaction mechanism of the asymmetric dihydroxylation with Sav- OsO_4 catalyst.

The substrate-last model postulates the formation of a Sav- OsO_4 complex. The substrate can bind to the constituted active site of the artificial metalloenzyme and be dihydroxylated. The same mechanism is believed for the Sharpless asymmetric dihydroxylation using a complex of OsO_4 and a cinchona alkaloid ligand. Similarly, naphthalene dioxygenase consists of a tight iron-binding site. Due to the absence of OsO_4 in the Sav crystal structure, however, a second model is proposed.

In the sandwich model, a transient substrate-Sav complex is formed prior to attack of the OsO_4 to the activated olefin. This model would explain the absence of OsO_4 in the crystal structure. It would allow a facile reoxidation of the osmium after one catalytic turnover. Furthermore, the lack of a protein- OsO_4 coordination would explain the low turnover frequency of the AD as compared to small molecule tertiary amine or imine ligands. However, further experiments would need to be carried out to prove the hypothesis: e.g. crystallization of Sav with styrene or ITC with Sav and styrene.

Irrespective of the correct reaction mechanism, low affinities of either Sav- OsO_4 or Sav-substrate have to be assumed from the experimental results. This is in contrast to the high affinity of complexes of Sav with biotinylated transition metal complexes. The Os-dependent artificial dihydroxylase is an example for the control of selectivity by weak interactions between protein, cofactor and substrate. The engineering of weak, transient interactions, however, is challenging compared to covalent ones.

5. Human Carbonic Anhydrase II as a Host for Piano-Stool Complexes Bearing a Sulfonamide Anchor

Human Carbonic Anhydrase II as a host for piano-stool complexes bearing a sulfonamide anchor†

Fabien W. Monnard,^a Tillmann Heinisch,^{ab} Elisa S. Nogueira,^a Tilman Schirmer^b and Thomas R. Ward^{*a}

Received 18th January 2011, Accepted 8th June 2011

DOI: 10.1039/c1cc10345h

d⁶-piano-stool complexes bearing an arylsulfonamide anchor display sub-micromolar affinity towards human Carbonic Anhydrase II (hCA II). The 1.3 Å resolution X-ray crystal structure of [(η⁶-C₆Me₆)Ru(bispy 3)Cl]⁺ ⋅ hCA II highlights the nature of the host–guest interactions.

In recent years there has been an increasing interest in scrutinizing the interactions between organometallic compounds and proteins.^{1–3} This surge is primarily driven by three factors: (i) the realization that proteins may be privileged targets for metallodrugs,^{4–6} (ii) inert transition metals offer versatile scaffolds for the design of enzyme inhibitors⁷ and (iii) combining an organometallic moiety with a protein scaffold may lead to artificial metalloenzymes with interesting catalytic properties.^{8–11} In this latter context, three different strategies have been exploited for the localization of an organometallic moiety within the protein scaffold: covalent,^{12–16} dative^{17–21} and supramolecular anchoring.^{22,23} Building upon our experience with artificial metalloenzymes based on the biotin-avidin technology,^{24–27} we set out to identify an alternative protein scaffold for the supramolecular assembly of the organometallic ⋅ protein systems.

The choice of the host protein was based on the following design criteria:

(i) Large binding pockets capable of accommodating metal complexes. We anticipated that this may allow in the future to rely on computational design for the rational tailoring of an active site.^{28–31}

(ii) Easily derivatizable inhibitors compatible with soft transition metals and low dissociation constants.^{32,33} This should ensure that, upon linking the organometallic moiety to the inhibitor, nearly quantitative localization of the metal fragment within the protein cavity would result.

^a Department of Chemistry, University of Basel, Spitalstrasse 51, CH-4056 Basel, Switzerland. E-mail: thomas.ward@unibas.ch; Fax: +41 61 267 10 05; Tel: +41 61 267 10 04

^b Biozentrum, University of Basel, Klingelbergstrasse 50/70, CH-4056 Basel, Switzerland. E-mail: tilman.schirmer@unibas.ch; Fax: +41 61 267 21 09; Tel: +41 61 267 20 89

† Electronic supplementary information (ESI) available: Modified protocol for the expression of hCA II in *E. coli*. Detailed description of the X-ray structure. Synthesis and characterization of the [(η⁶-arene)Ru(bispy 3)Cl]⁺. See DOI: 10.1039/c1cc10345h

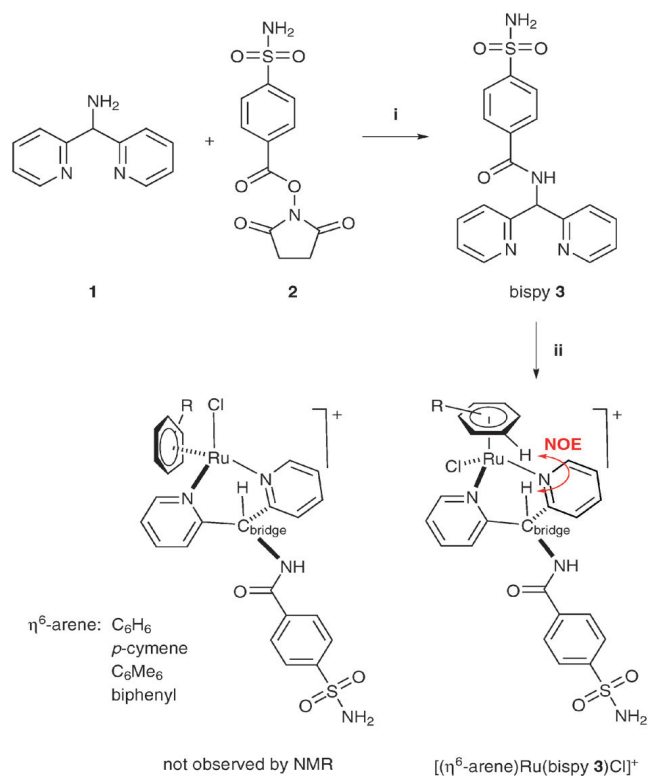
(iii) A robust, monomeric protein that is easy to overexpress and to purify.⁹ This could allow to apply directed evolution strategies for the optimization of the performance of the organometallic protein construct.

(iv) The host protein should be overexpressed in certain forms of cancer. With therapeutic applications in mind, this feature may be exploited to accumulate the metallo-prodrug in the cells requiring therapeutic action.^{34–36}

Based on the above considerations, we selected human Carbonic Anhydrase II (hCA II) as a model host for the incorporation of organometallic complexes.³⁷ hCA II is a stable monomeric protein (~29 kDa) with no post-translational modification. It is readily expressed in large amounts in *E. coli* and purified by affinity chromatography.³⁸ The Zn(II) ion is located at the base of a funnel-shaped cavity and arylsulfonamides, which bind tightly to zinc, have been thoroughly investigated as inhibitors. Their affinities vary over many orders of magnitude (down to sub-nanomolar).³⁹ Considering the size of the cavity (15 Å deep and 15 Å diameter at its mouth), we anticipated that, depending on the nature of the spacer between the arylsulfonamide anchor and the organometallic moiety,⁴⁰ hCA II may prove as a well-suited host. Finally, some CA isozymes (in particular CA IX) are overexpressed in certain forms of cancer.⁴¹

Thanks to their potential as catalysts and as metallodrugs, we selected a d⁶-piano-stool scaffold bearing an arylsulfonamide anchor as a model for incorporation within hCA II. The synthesis of [(η⁶-arene)Ru(bispy 3)Cl]⁺ is presented in Scheme 1 (see ESI† for full experimental details, including the production of recombinant hCA II).³⁸ NMR analysis of [(η⁶-benzene)Ru(bispy 3)Cl]⁺ revealed the presence of a single diastereomer as evidenced by an NOE cross-peak between the η⁶-benzene and HC_{bridge} (see Scheme 1 and ESI,† Fig. S1).

The binding profiles of [(η⁶-arene)Ru(bispy 3)Cl]⁺ towards hCA II were determined using the esterase assay based on the hydrolysis of *p*-nitrophenyl acetate at pH 8.0.^{42,43} Compared to the parent carboxylic acid 4-carboxybenzenesulfonamide, all complexes bearing the bispy 3 ligand display increased affinity. Interestingly, [(η⁶-biphenyl)Ru(bispy 3)Cl]⁺ displays the highest affinity towards hCA II, whereas [(η⁶-C₆Me₆)Ru(bispy 3)Cl]⁺ displays a significantly reduced affinity. These data illustrate the subtle complementarity between the piano-stool moiety and the funnel-shaped cavity (Table 1).



Scheme 1 Synthesis of $[(\eta^6\text{-arene})\text{Ru}(\text{bispy } \mathbf{3})\text{Cl}]^+$. *Reagents and conditions:* (i) H_2KPO_4 , $\text{H}_2\text{O}/\text{acetone}$ (1/6), rt, 24 h (93%); (ii) $[(\eta^6\text{-arene})\text{RuCl}_2]_2$, H_3CCN , reflux, 2 h (23–67%).

Table 1 Binding affinity of $[(\eta^6\text{-arene})\text{Ru}(\text{bispy } \mathbf{3})\text{Cl}]^+$ complexes determined by the decrease in hydrolytic activity of hCA II towards *p*-nitrophenyl acetate (see ESI[†])

Entry		K_i/nM
1	4-Carboxybenzenesulfonamide	569.2 ± 29.4
2	Bispy 3	45.3 ± 6.7
3	$[(\eta^6\text{-benzene})\text{Ru}(\text{bispy } \mathbf{3})\text{Cl}]^+$	194.1 ± 18.7
4	$[(\eta^6\text{-}p\text{-cymene})\text{Ru}(\text{bispy } \mathbf{3})\text{Cl}]^+$	275.3 ± 12.6
5	$[(\eta^6\text{-}C_6\text{Me}_6)\text{Ru}(\text{bispy } \mathbf{3})\text{Cl}]^+$	329.1 ± 16.1
6	$[(\eta^6\text{-biphenyl})\text{Ru}(\text{bispy } \mathbf{3})\text{Cl}]^+$	145.3 ± 11.9

To gain structural insight on the guest–host interactions, crystals of hCA II were soaked in a solution of $[(\eta^6\text{-}C_6\text{Me}_6)\text{Ru}(\text{bispy } \mathbf{3})\text{Cl}]^+$ and diffraction data were collected at the synchrotron to 1.3 Å resolution. After refinement of the protein structure, strong residual positive and anomalous difference density was apparent in the funnel-shaped sulfonamide-binding cavity, which could be modeled as the Ru-complex. The various interactions between the molecules’s benzene–sulfonamide anchoring group and the protein are reminiscent to related hCA II–sulfonamide complexes (see Fig. 1a and b and ESI[†]). Additionally, the head group, including ruthenium, bispyridine and hexamethylbenzene, interacts with the cavity’s “hydrophobic wall” (residues V121, F131, V135, L141, L198, P202, L204, see Fig. 1b). The piano-stool moiety lies at the entrance of the funnel-shaped sulfonamide binding site and the chlorine is exposed to the solvent. While the refinement of the bispy **3** part of the Ru-ligand gave the best results with an occupancy of 100%, for the ruthenium, hexamethylbenzene and chlorine the

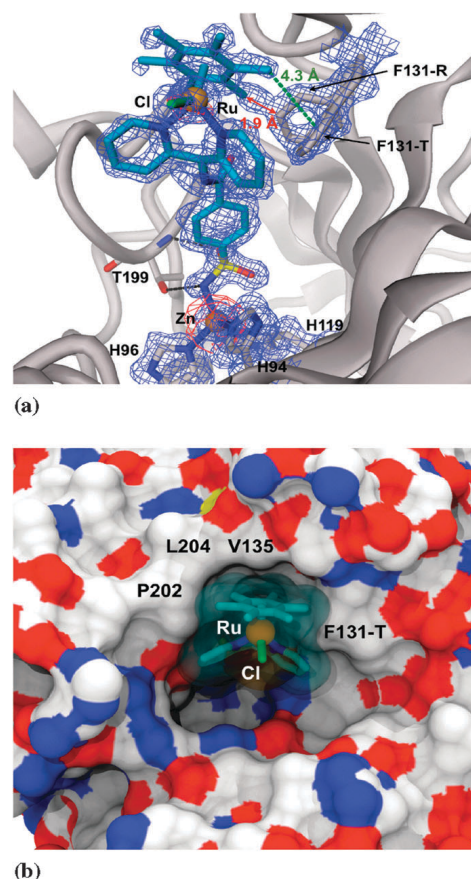


Fig. 1 Crystal structure of complex $[(\eta^6\text{-}C_6\text{Me}_6)\text{Ru}(\text{bispy } \mathbf{3})\text{Cl}]^+ \cdot \text{hCA II}$ (PDB code 3pyk). (a) Close-up view of the sulfonamide binding cavity. Hydrogen bonds between the sulfonamide anchoring group and protein are highlighted as black dotted lines. Upon ligand binding the phenyl of F131 undergoes a conformational change from F131-R to F131-T to prevent clashes (red arrow) and to form a CH/ π interaction (green dotted line). The 2Fo-Fc map is shown in blue at 1.0σ , the anomalous difference density map in red at 3.0σ . (b) Surface representation showing contacts between the ligand and the protein’s “hydrophobic wall” at the entrance of the ligand binding site.

occupancy was set to 50%. We assume that a partial dissociation of the metal from bispy **3** and the 10-fold increased affinity of the latter fragment for hCA II may explain this observation. The phenyl group of residue F131 was found to adopt two alternative, equally populated conformations. The dihedral angle χ_2 of the first, tense conformation (F131-T) has a value of 16° , whereas in the second, relaxed conformation (F131-R) has a χ_2 of 93° (Fig. 1a and b and ESI[†]). Clearly, the relaxed conformation is incompatible with ligand binding (clashes are indicated by a red arrow), whereas the tense conformation is stabilized by a CH/ π interaction between a methyl group of the ligands hexamethylbenzene and the F131 phenyl group (green dotted line).

The propitious position of the piano-stool complex at the entrance of the funnel-shaped sulfonamide binding site should allow to site specifically engineer the protein and/or the piano-stool moiety to improve interactions towards incoming substrates. Taken together, these findings lay the basis for the development of organometallic carbonic anhydrase inhibitors with potential use as drugs or as hybrid catalysts.

Financial support for this project comes from the SNF (Grants FN 200020_126366), Marie Curie Training Networks (FP7-ITN-238531, and FP7/2007-2013 grant agreement n° 238434), Novartis and the University of Basel. We thank Prof. C. A. Fierke (U of Michigan) for providing us the hCA II construct as well as Dr Lu Zheng for help in setting up the expression of hCA II and Dr Daniel Häussinger for NMR measurement.

Notes and references

- 1 U. Schatzschneider and N. Metzler-Nolte, *Angew. Chem., Int. Ed.*, 2006, **45**, 1504.
- 2 A. R. Timerbaev, C. G. Hartinger, S. S. Aleksenko and B. K. Keppler, *Chem. Rev.*, 2006, **106**, 2224.
- 3 M. Salmain, *Bioorganometallics: biomolecules, labelling medicine*, Wiley-VCH, Weinheim, 2005, pp. 181–213.
- 4 J. F. Neault and H. A. Tajmir-Riahi, *Biochim. Biophys. Acta, Protein Struct. Mol. Enzymol.*, 1998, **1384**, 153.
- 5 I. W. McNae, K. Fishburne, A. Habtemariam, T. M. Hunter, M. Melchart, F. Wang, M. D. Walkinshaw and P. J. Sadler, *Chem. Commun.*, 2004, 1786.
- 6 M. Liu, Z. J. Lim, Y. Y. Gwee, A. Levina and P. A. Lay, *Angew. Chem., Int. Ed.*, 2010, **49**, 1661.
- 7 E. Meggers, *Chem. Commun.*, 2009, 1001.
- 8 T. Heinisch and T. R. Ward, *Curr. Opin. Chem. Biol.*, 2010, **14**, 184.
- 9 M. T. Reetz, M. Rentzsch, A. Pletsch, A. Taglieber, F. Hollmann, R. J. G. Mondière, N. Dickmann, B. Höcker, S. Cerrone, M. C. Haeger and R. Sterner, *ChemBioChem*, 2008, **9**, 552.
- 10 Y. Lu, N. Yeung, N. Sieracki and N. M. Marshall, *Nature*, 2009, **460**, 855.
- 11 T. Ueno, S. Abe, N. Yokoi and Y. Watanabe, *Coord. Chem. Rev.*, 2007, **251**, 2717.
- 12 J. R. Carey, S. K. Ma, T. D. Pfister, D. K. Garner, H. K. Kim, J. A. Abramite, Z. Wang, Z. Guo and Y. Lu, *J. Am. Chem. Soc.*, 2004, **126**, 10812.
- 13 D. Qi, C. M. Tann, D. Haring and M. D. Distefano, *Chem. Rev.*, 2001, **101**, 3081.
- 14 P. J. Deuss, G. Popa, C. H. Botting, W. Laan and P. C. J. Kamer, *Angew. Chem., Int. Ed.*, 2010, **49**, 5315.
- 15 L. Rutten, B. Wiczorek, J.-P. B. A. Mannie, C. A. Kruithof, H. P. Dijkstra, M. R. Egmond, M. Lutz, R. J. M. Klein Gebbink, P. Gros and G. van Koten, *Chem.–Eur. J.*, 2009, **15**, 4270.
- 16 P. Haquette, B. Talbi, S. Canaguier, S. Dagorne, C. Fosse, A. Martel, G. Jaouen and M. Salmain, *Tetrahedron Lett.*, 2008, **49**, 4670.
- 17 T. Ueno, T. Koshiyama, S. Abe, N. Yokoi, M. Ohashi, H. Nakajima and Y. Watanabe, *J. Organomet. Chem.*, 2007, **692**, 142.
- 18 K. Okrasa and R. J. Kazlauskas, *Chem.–Eur. J.*, 2006, **12**, 1587.
- 19 Q. Jing, K. Okrasa and R. J. Kazlauskas, *Chem.–Eur. J.*, 2009, **15**, 1370.
- 20 Q. Jing and R. J. Kazlauskas, *ChemCatChem*, 2010, **2**, 953.
- 21 A. Fernández-Gacio, A. Codina, J. Fastrez, O. Riant and P. Soumillion, *ChemBioChem*, 2006, **7**, 1013.
- 22 C. L. Davies, E. L. Dux and A.-K. Duhme-Klair, *Dalton Trans.*, 2009, 10141.
- 23 C. Letondor and T. R. Ward, *ChemBioChem*, 2006, **7**, 1845.
- 24 M. E. Wilson and G. M. Whitesides, *J. Am. Chem. Soc.*, 1978, **100**, 306.
- 25 C.-C. Lin, C.-W. Lin and A. S. C. Chan, *Tetrahedron: Asymmetry*, 1999, **10**, 1887.
- 26 J. Collot, J. Gradinaru, N. Humbert, M. Skander, A. Zocchi and T. R. Ward, *J. Am. Chem. Soc.*, 2003, **125**, 9030.
- 27 M. T. Reetz, J. J.-P. Peyralans, A. Maichele, Y. Fu and M. Maywald, *Chem. Commun.*, 2006, 4318.
- 28 M. Faiella, C. Androzzi, R. T. M. de Rosales, V. Pavone, O. Maglio, F. Nastri, W. F. DeGrado and A. Lombardi, *Nat. Chem. Biol.*, 2009, **5**, 882.
- 29 J. B. Siegel, A. Zanghellini, H. M. Lovick, G. Kiss, A. R. Lambert, J. L. St Clair, J. L. Gallaher, D. Hilvert, M. H. Gelb, B. L. Stoddard, K. N. Houk, F. E. Michael and D. Baker, *Science*, 2010, **329**, 309.
- 30 T. R. Ward, *Angew. Chem., Int. Ed.*, 2008, **47**, 7802.
- 31 N. Yeung, Y.-W. Lin, Y.-G. Gao, X. Zhao, B. S. Russell, L. Lei, K. D. Miner, H. Robinson and Y. Lu, *Nature*, 2009, **462**, 1079.
- 32 I. D. Kuntz, K. Chen, K. A. Sharp and P. A. Kollman, *Proc. Natl. Acad. Sci. U. S. A.*, 1999, **96**, 9997.
- 33 X. Zhang and K. N. Houk, *Acc. Chem. Res.*, 2005, **38**, 379.
- 34 R. Briesewitz, G. T. Ray, T. J. Wandless and G. R. Crabtree, *Proc. Natl. Acad. Sci. U. S. A.*, 1999, **96**, 1953.
- 35 W. H. Ang, L. J. Parker, A. De Luca, L. Juillerat-Jeanneret, C. J. Morton, M. Lo Bello, M. W. Parker and P. J. Dyson, *Angew. Chem., Int. Ed.*, 2009, **48**, 3854.
- 36 M. Rami, J.-Y. Winum, A. Innocenti, J.-L. Montero, A. Scozzafava and C. T. Supuran, *Bioorg. Med. Chem. Lett.*, 2008, **18**, 836.
- 37 V. M. Krishnamurthy, G. K. Kaufman, A. R. Urbach, I. Gitlin, K. L. Gudiksen, D. B. Weibel and G. M. Whitesides, *Chem. Rev.*, 2008, **108**, 946.
- 38 S. K. Nair, T. L. Calderone, D. W. Christianson and C. A. Fierke, *J. Biol. Chem.*, 1991, **266**, 17320.
- 39 B. A. Grzybowski, A. V. Ishchenko, C.-Y. Kim, G. Topalov, R. Chapman, D. W. Christianson, G. M. Whitesides and E. I. Shakhnovich, *Proc. Natl. Acad. Sci. U. S. A.*, 2002, **99**, 1270.
- 40 K. M. Jude, A. L. Banerjee, M. K. Haldar, S. Manokaran, B. Roy, S. Mallik, D. K. Srivastava and D. W. Christianson, *J. Am. Chem. Soc.*, 2006, **128**, 3011.
- 41 N. J. Beasley, C. C. Wykoff, P. H. Watson, R. Leek, H. Turley, K. Gatter, J. Pastorek, G. J. Cox, P. Ratcliffe and A. L. Harris, *Cancer Res.*, 2001, **61**, 5262.
- 42 L. L. Kiefer and C. A. Fierke, *Biochemistry*, 1994, **33**, 15233.
- 43 A. L. Banerjee, M. Swanson, B. C. Roy, X. Jia, M. K. Haldar, S. Mallik and D. K. Srivastava, *J. Am. Chem. Soc.*, 2004, **126**, 10875.

Crystal Structure Analysis

Crystallization

hCA II was crystallized by hanging drop vapor diffusion using virtually the same conditions as described by Kim et al.:¹¹ 4.5 μL protein solution (20 mg/mL lyophilized hCA II in 50 mM Tris-sulfate (pH 8), 1 mM methyl mercuric acetate) and 0.5 μL precipitating buffer (2.6 M ammonium sulfate, 50 mM Tris-sulfate (pH 7.7)) were mixed and equilibrated against 500 μL precipitating buffer at 4 °C. Crystals appeared within two days. Single crystals were stabilized by soaking with glutaraldehyde using a method described by Lusty.¹² The central hollow of a sitting-drop plate was filled with 5 μL of a 50 % glutaraldehyde solution. The reservoir was filled with 300 μL precipitating buffer. A cover slide with hCA II crystals was placed upside down on the sitting-drop well and the system equilibrated at room temperature for 1 h. While native crystals did dissolve immediately after transfer them into a water droplet, glutaraldehyde-treated crystals did not dissolve even after 2 h, indicating the improved stability of the cross-linked crystals. The ligand soaking solution was prepared by mixing 9.5 μL precipitating buffer and 0.5 μL of a solution of 30 mM $[(\eta^6\text{-C}_6\text{Me}_6)\text{Ru}(\text{bispy } \mathbf{3})\text{Cl}]^+$ in 75 % DMSO. Single cross-linked hCA II crystals were transferred into the soaking solution and equilibrated for 7 h at room temperature. Immediately after soaking one crystal was subjected to the diffraction experiment, without intermediate storage in liquid nitrogen.

Data Collection and Structure Solution

Diffraction data of a $[(\eta^6\text{-C}_6\text{Me}_6)\text{Ru}(\text{bispy } \mathbf{3})\text{Cl}]^+ \subset \text{hCA II}$ crystal were collected at a wavelength of 1.0000 Å at the SLS beamline PXIII. Indexing and integration of the diffraction data was carried out with the program MOSFLM and scaling with the program SCALA of the CCP4 Suite (Table S3).¹³ The structure was solved by molecular replacement with program MOLREP¹³ using as a search model the structure of apo-hCAII (PDB code 2CBA), excluding water molecules. The initial protein model was refined by rigid body refinement followed by TLS and full atomic refine-

ment with program PHENIX.REFINE of the PHENIX package¹⁴ (Table S3). Energy minimized PDB coordinates of ligand $[(\eta^6\text{-C}_6\text{Me}_6)\text{Ru}(\text{bispy } \mathbf{3})\text{Cl}]^+$, excluding groups Ru, benzene and chloride, were calculated with the program PRODRG.¹⁵ The PRODRG output pdb file was used as input for program SKETCHER (part of program LIBCHECK¹³ of the CCP4 Suite) to generate a library file of the truncated ligand. After several rounds of refinement of the protein-ligand complex, the remaining moieties Ru, benzene and chloride were added to the pdb file and restraints of these groups were added to the ligand-restraints-file. Electron and anomalous difference densities were displayed with programs COOT¹⁶ and O,¹⁷ figures of the protein structure were drawn with DINO¹.

Table S3: Data Processing and Refinement

Data Processing	
Resolution (Å)	32.0 - 1.3
Space Group	P2 ₁
Cell dimensions	a=42.1Å, b=41.5Å, c=72.4 Å, $\beta=104.3^\circ$
R _{merge} (%)	3.9 (23.6)*
No.unique reflections	59043
Multiplicity	3.9 (3.1)
Completeness	98.8 (95.3)
I/sig(I)	15.4 (3.7)
Structure Refinement	
Resolution (Å)	30.6 - 1.3
R _{work} /R _{free}	14.6/18.3
B-factors (Å ²)	
Protein	13
Ligand	17
Water	32
R.m.s deviations	
Bond lengths (Å)	0.008
Bond angles (°)	1.40

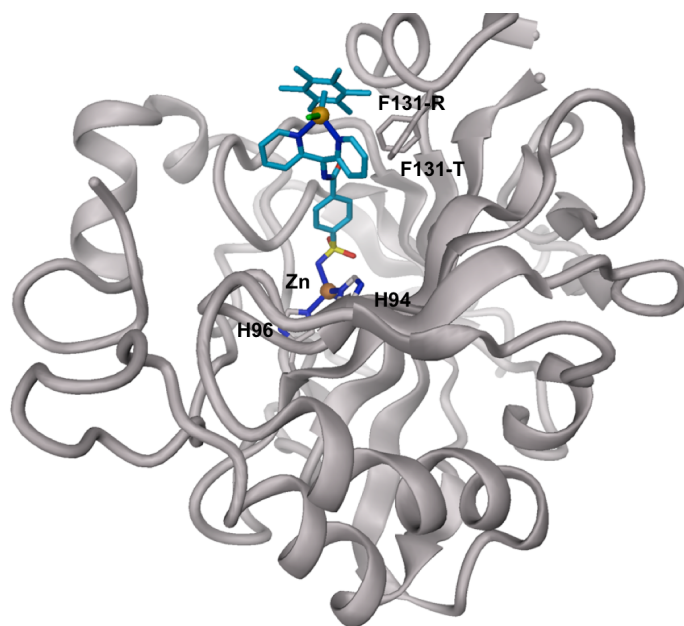
* values in parenthesis are for the highest resolution bin (1.37 - 1.30 Å).

¹www.dino3d.org

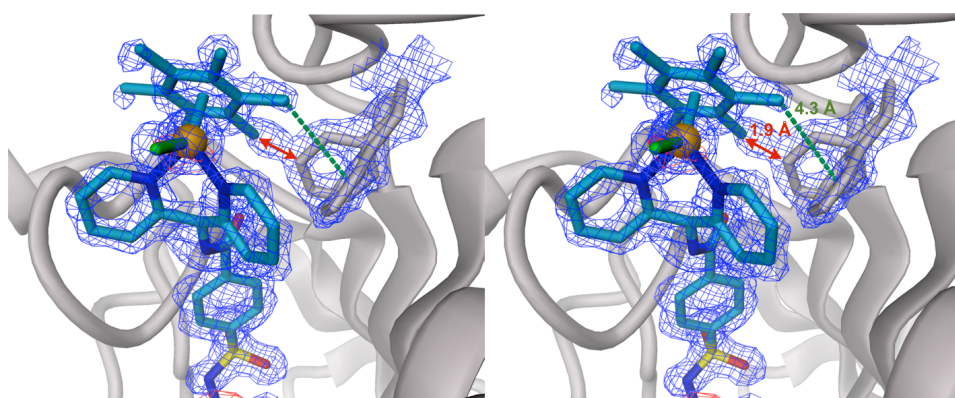
Structure Description

Overall Structure: The asymmetric unit comprises one molecule of hCA II. Residues 3 to 261 are defined by the electron density (see Figure S3). The imidazole groups of histidines 94, 96 and 119 coordinate to a Zn atom, which was indicated by a strong peak (20σ , note that the $f''_{Zn} = 2.4 e^-$ at the employed wavelength of 1.000 \AA) in the anomalous difference density map. Strong anomalous difference density (63σ) was also found close to the thiol group of C206. This was modeled as CH_3Hg^+ (PDB identifier MMC), which is present in the crystallization buffer (the f''_{Hg} is $8.3 e^-$ at the employed wavelength). The structure was deposited in the PDB with code 3pyk.

$[(\eta^6\text{-C}_6\text{Me}_6)\text{Ru}(\text{bispy } \mathbf{3})\text{Cl}]^+$ binding to protein: Residual positive electron density indicated the binding of $[(\eta^6\text{-C}_6\text{Me}_6)\text{Ru}(\text{bispy } \mathbf{3})\text{Cl}]^+$ in the conical sulfonamide binding cavity, reaching from the zinc binding site about 14 \AA towards the outer protein sphere. At the sulfonamide group, one lone electron pair of the deprotonated amino terminus is coordinated to the Zn^{2+} , whereas the proton forms an H-bond with O_γ of residue T199 (2.8 \AA). A sulfonamide oxygen forms an H-bridge with the T199 main-chain-amide (3.0 \AA) (Figure 1a). The benzene ring next to the sulfonamide group interacts with the side chains of residues V121 and L198 via van der Waals forces. A peak in the anomalous difference density (6σ) indicated the position of the Ru atom ($f''_{Ru} = 1.5 e^-$ at the given wavelength) at the exit of the sulfonamide binding site.



(a)



(b)

Figure S3: Crystal Structure of human carbonic anhydrase II in complex with ligand $[(\eta^6\text{-C}_6\text{Me}_6)\text{Ru}(\text{bispy } \mathbf{3})\text{Cl}]^+$. (a) Overall structure, (b) stereo view of the ligand binding site.

References

- (1) Renz, M.; Hemmert, C.; Meunier, B. *Eur. J. Org. Chem.* **1998**, 1998, 1271.
- (2) Jain, A.; Huang, S. G.; Whitesides, G. M. *J. Am. Chem. Soc.* **1994**, 116, 5057.
- (3) Bennett, M. A.; Huang, T.-N.; Matheson, T. W.; Smith, A. K. *Inorganic Synthesis* **2007**, 21, 74.
- (4) Bennett, M.; Smith, A. *J. Chem. Soc., Dalton Trans.* **1974**, 233.
- (5) Habtemariam, A.; Melchart, M.; Fernández, R.; Parsons, S.; Oswald, I.; Parkin, A.; Fabiani, F.; Davidson, J.; Dawson, A.; Aird, R.; Jodrell, I.; Sadler, P. J. *J. Med. Chem.* **2006**, 49, 6858.
- (6) Freedman, D. A.; Evju, J. K.; Pomije, M. K.; Mann, K. R. *Inorg. Chem.* **2001**, 40, 5711.
- (7) Banerjee, A. L.; Swanson, M.; Roy, B. C.; Jia, X.; Haldar, M. K.; Mallik, S.; Srivastava, D. K. *J. Am. Chem. Soc.* **2004**, 126, 10875.
- (8) Nair, S.; Calderone, T.; Christianson, D.; Fierke, C. *J. Biol. Chem.* **1991**, 266, 17320.
- (9) Vullo, D.; Franchi, M.; Gallori, E.; Antel, J.; Scozzafava, A.; Supuran, C. *J. Med. Chem.* **2004**, 47, 1272.
- (10) Studier, F.; Moffatt, B. *J. Mol. Biol.* **1986**, 189, 113.
- (11) Kim, C.; Chang, J.; Doyon, J.; Jr, T. B.; Fierke, C.; Jain, A.; Christianson, D. *J. Am. Chem. Soc.* **2000**, 122, 12125.
- (12) Lusty, C. *J. Appl. Crystallogr.* **1999**, 32, 106.
- (13) CCP4, *Acta Crystallogr., Sect. D: Biol.* **1994**, 50, 760.
- (14) Adams, P.; Afonine, P.; Bunkoczi, G.; Chen, V.; Davis, I.; Echols, N.; Headd, J.; Hung, L.; Kapral, G.; Grosse-Kunstleve, R.; McCoy, A. J.; Moriarty, N. W.; Oeffner, R.; Read, R. J.;

Richardson, D. C.; Richardson, J. S.; Terwilliger, T. C.; Zwart, P. H. *Acta Crystallogr., Sect. D: Biol. Crystallogr.* **2010**, *66*, 213.

(15) Schüttelkopf, A. W.; van Aalten, D. M. F. *Acta Crystallogr., D Biol Crystallogr* **2004**, *60*, 1355.

(16) Emsley, P.; Cowtan, K. *Acta Crystallogr., Sect. D: Biol. Crystallogr.* **2004**, *60*, 2126.

(17) Jones, T. A.; Zou, J. Y.; Cowan, S. W.; Kjeldgaard, M. *Acta Crystallogr A* **1991**, *47*, 110.

5.1. Author Contributions

General idea:

Thomas R. Ward

Synthesis of arylsulfonamide piano stool complexes:

Fabien Monnard

Production of hCAII variants:

Elisa Nogueira

Determination of the affinity of arylsulfonamide complexes for hCAII

Fabien Monnard

Crystal structure analysis:

Tillmann Heinisch, Tilman Schirmer

Manuscript writing:

Thomas R. Ward and all other authors

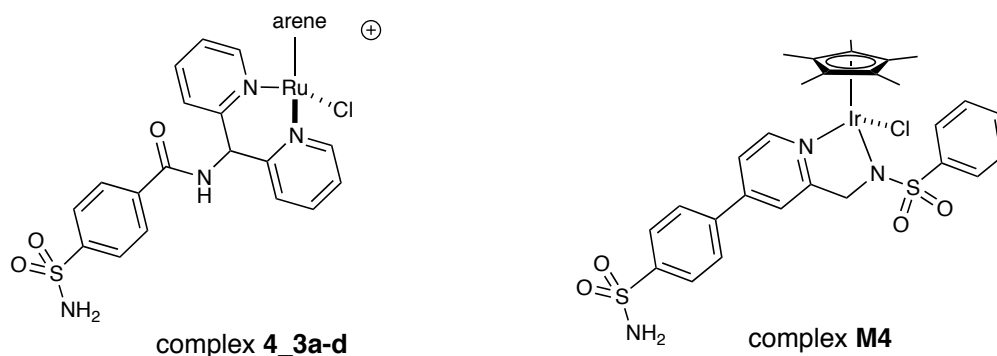
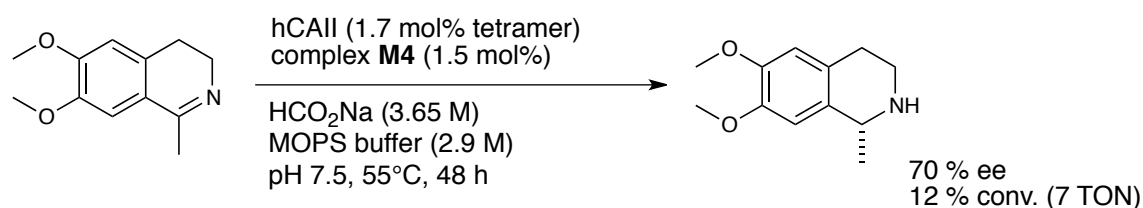
5.2. Comment on Publication

5.2.1. Structural Aspects of the Design of an Artificial Transfer Hydrogenase Based on Human Carbonic Anhydrase II

In this study, the potential of the hCAII-arylsulfonamide system to be used in AME design was investigated. As a model reaction, the ATH of cyclic imines was chosen (**Figure M16**). In a first step, the affinity and structures of different benzenesulfonamide-hCAII complexes had to be solved. The high-affinity ligand benzenesulfonamide was used to tether various bipyridine-Ru-arene complexes for subsequent complexation with hCAII. Only Ru-arene complex precursors with reported activity in the ATH of imines or ketones were used (benzene, *p*-cymene, C₆Me₆, and biphenyl).⁵⁶ The bipyridyl group was expected to act as a secondary recognition element via interaction with the hydrophobic hCAII residues P202, L204, V135 and P131.⁸⁴

An increase of affinity of the bipyridyl complex **4_3** by a factor of three (K_d = 45 nM) as compared to the amide benzenesulfonamide precursor was indeed observed. However, each Ru-arene function led to a 3-7 fold decrease in affinity. The crystal structure of hCAII in complex with the compound [(η⁶-C₆Me₆)Ru(**4_3**)Cl] was solved. In the structure, the hydrophobic interactions between the bipyridyl group and amino acids P202, L204, V135 and P131 were confirmed. Furthermore, a CH•••π bond was observed between a methyl group of the C₆Me₆ cap and the side chain of Phe131. However, since the side chain of Phe131 has to be rotated by about 80° from a relaxed into a tense state, the total energy balance for the establishment of the CH•••π bond is presumed to be negative. This would explain the low affinity of this complex as compared to the related benzene complex, which presumably does not require rotation of the Phe131 side chain for binding. Unfortunately, none of the Ru-arene complexes was active in catalysis.

After publication of the crystal structure and affinities of the inactive complexes, Günnaz et al. reported that bidentate ligand benzenesulfonamide-*N*-2-methylpyridine in complex with Ru-*p*-cymene yields high activity in the ATH of acetophenone.⁸⁵ Tethering benzenesulfonamide in *para*-position to benzenesulfonamide-*N*-2-methylpyridine yielded complex **M4**, which indeed was found to be active and enantioselective in the ATH of the salsolidine precursor inside hCAII (**Figure M16**). To analyze the structural differences between the inactive complexes **4_3a-d** and active **M4**, crystal structural studies and computational docking are currently in process.



arene = benzene, *p*-cymene, C₆Me₆, biphenyl

Figure M16: ATH of salsolidine precursor using hCAII-arylsulfonamide system.

5.2.2. Future Structure-Based Computational Design of Artificial Metalloenzymes Based on Human Carbonic Anhydrase II

Future AME development based on hCAII could be guided by structure-based computational design. Numerous studies have presented correlation functions derived from experimental structure-affinity data that allow *in silico* affinity predictions for novel ligands.^{86,87} The affinity of metal-containing ligands so far was hard to predict due to problems with metal parametrization. Schmid et al. have now presented a method of facile parametrization of piano stool transition metal complexes, which can be used *in silico* for affinity prediction.⁸⁸

However, *in silico* prediction of whole reaction pathways and transition states inside a protein scaffold is far more complex than affinity prediction since generally a multitude of possible conformations of enzyme-substrate intermediates, including high-energy arrangements, have to be sampled. High-throughput *in silico* screening methods such as Monte Carlo, that can handle various conformations in short time, do not consider high energy (low probability) conformations (e.g. transition states).⁸⁹ In contrast, more detailed algorithms for transition state calculation, such as QM or QM-MM, are low-throughput and the number of possible conformations needs to be restricted to only few e.g. by knowledge of the protein-cofactor structure or the cofactor-substrate transition state structure.

So far, the most promising strategy of AME design in hCAII is to start from an active metallocofactor and synthesize a number of arylsulfonamide-tethered derivatives prior to screening for activity and enantioselectivity in the presence of hCAII. In future, structural and functional data from these experiments can be used to create algorithms that may allow *in silico* metallocofactor design to achieve high activity and enantioselectivity.

IV Structural Analysis of Piano Stool Ruthenium Complexes Bound to hCAII and Streptavidin: Implications for Future Metallodrug Design

6. Introduction

Diseases are complex biological events. While classic drug development often relied on serendipity, today the knowledge of disease mechanisms and the structure and function of key biomolecules involved (e.g. proteins, DNA or RNA) allows the specific design of small drug molecules with high affinity and selectivity for target biomolecules.

Most drugs consist of a small number of atoms (e.g. H, C, N, O) and metals play only a marginal role in drug development. This is in contrast to the various functions that metals have in biological systems.^{4,5} Moreover, metal atoms have some specific properties, which can be exploited for drug design:

- metal complexes often are positively charged (they bind e.g. to DNA phosphate backbone, acidic amino acids)
- metals are Lewis acids that bind Lewis bases (e.g. DNA phosphate backbone, nucleobases, electron lone pairs of amino acids in proteins)
- metals are redox active, they can reduce/oxidize biomolecules
- metals can have multiple coordination geometries, which allows to build a large number of 3D architectures with high target affinity by structure-based design
- the coordination geometry can change with the redox state, which can be used to improve target selectivity (prodrug strategy).
- metals can be radioactive, which can be used to destroy tumor cells.
- metal complexes can be more stable *in vivo* than organic molecules, because of the lack of a degradation/efflux machinery.

7. Human Carbonic Anhydrase II as a Host for Piano-Stool Complexes Bearing a Sulfonamide Anchor

7.1. Comment on Publication

7.1.1. Structure-Based Design of Metallodrugs for Human Carbonic Anhydrase II

Structure-based drug design to date is common in industry and academic research. However, only few examples exist in literature about the structure-based rational design of metallodrugs.^{90,91}

Staurosporin inhibits many protein kinases with nanomolar affinity by mimicking the nucleobase as well as the ribose of ATP. Based on the crystal structure of a complex of staurosporin and protein kinase PIM 1, Meggers et al. have designed a metallo derivative of staurosporin with a sugar ring exchanged for a Ru-arene-CO half-sandwich group (**Figure M17**).⁹⁰ This organometallic compound has an affinity of 220 pM as compared to 65 nM of staurosporin for PIM 1, for which the metal inhibitor is highly selective with respect to other kinases. The crystal structure of complex PIM 1-Ru-complex demonstrates that no direct metal-protein interactions are present and that the high affinity is constituted solely by the geometrical constitution of the Ru complex. This demonstrates the potential of using the architectures of inert metal complexes as enzyme inhibitors.

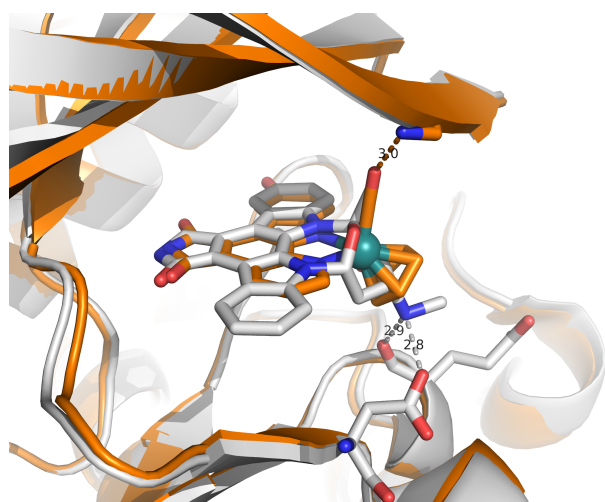


Figure M17: Superposition of crystal structures of complexes Pim 1-staurosporin (grey, PDB 1YHS) and the complex of Pim 1-ruthenium piano stool staurosporin mimick (orange, PDB 2BZI). Ruthenium is depicted as a green sphere; hydrogen bridges of staurosporin are shown as white dashed lines and those of its Ru-mimick in orange dashed lines.

Human carbonic anhydrases are key enzymes ubiquitous in all organisms that regulate essential physiological processes such as respiration, vision, signaling and memory, development and function of bones or muscles. Consequently, they are involved in a large number of diseases. Numerous hCA inhibitors are on the market or in clinical trial for the treatment of glaucoma, epilepsy, hypertension, osteoporosis or tumor suppression.⁵² The wealth of structural and functional data on hCA holds great potential to evaluate the scope and limitations of structure-based rational metallodrug design.

Jude et al. have demonstrated the ease of engineering a secondary recognition element in hCAII, which is based on an iminodiacetate (IDA) Cu²⁺ complex.⁹² Indeed, after optimization of the linker region, a benzenesulfonamide tethered IDA-Cu²⁺ complex with an affinity of 28 nM (as compared to 660 nM of benzenesulfonamide) for hCAII was obtained. In addition, this complex is more selective for hCAII as compared to hCAI by a factor of four. Crystal structure analysis of the protein-inhibitor complex revealed coordination of the IDA-Cu²⁺ group to the imidazole of His64, which is located opposite to the hydrophobic wall in the substrate-binding site. This result encourages the structure-based design of novel metal inhibitors for hCAII.

7.1.2. Piano Stool Complexes as Secondary Recognition Elements for the Inhibition of Human Carbonic Anhydrase II

Ruthenium-arene piano stool complexes as developed by Sadler and coworkers are in clinical trials as potential cancer therapeutics (**Figure M18**).⁹³⁻⁹⁵ The primary target of Ru-arene piano stool complexes are the nucleobases of DNA. However, Meggers and coworkers have shown the potential of a related Ru complex in kinase inhibition (**Figure M17**).

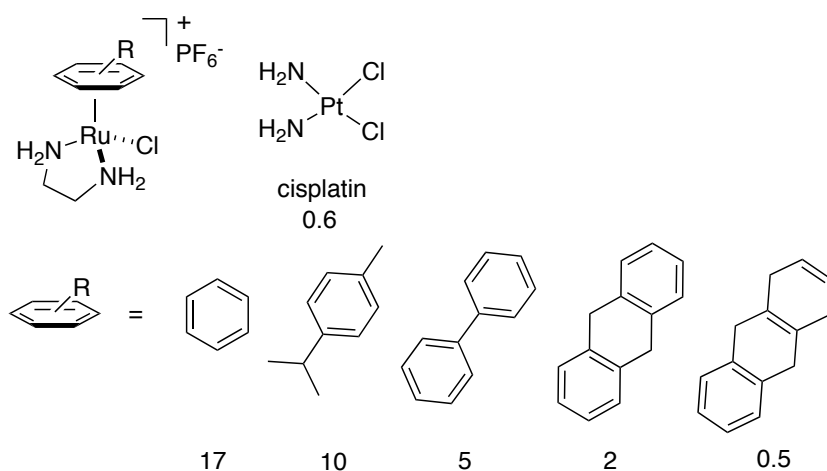


Figure M18: Metallo drugs that are on the market (cisplatin) or in clinical trials. Numbers indicate IC₅₀ values (in μM) in A2780 human ovarian cancer cells after 24 h incubation time.⁹⁴

In the study by Monnard et al., based on the crystal structure of hCAII, various benzenesulfonamide-bound bispyridyl-Ru-arene complexes were designed, and their potential as secondary metallo recognition elements in hCAII inhibition was tested.

As discussed above, the affinity of the bipyridyl complex **4_3c** was increased as compared to the amide precursor, while the Ru-arene functions tested led to a decrease in affinity. No direct Ru-protein coordination was observed in the crystal structure. Thus, the designed Ru-arene-bispyridyl groups do not act as secondary recognition elements. In contrast, the affinity is negatively affected by their presence. Complex **M4** was shown to have low nanomolar affinity (10 nM) for hCAII. The crystal structure of the complex will elucidate how the piano stool complex of **M4** acts as a secondary recognition element.

Based on the fact that the bispyridyl moiety, tethered to benzenesulfonamide, undergoes beneficial hydrophobic interactions with the hydrophobic wall of hCAII, piano stool metal functions could be linked to this scaffold in various positions. In accordance with Jude et al., a linker could position the free coordination site of a piano stool complex in proximity to the His64 side chain to coordinate it. Alternatively (or in addition), the arene cap could be designed to experience hydrophobic interactions with residues in proximity to His64, opposite of the hydrophobic wall. Next to ruthenium, metals iridium and rhodium or osmium could be tested for their impact on affinity. Moreover, a library of piano stool sulfonamide complexes should be tested not just against hCAII but also its isoforms (e.g. hCAI) to evaluate the target selectivity.

8. Chemo-Genetic Optimization of DNA Recognition by Metallo drugs Using a Presenter-Protein Strategy

Chemo-Genetic Optimization of DNA Recognition by Metallodrugs using a Presenter-Protein Strategy

Jeremy M. Zimbron,^[a] Alessia Sardo,^[a] Tillmann Heinisch,^[a, b] Therese Wohlschlager,^[c] Julieta Gradinaru,^[c] Claudia Massa,^[b] Tilman Schirmer,^{*,[b]} Marc Creus,^{*,[a]} and Thomas R. Ward^{*,[a]}

Dedicated to Dr. R.-Y. Mauverny

Abstract: The mode of action of precious metal anticancer metallodrugs is generally believed to involve DNA as a target. However, the poor specificity of such drugs often requires high doses and leads to undesirable side-effects. With the aim of improving the specificity of a ruthenium piano-stool complex towards DNA, we employed a presenter protein strategy based on the biotin-avidin technology. Guided by the X-ray

structure of the assembly of streptavidin and a biotinylated piano-stool, we explored the formation of metallodrug-mediated ternary complexes with the presenter protein and DNA. The assemblies bound more strongly to telo-

mere G-quadruplexes than to double-stranded DNA; chemo-genetic modifications (varying the complex or mutating the protein) modulated binding to these targets. We suggest that rational targeting of small molecules by presenter proteins could be exploited to bind metallodrugs to preferred macromolecular targets.

Keywords: G-quadruplexes • metallodrug • proteins • ruthenium • supramolecular chemistry

Introduction

DNA is a privileged target of anticancer metallodrugs like cisplatin. However, such drugs often suffer from high toxicity and drug resistance due to non-selective binding to other than oncogenic DNA.^[1] To minimize metallodrug toxicity, several interactions with cancer-associated DNA sequences would be desirable, but such extensive interactions are hard

to achieve with small-molecule drugs. Ultimately, designed assemblies of metallodrugs with presenter proteins^[2] may lead to effective mechanisms of small-molecule delivery to preferred macromolecular targets.

To increase selectivity of small molecule drugs for macromolecular targets, “surface borrowing” can be used to provide additional surface contacts through a presenter protein, which modulates the specificity and affinity of ligand-macromolecule interaction.^[2] The use of bifunctional molecules based on biotin-streptavidin technology has been used for targeting RNA, in which a contribution from protein contacts to the anti-tobramycin RNA aptamer was suggested.^[3] Inspired by these presenter protein strategies and our previous experience of enantioselective artificial metalloenzymes,^[4] we anticipated that metallodrug-mediated protein-DNA interactions could be engineered leading to a stable ternary metallodrug-protein-DNA complex (Figure 1). Such complexes with DNA would be reminiscent of the binding of high-mobility group (HMG)-domain proteins to platinated DNA that mediate cytotoxicity in vivo.^[5] Analogous mechanisms of action ultimately involving ternary complexes have also been described for other clinically useful drugs, such as the immunosuppressive antibiotic rapamycin.^[6]

[a] J. M. Zimbron, A. Sardo, T. Heinisch, Dr. M. Creus, Prof. T. R. Ward
University of Basel, Department of Chemistry
Spitalstrasse 51, 4056 Basel (Switzerland)
Fax: (+41) 61 267 10 05
E-mail: thomas.ward@unibas.ch
marc.creus@unibas.ch

[b] T. Heinisch, Dr. C. Massa, Prof. T. Schirmer
University of Basel, Biozentrum
Klingelbergstrasse 50/70, 4056 Basel (Switzerland)
Fax: (+41) 61 267 21 09
E-mail: tilman.schirmer@unibas.ch

[c] T. Wohlschlager, Dr. J. Gradinaru
University of Neuchâtel, Institute of Chemistry
Avenue de Bellevaux 51, 2009 Neuchâtel (Switzerland)

Supporting information for this article is available on the WWW under <http://dx.doi.org/10.1002/chem.201001573>.

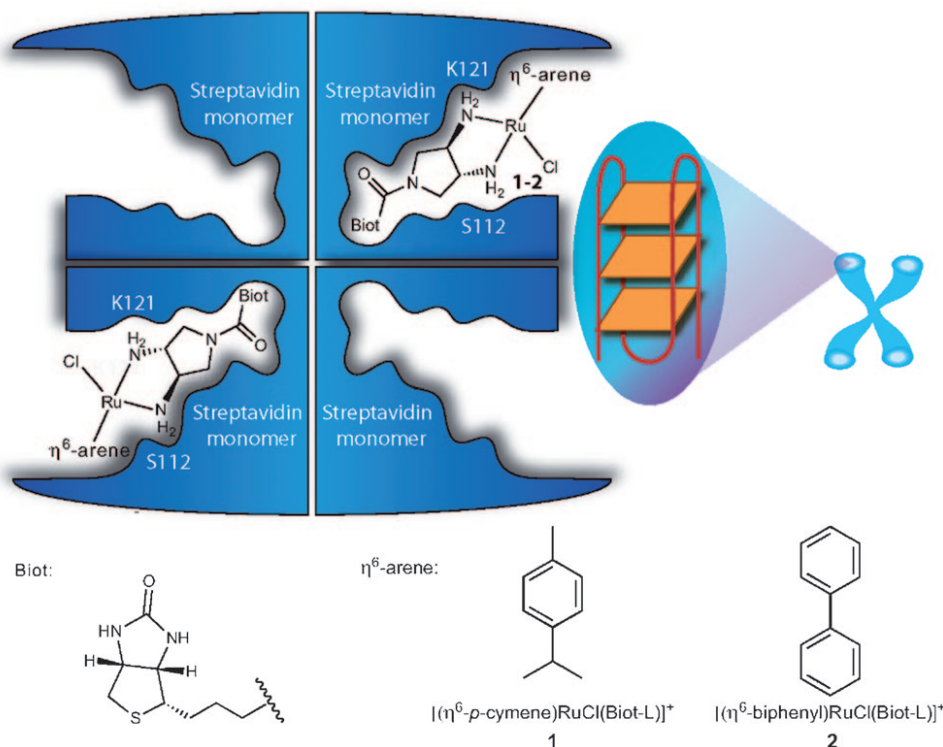


Figure 1. Presenter protein strategy for targeting telomeric DNA with ruthenium metallodrugs. The ruthenium drug embedded into tetrameric Sav in a 2:1 molar ratio forms a supramolecular complex that may allow extensive interactions with a DNA (here depicted as G-quadruplex telomeric DNA; G4A). Chemo-genetic optimization, that is, mutations of defined streptavidin residues (e.g., K121 and S112) or modifying the arene cap of the Ru complex, can modulate the affinity of the assembly for the DNA target. Compound **1** = $[(\eta^6\text{-}p\text{-cymene})\text{Ru}(\text{Biot-L})\text{Cl}]\text{CF}_3\text{SO}_3$ and **2** = $[(\eta^6\text{-biphenyl})\text{Ru}(\text{Biot-L})\text{Cl}]\text{CF}_3\text{SO}_3$; Biot-L = Biotin-*N*-(*R,R*)-3,4-diaminopyrrolidine.

Organometallic drugs have received increasing attention spurred on by their non cross-resistance with Pt-based drugs.^[7] Specifically, the study of ruthenium piano-stool complexes (e.g., see compounds **1** and **2**, Figure 1) as potential anti-tumour drugs has begun to establish structure–activity relationships.^[8] These studies also highlighted the importance of non-covalent interactions in the second coordination-sphere, such as hydrophobic interactions between the η^6 -arene ligand of the piano stool (Figure 1) and DNA that help improve selectivity.^[9] Recently, the nature of the second coordination sphere has also been shown to influence both kinetic- and thermodynamic properties of the binding to proteins, which constitute alternative macromolecular targets of anticancer drugs.^[10]

Results and Discussion

Construction of a presenter protein and metallodrug assembly: As proof-of-concept that target selectivity can be engineered into a supramolecular assembly of drug and presenter protein, we synthesized a biotinylated metallodrug (compound **1**, Figure 1) inspired by promising anticancer Ru^{II} piano-stool complexes,^[7] for incorporation into streptavidin (Sav). The strong binding affinity of Sav for **1** was confirmed

by isothermal titration calorimetry (ITC; $K_d < 60$ nM; Figure 2).

X-ray structure: The crystal structure of the 1Cav tetramer assembly determined at 2.0 Å resolution (Figure 3 and Supporting Information Figures S1–S3) from protein crystals soaked in excess of **1** shows that the four biotin binding sites are fully occupied with the metallodrug. Ruthenium is coordinated by four ligands, two amino groups of the 3,4-(*R,R*)-ligand, a chloride molecule and the aromatic ring of the *p*-cymene (Table 1). The metal complex has a distorted tetrahedral “piano-stool”-like geometry. In addition to the well documented biotin–Sav interactions,^[11] other interactions between **1** and Sav found in the crystal structure enforce the localisation of the piano-stool moiety within the biotin binding pocket (Figure 3): 1) hydrogen bonding of a diaminopyrrolidine nitrogen to the side

Table 1. Geometrical properties of the primary coordination sphere of the ruthenium in **1** as bound to streptavidin. For simplicity the hydrogen atoms of the amine groups and the neighbouring atoms of the pyrrolidine carbons are omitted. Angles [°] and distances [Å] relative to the *p*-cymene group refer to the centre of the aromatic ring.

N ¹ –Ru–N ²	83	N ¹ –Ru	2.48
N ² –Ru–Cl	67	N ² –Ru	2.37
Cl–Ru–N ¹	97	Cl–Ru	2.83
cym–Ru–N ¹	130	cym–Ru	1.83
cym–Ru–N ²	139		
cym–Ru–Cl	121		
N ¹ –C ¹ –C ² –N ¹	89		

chain of S112; 2) apolar interactions of *p*-cymene with Thr114 (Supporting Information, Figure S3) and 3) indirect binding of the labile chloride (or water) ligand to the backbone carbonyl of S122 through a well-ordered water molecule. The diaminopyrrolidine S112 H-bond is reminiscent of a critical interaction between a Pt ligand N–H group and the phosphate backbone of double-stranded DNA (dsDNA)

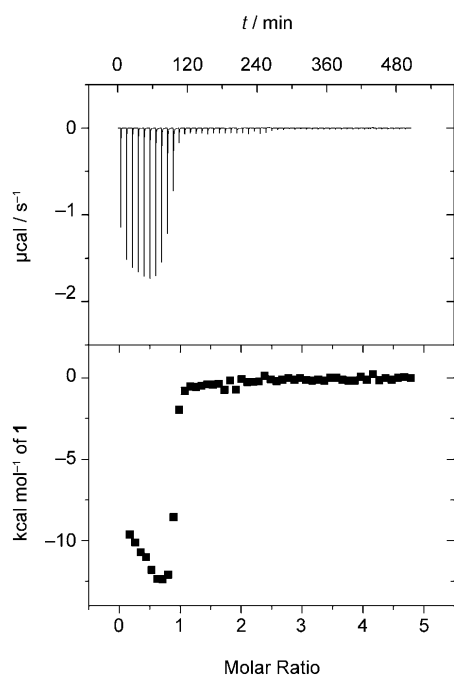


Figure 2. ITC profile for the binding of **1** to Sav. Titration was carried out at 25 °C in 3-(*N*-morpholino)propanesulfonic acid (MOPS) buffer (75 mM) at pH 6.5 with 10 mM of KOH. Every 4 min, 5 μ L of **1** (1 mM) was injected in the reaction cell ($V_{\text{cell}} = 1.5$ mL) filled with Sav (40 μ M of monomer). The heat values are plotted as a function of **1**/Sav molar ratio, to give the corresponding binding isotherms. The resulting isotherms were then fitted to a two set binding sites model. Although binding was strong and probably beyond the sensitivity of ITC, each tetramer of Sav bound approximately four complexes of **1** with affinities of $K_d < 60$ nM.

identified by Lippard in both cisplatin and oxaliplatin X-ray structures.^[12]

In the crystal structure, symmetry related *cis*-Ru atoms are 10.4 Å apart (Figure 3). In the absence of a neighbouring *cis* compound **1** (see Supporting Information: Video 1), the size and charge of the pocket would allow multiple interactions with an incoming DNA molecule. The orientation of the labile Ru–Cl bond is compatible with coordination to electron-rich N⁷ atoms of purines^[13] in an *endo*-base of single-stranded DNA (ssDNA).

Metallodrug binding to quadruplex DNA: Although the target of DNA-binding metallodrugs is generally thought to be mainly dsDNA, G-quadruplexes also offer attractive alternative therapeutic targets,^[14] they are abundant in telomeres at the end of chromosomes and are found as potential regulatory elements in genes, including oncogenes. Thus, we next investigated the binding of **1**Cav, assembled by mixing two equivalents of complex **1** with one equivalent of tetrameric Sav, to a model G-quadruplex telomeric DNA, namely G4A, consisting of 39 bases (Figures 4 and 5).^[15]

ITC titration (Figure 4a) suggests the formation of a ternary complex between the drug-presenter protein assembly (**1**Cav) and G4A, with sub-micromolar affinity (Table 2,

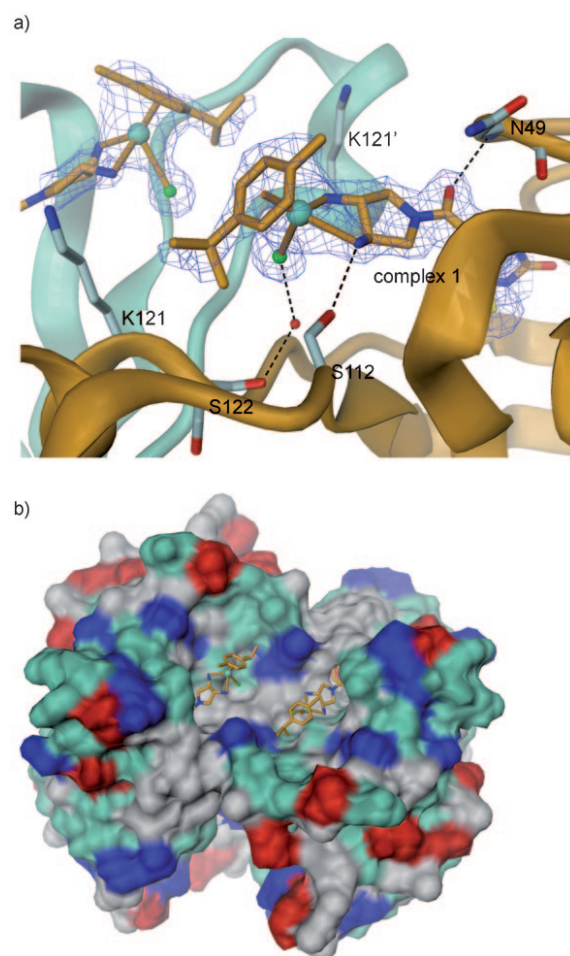


Figure 3. Crystal structure of **1** embedded into the Streptavidin presenter protein (**1**Cav). a) Close-up view of **1** bound to a Sav monomer (orange) also showing the *cis*-related ruthenium moiety (upper-left corner) that is bound to the symmetry-related Sav monomer (aquamarine). Selected Sav residues are shown in full and are labelled. Primed residues belong to the symmetry-related monomer. The 2 Fo–Fc electron density map of **1** is contoured at 1.0 σ . The ruthenium atom is tetrahedrally coordinated by two amino groups of the diaminopyrrolidine, the *p*-cymene and a putative chloride ion (shown in green). b) Molecular surface representation of the Sav tetramer showing two *cis*-related ruthenium moieties. The Sav surface is coloured according to amino acid, with blue = basic residues; red = acidic residues; green = polar residues; grey = hydrophobic residues. The structure has been deposited in the Protein Data Bank (www.pdb.org) with accession code 2WPU.

entry 2). The binding of Sav alone with G4A was markedly weaker in the absence of complex **1** as determined by electrophoretic mobility-shift assays (EMSA; compare Table 2, entries 1 and 2) and by ITC (Figure 4b). EMSA gels (Figure 5) and ITC (Figure 4c) using G4A as target were also carried out with **1** alone (in the absence of Sav). These data reveal the formation of a mixture of fast migrating species that cannot be resolved by EMSA or by ITC, supporting the expected multiple strong binding events to the DNA: there is ample experimental evidence for related Ru piano-stool complexes that display preferential binding to N⁷ guanine in DNA;^[13] a QM–MM calculation predicts a K_d

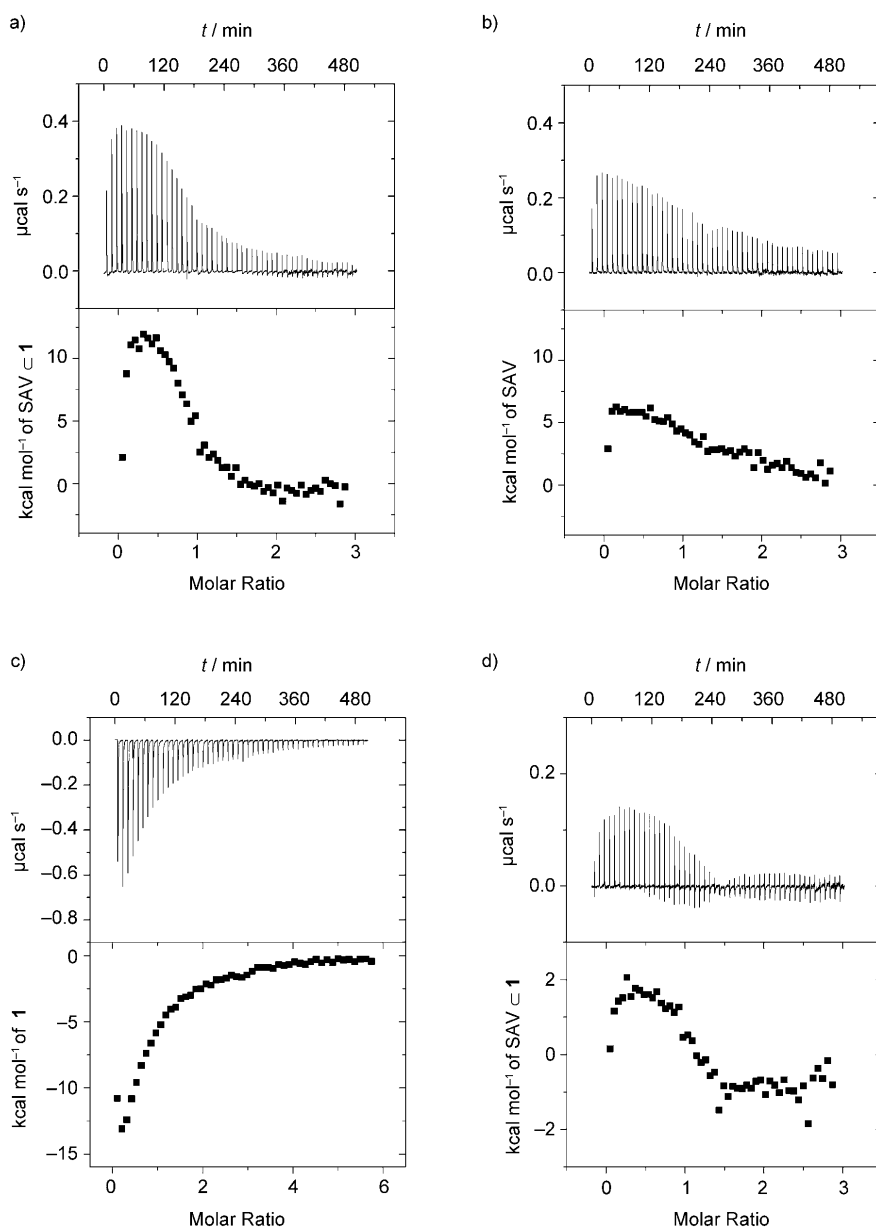


Figure 4. DNA-binding monitored by ITC: a) binding of **1CSav** to G4A: a single set of identical sites model provided an association constant of $(1.35 \pm 0.28) \times 10^6 \text{ M}^{-1}$, enthalpy of $(1.23 \pm 0.355) \times 10^4 \text{ kcal mol}^{-1}$, and stoichiometry of 0.90 ± 0.02 ; b) binding of Sav to G4A: a single set of identical sites model gives an association constant of $(6.56 \pm 2.35) \times 10^4 \text{ M}^{-1}$, enthalpy of $(1.055 \pm 0.124) \times 10^3 \text{ kcal mol}^{-1}$, and stoichiometry of 1.81 ± 0.09 (the binding affinity of the protein alone is more than ten times weaker than in the presence of compound **1**); c) binding of **1** to G4A is apparently strong, exothermic in the conditions used and very different from that found for the ruthenium drug assembled with the presenter protein (see Supporting Information); d) binding of **1CSav** to a “scrambled” telomeric DNA (scG4A) is markedly different and cannot be fitted to a one-site binding-model (compare panels d and a).

of $0.1 \mu\text{M}$ for a related Ru piano stool.^[16] Addition of **1CSav** produced a concentration-dependent change in migration of G4A in EMSA, leading to a single slow migrating species at high concentration that is also consistent with the formation of a ternary complex with a defined 1:1 stoichiometry (DNA/**1CSav**) (Figure 4). Affinities obtained by varying the ratio of **1**/Sav from 1:1 to 4:1 are comparable (Table 2 entries 2, 14 and 15 and Supporting Information Figure S4). The 2:1 ratio was selected for all subsequent studies as it

yielded a well defined 1:1 stoichiometry (**1CSav**/G4A) by ITC (Figure 4a) and EMSA (Figure 5).

Selectivity for single stranded DNA (ssDNA):

To test whether **1CSav** recognizes structural features of G4A or simply its nucleotide content, we used a scrambled telomeric sequence (scG4A) that could not form a G-quadruplex structure. The binding of **1CSav** to this control oligonucleotide (scG4A) was measurably weaker than for G4A, which is bound stoichiometrically in our EMSA assay (Table 2, entries 2 and 11). The ITC titration curve of scG4A could not be fitted to a one-site binding model (Figure 4d). Therefore, under these conditions, **1CSav** binds strongly to the G-quadruplex in a defined 1:1 stoichiometry that fits a single-binding site mechanism and also binds to other ssDNA with marginally less affinity and in a complex mode.

Competitive binding:

To test the selectivity of a ternary complex with DNA in the presence of potentially interfering macromolecules, first competition studies with glutathione were carried out. Glutathione has been shown to coordinate anti-cancer Ru complexes in vitro^[17] and has also been implicated in metallodrug inactivation in vivo.^[1,18] Although complex **1** could bind glutathione (Supporting Information Figure S5 and Table 2), the presence of a 300-fold excess glutathione with respect to G4A (final concentration of glutathione = 1 mM; i.e., within the physiological range) did not appreciably affect formation of the complex with G4A as evidenced by EMSA (Figure 5).

An excess of competing ssDNA co-incubated with G4A (up to 157 equivalents of competing ssDNA with respect to G4A) lowers binding of the metallodrug–protein assembly as determined by EMSA, but only marginally (Table 2 entries 12 and 13 and Figure 6a). The 12mer ssDNA was better at inhibiting G4A binding than the GGG-trinucleo-

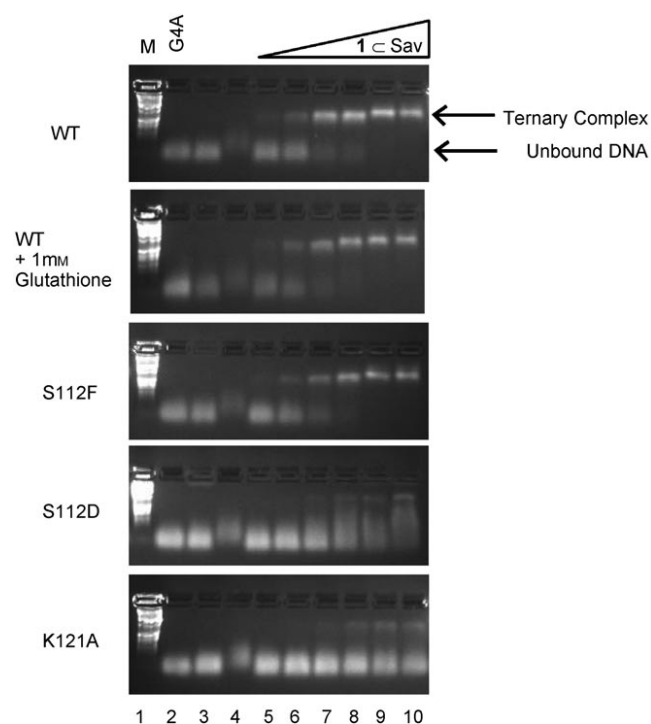


Figure 5. Binding of assembly of metallodrug and presenter protein (**1CSav**) to G4A monitored by electrophoretic mobility shift assay (EMSA) on agarose gels: EMSA on agarose gels of **1CSav** variants wild-type (WT); WT in the presence of 1 mM glutathione; S112F; S112D or K121A incubated with G4A. Lane 1: DNA Marker. Lane 2: G4A. Lane 3: G4A (3.3 μM) + Sav (39.6 μM); Lane 4: G4A (3.3 μM) + **1** (85.7 μM). Lanes 5–10: G4A (3.3 μM) + **1CSav** at increasing concentrations: 0.8, 1.6, 3.9, 7.9, 19.8, 39.6 μM , representing a **1CSav**/G4A ratio from 0.2 to 12. In all cases 500 ng of DNA was loaded onto the gel.

Table 2. Summary of dissociation constants (K_d) of Ru–Sav assemblies for various DNA targets, as estimated from EMSA.

Entry	DNA Target	Metal complex	Ratio Ru/Sav	Sav	K_d estimated by EMSA [μM]
1	G4A	none	–	WT	> 145 ^[a]
2	G4A	1	2	WT	< 1.6 ^[b,c]
3	G4A	1	2	S112F	< 1.6 ^[c]
4	G4A	1	2	S112D	12.2
5	G4A	1	2	K121A	28
6	G4A	1	2	WT	< 1.6 ^[c]
	(GSH) ^[d]				
7	dsOnc	1	2	WT	37.9
8	dsOnc	1	2	S112F	37.9
9	dsOnc	2	2	WT	37.9
10	dsOnc	2	2	S112F	18.2
11	scG4A ^[e]	1	2	WT	2.3
12	G4A	1	2	WT	2
	(GGG) ^[d]				
13	G4A	1	2	WT	5.4
	(12mer) ^[d]				
14	G4A	1	1	WT	2.3
15	G4A	1	4	WT	< 1.6 ^[c]

[a] K_d determined by ITC: 15.2 μM (see Supporting Information; Figure S6); [b] K_d determined by ITC: 0.74 μM ; [c] Binding was stoichiometric and probably beyond the sensitivity of these EMSA; [d] In brackets competing species: glutathione (GSH), trinucleotide GGG (GGG) and ssDNA 12mer (12mer); [e] “Scrambled” G4A has identical nucleotide content to G4A but with a different sequence and structure.

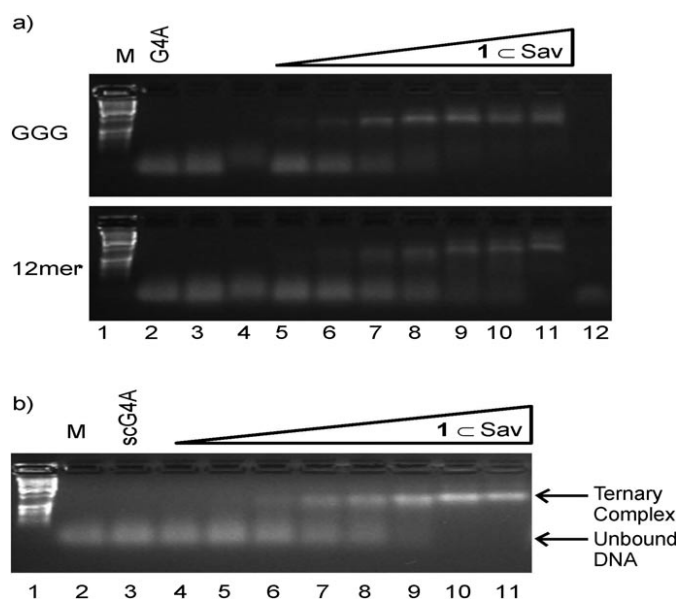


Figure 6. Binding of assembly of metallodrug and presenter protein (**1CSav**) to ssDNA, monitored by EMSA on agarose-gels: a) Binding to G4A DNA in the presence of competing DNA substrates. Lane 1: Marker (M). Lane 2: G4A. Lane 3: G4A (3 μM) + GGG trinucleotide (206.5 μM) or 12mer ssDNA (462 μM) respectively. Lane 4: G4A (3 μM) + GGG (206.5 μM) or 12mer (462 μM) respectively + complex **1** (76.5 μM). Lane 5–10: GGG (206.5 μM) or 12mer (462 μM) were co-incubated with G4A (3 μM) and the **1CSav** assembly at increasing concentrations: 0.7, 1.4, 3.5, 7, 17.7, 35.3 μM ; under these conditions, the molar ratio **1CSav**/G4A ranges from 0.2 to 12, while GGG/G4A and 12mer/G4A ratio is 69 and 154, respectively. Lane 11: G4A (3 μM) and **1CSav** assembly (35.3 μM). Lane 12: GGG (206.5 μM) or 12mer (462 μM) in the presence of **1CSav** assembly (35.3 μM); GGG or 12mer are barely visible by ethidium bromide staining due to lack of intercalation of the dye in ssDNA. b) Binding to a ssDNA with a “scrambled” G4A sequence (scG4A) unable to form a DNA quadruplex. Lane 1: DNA Marker. Lane 2: ScG4A. Lanes 3–11: G4A (3.3 μM) + **1CSav** at increasing concentrations: 0.4, 0.6, 0.8, 1.6, 3.2, 3.9, 7.9, 19.8, 39.6 μM , representing a **1CSav**/G4A ratio from 0.12 to 12. In all cases 500 ng of scG4A was loaded onto the gel.

tide, which may intimate the existence of a more extended interaction with the **1CSav** assembly compared with the smaller GGG-trinucleotide. These results support the notion that G4A is a privileged target.

Genetic control of the second coordination sphere: Next, we investigated the influence of the second coordination sphere on G4A binding through site-directed mutagenesis. The crystal structure reveals two lysines (K121 of the two adjacent monomers) within 10 Å of the Ru, at the entrance of the largely hydrophobic biotin binding pocket (Figure 3). Mutation of this positively-charged residue (K121A) decreased affinity significantly (Figure 5 and Table 2 entry 5). A decrease in affinity upon lysine mutation has also been observed in other nucleic acid binding proteins^[19] and suggests that the lysines might form a salt bridge with the phosphate backbone. Similarly, the introduction of a negative charge in the vicinity of the Ru (S112D) also reduced binding-affinity (Figure 5 and Table 2 entry 4), perhaps caused

by charge repulsion. In contrast, the introduction of an aromatic residue at the same position (S112F) did not appreciably change the affinity for G4A (Figure 5 and Table 2 entry 3). These results show that DNA binding of the cationic Ru complex **1** is influenced by the second coordination sphere provided by the protein, particularly by charged residues in the vicinity of Ru.

Chemo-genetic optimization for improved binding to dsDNA: We also explored whether Sav could present metal-**1** to dsDNA (Figure 7 and Table 2 entries 7 and 8).

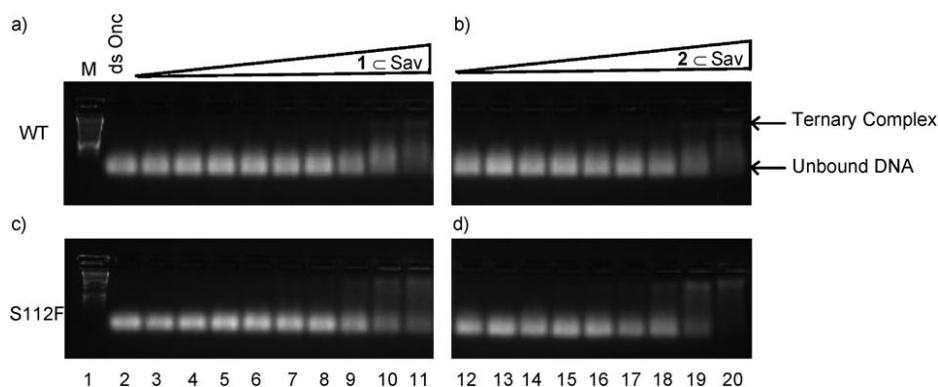


Figure 7. Chemo-genetic optimization of assemblies of drug-presenter proteins improves binding to dsDNA. Comparison of WT streptavidin (a and c) to a genetic variant S112F (b and d) illustrates that the nature of the metal-**1** and presenter protein can influence the binding to dsDNA, as revealed by EMSA on agarose gels. Lane 1: Marker (M). Lane 2: dsOnc. Lanes 3–11: dsOnc (3.12 μM) + concentration increase of **1C Sav**: 0.4, 0.6, 0.8, 1.6, 3.2, 3.9, 7.9, 19.8, 39.6 μM with a **1C Sav**/dsOnc ratio from about 0.12 to 12. Lanes 12–20: dsOnc (3.12 μM) + concentration increase of **2C Sav**: 0.4, 0.6, 0.8, 1.6, 3.2, 3.9, 7.9, 19.8, 39.6 μM with a **2C Sav**/dsOnc ratio from about 0.12 to 12. In all cases 500 ng of DNA was loaded onto the gel.

For this purpose, we used an 18 base pair dsDNA that includes the sequence of the common Braf V599E oncogenic mutation (dsOnc).^[20] Compared with the affinity for G4A ($K_d \approx < 1.6 \mu\text{M}$ as estimated by EMSA; Figure 5), the affinity for dsOnc is significantly lower, with $K_d \approx 37.9 \mu\text{M}$ (Figure 7a and Table 2 entry 7). We hypothesize that a different organization of functional groups, as well as the reduced flexibility of dsDNA, hampers efficient interaction between the ruthenium and nucleophilic sites on the bases. To further demonstrate that DNA binding can be fine-tuned using an assembly of drug and presenter protein, we sought to improve binding to dsDNA chemo-genetically, either with an intercalator,^[21] such as η^6 -biphenyl piano-stool complex **2**, or by genetic introduction of an aromatic residue to the position closest to Ru (S112). The biphenyl-containing S112F variant (**2C Sav** S112F) increased the affinity to dsOnc (Figure 7d and Table 2 entry 10), suggesting that modulation of non-covalent interactions in complexes of metal-**1** and presenter proteins can be engineered chemo-genetically to afford more specialised binders.

The importance of the extended second coordination sphere that is provided by the presenter protein for selective binding of a small molecule to a macromolecular target is shown by the following: 1) the different modes of binding of

cationic Ru complex **1** to G4A in presence or absence of Sav and 2) the influence of chemogenetic modifications on DNA binding, for example decreasing binding to G4A using a K121A mutant or by increasing the affinity for dsDNA by a judicious combination of genetic variant (S112F) and complex **2** (containing a biphenyl arene cap). In contrast, selective DNA binding is difficult to achieve with small metal-**1**, because there are only limited interactions available for recognition of the target.

Conclusion

We have shown that a supra-molecular assembly consisting of a metal-**1** (i.e., biotinylated ruthenium piano stool) combined with a presenter protein (i.e., streptavidin) modulates the recognition profile in vitro through the provision of additional non-covalent interactions. Such extended contacts, which are not typically available to small molecule drugs, allow modulation of affinity and selectivity towards DNA telomeres, even in the presence of competing targets (such as glutathione and dsDNA).

In the present form such assemblies cannot be delivered easily into cells, thus hampering in vivo studies. To overcome this challenge, our current alternative efforts include the following: 1) appending cell-penetrating peptide sequences to the presenter protein; 2) exploring non-DNA,^[10] extracellular targets, which circumvents the need for intracellular delivery and 3) exploiting endogenous species as presenter proteins, such as those overexpressed in cancer cells. The latter would thus only require cell penetration of the metal-**1**. The ultimate aim of these experiments is to use such tethered or cross-linking drugs^[6,22] in which an initial kinetic binder^[23] does not merely act as a “carrier”^[24] or “reservoir”^[25] but also chaperones the drug selectively to a macromolecular target in vivo, contributing ultimately to the inhibitory (bio-active) species.

Experimental Section

Experimental details can be found in the Supporting Information.

Acknowledgements

This work was funded by the Swiss National Science Foundation (Grants FN: 200020-113348 and 200020-126366) as well as COST D39 and by generous support to M.C. from the Treubelfonds (Basel). The authors would like to acknowledge Dr. André Ziegler for help with interpretation of ITC data and both Maurus Schmid and Thibaud Rossel for assistance with the design of figures. We are also grateful to C. R. Cantor for the streptavidin expression plasmid and Umicore for a loan of ruthenium.

- [1] L. Kelland, *Nat. Rev. Cancer* **2007**, *7*, 573.
- [2] R. Briesewitz, G. T. Ray, T. J. Wandless, G. R. Crabtree, *Proc. Natl. Acad. Sci. USA* **1999**, *96*, 1953.
- [3] I. Harvey, P. Garneau, J. Pelletier, *Proc. Natl. Acad. Sci. USA* **2002**, *99*, 1882.
- [4] M. Creus, A. Pordea, T. Rossel, A. Sardo, C. Letondor, A. Ivanova, I. Letrong, R. E. Stenkamp, T. R. Ward, *Angew. Chem.* **2008**, *120*, 1422; *Angew. Chem. Int. Ed.* **2008**, *47*, 1400.
- [5] Q. He, U. M. Ohndorf, S. J. Lippard, *Biochemistry* **2000**, *39*, 14426.
- [6] L. A. Banaszynski, C. W. Liu, T. J. Wandless, *J. Am. Chem. Soc.* **2005**, *127*, 4715.
- [7] P. C. Bruijninx, P. J. Sadler, *Curr. Opin. Chem. Biol.* **2008**, *12*, 197.
- [8] a) C. S. Allardyce, P. J. Dyson, D. J. Ellis, S. L. Heath, *Chem. Commun.* **2001**, 1396; b) R. E. Morris, R. E. Aird, P. d. S. Murdoch, H. Chen, J. Cummings, N. D. Hughes, S. Parsons, A. Parkin, G. Boyd, D. I. Jodrell, P. J. Sadler, *J. Med. Chem.* **2001**, *44*, 3616.
- [9] F. Wang, A. Habtemariam, E. P. van der Geer, R. Fernandez, M. Melchart, R. J. Deeth, R. Aird, S. Guichard, F. P. Fabbiani, P. Lozano-Casal, I. D. Oswald, D. I. Jodrell, S. Parsons, P. J. Sadler, *Proc. Natl. Acad. Sci. USA* **2005**, *102*, 18269.
- [10] I. W. McNae, K. Fishburne, A. Habtemariam, T. M. Hunter, M. Melchart, F. Wang, D. M. Walkinshaw, P. J. Sadler, *Chem. Commun.* **2004**, 1786.
- [11] P. C. Weber, D. H. Ohlendorf, J. J. Wendoloski, F. R. Salemme, *Science* **1989**, *243*, 85.
- [12] A. P. Silverman, W. Bu, S. M. Cohen, S. J. Lippard, *J. Biol. Chem.* **2002**, *277*, 49743.
- [13] H.-K. Liu, J. S. Berners-Price, F. Wang, A. J. Parkinson, J. Xu, J. Bella, P. J. Sadler, *Angew. Chem.* **2006**, *118*, 8333; *Angew. Chem. Int. Ed.* **2006**, *45*, 8153.
- [14] S. Balasubramanian, S. Neidle, *Curr. Opin. Chem. Biol.* **2009**, *13*, 345.
- [15] F. X. Han, R. T. Wheelhouse, L. H. Hurley, *J. Am. Chem. Soc.* **1999**, *121*, 3561.
- [16] C. Gossens, I. Tavernelli, U. Rothlisberger, *J. Am. Chem. Soc.* **2008**, *130*, 10921.
- [17] a) C. G. Hartinger, A. Casini, C. Duhot, Y. O. Tsybin, L. Messori, P. J. Dyson, *J. Inorg. Biochem.* **2008**, *102*, 2136; b) F. Wang, S. Weidt, J. Xu, C. L. Mackay, P. R. R. Langridge-Smith, P. J. Sadler, *J. Am. Soc. Mass Spectrom.* **2008**, *19*, 544; c) F. Wang, J. Xu, A. Habtemariam, J. Bella, P. J. Sadler, *J. Am. Chem. Soc.* **2005**, *127*, 17734.
- [18] a) J. Reedijk, *Chem. Rev.* **1999**, *99*, 2499; b) D. Wang, S. J. Lippard, *Nat. Rev. Drug Discovery* **2005**, *4*, 307.
- [19] a) P. Buczek, M. P. Horvath, *J. Mol. Biol.* **2006**, *359*, 1217; b) J. Tan, C. Vonrhein, O. S. Smart, G. Bricogne, M. Bollati, Y. Kusov, G. Hansen, J. R. Mesters, C. L. Schmidt, R. Hilgenfeld, *PLoS Pathog.* **2009**, *5*; c) D. E. Draper, *J. Mol. Biol.* **1999**, *293*, 255.
- [20] H. Namba, M. Nakashima, T. Hayashi, N. Hayashida, S. Maeda, T. I. Rogounovitch, A. Ohtsuru, V. A. Saenko, T. Kanematsu, S. Yamashita, *J. Clin. Endocrinol. Metab.* **2003**, *88*, 4393.
- [21] H. Chen, J. A. Parkinson, S. Parsons, R. A. Coxall, R. O. Gould, P. J. Sadler, *J. Am. Chem. Soc.* **2002**, *124*, 3064.
- [22] a) O. Novakova, A. A. Nazarov, C. G. Hartinger, B. K. Keppler, V. Brabec, *Biochem. Pharmacol.* **2009**, *77*, 364; b) W. H. Ang, A. De Luca, C. Chapuis-Bernasconi, L. Juillerat-Jeanneret, M. Lo Bello, P. J. Dyson, *ChemMedChem* **2007**, *2*, 1799; c) K. R. Barnes, A. Kutikov, S. J. Lippard, *Chem. Biol.* **2004**, *11*, 557; d) G. Jaouen, S. Top, A. Vessières, G. Leclercq, M. J. McGlinchey, *Curr. Med. Chem.* **2004**, *11*, 2505.
- [23] a) A. R. Timerbaev, C. G. Hartinger, S. S. Aleksenko, B. K. Keppler, *Chem. Rev.* **2006**, *106*, 2224; b) A. Casini, C. Gabbiani, E. Michelucci, G. Pieraccini, G. Moneti, P. J. Dyson, L. Messori, *J. Biol. Inorg. Chem.* **2009**, *14*, 761; c) J. Reedijk, *Proc. Natl. Acad. Sci. USA* **2003**, *100*, 3611.
- [24] F. Kratz, *J. Controlled Release* **2008**, *132*, 171.
- [25] B. Wu, P. Droge, C. A. Davey, *Nat. Chem. Biol.* **2008**, *4*, 110.

Received: June 4, 2010
Published online: September 28, 2010

CHEMISTRY

A EUROPEAN JOURNAL

Supporting Information

© Copyright Wiley-VCH Verlag GmbH & Co. KGaA, 69451 Weinheim, 2010

Chemo-Genetic Optimization of DNA Recognition by Metallodrugs using a Presenter-Protein Strategy

**Jeremy M. Zimbron,^[a] Alessia Sardo,^[a] Tillmann Heinisch,^[a, b] Therese Wohlschlager,^[c]
Julieta Gradinaru,^[c] Claudia Massa,^[b] Tilman Schirmer,^{*[b]} Marc Creus,^{*[a]} and
Thomas R. Ward^{*[a]}**

Crystallization

X-Ray Crystallography

Apo-streptavidin was crystallized using the hanging drop vapor diffusion technique, as described elsewhere.^[6] Rhombohedrally shaped crystals were obtained by mixing 5 μ L protein solution (26 mg/mL in water) with 5 μ L crystallization buffer (2 M $(\text{NH}_4)_2\text{SO}_4$, 0.1 M Na acetate, pH 4.0) and equilibrating the droplet against a reservoir of 500 μ L crystallization buffer for 24 h at room temperature. The soaking solution containing $[(\eta^6\text{-}p\text{-cymene})\text{Ru}(\text{Biot-L})\text{Cl}]$ (Biot-L= Biotin-*N*-(*R,R*)-3,4-diaminopyrrolidine) -compound **1**- was prepared by mixing 9 μ L stabilization buffer (3 M $(\text{NH}_4)_2\text{SO}_4$, 0.1 M Na acetate, pH 4.0) with 1 μ L compound **1** solution (50 mM in water). Lyophilized streptavidin (about 100–300 μ g) was added to the soaking solution subsequently to scavenge non-modified biotin. A single apo-streptavidin crystal was soaked for 24 h at room temperature. Then, the crystal was placed into cryo buffer (1.5 M $(\text{NH}_4)_2\text{SO}_4$, 0.1 M Na acetate pH 4.0, 25 % glycerol) for 30 s before it was shock frozen in liquid nitrogen.

Diffraction data collection, structure solution and refinement

Diffraction data were collected at the Swiss Light Source (beamline X06DA) using a mar225 mosaic CCD detector at a wavelength of 1.589 Å. The crystal diffracted to beyond 2 Å resolution. Crystallographic data are given in **Supporting Table 1**. Crystal indexing and data processing was carried out using programs MOSFLM/SCALA of the CCP4 suite. The phase problem was solved by rigid body refinement with program REFMAC 5.5 of the CCP4 suite.^[7] For this, the model of the isomorphous crystal structure of the [η^6 -(benzene)RuCl-(Biot-L)] C S112-streptavidin (PDB reference code 2QCB) was used,^[3] with biotinylated Ru complex and water molecules removed. Full atom refinement against the maximum likelihood target including TLS refinement was performed with REFMAC 5.5.^[8] Restrained individual B-factors were refined at later stage. SigmaA weighted Fo-Fc and 2Fo-Fc electron density maps^[9] as well as anomalous scattering difference maps^[10] were displayed with O^[11] and COOT.^[12] PyMOL was used to produce the structural figures for this paper. Coordinates and structure factors have been deposited in the Protein Data Bank with identifier 2WPU.

Supporting Table 1. Data collection and refinement statistics for compound **1** C streptavidin.*

Data Collection	
Resolution (Å)	28.8 – 2.0
Space Group	I4 ₁ 22
Cell Dimensions (Å)	a = 57.7 b = 57.7 c = 183.7
R _{merge} (%)	7.9 (28.1)
No. unique reflections	10764
Multiplicity	10.1 (3.4)
Completeness	97.9 (86.3)
I/s(I)	17.6 (4.5)
Refinement	
Resolution (Å)	28.8 – 2.0
R _{work} /R _{free} (%)	17.2/ 19.8
No. atoms	
Protein	1768
Ligand/ions	73
Water	391
B-factors (Å ²)	
Protein	22.0
[? ⁶ -(<i>p</i> -cymene)-RuCl(Biot- L)] 1	26.7
Water	40.0
R.m.s deviations	
Bond length (Å)	0.020
Bond angles (°)	1.25

*Values in parentheses are for the highest-resolution shell.

Overall Structure

The final protein model comprised residues 13–134 with 96.7 % of the residues found in the most-favored regions of a Ramachandran plot, and no Ramachandran outliers. As observed before^[3], both the N-terminal T7 tag (residues 1–12) and 25 residues at the C-terminus are not resolved, probably due to disorder (**Fig. S1**).

After modeling the well-resolved biotin moiety, the Fo-Fc electron density map showed strong residual density extending outwards from the biotin, which could be easily interpreted as $[(\eta^6\text{-}p\text{-cymene})\text{Ru}(\text{Biot-L})\text{Cl}]$ (Biot-L= Biotin-N-(R,R)-3,4-diaminopyrrolidine), compound **1** (**Fig.S1c**). The anomalous scattering difference map was consistent with the sulfur and ruthenium located in the biotinylated complex **1** as well as with a sulfate molecule located close to His87 (**Fig. S3d**).

Streptavidin forms a tight crystallographic tetramer of 222 (D2) symmetry with all four biotin binding sites fully occupied with compound **1**. Residues of two loop regions close to the ruthenium head group show slightly increased average B-factors (Ser 88 (19 Å²), Ser112 (20 Å²), Thr114 (21 Å²), Asn118 (28 Å²), Trp120 (21 Å²), Lys121 (26 Å²)) compared to β-barrel residues next to the biotin head group (Ser27 (19 Å²), Tyr43 (15 Å²), Asp128 (15 Å²)). The B-factors of the Ru-biotin atoms vary from 14 Å² (for the strongly bound biotin moiety) to 48 Å²

(for the solvent-exposed ruthenium head group) (**Fig.S2**). Thereby, the isopropyl and methyl group of *p*-cymene exhibit the highest B-factors (40-43 Å²) and electron density for these groups in the 2Fo-Fc map is only about 1σ, indicating that *p*-cymene is probably rotationally disordered around the ring normal. The B-factors of the ruthenium head group are only about 10 Å larger than the surrounding residues.

Apart from the interactions of the biotin core with the streptavidin β-barrel that are discussed elsewhere^[13] the ruthenium head group interacts with loop regions of one streptavidin monomer (**Fig.S3**). We observed the loss of a H-bridge between the side chain of Ser88 and the carboxylic group of biotin due to its amidation.

Finally, the model also contains 116 water molecules, one sulfate and one glycerol molecule.

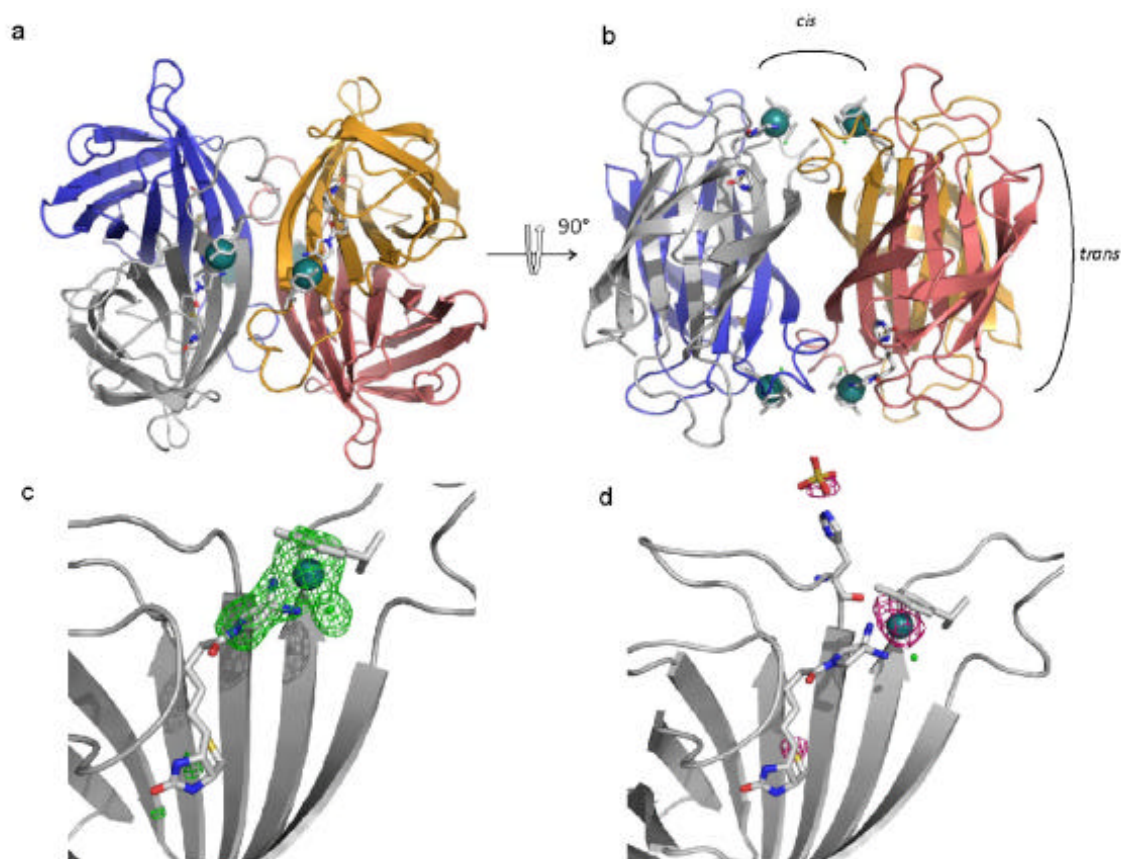


Fig.S1 Crystal structure of tetrameric **1 C Sav**: overall structure (**a** and **b**) and detail of complex **1** bound to streptavidin monomer (**c** and **d**). (**a**) Top view of tetrameric **1 C Sav** showing the two biotinylated piano-stool complexes in relative *cis*-constellation. (**b**) Side view on tetrameric **1 C Sav**. *Cis*- and *trans*-constellations of complexes **1** are indicated. See also **Fig.3a**. (**c**) Residual electron density in the F_o-F_c omit map of the head-group comprising the piano-stool moiety contoured at 3σ . (**d**) Anomalous scattering difference map contoured at 4.5σ .

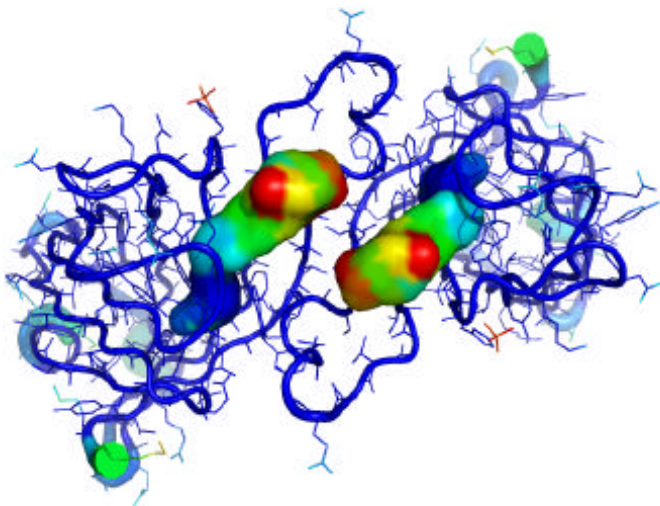


Fig.S2 Detailed view of two *cis*-related biotinylated piano-stool complexes (compound **1**) bound by two streptavidin monomers. Compound **1** is represented by its surface and color-coded according to B-factors that range from 12 Å² (blue) to 43 Å² (red).

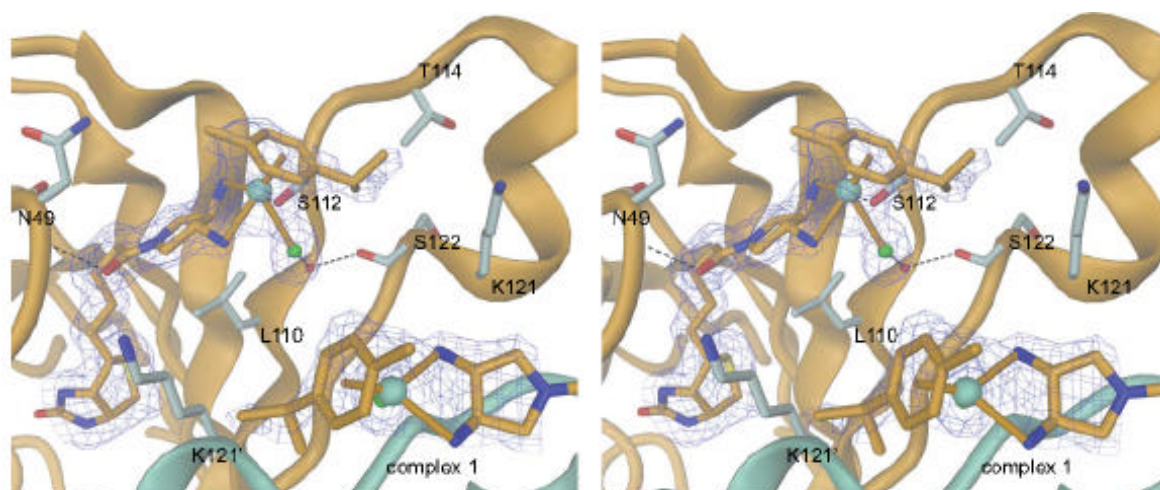


Fig.S3 Stereoview on the binding site between streptavidin and the head group of Ru-biotin. Close-up view of the ruthenium head group of **1** bound to a Sav monomer (orange) and partially interacting with another Sav monomer (aquamarine) also containing complex **1** (toward the right of the image). Selected residues are shown with side-chains and are labeled. Primed residues belong to the monomer in aquamarine. The 2 Fo-Fc electron density map of complex **1** bound to one Sav monomer is contoured at 1.0 σ . Hydrogen bonds are shown as dashed lines: a water bridges the labile chloride ligand and the carbonyl of Ser122; the side-chain hydroxyl of Ser112 hydrogen-bonds with a Ru-bound amine; the main-chain amide of Asp49 is H-bonded to the carbonyl of the biotin moiety of **1**. See also **Fig.3a**.

Ruthenium coordination

In the "piano-stool"-like conformation of the complex, the angles between the legs varying between 68° and 92° (**Fig.4**). The aromatic *p*-cymene is located approximately perpendicularly to the axial coordination direction at a distance of 1.83 \AA to the ruthenium and displays significantly larger angles compared to these between the legs. The $\text{N}^1\text{-C}^1\text{-C}^2\text{-N}^2$ torsion angle is 89° which is by 21° larger than the angle obtained after PRODRG^[14] energy minimization of 3,4-(*R,R*)-diaminopyrrolidine. The bond lengths between ruthenium and the amino groups are 2.48 and 2.37 \AA , respectively, which is about $0.2\text{-}0.3 \text{ \AA}$ longer compared to an average value of 2.12 \AA ($\sigma = 0.025 \text{ \AA}$) of $\text{Ru-NH}_2\text{R}$ bonds derived from 27 structures in the Cambridge Structural Data Base (CSDB).^[15] The distance between ruthenium and chloride is 2.83 \AA . This is by 0.41 \AA longer than the average of 2.42 \AA ($\sigma = 0.049 \text{ \AA}$) derived from 115 structures in the CSDB.^[15] We also tried to model a water molecule in the electron density. The B-factor of water (37 \AA^2) was smaller than that of chloride (47 \AA^2) while the B-factor of the ruthenium atom was the same in both cases (41 \AA^2). Therefore, it is probably chloride that is bound to ruthenium. Furthermore, the distance between ruthenium and water is 2.73 \AA , which is significantly larger compared to an average of 2.07 \AA ($\sigma = 0.050 \text{ \AA}$) extracted from 12 structures of the CSDB.^[15] Nevertheless, partial substitution of chloride by water cannot be excluded, since no chloride was provided during the

crystallization and soaking process. The aromatic *p*-cymene undergoes π -bonding to ruthenium. The distances between ruthenium and the carbon atoms of the aromatic *p*-cymene ring are between 2.15 and 2.34 Å.

Complex-DNA Interactions

The pocket in which the ruthenium head group is located is composed mainly of polar (Asn₁49, Ser₂69, Asn₁85, Thr₁115, Asn₁118) and basic (His₁87, Arg₁84, Lys₁121, Lys₃121) residues from three different streptavidin monomers (subscripted letters next to residue identifier refer to different monomers). When omitting one of the *cis*-related Ru-biotin (which would be the predominant constellation in a 2 : 1 assembly of **1** C Sav, as used for DNA-binding studies) a large pocket would be available for DNA binding (**Supplementary Video 1**). This pocket might provide a suitable binding groove for DNA: ionic interactions between the DNA phosphate groups and the positively charged residues on the protein surface (*e.g.* K121) as well as the substitution of the ruthenium-bound chloride by a nucleotide-base nitrogen (N⁷ or N¹ in case of purine bases and N³ in case of pyrimidine bases)^[16] is conceivable.

- [1] F. X. Han, R. T. Wheelhouse, L. H. Hurley, *J. Am. Chem. Soc.* **1999**, *121*, 3561.
- [2] H. Namba, M. Nakashima, T. Hayashi, N. Hayashida, S. Maeda, T. I. Rogounovitch, A. Ohtsuru, V. A. Saenko, T. Kanematsu, S. Yamashita, *J. Clin. Endocrinol. Metab.* **2003**, *88*, 4393.
- [3] M. Creus, A. Pordea, T. Rossel, A. Sardo, C. Letondor, A. Ivanova, I. Letrong, R. E. Stenkamp, T. R. Ward, *Angew. Chem. Int. Ed.* **2008**, *47*, 1400.
- [4] a)A. Habtemariam, M. Melchart, R. Fernandez, S. Parsons, D. H. Oswald Iain, A. Parkin, P. A. Fabbiani Francesca, E. Davidson James, A. Dawson, E. Aird Rhona, I. Jodrell Duncan, J. Sadler Peter, *J. Med. Chem.* **2006**, *49*, 6858;
b)M. A. Bennett, A. K. Smith, *J. Chem. Soc., Dalt. Trans.* **1974**, 233.
- [5] D. W. P. M. Lowik, M. D. Weingarten, M. Broekema, A. J. Brouwer, W. C. Still, R. M. J. Liskamp, *Angew. Chem. Int. Ed.* **1998**, *37*, 1846.
- [6] A. Pahler, W. A. Hendrickson, M. A. Kolks, C. E. Argarana, C. R. Cantor, *J. Biol. Chem.* **1987**, *262*, 13933.
- [7] S. Bayley, *Acta Crystallogr. D Biol. Crystallogr.* **1994**, *50*, 760.
- [8] A. T. Brunger, *Acta Crystallogr. D Biol. Crystallogr.* **1993**, *49*, 24.
- [9] R. J. Read, *Acta Crystallogr. A Found. Crystallogr.* **1986**, *A42*, 140.

- [10] G. Strahs, J. Kraut, *J. Mol. Biol.* **1968**, *35*, 503.
- [11] T. A. Jones, J. Y. Zou, S. W. Cowan, M. Kjeldgaard, *Acta Crystallogr. A* **1991**, *47* 110.
- [12] P. Emsley, K. Cowtan, *Acta Crystallogr. D Biol. Crystallogr.* **2004**, *60*, 2126.
- [13] P. C. Weber, D. H. Ohlendorf, J. J. Wendoloski, F. R. Salemme, *Science* **1989**, *243*, 85.
- [14] A. W. Schuttelkopf, D. M. van Aalten, *Acta Crystallogr. D Biol. Crystallogr.* **2004**, *60*, 1355.
- [15] A. G. Orpen, L. Brammer, F. H. Allen, O. Kennard, D. G. Watson, R. Taylor, *J. Chem. Soc., Dalton Trans.* **1989**, S1.
- [16] H. Chen, J. A. Parkinson, R. E. Morris, P. J. Sadler, *J. Am. Chem. Soc.* **2003**, *125*, 173.

8.1. Author Contributions

General idea:

Thomas R. Ward, Marc Creus

Synthesis of biotinylated Ru-arene sulfonamide complexes:

Jeremy Zimbron, Julieta Gardinaru

Production of Sav mutants:

Alessia Sardo, Therese Wohlschlager

EMSA tests and ITC:

Jeremy Zimbron, Alessia Sardo, Marc Creus

Crystal structure analysis:

Tillmann Heinisch, Claudia Massa, Tilman Schirmer

Manuscript writing:

Marc Creus, Thomas R. Ward and all other authors

V Towards in Vivo Catalysis with Artificial Metalloenzymes

9. Introduction

Artificial metalloenzymes are desired to be functional in biological systems amongst others for three different reasons: i) to optimize AMEs by directed evolution, ii) to implement AMEs in metabolic pathways and iii) for the selective transformation of a prodrug into a drug by employment of an AME.

9.1. Directed Evolution of Artificial Metalloenzymes

The potential of artificial metalloenzymes based on the streptavidin-biotin technology, and other systems in asymmetric catalysis has been demonstrated: high enantioselectivity and turnover number, reactivity in water at room temperature. The principle opportunity of such systems to be further optimized (e.g. high substrate scope, TON, TOF) by chemical and genetic means can be acquired by the development of high-throughput *in vivo* screening technologies. Three main problems need to be addressed to do high-throughput screening of streptavidin-biotin-based AMEs: i) the inactivation of many metallocofactors by the cellular matrix (mainly by thiol groups, e.g. glutathione), ii) the occupation of Sav with intrinsic biotin and iii) the transportation of the cofactor into the cytosol.

9.2. Artificial Metalloenzymes in Metabolic Engineering

The application of whole cells (e.g. *E. coli*, bakers yeast) as biocatalyst is thousands of years old. To date, numerous technologies are applied to find a good cellular biocatalyst for a reaction of interest: i) screening of many microorganisms,⁹⁶ ii) screening of metagenomes⁹⁷ or iii) metabolic engineering.⁹⁸ In the latter technique model organisms (e.g. *E. coli*, bakers yeast) are genetically engineered and equipped with heterologous DNA that expresses enzymes relevant for the production of pharmaceuticals, fine chemicals or biofuels.

In principle, synthetic metabolic pathways can be equipped with AMEs to i) reduce the number of reaction steps by the use of bioorthogonal reactions (e.g. olefin metathesis) or ii) to provide alternative reaction conditions using cheap starting materials (e.g. formate with ATHase). Conceptually, an optimized AME can be coexpressed with the metabolic pathway

in a heterologous host. Alternatively, an AME can be encapsulated into a cell-permeable nanoreactor which is taken up by endocytosis.

9.3. Artificial Metalloenzymes in the Prodrug Strategy

AMEs that catalyze bioorthogonal reactions (i.e. no background reactivity of the catalyst or the substrate with any biomolecule in the organism) can be used to release a drug from an inactive prodrug by reaction with a bioorthogonal caging function. AMEs can be encapsulated in vesicles that are surface-functionalized with cell-recognition motifs. The AME would be transported by the vesicle to the site of interest in the body. An administered unselective prodrug would only be transformed into the active drug once it got in contact with the AME in the target tissue.

9.4. Vesicular Delivery Systems for the Cellular Uptake of Enzymes

Amphiphilic molecules can self-assemble to mimic natural membranes and form vesicles. Properties of the vesicles like i) size/inner volume, ii) solubility in water, iii) pH-, oxidation-, temperature-, magnetic field-, enzyme-stability, iv) incorporation/permeability of cargo or v) cell-permeability can be engineered by the selected use of different chemical building blocks (e.g. **Figure M19**).⁹⁹ Vesicular drug delivery systems (DDS) are important medical tools to shield drugs from biodegradation and to improve the pharmacokinetics and target selectivity.¹⁰⁰ Both, specific uptake of DDSs in human cells by surface-functionalization with receptor recognition tags and unspecific endocytosis of unfunctionalized DDSs e.g. by human macrophages is possible.

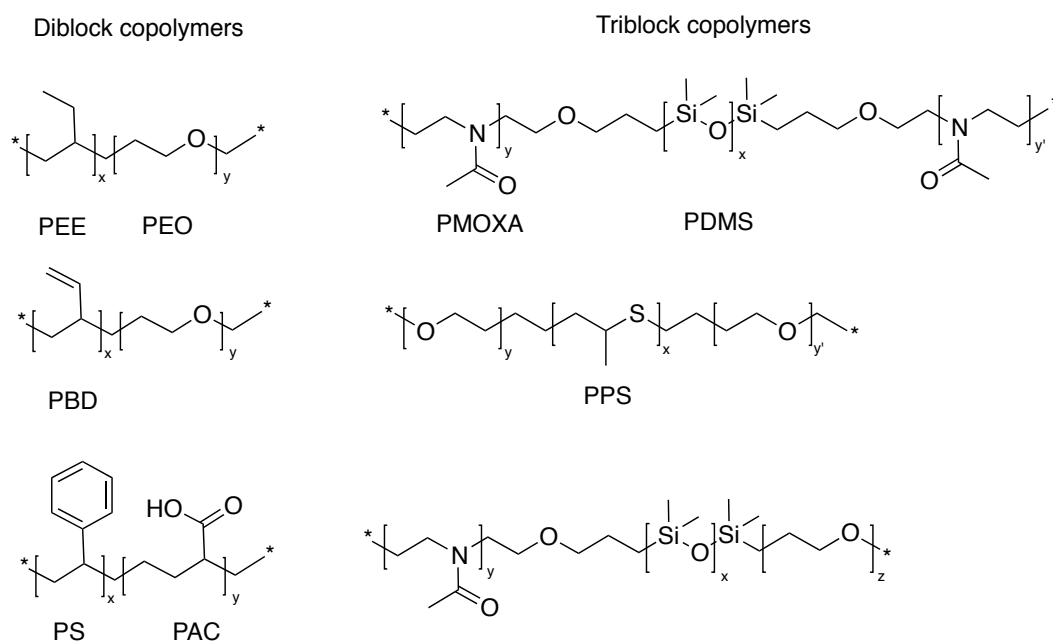


Figure M19: Vesicle-forming diblock- and triblock-copolymers. The copolymers are made by combination of polymers poly(ethylene ethylene) (PEE), poly(ethylene oxide) (PEO), poly(methyloxazoline) (PMOXA), poly(dimethylsiloxane) (PDMS), poly(butadiene) (PBD), poly(propylene sulfide) (PPS), poly(styrene) (PS) or poly(acrylic acid) (PAC).⁹⁹

Meier and coworkers have encapsulated numerous enzymes and enzyme cascades (e.g. beta-lactamase, lipase, peptidase, peroxidase) in PMOXA- β -PDMS- β -PMOXA-type vesicles.¹⁰¹ Since the membrane of these vesicles is permeable only for very small or hydrophobic solutes, bacterial porin protein OmpF, which is selective for polar compounds, was incorporated into the membrane.¹⁰² Although the length of the individual blocks of the synthetic membrane is significantly larger than the transmembrane part of OmpF, strong compression of the polymer is entropically favored and allows incorporation of functional porins.¹⁰³ Inside the stable nanoreactors, enzymes remain functional for several months. It has been reported that human macrophages can take up PMOXA- β -PDMS- β -PMOXA-type nanocontainers unspecifically. However, functionalization of the vesicle surface with poly guanine tags, which specifically recognize cell surface receptors, increases the rate of endocytosis.¹⁰⁴ Meier and coworkers detected surface-functionalized vesicles charged with a fluorescent dye in lysosomes, the Golgi apparatus and the endoplasmic reticulum of macrophages after 1 h incubation time. The vesicles remained structurally integer inside the cell for at least 36 hours. Moreover, trypsin-loaded PMOXA- β -PDMS- β -PMOXA vesicles (but not empty ones) were found to catalyze the release of a dye from a non-fluorescent peptide substrate inside the macrophage. These results encourage the idea to use PMOXA- β -

PDMS- β -PMOXA-based nanoreactors equipped with streptavidin-biotin-based AMEs for *in vivo* catalysis.

10. Fluorescence-Based Assay for the Optimization of Artificial Transfer Hydrogenase Activity within a Biocompatible Compartment

DOI: 10.1002/cctc.200

Fluorescence-Based Assay for the Optimization of Artificial Transfer Hydrogenase Activity within a Biocompatible Compartment

Tillmann Heinisch^[a], Karolina Langowska^[b], Pascal Tanner^[b], Jean-Louis Reymond^[c], Wolfgang Meier^[b], Cornelia Palivan^[b] and Thomas R. Ward^{[a]*}

In recent years, artificial metalloenzymes which result from incorporation of an organometallic cofactor within a host protein have emerged as an alternative to the more traditional catalysts.^[1] We recently reported an artificial transfer hydrogenase (ATHase) for the enantioselective reduction of imines.^[2,3] The ATHase, consisting of a biotinylated [Cp*Ir(Biot-*p*-L)Cl] combined with streptavidin (Sav hereafter), was shown to remain active under dilute conditions and was compatible with cellular debris. While such characteristics are common for enzymes, very few homogeneous catalysts have been shown to function under such conditions.^[4] We thus contemplated the possibility of adapting the ATHase for use in chemical biology. With this goal in mind, we identified two challenges which need to be addressed: i) the development of a transfer-hydrogenation reaction which leads to the generation of a fluorescent signal^[5] and ii) the incorporation of the functional ATHase in a biocompatible compartment, Figure 1.^[6]

In order to develop a transfer hydrogenation reaction giving rise to a fluorescence signal, we relied on the propensity of enones to undergo 1,4-addition in the presence of d⁶-pianostool transfer hydrogenation catalysts.^{[3d],[7]} For this purpose, we designed the enone-substrate **1** bearing a caged dye. We speculated that the reduced ketone intermediate **2** would spontaneously undergo E1cB elimination under physiological conditions thus releasing umbelliferone **3**, Scheme 1 (See SI for the synthesis and characterization of enone **1**).

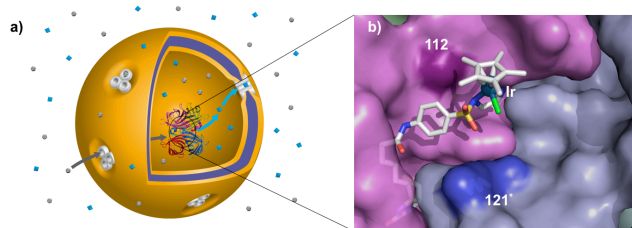
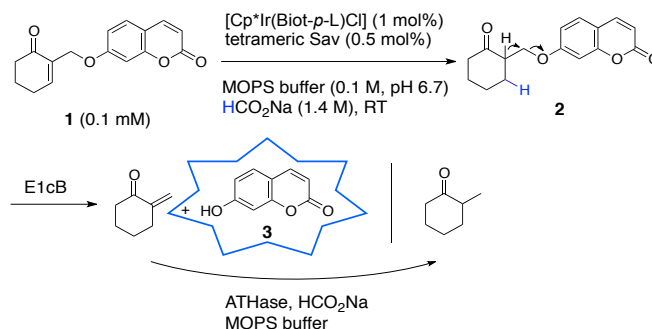


Figure 1. Encapsulation of a hybrid catalyst (protein ribbon display) within a polymersome (orange-blue capsule, block-co-polymer PMOXA- β -PDMS- β -PMOXA) equipped with a pore protein (grey trimer, bacterial pore protein OmpF) affords catalytically active artificial organelles (a). The hybrid catalyst results from the supramolecular incorporation of a biotinylated pianostool complex [Cp*Ir(Biot-*p*-L)Cl] (stick representation) within streptavidin (solvent-accessible surface displayed, X-ray crystal structure, PDB code 3PK2) (b).



Scheme 1. Fluorescence-based assay for the detection of transfer hydrogenase activity.

When subjected to transfer hydrogenation in the presence of ATHase (1 μ M [Cp*Ir(Biot-*p*-L)Cl], 0.5 μ M tetrameric Sav), aqueous solutions containing enone **1**, rapidly became fluorescent (λ_{ex} and λ_{em} = 323 and 470 nm, respectively), Figure 2. GC- and HPLC chromatographic analysis of the reaction mixture revealed the formation of umbelliferone and 2-methylcyclohexanone as main products (See SI).

With this straightforward fluorescent assay at hand, the

[a] Tillmann Heinisch, Prof. Dr. Thomas R. Ward
Institut für Anorganische Chemie, Universität Basel
Spitalstrasse 51, 4056 Basel, (Switzerland)
Fax: (+41) 61-267-1005
E-mail: thomas.ward@unibas.ch

[b] K. Langowska, P. Tanner, Prof. Dr. W. Meier, Dr. C. Palivan
Institut für Physikalische Chemie, Universität Basel
Klingelbergstrasse 80, 4056 Basel (Switzerland)

[c] J.-L. Reymond
Universität Bern
Freiestrasse 3, 3012 Bern (Switzerland)

Supporting information for this article is available on the WWW
under <http://dx.doi.org/10.1002/cctc.200xxxxx>

performance of the ATHase was optimized by screening various Sav isoforms bearing mutations in the proximity of the Ir-center. For this purpose, positions Ser-112 or Lys-121 were selected. While most mutations had little or a deleterious effect on the ATHase activity, Lys121Phe and Lys121Tyr lead to a significant increase in fluorescence in the presence of the corresponding ATHases [Cp*Ir(Biot-*p*-L)Cl]·Sav_{K121F} and [Cp*Ir(Biot-*p*-L)Cl]·Sav_{K121Y} (abbreviated ATHase_{K121F} and ATHase_{K121Y} hereafter), Figure 2. In the presence of ATHase_{K121F}, fifty turnovers were observed by HPLC after 22 hours.

With chemical biology applications in mind, the following challenges facing ATHase need to be addressed: i) cell penetration properties, ii) catalytic activity *in vivo* and iii) non-immunogenicity. In view of the size of the artificial metalloenzyme (Mw 65 kDa, thus limited uptake by passive diffusion or endocytosis)^[8] and the reported immunogenicity of Sav,^[9] we sought to incorporate it into a biocompatible polymersome.^[6e-f] In recent years, Meier and coworkers addressed the challenges outlined above by developing artificial organelles.^[10] These consist of a triblock ABA copolymer poly(2-methyloxazoline)- β -poly(dimethylsiloxane)- β -poly(2-methyl-oxazoline) (PMOXA- β -PDMS- β -PMOXA hereafter) which, even in the presence of an enzyme, self-assembles in aqueous solution to yield catalytically active compartments of nanometer size. These were shown to i) penetrate human macrophages by endocytosis, ii) remain stable for several days without leakage of the cargo and iii) be non-immunogenic.^[10c] Addition of the bacterial pore protein OmpF, favors the transit of small hydrophobic molecules (Mw < 600 Da) between the artificial organelle and its environment, Figure 1 a.^[11]

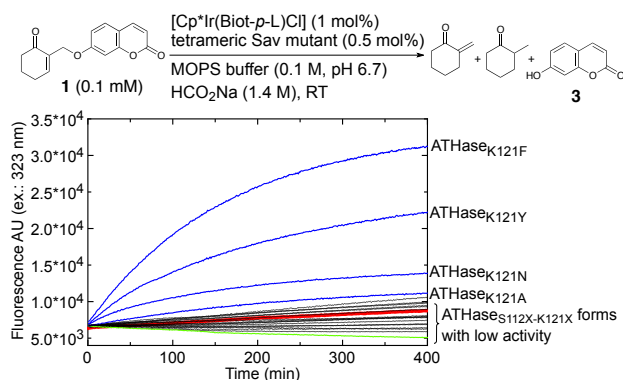


Figure 2. Genetic optimization of the catalytic performance of the ATHase revealed by the increase in fluorescence upon reduction of substrate **1** with concomitant release of umbelliferone **3**. [Cp*Ir(Biot-*p*-L)Cl]·Sav_{WT} (red, background fluorescence in the absence of ATHase: green), Sav mutants with significantly improved activity are highlighted in blue.

The most active artificial metalloenzyme identified above (ATHase_{K121F}) was encapsulated in PMOXA- β -PDMS- β -PMOXA by self-assembly in presence and absence of the bacterial pore protein OmpF to yield the corresponding vesicles abbreviated ATHase_{K121F}⊂nanoreactor and ATHase_{K121F}⊂nanoreactor_{OmpF}. The self-assembly process was followed by extensive dialysis to remove the non-encapsulated ATHase and non-incorporated OmpF. Titration experiments with biotin-4-fluorescein revealed no residual streptavidin on the nanoreactor's outer-surface after

dialysis (See SI). The resulting vesicles were characterized by transmission electron microscopy imaging as well as fluorescence correlation spectroscopy (FCS) (See SF 9). The spherical nanocompartments display a diameter varying between 10 - 100 nm (Figure 3, left). The encapsulated iridium concentration of ATHase_{K121F} in a nanoreactor sample was determined by ICP-MS: ATHase_{K121F}⊂nanoreactor 7 μ M and ATHase_{K121F}⊂nanoreactor_{OmpF} 22 μ M. This corresponds to a total encapsulation efficiency of ca. 7 % and 22 %, respectively. As previously observed the encapsulation efficiency varies depending on the protein type.^[10d]

Next, the catalytic activity of both ATHase_{K121F}⊂nanoreactor_{OmpF} and ATHase_{K121F}⊂nanoreactor was evaluated by fluorescence. Catalytic amounts (1 mol% based on iridium concentration as determined by ICP-MS) of either ATHase_{K121F}⊂nanoreactor and ATHase_{K121F}⊂nanoreactor_{OmpF} were added to substrate **1** in the presence of sodium formate at pH 6.7. The activity of ATHase_{K121F}⊂nanoreactor is significantly reduced compared to free ATHase_{K121F}. Introduction of OmpF to the nanoreactor contributes to partially restore the ATHase activity, which remains well below that of the free ATHase_{K121F}. We speculate that the hydrophobic character of both substrate **1** and product **3** hamper their rapid transit through OmpF which is selective for polar solutes, Figure 3.^[11] These findings support a porin-selective migration of substrate **1** into the nanoreactor, although passive diffusion through PMOXA- β -PDMS- β -PMOXA occurs to some extent as well. The activity of the ATHase_{K121F}⊂nanoreactor_{OmpF} gradually decreases upon going from pH 7.5 to pH 5.0 (See SF 7), thus suggesting that such systems may be compatible with cytosolic (pH 7.5) as well as early endosomal environments (pH 6.0).^[12] Control experiments with empty nanoreactors, that were prepared analogous to the catalytically competent nanoreactors, showed no fluorescence, suggesting that the empty nanoreactors are not catalytically competent.

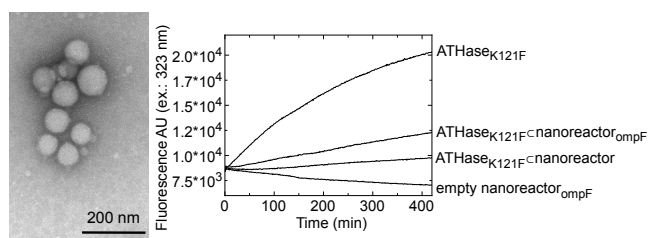


Figure 3. Transmission electron microscopy (TEM) image of ATHase_{S112A}⊂nanoreactor_{OmpF} (left). Activity profile of encapsulated and non-encapsulated ATHase_{K121F} for the reaction with substrate **1** (right). The reactions were carried out at 25 °C at pH 6.7 (100 mM MOPS) using 100 μ M substrate **1**, 0.5 mol% tetrameric Sav_{K121F}, 1 mol% [Cp*Ir(Biot-*p*-L)Cl] and 1.4 M HCO₂Na. The concentration of ATHase_{K121F} inside nanoreactor was determined by ICP-MS.

Within its spatiotemporal distribution limit, laser scanning microscopy (LSM) experiments highlight the formation of umbelliferone **3** in the presence of catalytically competent nanoreactors. For visualization purposes, sulforhodamine B (a dye which is known to remain stranded within vesicles^[10c]) was incorporated within the nanoreactors. Catalytic amounts (4 mol%) of ATHase_{K121F}-loaded and control samples of nanoreactor_{OmpF} lacking the ATHase (but including sulforhodamine B), were incubated with substrate **1** and formate

at pH 6.7. The generation of a fluorescence signal was detected after 90 minutes in the proximity of ATHase_{K121F}Cnanoreactor_{OmpF}. In contrast, the empty nanoreactor_{OmpF} did not lead to the generation of the fluorescence from umbelliferone **3** (Figure 4 c and d). This observation highlights i) the activity of the nanoreactors and ii) the slow diffusion of the generated umbelliferone **3** (but not sulforhodamine B) out of the nanoreactor as expected from its polar character.

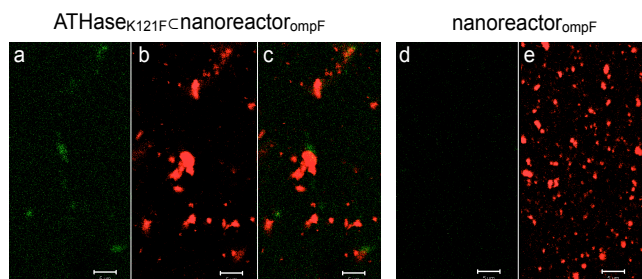


Figure 4. Laser scanning microscopy (LSM) images highlighting umbelliferone **3** formation (green color) only in the presence of catalytically competent ATHase_{K121F}Cnanoreactor_{OmpF} (a and c), while the empty nanoreactor_{OmpF} is inactive (d). Sulforhodamine B (red color, b, c, e) was co-encapsulated to help localize the nanoreactors. The presence of umbelliferone **3** occurs primarily in the proximity to vesicles (c, superposition of a and b). The reactions were carried out in presence of 250 μM substrate **1**, ~2 mol% tetrameric Sav_{K121F} and ~4 mol% [Cp*Ir(Biot-p-L)Cl] inside nanoreactor_{OmpF} and 1.5 M HCO₂Na at pH 6.7 (100 mM MOPS) for 90 min at room temperature. The scalebars represent 5 μm.

Herein we report our efforts to develop a fluorescence-based assay to visualize transfer hydrogenase activity. For this purpose, enone **1** bearing a caged dye was synthesized and shown to undergo a cascade 1,4-addition followed by an E1cB elimination leading to the release of umbelliferone **3**. Genetic optimization of the ATHase led to the identification of artificial metalloenzymes with significantly improved activities (initial rates of ATHase_{WT} and ATHase_{K121F} 7.5 and 147 AU/min, respectively). It was further shown that ATHase activity was maintained upon incorporation of the artificial metalloenzyme within a biocompatible vesicle. Importantly, these nanocontainers remain active under highly dilute conditions (i.e. 1 μM Ir-concentration) and are stable under aerobic physiological conditions for several months (See SF 8). Current efforts are aimed at testing these functional artificial organelles *in vivo*.

Acknowledgements

TRW thanks Prof. K. Gademann for enlightening discussions. This research was supported by the the Swiss Nanoscience Institute, NCCR nanoscale science, the SNF (grants 200020_126366 and 200020_144354) and the Marie Curie training network (BioChemLig FP7-ITN-238434). We thank Prof. C. R. Cantor for the Sav gene and Umicore for a loan of iridium.

Keywords: artificial metalloenzymes • fluorescence assay • nanoreactors • transfer hydrogenation

- [1] Abe, T. Ueno, Y. Watanabe, *Top. Organomet. Chem.* **2009**, *25*, 25-43; e) F. Rosati, G. Roelfes, *ChemCatChem* **2010**, *2*, 916-927; f) Y. Lu, N. Yeung, N. Sieracki, N. M. Marshall, *Nature* **2009**, *460*, 855-862; g) C. Cavazza, C. Bochet, P. Rousselot-Pailley, P. Carpentier, V. Cherrier, L. Martin, C. Marchi-Delapierre, J. C. Fontecilla-camps, S. Ménage, *Nat. Chem.* **2010**, *2*, 1069-1076; h) P. J. Deuss, G. Popa, C. H. Botting, W. Laan, P. C. J. Kamer, *Angew. Chem.* **2010**, *122*, 5443-5445; *Angew. Chem. Int. Ed.* **2010**, *49*, 5315-5317; i) T. Matsuo, D. Murata, Y. Hisaeda, H. Hori, T. Hayashi, *J. Am. Chem. Soc.* **2007**, *129*, 12906-12907.
- [2] M. Dürrenberger, T. Heinisch, Y. M. Wilson, T. Rossel, E. Nogueira, L. Knörr, A. Mutschler, K. Kersten, M. J. Zimbron, J. Pierron, T. Schirmer, T. R. Ward, *Angew. Chem.* **2011**, *123*, 3082-3085; *Angew. Chem. Int. Ed.* **2011**, *50*, 3026-3029.
- [3] Literature on non-enzymatic transfer hydrogenation: a) T. Ikariya, K. Murata, R. Noyori, *Org. Biom. Chem.* **2006**, *4*, 393-406; b) R. Noyori, S. Hashiguchi, *Acc. Chem. Res.* **1997**, *30*, 97-102; c) M. Yamakawa, I. Yamada, R. Noyori, *Angew. Chem.* **2001**, *113*, 2900-2903; *Angew. Chem. Int. Ed.* **2001**, *40*, 2818-2821; d) M. Watanabe, K. Murata, T. Ikariya, *J. Am. Chem. Soc.* **2003**, *125*, 7508-7509; e) X. Wu, J. Liu, X. Li, A. Zanotti-Gerosa, F. Hancock, D. Vinci, J. Ruan, J. Xiao, *Angew. Chem.* **2006**, *118*, 6870-6874; *Angew. Chem. Int. Ed.* **2006**, *45*, 6718-6722; f) C. Wang, C. Li, X. Wu, A. Pettman, J. Xiao, *Angew. Chem.* **2009**, *121*, 6646-6650; *Angew. Chem. Int. Ed.* **2009**, *48*, 6524-6528; g) C. Li, J. Xiao, *J. Am. Chem. Soc.* **2008**, *130*, 13208-13209; h) S. Betanzos-Lara, Z. Liu, A. Habtemariam, A. M. Pizarro, B. Qamar, P. J. Sadler, *Angew. Chem.* **2012**, *124*, 3963-3966; *Angew. Chem. Int. Ed.* **2012**, *51*, 3897-900; i) F. Joo, *Acc. Chem. Res.* **2002**, *35*, 738-745; j) S. Ogo, K. Uehara, T. Abura, S. Fukuzumi, *J. Am. Chem. Soc.* **2004**, *126*, 3020-3021; k) O. Saidi, J. M. Williams, *J. Top. Organomet. Chem.* **2011**, *34*, 77-106.
- [4] a) C. Streu, E. Meggers, *Angew. Chem.* **2006**, *118*, 5773-5776; *Angew. Chem. Int. Ed.* **2006**, *45*, 5645-5648; b) R. M. Yusop, A. Unciti-Broceta, E. M. V. Johansson, R. M. Sánchez-Martín, M. Bradley, *Nat. Chem.* **2011**, *3*, 239-243; c) N. Li, R. K. V. Lim, S. Edwardraja, Q. Lin, *J. Am. Chem. Soc.* **2011**, *133*, 15316-15319; d) L. Adriaenssens, L. Severa, J. Vávra, T. Šálová, J. Hývl, M. Čížková, R. Pohl, D. Šaman, F. Teplý, *Collect. Czech. Chem. Commun.* **2009**, *74*, 1023-1034.
- [5] a) J.-L. Reymond, V. S. Fluxà, N. Maillard, *Chem. Commun.* **2009**, 34-46; b) J.-P. Goddard, J.-L. Reymond, *Curr. Opin. Biotech.* **2004**, *15*, 314-322; c) D. Wahler, J.-L. Reymond, *Angew. Chem.* **2002**, *114*, 1277-1280; *Angew. Chem. Int. Ed.* **2002**, *41*, 1229-1232; d) J.-L. Reymond, *Enzyme Assays: High-throughput Screening, Genetic Selection and Fingerprinting*; 1st ed.; Wiley-VCH, 2006.
- [6] a) A. J. Dzieciol, S. Mann, *Chem. Soc. Rev.* **2012**, *41*, 79-85; b) T. Koshiyama, N. Yokoi, T. Ueno, S. Kanamaru, S. Nagano, Y. Shiro, F. Arisaka, Y. Watanabe, *Small* **2008**, *4*, 50-54; c) S. Abe, K. Hirata, T. Ueno, K. Morino, N. Shimizu, M. Yamamoto, M. Takata, E. Yashima, Y. Watanabe, *J. Am. Chem. Soc.* **2009**, *131*, 6958-6960; d) T. Ueno, M. Suzuki, T. Goto, T. Matsumoto, K. Nagayama, Y. Watanabe, *Angew. Chem.* **2004**, *116*, 2581-2584; *Angew. Chem. Int. Ed.* **2004**, *43*, 2527-2530; e) D. E. Discher, A. Eisenberg, *Science* **2002**, *297*, 967-973; f) D. M. Vriezema, P. M. L. Garcia, N. Sancho Oltra, N. S. Hatzakis, S. M. Kuiper, R. J. M. Nolte, A. E. Rowan, J. C. M. van Hest, *Angew. Chem.* **2007**, *119*, 7522-7526; *Angew. Chem. Int. Ed.* **2007**, *46*, 7378-7382; g) B. Wörsdörfer, K. J. Woycechowsky, D. Hilvert, *Science* **2011**, *331*, 589-592.
- [7] X. Li, L. Li, Y. Tang, L. Zhong, L. Cun, J. Zhu, J. Liao, J. Deng, *J. Org. Chem.* **2010**, *75*, 2981-2988.
- [8] L. E. Chalifour, K. Dakshinamurti, *Biochim. Biophys. Acta* **1982**, *721*, 64-69.
- [9] a) H. B. Breitz, P. L. Weiden, P. L. Beaumier, D. B. Axworthy, C. Seiler, F.-min Su, S. Graves, K. Bryan, J. M. Reno, *J. Nuc. Med.* **2000**, *41*, 131-140; b) D. L. Meyer, J. Schultz, Y. Lin, A. Henry, J. Sanderson, J. M. Jackson, S. Goshorn, A. R. Rees, S. S. Graves, *Protein Science* **2001**, *10*, 491-503.

- [10] a) P. Tanner, P. Baumann, R. Enea, O. Onaca, C. Palivan, W. Meier, *Acc. Chem. Res.* **2011**, *10*, 1039-1049; b) W. Meier, C. Nardin, M. Winterhalter, *Angew. Chem.* **2000**, *112*, 4747-4750; *Angew. Chem. Int. Ed.* **2000**, *39*, 4599-4602; c) N. Ben-Haim, P. Broz, S. Marsch, W. Meier, P. Hunziker, *Nano Lett.* **2008**, *8*, 1368-1373; d) P. Tanner, O. Onaca, V. Balasubramanian, W. Meier, C. G. Palivan, *Chem.-Eur. J.* **2011**, *17*, 4552-4560. e) W. Meier; *Chem. Commun* **2012**, DOI:10.1039/C2CC36345C.
- [11] H. Nikaido, M. Vaara, *Microbiol. Rev.* **1985**, *49*, 1-32.
- [12] T. Nishi, M. Forgac, *Nat. Rev. Mol. Cel. Biol.* **2002**, *3*, 94-103.
-

Received:
Published online:

Supporting Information

Fluorescence-Based Assay for the Optimization of Artificial Transfer Hydrogenase Activity within a Biocompatible Compartment

Tillmann Heinisch, Karolina Langowska, Pascal Tanner, Jean-Louis Reymond, Wolfgang Meier, Cornelia Palivan and Thomas R. Ward*

General Information

Analytical RP-HPLC (Agilent Series 1100):

Separations were carried out with a Dr. Maisch Reprospher C18-DE column (150 x 4.6 mm, 5 μ m particle size) using eluent A (water, 0.1 % trifluoroacetic acid (TFA)) and B (acetonitrile, 0.1 % TFA). The following method was used: flow rate 1 mL/min, detection of umbelliferone and its derivatives at 323 nm; 0 - 2 min (80 % A, isocratic), 2 - 10 min (gradient 80 \rightarrow 20 % A).

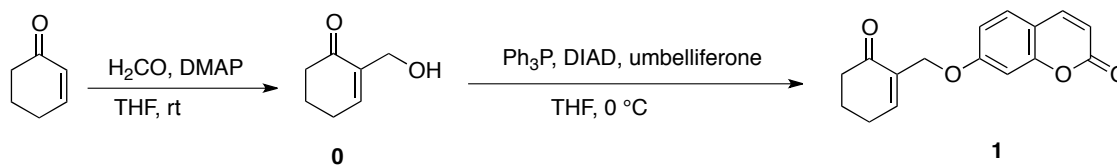
Semi-preparative RP-HPLC (Waters PrepLC4000):

Separations were carried out with a Dr. Maisch Reprospher C18-DE column (150 x 20 mm, 5 μ m particle size) using eluent A (water, 0.1 % TFA) and B (acetonitrile). The following method was used: flow rate 15 mL/min, UV detection at 254 nm; 0-3 min (70 % A, isocratic), 3-18 min (gradient 70 \rightarrow 20 % A).

Chiral phase GC (FID, Agilent 6890 Series):

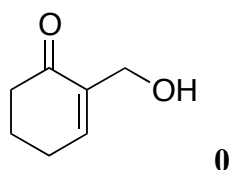
Separations were carried out on a Supelco- β -dex 120 (60 m x 0.25 mm, 0.25 μ m film thickness). The following method was applied: 0 - 30 min (70 $^{\circ}$ C, isothermal).

Substrate Synthesis



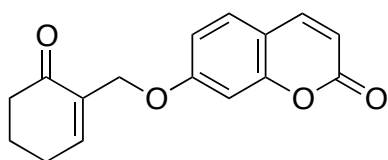
Supporting Figure 1: Two-step synthesis of substrate 1

Synthesis of Compound 0



The synthesis of alcohol **0** was carried out following a literature protocol.^[1] To a solution of 1-cyclohex-2-enone (14.9 g, 155 mmol) and 4-dimethylaminopyridine (DMAP, 1.83 g, 15 mmol) in 50 mL THF a 37 % aqueous formaldehyde solution (25.2 g, 310 mmol) was added and the mixture was stirred at room temperature for 20 h. To the brown solution, 1.5 N hydrochloric acid was added dropwise until the color of the solution turned red (final pH 2 - 4). The aqueous solution was extracted with 2x 100 mL DCM and washed with saturated bicarbonate solution and brine. The organic layer was dried with Na₂SO₄ before the solvent was evaporated at the rotavap. Silicagel flash chromatography with an eluent mix of EtOAc:Hex (2:3) yielded 10.5 g (55 % yield) of a yellow oil. NMR-Spectroscopy: ¹H-NMR (400 MHz, CDCl₃): δ 6.88 (1H, t, *J* = 4.2, H_{allyl}), 4.14 (2H, d, *J* = 1.4, CH₂), 3.17 (1H, bs, H_{alcohol}), 2.36 - 2.29 (4H, m, CH₂), 1.93 - 1.88 (2H, m, CH₂). ¹³C-NMR (400 MHz, CD₃CN): δ 200.4, 146.7, 138.2, 61.1, 38.1, 25.5, 22.6

Synthesis of Substrate 1

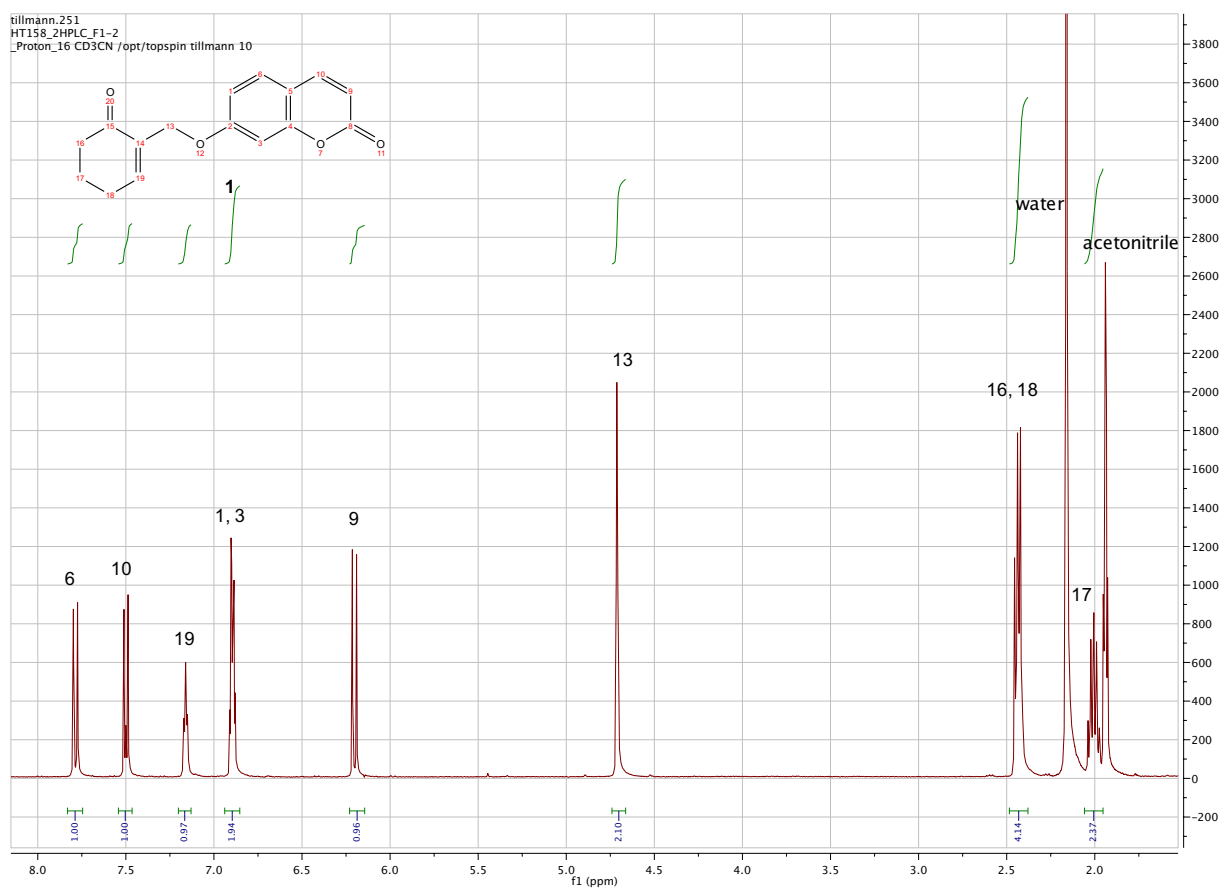


A 25 mL Schlenk flask was flame-dried under vacuum and flushed several times with nitrogen before adding umbelliferone (64.2 mg, 0.40 mmol) and triphenylphosphine (105 mg, 0.40 mmol), which were dissolved in 5 mL dry THF by stirring at room temperature. Next, alcohol **0** (50 mg, 0.40 mmol) was added and the solution was cooled to 0 °C on an ice bath. To start the reaction, diisopropyl azodicarboxylate (DIAD, 80.9 mg, 0.40 mmol) was added within 10 min to the colorless solution. After thirty minutes, the mixture was allowed to warm up to room temperature. The progress of the reaction was followed by reversed-phase HPLC, which indicated reaction completion after 2 hours. The reaction mixture was first separated by silicagel chromatography (EtOAc:Hex 1:2), which yielded a mixture of umbelliferone and substrate **1**. Pure compound **1** was obtained after additional purification by semi-preparative HPLC (see details above). Acetonitrile

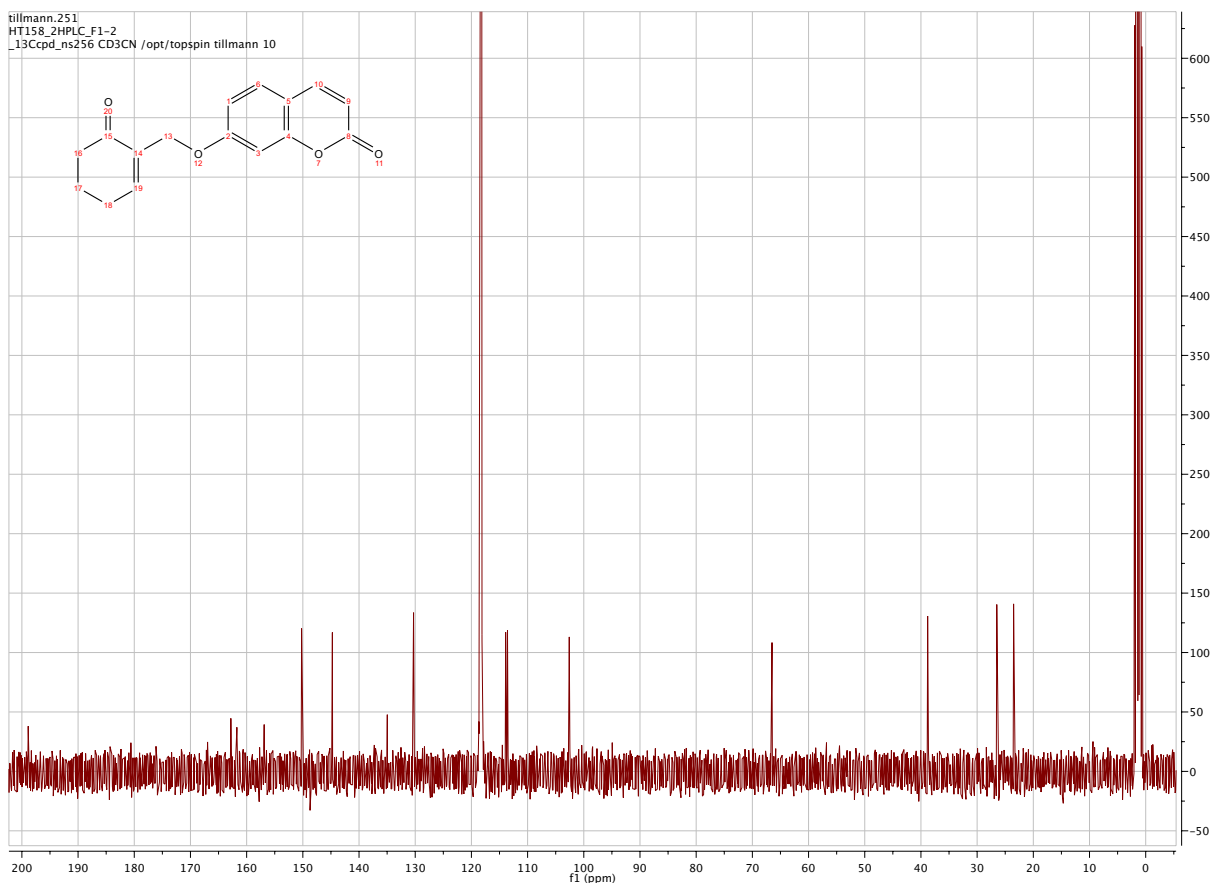
was removed under reduced pressure. The remaining aqueous solution was frozen in a liquid nitrogen bath prior to lyophilization overnight to yield a white powder of substrate **1** (48 mg, 45 % yield).

MS (ESI, positive mode, Bruker Micro-TOF): m/z 271.10 $[M + H^+]$, 293.1 $[M + Na^+]$ calculated mass for $C_{16}H_{14}O_4$ 270.09

1H -NMR (400 MHz, CD_3CN): δ 7.78 (1H, d, $J = 9.6$, H_{Ar}), 7.49 (1H, d, $J = 9.3$, H_{Ar}), 7.16 (1H, t, $J = 4.2$, H_{allyl}), 6.90 - 6.87 (2H, m, H_{Ar}), 6.20 (1H, d, $J = 9.5$, H_{Ar}), 4.70 (2H, d, $J = 1.4$, CH_2), 2.45 - 2.40 (4H, m, CH_2), 2.03 - 1.97 (2H, m, CH_2)



^{13}C -NMR (400 MHz, CD_3CN): δ 198.9, 162.8, 161.7, 156.9, 150.2, 144.7, 135.0, 130.3, 113.9, 113.6, 102.6, 66.5, 38.8, 26.5, 23.5



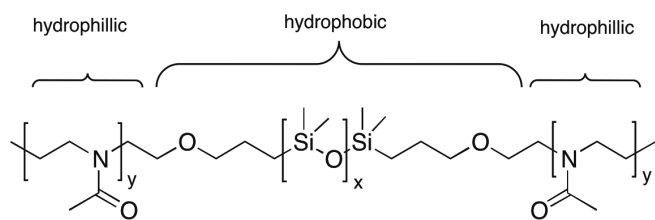
Synthesis of [Cp*Ir(Biot-p-L)Cl]

Complex [Cp*Ir(Biot-p-L)Cl] was synthesized according to Letondor et al.^[2]

Synthesis of PMOXA-β-PDMS-β-PMOXA (PMOXA₁₆-PDMS₇₂-PMOXA₁₆) block copolymer.

Poly(2-methyloxazoline)-*block*-poly(dimethylsiloxane)-*block*-poly(2-methyloxazoline) (PMOXA₁₆-PDMS₇₂-PMOXA₁₆) (**Supporting Figure 2**) block copolymer was synthesized by cationic ring opening living polymerization (CROP) according to the method.^{1,[3]}

¹ Langowska K.; Meier W.; 1st International Conference on Antimicrobial Research, Valladolid, Spain, November 3-5 2012: In situ synthesis of antibiotics inside nanoreactors. [online] <http://formatex.org/icar2010/acceptedabstracts.php> (accessed July 3, 2012)



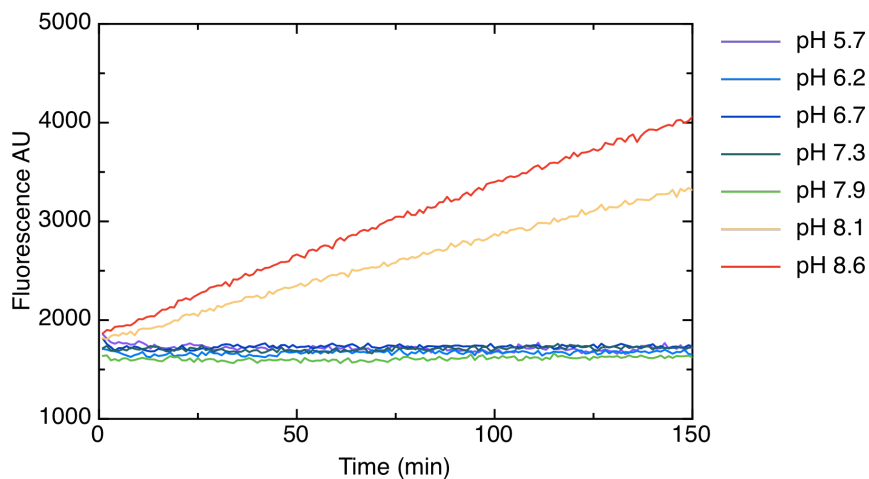
Supporting Figure 2: PMOXA- β -PDMS- β -PMOXA block copolymer.

Expression and Purification of Streptavidin Mutants

Sav mutants were expressed and purified as described in Humbert et al. and Klein et al.^{[4],[5]}

pH Stability of Substrate 1

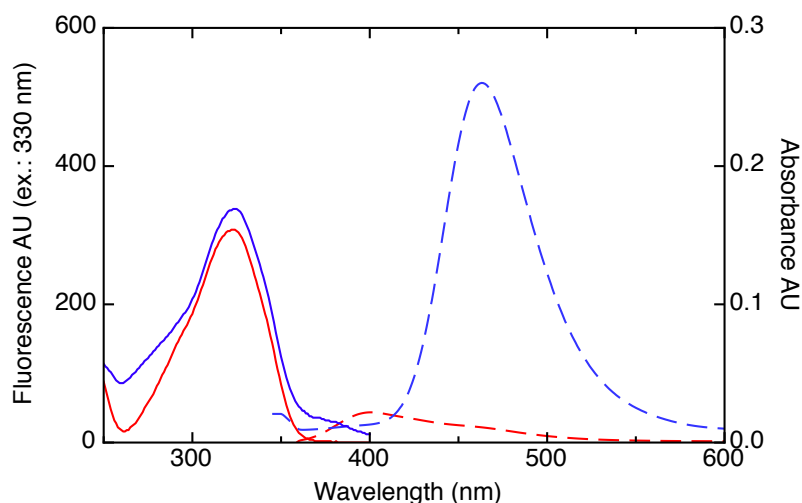
To determine the stability of the umbelliferone derivative **1** at different pH values, solutions of 50 μ M **1** in 100 mM MES (pH 5.7), 100 mM MES (pH 6.2), 100 mM MOPS (pH 6.7), 100 mM MOPS (pH 7.3), 100 mM MOPS (pH 7.9), 100 mM Tris (pH 8.1) and 100 mM Tris (pH 8.6) were prepared and the solution's emission at 470 nm ($\lambda_{\text{excitation}} = 323$ nm) was followed over time on a Tecan Safire plate reader (**Supporting Figure 3**).



Supporting Figure 3: pH stability of substrate **1**.

Determination of Absorption and Emission Maximum of Umbelliferone and Substrate 1

Stock solutions of umbelliferone and substrate **1** (10 mM in DMF) were diluted 1000x in 100 mM MOPS, pH 6.7 before measuring absorption (Shimadzu, UV-1800) and emission spectra (excitation wavelength 330 nm, on a Shimadzu, RF-5301PC) in a quartz cuvette (**Supporting Figure 4**).



Supporting Figure 4: Absorption (solid line) and fluorescence (dashed line) spectra of substrate **1** (red) and umbelliferone (blue)

General Procedure for Transfer Hydrogenation of 1 by ATHase

The following stock solutions were prepared: (I) 3 M sodium formate in 100 mM MOPS, pH 6.7, (II) 0.0275 mM tetrameric Sav mutant in 100 mM MOPS, pH 6.7, (III) 0.550 mM [Cp*Ir(Biot-*p*-L)Cl] in DMF, (IV) 0.2 mM substrate **1** in 10 % DMF and 100 mM MOPS, pH 6.7.

To prepare an ATHase stock solution of 50 μ M concentration (with respect to the biotinylated iridium complex), the stock solutions of Sav mutant (II) and of complex [Cp*Ir(Biot-*p*-L)Cl] (III) were mixed in the ratio 10:1 and were incubated for 10 min. Unless otherwise mentioned, reactions were carried out as following: In a 96-well black Nunc plate, 120 μ L stock solution I (1.44 μ M final formate concentration) were mixed with 5 μ L ATHase stock solution (final concentration of biotinylated iridium complex 1 μ M). The reaction was initiated by addition of 125 μ L substrate stock solution (IV) (final substrate concentration 100 μ M) and vigorous shaking of the 96-well plate in a plate reader (Tecan Safire). Fluorescence change was followed at 25 $^{\circ}$ C in 1 min intervals at excitation and emission wavelengths of 323 and 470 nm, respectively. Prior to measuring,

samples were shaken for 10 seconds. All samples were determined in triplicate.

Transfer Hydrogenation of 1 with Different ATHase Mutants

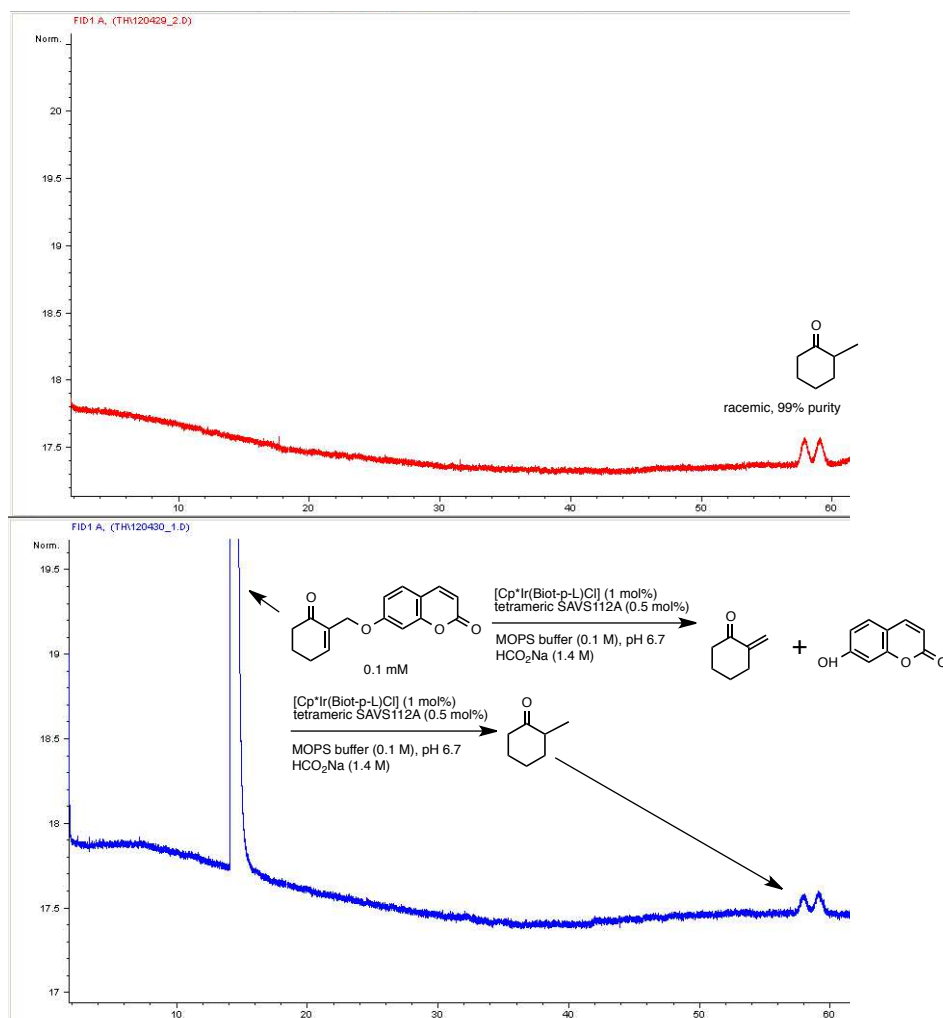
Supporting Table I: Initial rates of reactions of ATHase_{S112X-K121X} mutants with substrate **1** and conversion/turnover number of ATHase_{K121F}. The reaction conditions used were those described above using 1 μ M complex [Cp*Ir(Biot-*p*-L)Cl] and 0.5 μ M tetrameric Sav mutant.

Sav mutant	Initial rate (AU/min)
No ATHase	-7
WT	7.5
S112A	5
S112R	4
S112T	8
S112K	2
S112E	-5
S112F	13
S112L	1
S112V	7
S112Y	7
S112Q	-3
S112N	0
S112C	0
S112H	5
K121H	-5
K121D	1
K121A	22
K121R	13
K121F	147 ^a
K121Y	96
K121N	54

^aThe conversion (50%), corresponding to 50 turnovers, was determined using the HPLC method described in the general information. The response factor (1.1) between umbelliferone **3** and enone **1** at 323 nm was established using purified compounds **1** and **3**. The substrate conversion was then determined by integration of the peak areas of substrate **1** and product **3**. No other product could be

detected by ^1H NMR.

Characterization of Reaction Products by Chiral-Phase GC



Supporting Figure 5: A reaction in presence of ATHase_{S112A} was carried out as described above. For GC analysis of the reaction products, the reaction mixture was extracted with Et₂O and the organic phase was analyzed by chiral-phase GC as described above. Comparison of the chromatogram with that of pure racemic 2-methylcyclohexanone (red curve) indicates exclusive formation of (rac)-2-methylcyclohexanone in presence of ATHase_{S112A}.

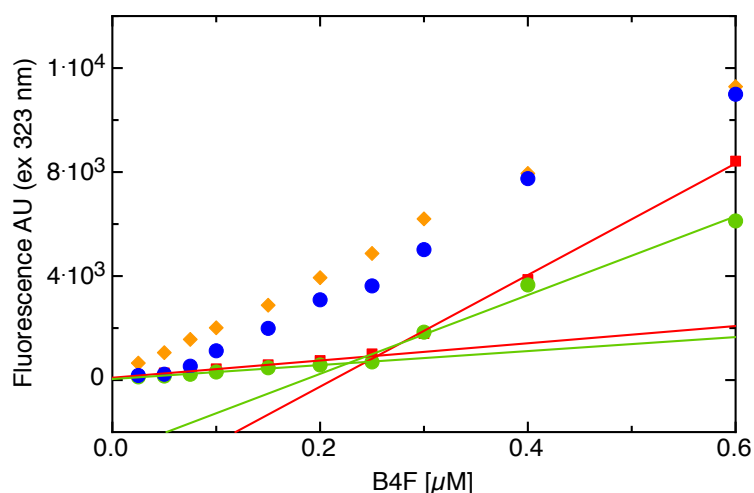
Preparation of Catalytic Nanoreactors

In a 10 mL flask 15 mg PMOXA₁₆-PDMS₇₂-PMOXA₁₆ polymer were dissolved in 1 mL EtOH using a vortex. If needed 200 μL OmpF stock solution (1.7 mg/mL in H₂O) were added to the suspension. Next, the suspension was connected to a rotavap and the EtOH was evaporated (40 $^{\circ}\text{C}$, 160 mbar) for 15 - 30 min. The pressure was then reduced to 70 mbar for another 30 min to remove water until a thin film remained at the bottom of the flask. To form the nanoreactors, 2 mL ATHase

solution (0.05 mM tetrameric Sav mutant and 0.1 mM complex [Cp*Ir(Biot-*p*-L)Cl] in 100 mM MOPS, pH 6.7) were added to the polymer film and the mixture was stirred for 12 hours after which the solution became turbid. The suspension was transferred into a dialysis tube (300 kDa cut off) and dialyzed against 3x 500 mL of 10 mM MOPS, pH 6.7, for 72 hours. Finally, the suspension was stored at 4 °C.

Control Experiments to Measure ATHase Adhesion on the Nanoreactor Surface

Because of the high affinity ($K_D < 10^{-14}$ M), the fast association and the non-cooperative binding of the fluorescent molecule biotin-4-fluorescein (B4F) to Sav, it is routinely used to determine the number of free biotin binding sites in Sav.^[6] To determine if residual streptavidin is present on the nanoreactor outer surface, 0.05 mM tetrameric Sav_{WT} were incubated with 2.0 eq. (0.1 mM) [Cp*Ir(Biot-*p*-L)Cl] in 100 mM MOPS buffer (pH 6.7) thus affording only half occupied streptavidin tetramers. Such tetramers are thus prone to bind up to two equivalents B4F. ATHase_{WT} was encapsulated in the presence and the absence of OmpF. After extensive dialysis, samples of nanoreactors were diluted 10x and were titrated with aliquots of B4F (0.025 – 2 μM) in 100 mM MOPS (pH 6.7). The fluorescence of the resulting samples was measured. All measurements were carried out in triplicate. After the first measurement, ATHase_{WT} nanoreactor was treated with 2 % triton X 100 for 2 days at 4 °C and the fluorescence measurement was repeated. Fluorescence quenching is detected in samples of nanoreactor in presence of pore OmpF highlighting B4F binding to streptavidin inside the nanoreactor (**Supporting Figure 6**). In absence of OmpF fluorescence quenching of B4F is only detected after preincubation of the nanoreactor with detergent for 2 days. This strongly supports the absence of streptavidin on the nanoreactor outer surface after extensive dialysis. As expected, the control experiment with 1 μM BSA did not yield any fluorescence quenching.



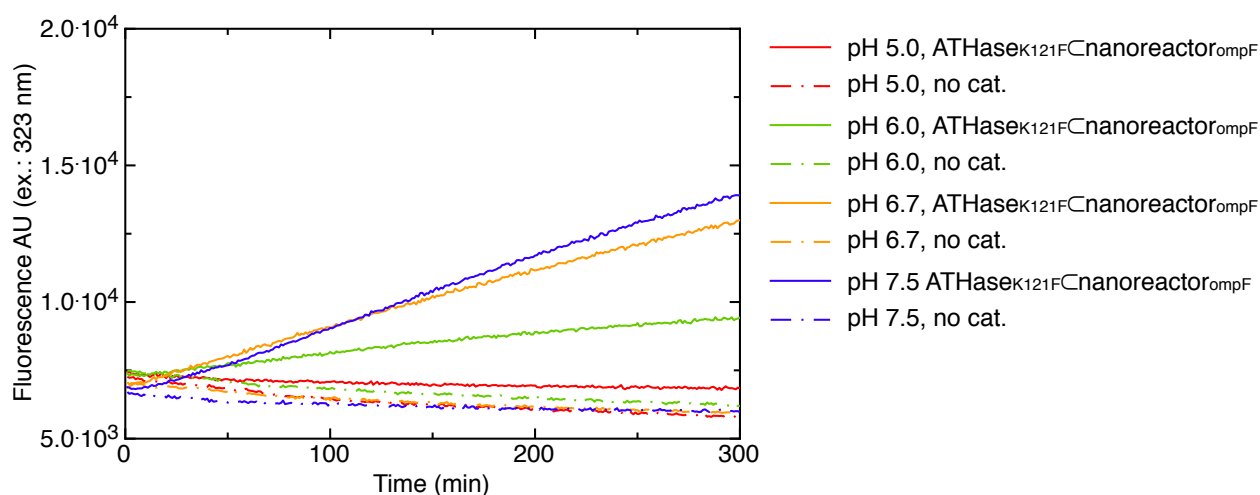
Supporting Figure 6: Investigation of nanoreactors for Sav binding on the outer surface by B4F titration in presence of: ATHase_{WT} nanoreactor_{OmpF} (green circles, molar ratio tetrameric Sav: complex [Cp*Ir(Biot-*p*-L)Cl] is 0.5:1.0), ATHase_{WT} nanoreactor (blue circles, molar ratio tetrameric Sav : complex [Cp*Ir(Biot-*p*-L)Cl] is 0.5:1.0), ATHase_{wild-Type} nanoreactor incubated in presence of 2 % triton X 100 for 2 days (red squares) and BSA (orange diamonds). Intersections of lines indicate saturation of streptavidin with B4F.

Determination of the Concentration of [Cp*Ir(Biot-*p*-L)Cl] Inside the Nanoreactors by ICP-MS

Samples of purified ATHase_{K121F} nanoreactor_{OmpF} and ATHase_{K121F} nanoreactor were analyzed by Solvias LTD by ICP-MS analysis. The iridium concentrations were 3.9/4.5 mg/kg (duplicate) (average: 22 μM iridium) and 1.4/1.4 mg/kg (duplicate) (7.3 μM iridium) for ATHase_{K121F} nanoreactor_{OmpF} and ATHase_{K121F} nanoreactor, respectively.

pH-Dependency of the Activity of ATHase_{K121F} Nanoreactor_{ompF}

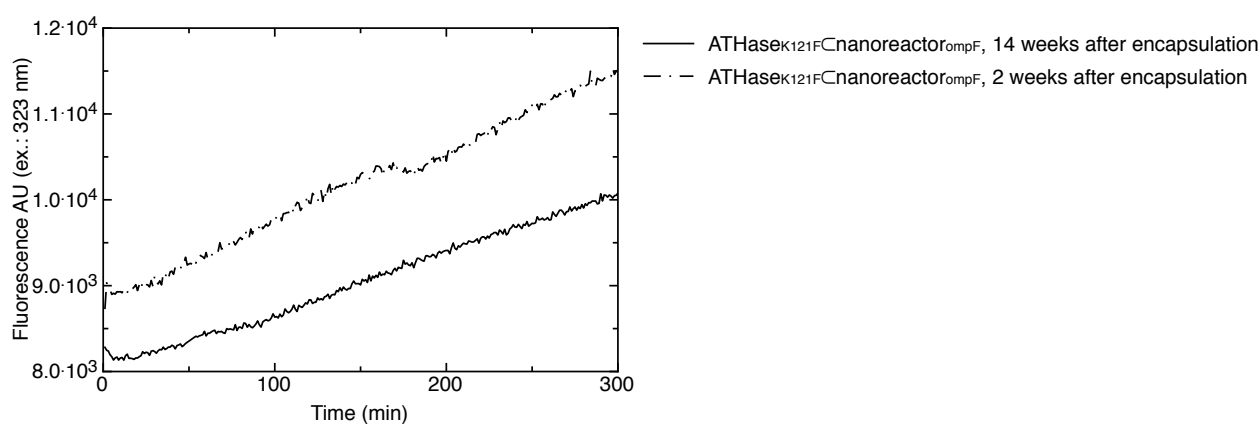
With *in vivo* applications of ATHase_{K121F} nanoreactor_{OmpF} in mind, the colorimetric assay was tested at pH 7.5 (to simulate cytosol), pH 6.0 (to simulate early endosomes) and pH 5.0 (to simulate late endosomes and lysosomes).^[7] Reactions were carried out as described in the general procedure using a final concentration of 2 μM (2 mol%) ATHase_{K121F} inside nanoreactor_{OmpF}. To adjust the pH, buffers using acetic acid (pH 5.0), MES (pH 6.0) and MOPS (pH 6.7 and 7.5) were used (**Supporting Figure 7**).



Supporting Figure 7: PH-dependency of reactivity of $\text{ATHase}_{\text{K121F}}\text{Cnanoreactor}_{\text{ompF}}$.

Stability of $\text{ATHase}_{\text{K121F}}\text{Cnanoreactor}_{\text{ompF}}$

To investigate the stability of the most reactive $\text{ATHase}_{\text{K121F}}$ inside the $\text{nanoreactor}_{\text{ompF}}$, the colorimetric activity was measured two weeks and 14 weeks after the encapsulation. The $\text{ATHase}_{\text{K121F}}\text{Cnanoreactor}_{\text{ompF}}$ was stored under aerobic conditions at 4 °C. Catalytic reactions were carried out as described in the general procedure using 1 μM (1 mol%) $\text{ATHase}_{\text{K121F}}$ in the $\text{nanoreactor}_{\text{ompF}}$.

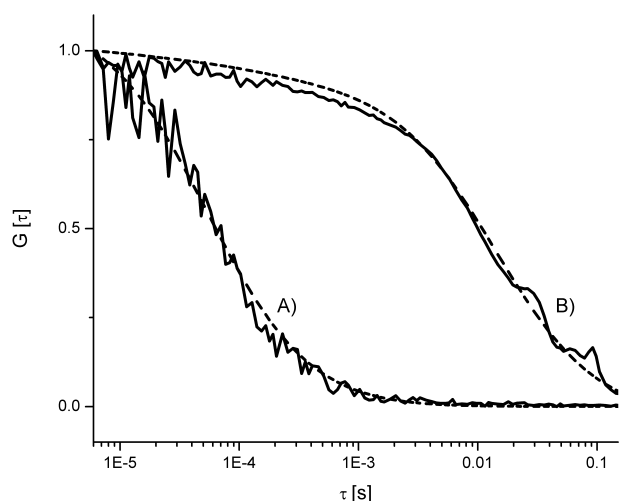


Supporting Figure 8: Stability of $\text{ATHase}_{\text{K121F}}\text{Cnanoreactor}_{\text{ompF}}$ under aerobic conditions.

Determination of the Hydrodynamic Radius of the Catalytic Nanoreactors by Fluorescence Correlation Spectroscopy (FCS)

Fluorescence correlation spectroscopy (FCS) measurements were performed at room temperature in special chambered quartz glass holders (Lab-Tek; 8-well, NUNC A/S), on a Zeiss LSM 510-META/ConfoCor2 laser-scanning microscope equipped with a Helium/Neon laser (543 nm) and a 40x water-immersion objective (Zeiss C/Apochromat 40x, NA 1.2), with pinhole adjusted to 78 μm . Spectra were recorded over 10 s, and each measurement was repeated 30 times. The excitation power of the HeNe laser was $P_L = 1 \text{ mW}$, and the excitation transmission at 543 nm was 5%. The diffusion time for the free dye (sulforhodamine B) was independently determined and fixed in the fitting procedure. The results were presented as a mean value of three independent measurements.

The encapsulation of a fluorescent dye was analyzed via fluorescence correlation spectroscopy. Laser-induced fluorescence of molecules passing through a small confocal probe volume auto-correlates over time and provides information on the diffusion time of the molecule, τ_D .^[8] Differences in diffusion times are related to changes in the hydrodynamic radius via the Stokes-Einstein relation, and permit the determination of interactions with larger assemblies such as the encapsulation in polymeric systems.^[9] The normalized FCS autocorrelation curves of dye-containing vesicle solutions were compared to those of free dye. (**Supporting Figure 9**) Significant differences in the diffusion times were obtained. While the diffusion time of the free dye was calculated to $47 \pm 7 \mu\text{s}$, the best fit of the autocorrelation function of the dye-containing vesicle solution, taking into account only one population, resulted in a clearly increased diffusion time of $10.8 \pm 1.6 \text{ ms}$. This points out that sulforhodamine B is most probably encapsulated inside the aqueous cavity of polymeric vesicles. The diffusion time was used in order to calculate the hydrodynamic radius of the free dye and the dye-encapsulated vesicles according to the Stokes-Einstein equation.^[10] The hydrodynamic radius of sulforhodamine B was evaluated to be $0.5 \pm 0.1 \text{ nm}$, which corresponds to the theoretical value of 0.6 nm calculated on basis of the molecular weight of the dye. For the measured vesicles, the hydrodynamic radius was determined to $126 \pm 19 \text{ nm}$. This is in good agreement with observations from TEM microscopy.



Supporting Figure 9: Normalized FCS autocorrelation curves of A) free sulforhodamine B and B) sulforhodamine B-encapsulated vesicles. Dotted lines are fitted curves.

Imaging the Cleavage of Substrate 1 Inside the Catalytic Nanoreactors by Fluorescence Microscopy

Fluorescent product formation by catalyst- and sulforhodamine B-encapsulated vesicles were imaged with a confocal laser scanning microscope (Zeiss LSM 510-META/Confcor2), in LSM mode, using the Laser Diode 405 (405 nm) with a power of 25 mW and 30 % transmission and a Helium/Neon laser (543 nm), power 1 mW, 28.5 % transmission, in combination with a 40x water-immersion objective (Zeiss C/Apochromat 40x, NA 1.2). Pinhole-, gain-, amplifier offset- and amplifier gain-settings were corrected for solvent-background and fixed for further measurements. The settings were crosschecked in order to exclude imaging artefacts.

20 μ L of the vesicle solutions were placed in special chambered quartz glass holders (Lab-Tek; 8-well, NUNC A/S) and the measurements of the samples containing catalyst-encapsulated vesicles as well as of vesicles without catalyst after addition of substrate respectively were performed at room temperature for duration of 90 min.

SI Bibliography

- [1] F. Rezgui; M. M. ElGaied; *J. Chem. Res.* **1999**, 576–577.
- [2] C. Letondor; A. Pordea; N. Humbert; A. Ivanova; S. Mazurek; M. Novic; T. R. Ward; *J. Am. Chem. Soc.* **2006**, *128*, 8320–8328.
- [3] C. Nardin; T. Hirt; J. Leukel; W. Meier; *Langmuir* **2000**, *16*, 1035–1041.
- [4] N. Humbert; A. Zocchi; T. R. Ward; *Electrophoresis* **2005**, *26*, 47–52.
- [5] G. Klein; N. Humbert; J. Gradinaru; A. Ivanova; F. Gilardoni; U. E. Rusbandi; T. R. Ward; *Angew. Chem. Int. Ed.* **2005**, *44*, 7764–7767.
- [6] G. Kada; H. Falk; H. J. Gruber; *Biochim. Biophys. Acta* **1999**, *1427*, 33–43.
- [7] C. Lafourcade; K. Sobo; S. Kieffer-Jaquinod; J. Garin; F. G. van der Goot; *PloS one* **2008**, *3*, e2758.
- [8] S. Litvinchuk; Z. Lu; P. Rigler; T. D. Hirt; W. Meier; *Pharm. Res.* **2009**, *26*, 1711-1717.
- [9] F. Axthelm; O. Casse; W. H. Koppenol; T. Nauser; W. Meier; C. G. Palivan; *J. Phys. Chem. B* **2008**, *112*, 8211-8217.
- [10] P. Zhang; L. Li; C. Dong; H. Qian; J. Ren; *Anal. Chim. Acta* **2005**, *546*, 46–51. J.

10.1. Author Contributions

General idea:

Thomas R. Ward

Synthesis of substrate:

Tillmann Heinisch, Jean-Louis Reymond

Activity screening of Sav mutants:

Tillmann Heinisch

Synthesis and characterization of polymer:

Karolina Langowska

Production of nanoreactors:

Tillmann Heinisch, Karolina Langowska

Transmission electron microscopy experiments:

Karolina Langowska

Fluorescence microscopy experiments:

Pascal Tanner, Tillmann Heinisch

Manuscript writing:

Tillmann Heinisch, Thomas R. Ward and all other authors

10.2. Comment on Publication

10.2.1. Compatibility of the Fluorescence Assay with *in Vivo* Conditions

The stability of quenched umbelliferone **6_1** in a cellular matrix was tested in an *E. coli* cell free extract which was resuspended in an aqueous buffer at pH 7.3. Shortly after addition of the substrate, fluorescence release was observed (**Figure M20a**). Cellular thiol compounds were suspected to react with the Michael-acceptor function of the substrate. To test this hypothesis, the substrate was added to an aqueous solution with 3 mM glutathione (the estimated concentration of glutathione in the cytosol of *E. coli* is 17 mM)¹⁰⁵ and buffered at pH 6.7. Indeed, a rapid increase in fluorescence was observed immediately after the start of the reaction (**Figure M20b**).

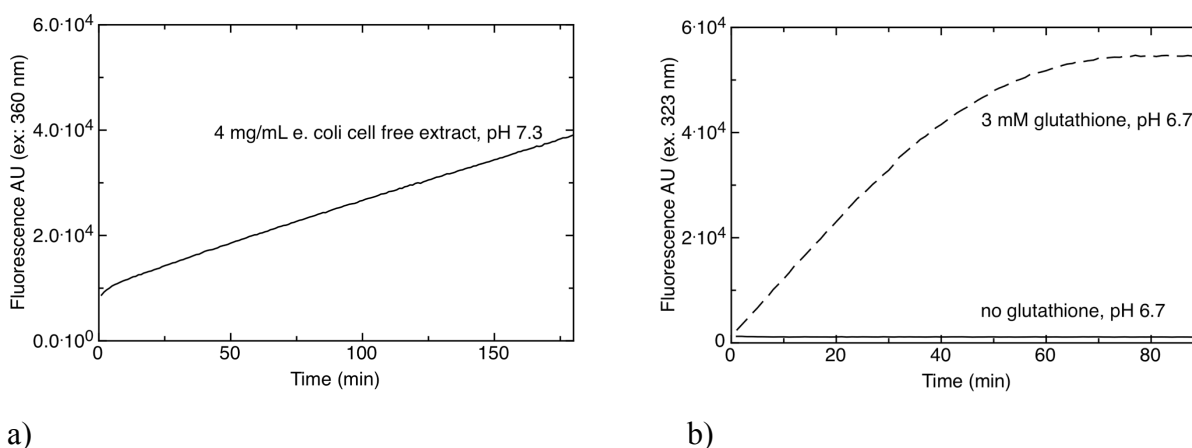


Figure M20: Stability of quenched umbelliferone **6_1** in *E. coli* cell free extract (a) and in presence of glutathione (b).

10.2.2. Outlook

Although we choose an artificial transfer hydrogenase developed in our group with high TON and TOF for encapsulation in PMOXA- β -PDMS- β -PMOXA type vesicles, in principal any AME can be encapsulated. The priority of future experiments will be the demonstration of *in vivo* activity of encapsulated AMEs. Towards this end, a substrate has to be developed together with an AME, which is bioorthogonal. For example, an encapsulated olefin metathesis AME could be used in conjunction with a non-fluorescent bis-olefin substrate that would become fluorescent upon ring-closing metathesis.⁴⁷

Moreover, in addition to the AME, other enzymes can be encapsulated to test the concept of reaction cascades in a nanoreactor.¹⁰⁶

The 1,4 addition of an enone by a ATHase was demonstrated for the first time in this work. This concept can be expanded towards other enones with multiple substitution patterns and functionalizations. Of special interest would be to test the potential of the ATHase in the ATH of enones.

VI Quantitative Model of a Streptavidin- $K_2[OsO_2(OH)_4]$ Crystal with an Ambiguous Packing Disorder

11. Introduction

The Bragg reflections scattered by a crystal lattice represent a time- and space-average of a multitude of different atomic positions within the crystal. Positional variation of molecules within the crystal is not expressed in the diffraction pattern as long as it does not affect the periodicity of translation of individual unit cells. Once the periodicity is altered or broken, it is manifested by an increased symmetry of the crystal lattice (e.g. indication for merohedral twinning), the presence of satellite reflections next to the Bragg reflections (indication for alternative unit cells) or by diffuse spots (indication for non-periodic disorder).¹⁰⁷ Although the crystallization of most small molecules and proteins can be achieved without significant packing defects, pathological crystals exist for which, in order to solve the structure, it is essential to understand and model the packing disorder.^{108,109} In this study, upon soaking an apo-Sav crystal with $K_2[OsO_2(OH)_4]$, problems were encountered in structure solution, which were traced back to an incommensurate crystal packing disorder.

12. Experimental Part

Sav Crystallization and $K_2[OsO_2(OH)_4]$ Soaking:

Purified wild type Sav (a construct with the 12 N-terminal residues of native Sav replaced for a T7-tag) was crystallized by the sitting-drop vapor-diffusion technique within one week. A volume of 0.2 μ L of a protein stock solution (15 mg/mL in water) was mixed with 0.2 μ L of crystallization buffer (0.2 M magnesium acetate, 30 % PEG 3350, pH 7.5). The flat, square-shaped crystals were soaked for 1 h in 10 μ L of an osmium solution (10 mM $K_2[OsO_2(OH)_4]$, 0.2 M magnesium acetate, 30 % PEG 3350, pH 7.5). After the soaking, crystals were shock-frozen in liquid nitrogen.

X-ray Data Collection:

Diffraction data were collected at the Swiss Light Source beam line PX3 at a wavelength of 0.9793 Å at 100 K to a resolution of 2.4 Å. Reflection sampling was carried out on a CCD detector at a ϕ -slicing resolution of 1° per image.

Data Indexing, Processing, Molecular Replacement and Structure Refinement:

The diffraction data was indexed and processed using software MOSFLM (ccp4 suite). Program POINTLESS (ccp4 suite) was consulted for analysis of the crystal lattice and space group determination. The integrated reflections were merged and truncated using software SCALA and TRUNCATE (both ccp4 suite), respectively. Molecular replacement was carried out with MOLREP (ccp4 suite) and rigid body, as well as full atomic refinement with program REFMAC 5 (ccp4 suite). Program O was used to illustrate the crystal packing and the electron density distribution. Diagrams were drawn with PROFIT.

13. Results and Discussion

Data Processing in P1 and Analysis of Crystal Lattice:

The reflections were indexed in space group P1 with the unit cell dimensions being very close to those of a cuboid (a virtually the same as b; α , β and γ close to 90°, **Table M3**). Inspection of the indexed reciprocal lattice indicated sharp reflections on lattice planes orthogonal to c^* (**Figure M27**). In contrast, diffuse reflections were observed along c^* , e.g. on lattice plane $[-2\ k\ 1]$. The observation of diffuse reflections along c^* will be rationalized later in this chapter.

After integration of the reflections in P1, analysis of the crystal lattice with POINTLESS revealed two 2-fold symmetry axes along the two diagonals of the a,b-face of the P1 cell and an additional 2-fold axis along c. These observations indicated the presence of a Cmmm space group.

Merging of Reflections in P1,C222 and C2:

To find the correct space group, the P1-processed data were reprocessed and scaled in all space groups that correspond to Cmmm (**Table M3**, C222₁ not shown). Note that the assignment of the crystallographic axis in C2 can be either along $[1\ 1\ 0]$ (C2a) or $[-1\ 1\ 0]$ (C2b) with respect to the triclinic cell. Scaling in C2a gave slightly better statistics.

Table M3: Statistics of data processing and merging of different space groups compatible with the osmium-soaked Sav crystal.

	P1	C222	C2a	C2b	C2 (2bc3)
Space Group	P1	C222	C2	C2	C2
a	57.46	81.20	81.20	81.60	81.70
b	57.66	81.60	81.60	81.20	82.39
c	91.50	91.50	91.50	91.50	46.71
α	89.90	90	90	90	90
β	89.73	90	90.26	90.12	103.48
γ	90.28	90	90	90	90
R_{sym}		0.109	0.095	0.104	
I/s(I)		8.4	6.7	5.6	
Multiplicity		4.6	2.7	2.5	
N_{ref}		7154	11926	12889	

The Molecular Replacement Model and Native Patterson Map:

First, molecular replacement in the highest symmetry space group C222 was carried out. As a search model, the Sav dimer (half of one Sav homotetramer) in the asymmetric unit of the structure with pdb code 2bc3 was used. The search model crystalized in a monoclinic C2 cell with the lengths of axes a and b, as well as the angles α and γ being virtually identical to the corresponding axes and angles in the C222 cell (**Table M3**). In 2bc3, the crystallographic dyad along b is identical with the local 2-fold axis r that relates the two monomers of the dimer in the AU (**Figure M21a, Figure M23a and b**). Application of the local dyad q, which is close to parallel to a, constitutes the Sav tetramer. Alternatively, the Sav tetramer can be formed by application of the rotational symmetry along the local 2-fold axis p, which is virtually orthogonal to a and b. In the a,b-plane, neighboring Sav tetramers form c-centered layers (**Figure M21b**). Neighboring layers span an angle equal to unit cell angle β with the a,b-plane. The relative translation in b-direction, $\pm\Delta b$, of successive layers can be calculated as

$$\Delta b = c * \sin(\beta \pm 90^\circ) = 46.7 \text{ \AA} * \sin(103.5^\circ \pm 90^\circ) = \pm 10.5 \text{ \AA}$$

In fractional coordinates, this is equal to $\Delta y = \pm 0.13$. The translation vector of successive layers in all three dimensions is (0.00 0.13 0.50).

A strong (12 σ) pseudo-origin peak with coordinates (0.00 -9.28 45.75) was detected in the native Patterson map of the C222 cell. This corresponds to the fractional coordinates (0.00 0.11 0.50), which are virtually identical to the translation vector of two successive layers in the search model. This observation and the similarities of the crystallographic c-faces, strongly suggest an identical packing of successive a,b-layers in the crystal 2bc3 and the osmium-soaked crystal. However, the Bragg reflections of the osmium-soaked crystal did not allow the indexing in C2 with the same unit cell dimensions as the search model 2bc3.

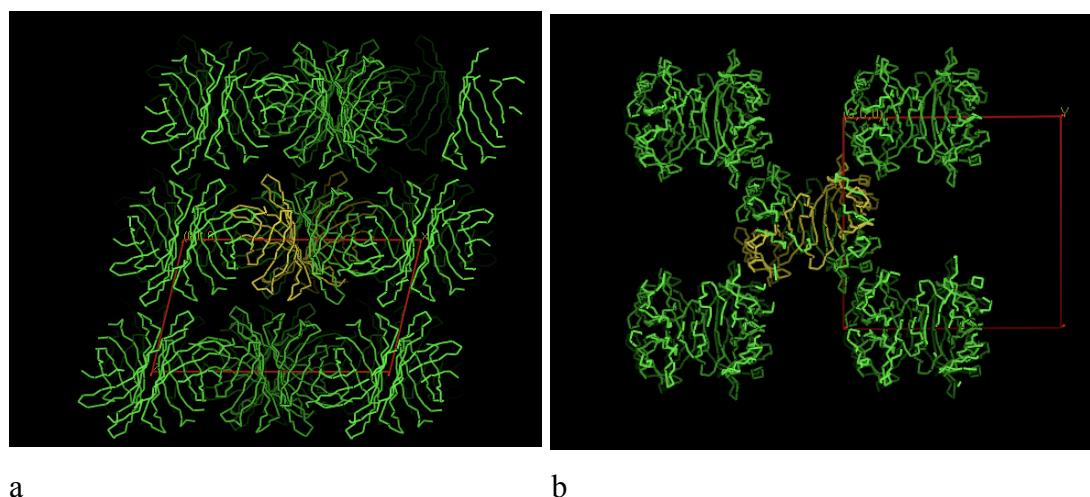


Figure M21. Crystal packing of streptavidin structure with pdb code 2bc3 (space-group C2). a) Representation of b-face with view along b (a horizontal). b) Representation of c-centered face with view along c (b horizontal).

Molecular Replacement in C222:

As expected from the volume of the C222 cell and a number of eight AUs in the unit cell, a Sav dimer was found in the MR search procedure. Besides axes a and b, that are exchanged in C222 relative to the search model, the c-face is equally organized in both crystals. However, due to the doubled length of axis c (**Figure M23c**), the unit cell accommodates two a,b-layers (layer I and II), which are related by a crystallographic 2_1 -axis along c. The dimer in the asymmetric unit can be transformed into a tetramer by application of the crystallographic dyad along b (equal to local q axis), the crystallographic dyad parallel a (equal to local r axis) and the local 2-fold rotation axis parallel c (equal to local p axis, **Figures M22a and b and Figure M23c**). Since the orientations of axes c and

p are virtually identical (0.55°), the same is true for the orientation of layers I and II. Thus, application of the 2_1 -screw symmetry along c is virtually identical to a translation of a Sav dimer along vectors $\pm t$, which correspond to the pseudo-translation peak in the native Patterson map and the orientation of the c axis in the search model.

Rigid body refinement of the crystal in C222 converged at a relatively high value of R_{free} of 40 %. Molecular Replacement (MR hereafter) in C222₁ did not yield a solution. For this reason the MR and refinement procedures were repeated in lower symmetry space group C2a.

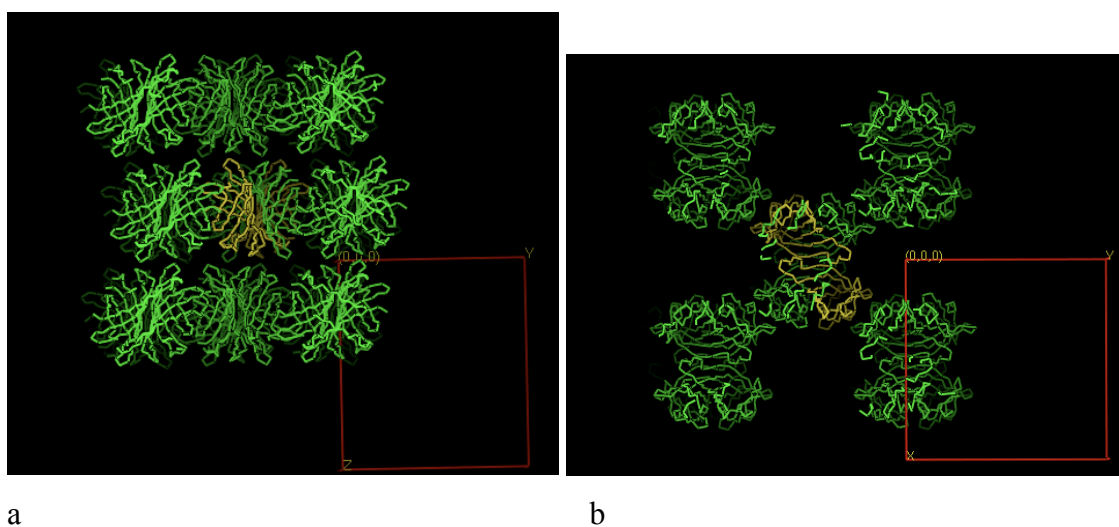


Figure M22. Crystal packing of osmium-soaked Sav crystal (space-group C222). a) Representation of a-face (b horizontal). b) Representation of c-centered face with view along c (b horizontal). Note: molecular axis q (horizontal) is congruent with crystallographic dyad in b direction ($z=1/4$), see also **Figure M23c**.

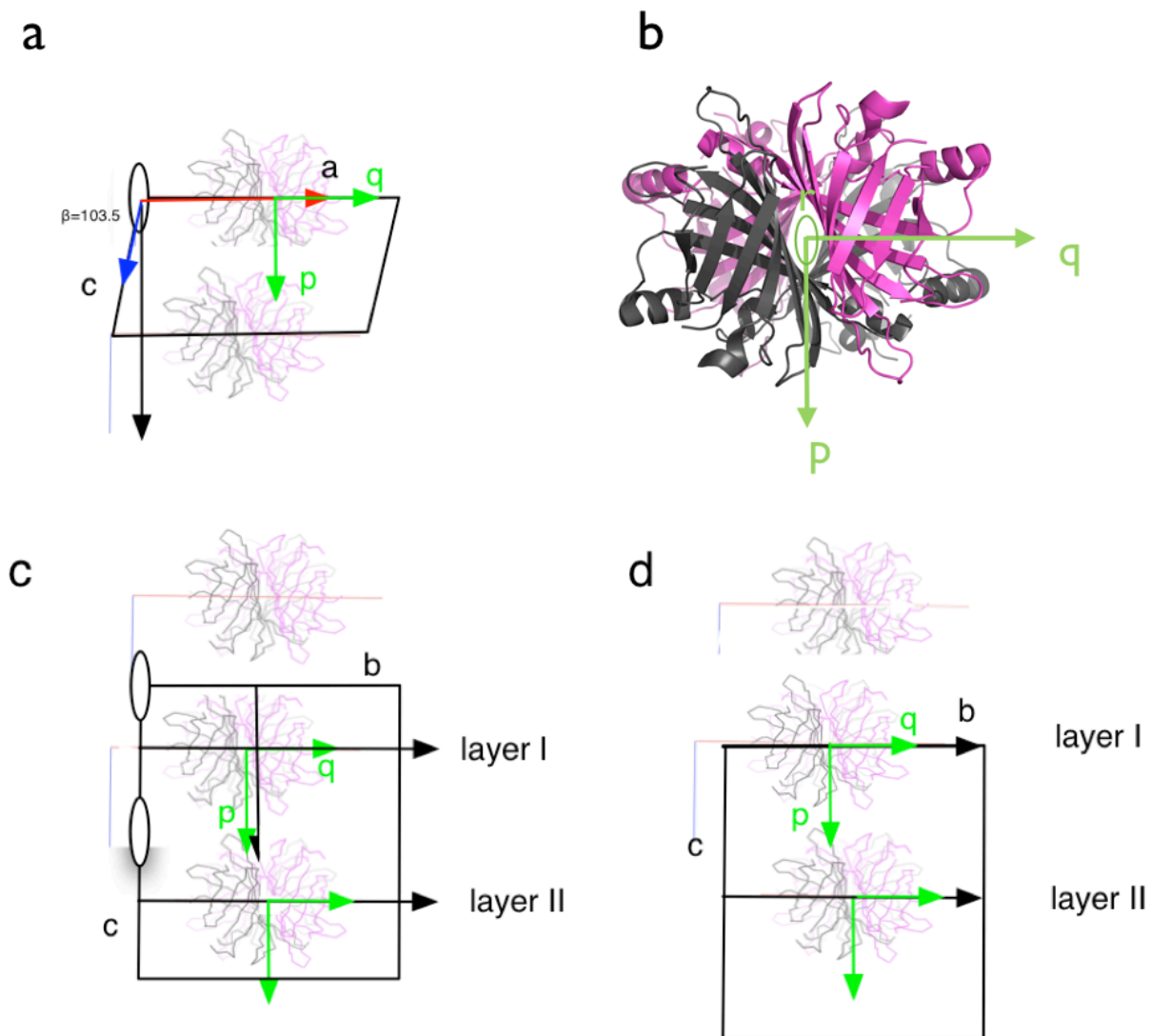


Figure M23: Locations of local (green color, see panel b for axes' definition) and crystallographic (black color) symmetry axes in 2bc3 (a), C222 (c) and C2 (d). 2-fold rotational symmetry axes are shown as arrows and ellipses, 2_1 -screw symmetry axes are shown as half-arrows.

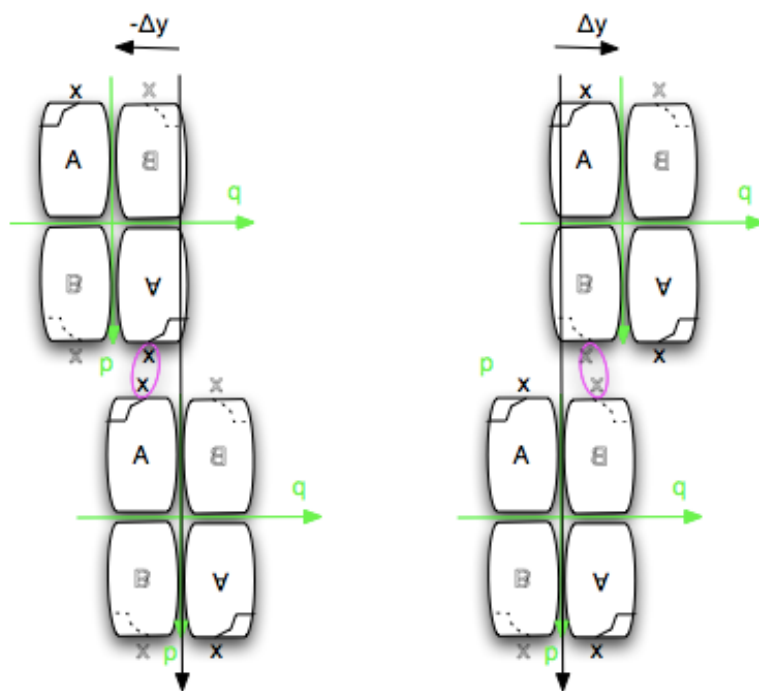


Figure M24: Ambiguity of stacking of successive a,b-layers of Sav tetramers (barrels) in $\pm\Delta b$.

Molecular Replacement in C2 and Ambiguous Packing Disorder:

When reducing the symmetry from C222 to C2a, all crystallographic symmetry axes along a and c become local symmetry axes. Sav tetramers in layer I and II are not anymore related by a 2_1 -screw axis along c. Instead, the volume of the AU is doubled and accommodates two Sav dimers, one in layer I and a second in layer II. Here, a packing ambiguity occurs in layer II, since the second dimer can be located either in position (0.00 0.11 0.50) or (0.00 -0.11 0.50) (**Figure M24**). To proof this, a search procedure to find the dimer position in layer II with the lowest R-factor was carried out by rigid body refinement (**Figure M25**). Indeed, two clear minima were found in positions (0, 9.31, 45.75) (ghosta) and (0, -9.31, 45.75) (ghostb).

To investigate the average relative abundance of the two dimers in positions (0, 9.31, 45.75) and (0, -9.31, 45.75) throughout the whole crystal, the occupancy with the minimum R-factor was determined (**Figure M26**). For each dimer in position (0, 9.31, 45.75) and (0, -9.31, 45.75), a minimum was detected at an occupancy of 0.2 (the dimer in layer I was set to 100 % occupancy). However, a model including both dimers with each an occupancy of 0.2 in layer II and one dimer with 100 % occupancy in layer I yielded a

significantly worse R-factor. This could be due to the technical problem of excluding intermolecular interactions (between the dimers in layer II) in the refinement procedure.

In summary, the rigid body search procedure for the optimal position and occupancy of the Sav dimer in layer II of the AU of the monoclinic unit cell yielded two equivalent solutions and confirms the hypothesis of an ambiguous disorder of the packing of successive a,b-layers.

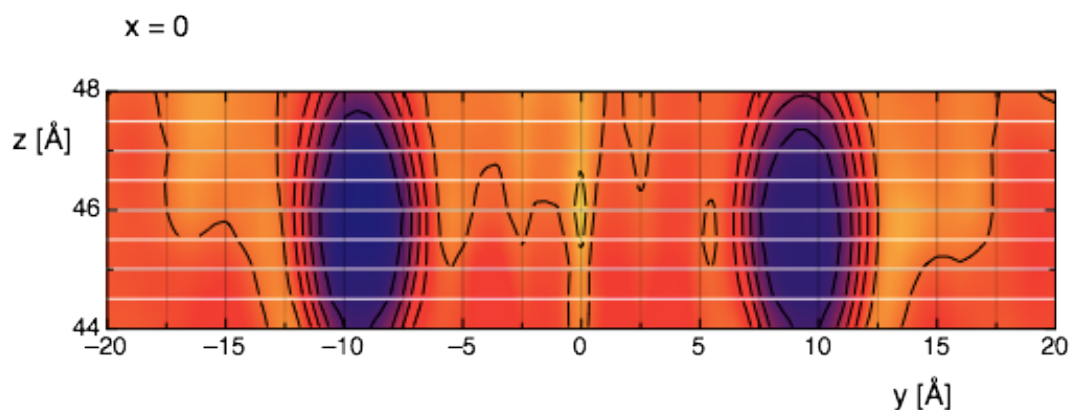


Figure M25. R-factor search for position of dimer in layer II with fixed dimer in layer I (at 100 % occupancy) with rigid body refinement. Blue color represents low and red high R-value.

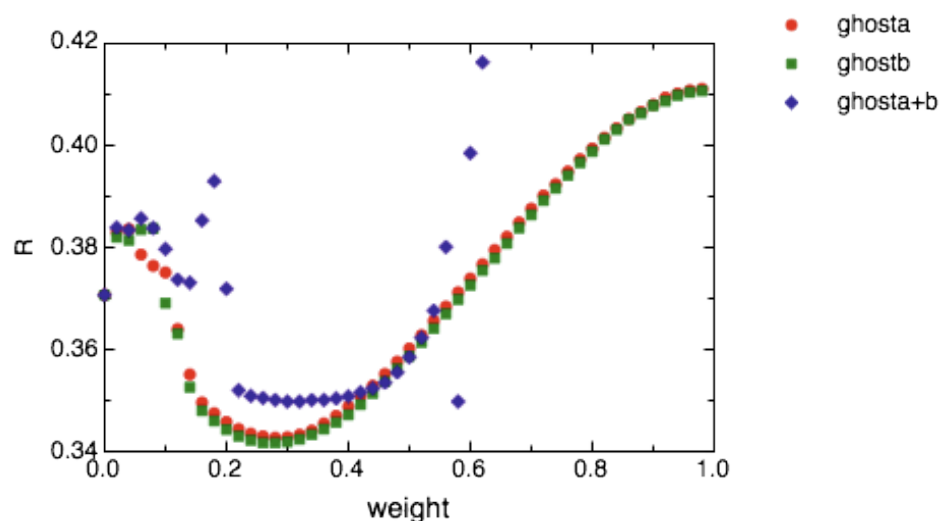
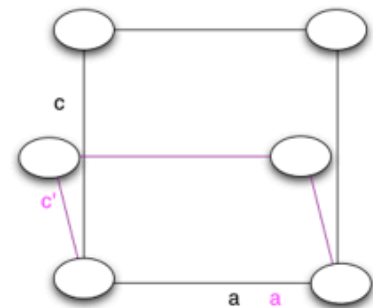
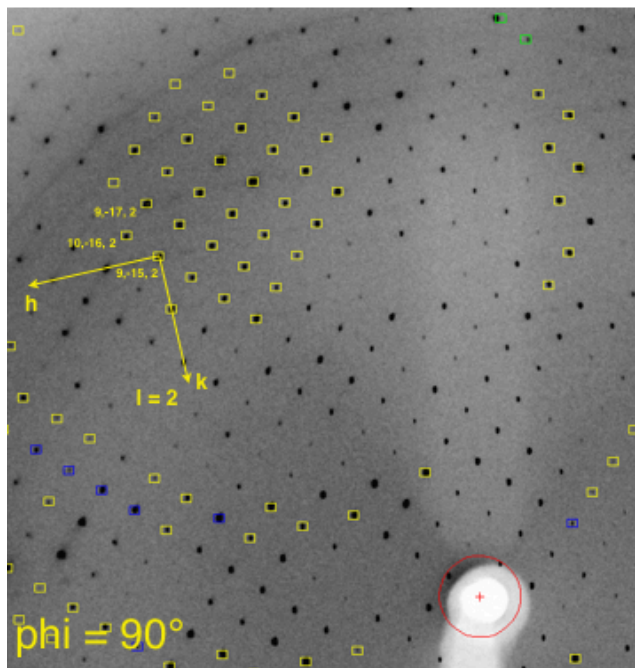
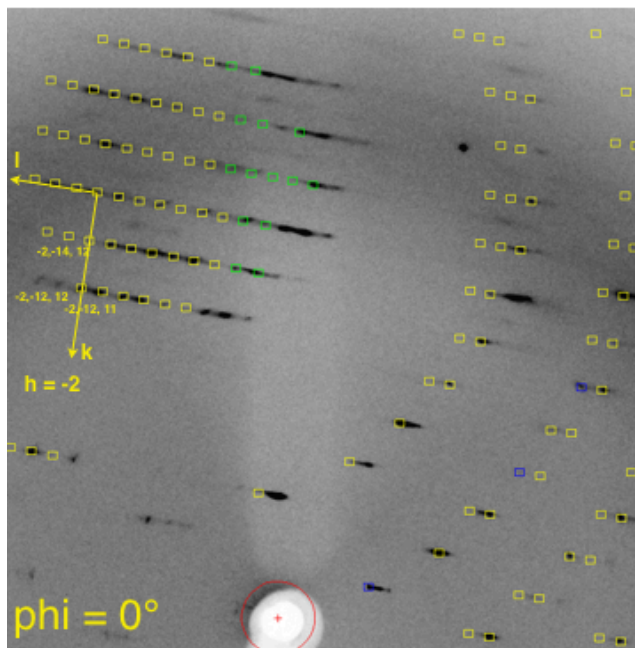


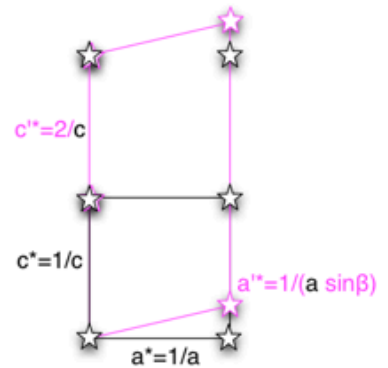
Figure M26. R-factor search for occupancy of dimer in layer II with fixed dimer in layer I (at 100 % occupancy) with rigid body refinement. Dimers in layer II were positioned at the optimal positions that are as given in **Figure M25** (Ghosta: $x,y,z=0, 9.31, 45.75$ Å; ghostb = $0, -9.31, 45.75$; ghosta+b: both positioned).

Diffuse Scattering:

With the physical model of an ambiguous Sav dimer displacement along b at hand, the diffuse reflections in the reciprocal lattice can be rationalized. As a consequence of the displacement, two unit cells with different angles β can be drawn which show a displacement of the reflections in the reciprocal space along c^* (**Figure M27, right panel**). Indeed, diffuse reflections in the reciprocal lattice are observed exclusively along c^* (**Figure M27, left panels**).



$$\begin{aligned} c/2/c' &= \cos(\beta-90) = \sin \beta \\ c/2 &= c' \sin \beta \end{aligned} \quad (I)$$



$$\begin{aligned} \text{in general: } c^* &= 1/(c' \sin \beta) \quad (II) \\ (I) \text{ in } (II) \quad c^* &= 2/c \end{aligned}$$

Figure M27: (Left panels) Photographs of the reciprocal space layers $[-2 k I]$ (upper

panel) and [h k 2] (lower panel). Reflections are diffuse only in c^* direction. (Right panel) Representation of $2bc3$ cell (pink) and $C222/C2$ cells of osmium-soaked crystal (black) in the real (upper panel) and the reciprocal space (lower panel). Displacement of layer II in $\pm\Delta b$ yields displacement of reflections in $\pm\Delta c^*$ in the reciprocal space.

Quantitative Model of Ambiguous Crystal Packing Disorder:

The displacement in fractional coordinates of an a,b-layer n_i relative to its next neighbors, $n_{i\pm 1}$, is $(0.00 \pm 0.11 \pm 0.50)$. Since y is not an integer multiple of the displacement Δy (± 0.11), the packing disorder is incommensurate. Given there is an incommensurate ambiguity of packing of successive layers, the question arises, how is the system forming packing periodicity in direction b as is observed by the Bragg reflections along c^* in the reciprocal space?

The probability of a layer n_i ($i=1,2,3,\dots$) of a population of N successive a,b-layers to be located in either $(0.00 \ 0.11 \ 0.50)$ or $(0.00 \ -0.11 \ 0.50)$ relative to layer n_{i-1} is given by the Pascal triangular. Layer positions in proximity to the symmetry axis of the triangular have the highest probabilities. To test whether the packing of the osmium-soaked crystal can be described by the probability distribution of the Pascal triangular, the probabilities of the dimer positions within an average unit cell were calculated given that the sum of probabilities equals one over all possible positions in one layer (**Figure M28**). Dimer locations of maximum probability are indeed found at the origin of the cell and at the end points of vectors $(0.00 \ 0.11 \ 0.50)$ and $(0.00 \ -0.11 \ 0.50)$. This is in accordance with the results from the native Patterson map and the rigid body refinement. Moreover, the occupancies with minimal R-factor of the molecules in positions $(0.00 \ 0.11 \ 0.50)$ and $(0.00 \ -0.11 \ 0.50)$ as found by rigid body refinement (**Figure M26**) and the Pascal triangular-probabilities of molecules in the same positions have almost the same value (0.200 and 0.235, respectively). Thus, the positional probability distribution of Sav molecules in the unit cell as given by the Pascal triangular is a good quantitative model of the average a,b-layer distribution in the crystal and explains the formation of packing periodicity in b direction and Bragg (as well as diffuse) reflections along c^* in the reciprocal space.

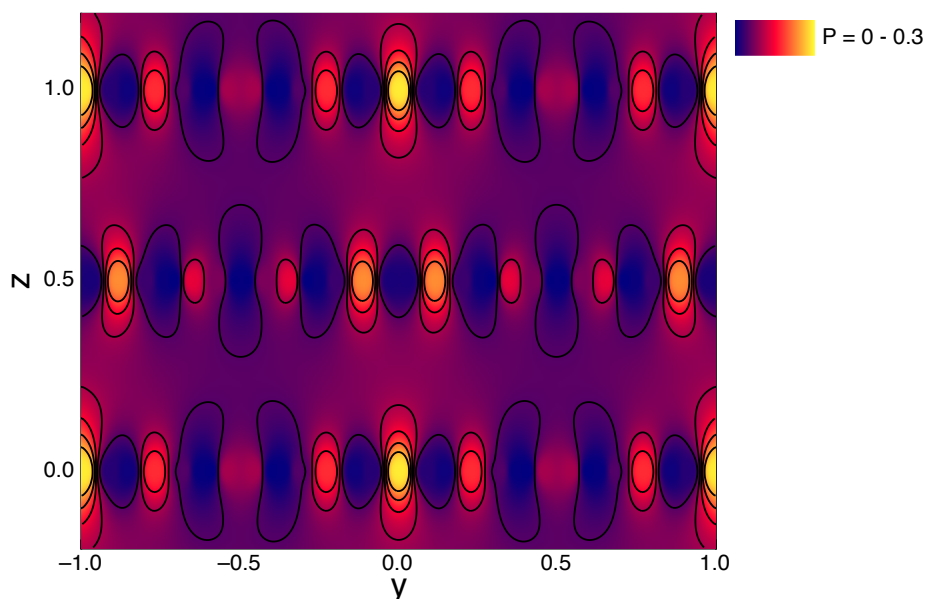


Figure M28: Representation of the probability distribution (colors blue to yellow) of different locations of Sav in the monoclinic unit cell according to the Pascal triangular. The total probability in each layer I ($0 \leq y < 1$, $z=0$) and II ($0 \leq y < 1$, $z=0.5$) equals one.

Structure Solution in C2:

With no other method at hand, the structure was solved in C2 with only one dimer in layer I and an empty layer II (Table M4). Pronounced electron density in the $2|F_o|-|F_c|$ map was only found in layer I (Figure M29a). The overall structure of the Sav tetramer is the same as in 2bc3. However, 24 residues at the C-terminal end are not resolved in the electron density, probably due to high flexibility. The two biotin-binding pockets in the AU are empty. Positive electron density in the $|f_o|-|f_c|$ map was apparent in proximity to the side chain-nitrogens of residues His127, His80, Lys132 and Lys80. Furthermore, in the same positions anomalous scattering density peaks were found. Since the wavelength of 0.9793 Å of the data collection is close to the L-I absorption edge of osmium and with an osmium- f'' of 11-12 e^- , the anomalous density peaks can be attributed to osmium binding. This is in accordance with the electron donor and metal coordinating properties of the side chain nitrogens $N\epsilon$ and $N\zeta$ of His and Lys, respectively. Indeed, Os could be modeled in the four positions.

When filling up layer II with either of the two dimers in position (0.00 0.11 0.50) or (0.00 - 0.11 0.50), the osmium, which is coordinated to the side chain of His87, is located in the interface of two layers I and II (Figure M29b). In the search model 2bc3, this position is occupied by a SO_4^{2-} from the buffer solution.

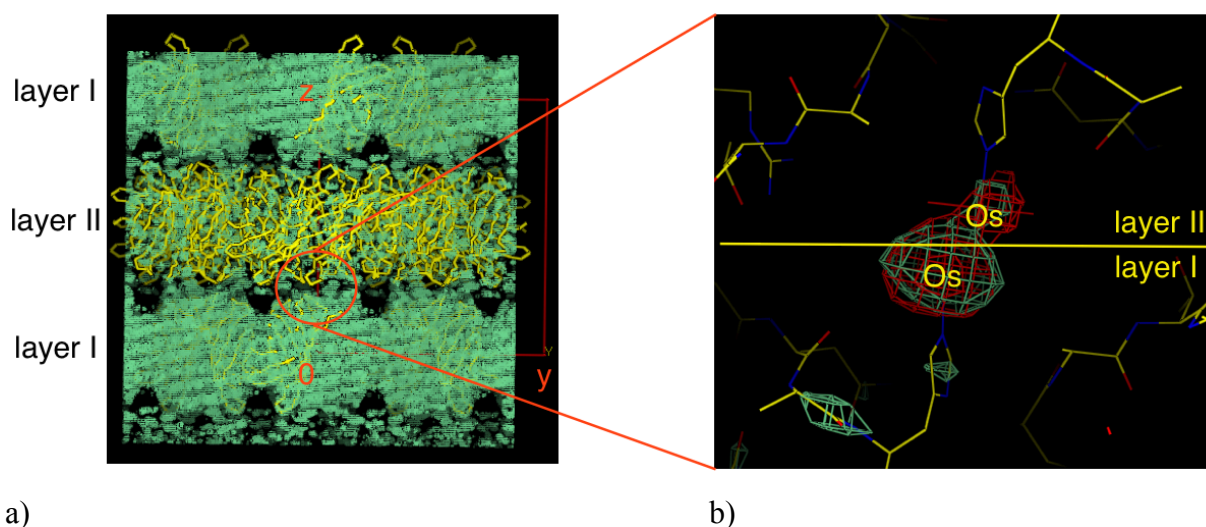


Figure M29: Representation of $2|F_o|-|F_c|$ electron density map (aquamarine, at 3σ in a and at 4.1σ in b) and anomalous difference density map (red, at 3.2σ) of the structure of the osmium-soaked Sav crystal solved in the C2 unit cell. Layer I is contoured much stronger than layer II by the $2|F_o|-|F_c|$ map (a). Osmium atoms are bound next to His87 in the interface between layer I and II (b).

Table M4: Structure refinement of the monoclinic unit cell (C2a) with only one dimer in the AU.

	R	R_{free}	rmsd bonds (Å)
MR (10-4 Å)	44.6 %		
Rigid body refinement (10-4 Å)	39.4 %	35.7 %	
Full atom refinement (10-2.4 Å), r1	30.6 %	32.9 %	0.019
r2 (with TLS)	29.7 %	30.9 %	0.019
r3 (with TLS)	29.8 %	30.6 %	0.014

14. Summary

In summary, the pathologic observations of an osmium-soaked Sav crystal with respect to i) diffuse scattering along c^* , ii) a pseudo-origin peak in the native Patterson map and iii) the problematic rigid body and full refinement could be rationalized by an incommensurate ambiguous crystal packing disorder. The time and space average of the osmium-soaked Sav crystal is best represented by a unit cell with C2 symmetry and two Sav dimers in the AU. One Sav dimer in the AU is located within the c-centered layer I. The second dimer can occupy two positions in layer II with equal likelihood. Using the probability distribution of the Pascal triangular, a quantitative model of the average crystal packing could be derived, that correctly predicts the positions of layers I and II.

VII Bibliography

- (1) Eriksson, T.; Björkman, S.; Roth, B.; Höglund, P. *J. Pharm. Pharmacol.* **2000**, *52*, 807–817.
- (2) *Comprehensive Asymmetric Catalysis, Vol. I-III*; Jacobsen, E. N.; Pfaltz, A.; Yamamoto, H., Eds.; 1. ed.; Springer: Heidelberg, 1999.
- (3) Fersht, A. *Structure and Mechanism in Protein Science: A Guide to Enzyme Catalysis and Protein Folding*; 1. ed.; W. H. Freeman, 1998.
- (4) Lippard, S. J.; Berg, J. M. *Principles of Bioinorganic Chemistry*; 1. ed.; University Science Books: Mill Valley, CA, 1994.
- (5) Andreini, C.; Bertini, I.; Cavallaro, G.; Holliday, G. L.; Thornton, J. M. *J. Biol. Inorg. Chem.* **2008**, *13*, 1205–1218.
- (6) Heinisch, T.; Ward, T. R. *Curr. Opin. Chem. Biol.* **2010**, *14*, 184–199.
- (7) Reetz, M. T. *Top. Organomet. Chem.* **2009**, *25*, 63–92.
- (8) Abe, S.; Ueno, T.; Watanabe, Y. *Top. Organomet. Chem.* **2009**, *25*, 25–43.
- (9) Rosati, F.; Roelfes, G. *ChemCatChem* **2010**, *2*, 916–927.
- (10) Lu, Y.; Yeung, N.; Sieracki, N.; Marshall, N. M. *Nature* **2009**, *460*, 855–862.
- (11) *Catalytic Antibodies*; Keinan, E., Ed.; 1. ed.; Wiley-VCH: Weinheim, 2005.
- (12) Richter, F.; Leaver-Fay, A.; Khare, S. D.; Bjelic, S.; Baker, D. *PloS one* **2011**, *6*, e19230.
- (13) Romero, P. a; Arnold, F. H. *Nat. Rev. Mol. Cell Biol.* **2009**, *10*, 866–76.
- (14) Wilson, M. E.; Whitesides, G. M. *J. Am. Chem. Soc.* **1978**, *100*, 306–307.
- (15) Chen, C.-H. B.; Sigman, D. S. *Science* **1987**, *237*, 1197–1201.
- (16) Qi, D.; Tann, C. M.; Haring, D.; Distefano, M. D. *Chem. Rev.* **2001**, *101*, 3081–3111.
- (17) Panella, L.; Broos, J.; Jin, J.; Fraaije, M. W.; Janssen, D. B.; Jeronimus-Stratingh, M.; Feringa, B. L.; Minnaard, A. J.; de Vries, J. G. *Chem. Commun.* **2005**, *23*, 5656–5658.
- (18) Carey, J. R.; Ma, S. K.; Pfister, T. D.; Garner, D. K.; Kim, H. K.; Abramite, J.; Wang, Z.; Guo, Z.; Lu, Y. *J. Am. Chem. Soc.* **2004**, *126*, 10812–10813.

- (19) Oltra, N. S.; Roelfes, G. *Chem. Commun.* **2008**, 6039–6041.
- (20) Fournier, P.; Fiammengo, R.; Jäschke, A. *Angew. Chem. Int. Ed.* **2009**, 48, 4426–4429.
- (21) Ward, T. R. *Acc. Chem. Res.* **2011**, 44, 47–57.
- (22) Reetz, M. T.; Peyralans, J. J.-P.; Maichele, A.; Fu, Y.; Maywald, M. *Chem. Commun.* **2006**, 4318–4320.
- (23) Mahammed, A.; Gross, Z. *J. Am. Chem. Soc.* **2005**, 127, 2883–2887.
- (24) Podtetenieff, J.; Taglieber, A.; Bill, E.; Reijerse, E. J.; Reetz, M. T. *Angew. Chem. Int. Ed.* **2010**, 49, 5151–5155.
- (25) Reetz, M. T.; Jiao, N. *Angew. Chem. Int. Ed.* **2006**, 45, 2416–2419.
- (26) Yeung, N.; Lin, Y.-W.; Gao, Y.-G.; Zhao, X.; Russell, B. S.; Lei, L.; Miner, K. D.; Robinson, H.; Lu, Y. *Nature* **2009**, 462, 1079–1082.
- (27) Pordea, A.; Creus, M.; Panek, J.; Duboc, C.; Mathis, D.; Novic, M.; Ward, T. R. *J. Am. Chem. Soc.* **2008**, 130, 8085–8088.
- (28) Matsuo, T.; Murata, D.; Hisaeda, Y.; Hori, H.; Hayashi, T. *J. Am. Chem. Soc.* **2007**, 129, 12906–12907.
- (29) Jing, Q.; Kazlauskas, R. *J. ChemCatChem* **2010**, 2, 953–957.
- (30) Lee, H. S.; Schultz, P. G. *J. Am. Chem. Soc.* **2008**, 130, 13194–13195.
- (31) Reetz, M. T.; Carballeira, J. D. *Nat. Prot.* **2007**, 2, 891–903.
- (32) Kada, G.; Falk, H.; Gruber, H. J. *Biochim. Biophys. Acta* **1999**, 1427, 33–43.
- (33) Weber, P. C.; Ohlendorf, D. H.; Wendoloski, J.; Salemme, F. R. *Science* **1989**, 243, 85–88.
- (34) Jones, M. L.; Kurzban, G. P. *Biochemistry* **1995**, 34, 11750–11756.
- (35) Loosli, A. Investigation of Second Coordination Sphere Interactions Between Biotinylated Coordination Complexes and (Strept)Avidin: CD Spectroscopy as a Powerful Tool for Stability Constant Determinations, PhD Thesis, Université de Neuchâtel, 2004.
- (36) González, M.; Argaraña, C. E.; Fidelio, G. D. *Biomol. Eng.* **1999**, 16, 67–72.
- (37) Lo, C. New Challenges for Artificial Metalloenzymes Based on the Biotin-(Strept)avidin Technology, PhD Thesis, University of Basel, 2012.
- (38) Hyster, T. K.; Knorr, L.; Ward, T. R.; Rovis, T. *Science* **2012**, 338, 500–503.

- (39) Collot, J.; Gradinaru, J.; Humbert, N.; Skander, M.; Zocchi, A.; Ward, T. R. *J. Am. Chem. Soc.* **2003**, 125, 9030–9031.
- (40) Skander, M.; Malan, C.; Ivanova, A.; Ward, T. R. *Chem. Commun.* **2005**, 4815–4817.
- (41) Skander, M.; Humbert, N.; Collot, J.; Gradinaru, J.; Klein, G.; Loosli, A.; Sauser, J.; Zocchi, A.; Gilardoni, F.; Ward, T. R. *J. Am. Chem. Soc.* **2004**, 126, 14411–14418.
- (42) Klein, G.; Humbert, N.; Gradinaru, J.; Ivanova, A.; Gilardoni, F.; Rusbandi, U. E.; Ward, T. R. *Angew. Chem. Int. Ed.* **2005**, 44, 7764–7767.
- (43) Letondor, C.; Pordea, A.; Humbert, N.; Ivanova, A.; Mazurek, S.; Novic, M.; Ward, T. R. *J. Am. Chem. Soc.* **2006**, 128, 8320–8.
- (44) Letondor, C.; Humbert, N.; Ward, T. R. *PNAS* **2005**, 102, 4683–7.
- (45) Creus, M.; Pordea, A.; Rossel, T.; Sardo, A.; Letondor, C.; Ivanova, A.; Letrong, I.; Stenkamp, R. E.; Ward, T. R. *Angew. Chem. Int. Ed.* **2008**, 1400–1404.
- (46) Pierron, J.; Malan, C.; Creus, M.; Gradinaru, J.; Hafner, I.; Ivanova, A.; Sardo, A.; Ward, T. R. *Angew. Chem.* **2008**, 120, 713–717.
- (47) Lo, C.; Ringenberg, M. R.; Gnanndt, D.; Wilson, Y.; Ward, T. R. *Chem. Commun.* **2011**, 47, 12065–12067.
- (48) Stayton, P. S. Modified-Affinity Streptavidin, US-Patent, **1998**.
- (49) Ting, A. Y.; Howarth, M. R. Monovalent Streptavidin Compositions, US-Patent, **2005**.
- (50) Cicmanec, J. F.; Lichstein, H. C. *J. Bact.* **1978**, 133, 270–278.
- (51) Krishnamurthy, V. M.; Kaufman, G. K.; Urbach, A. R.; Gitlin, I.; Gudiksen, K. L.; Weibel, D. B.; Whitesides, G. M. *Chem. Rev.* **2008**, 108, 946–1051.
- (52) Supuran, C. T. *Nat. Rev. Drug. Disc.* **2008**, 7, 168–181.
- (53) Faber, K. *Biotransformations in Organic Synthesis*; 6. ed.; Springer: Heidelberg, 2011.
- (54) Gladiali, S.; Alberico, E. *Chem. Soc. Rev.* **2006**, 35, 226–236.
- (55) Hartwig, J. *Organotransition Metal Chemistry: From Bonding to Catalysis*; 1. ed.; University Science Books, 2009.
- (56) Noyori, R.; Hashiguchi, S. *Acc. Chem. Res.* **1997**, 30, 97–102.
- (57) Martins, J. E. D.; Clarkson, G. J.; Wills, M. *Org. Lett.* **2009**, 11, 847–850.

- (58) Kadyrov, R.; Riermeier, T. H. *Angew. Chem. Int. Ed.* **2003**, 42, 5472–5474.
- (59) *Asymmetric Catalysis on Industrial Scale*; Blaser, H.-U.; Federsel, H.-J., Eds.; 2. ed.; Wiley-VCH: Weinheim, 2010.
- (60) *Chiral Amine Synthesis: Methods, Developments and Applications*; Nugent, T. C., Ed.; 1. ed.; Wiley-VCH: Weinheim.
- (61) Roth, P.; Andersson, G.; Somfai, P. *Chem. Commun.* **2002**, 1752–1753.
- (62) *Transition Metals for Organic Synthesis*; Beller, M.; Bolm, C., Eds.; 2. ed.; Wiley-VCH: Weinheim, 2004.
- (63) Evanno, L.; Ormala, J.; Pihko, P. M. *Chem.-Eur. J.* **2009**, 15, 12963–12967.
- (64) Mao, J.; Baker, D. C. *Org. Lett.* **1999**, 1, 841–843.
- (65) Wu, J.; Wang, F.; Ma, Y.; Cui, X.; Cun, L.; Zhu, J.; Deng, J.; Yu, B. *Chem. Commun.* **2006**, 1766–1768.
- (66) Ramaswamy, S.; Scholze, M.; Plapp, B. V *Biochemistry* **1997**, 36, 3522–3527.
- (67) Mitsukura, K.; Suzuki, M.; Shinoda, S.; Kuramoto, T.; Yoshida, T.; Nagasawa, T. *Biosci. Biotechnol. Biochem.* **2011**, 75, 1778–1782.
- (68) Abrahamson, M. J.; Vázquez-Figueroa, E.; Woodall, N. B.; Moore, J. C.; Bommarius, A. S. *Angew. Chem. Int. Ed.* **2012**, 51, 3969–3972.
- (69) Vaijayanthi, T.; Chadha, A. *Tetrahedron Asymmetry* **2008**, 19, 93–96.
- (70) Payton, C. W.; Chang, Y. *J. Bact.* **1982**, 149, 864–871.
- (71) Mitsukura, K.; Suzuki, M.; Tada, K.; Yoshida, T.; Nagasawa, T. *Org. Biom. Chem.* **2010**, 8, 4533–4535.
- (72) Wu, X.; Li, X.; Zanutti-Gerosa, A.; Pettman, A.; Liu, J.; Mills, A. J.; Xiao, J. *Chem.-Eur. J.* **2008**, 14, 2209–2222.
- (73) Li, C.; Xiao, J. *J. Am. Chem. Soc.* **2008**, 130, 13208–13209.
- (74) Kolb, H. C.; Vannieuwenhze, M. S.; Sharpless, K. B. *Chem. Rev.* **1994**, 94, 2483–2547.
- (75) Schröder, M. *Chem. Rev.* **1980**, 187–213.
- (76) Minato, M.; Yamamoto, K.; Tsuji, J. *J. Org. Chem.* **1990**, 766–768.
- (77) Kwong, H.; Sorato, C.; Ogino, Y.; Chen, H.; Sharpless, K. B. *Tet. Lett.* **1990**, 31, 2999–3002.

- (78) Ahrgren, L.; Sutin, L. *Org. Proc. Res. Dev.* **1997**, 1, 425–427.
- (79) Jonsson, S. Y.; Färnegardh, K.; Bäckvall, J.-E. *J. Am. Chem. Soc.* **2001**, 123, 1365–1371.
- (80) Döbler, C.; Mehlretter, G.; Beller, M. *Angew. Chem. Int. Ed.* **1999**, 38, 3026–3028.
- (81) Resnick, S. M.; Gibson, D. T. *J. Ind. Micro.* **1996**, 17, 438–457.
- (82) Karlsson, A.; Parales, J. V.; Parales, R. E.; Gibson, D. T.; Eklund, H.; Ramaswamy, S. *Science* **2003**, 299, 1039–1042.
- (83) Hudlicky, T.; Reed, J. *Synlett* **2009**, 5, 685–703.
- (84) Jain, A.; Whitesides, G. M.; Alexander, R. S.; Christianson, D. W. *J. Med. Chem.* **1994**, 37, 2100–2105.
- (85) Günnaz, S.; Özdemir, N.; Dayan, S.; Dayan, O.; Çetinkaya, B. *Organometallics* **2011**, 4165–4173.
- (86) Grzybowski, B. a; Ishchenko, A. V; Kim, C.-Y.; Topalov, G.; Chapman, R.; Christianson, D. W.; Whitesides, G. M.; Shakhnovich, E. I. *PNAS* **2002**, 99, 1270–1273.
- (87) Schmid, M.; Nogueira, E. S.; Monnard, F. W.; Ward, T. R.; Meuwly, M. *Chem. Sci.* **2012**, 3, 690–700.
- (88) Schmidt, M. et al., Manuscript in preparation.
- (89) Bartels, C. *Chem. Phys. Let.* **2000**, 331, 446–454.
- (90) Debreczeni, J. E.; Bullock, A. N.; Atila, G. E.; Williams, D. S.; Bregman, H.; Knapp, S.; Meggers, E. *Angew. Chem. Int. Ed.* **2006**, 45, 1580–1585.
- (91) Cígler, P.; Kozísek, M.; Rezácová, P.; Brynda, J.; Otwinowski, Z.; Pokorná, J.; Plešek, J.; Grüner, B.; Dolecková-Maresová, L.; Mása, M.; Sedláček, J.; Bodem, J.; Kräusslich, H.-G.; Král, V.; Konvalinka, J. *PNAS* **2005**, 102, 15394–15399.
- (92) Jude, K. M.; Banerjee, A. L.; Haldar, M. K.; Manokaran, S.; Roy, B.; Mallik, S.; Srivastava, D. K.; Christianson, D. W. *J. Am. Chem. Soc.* **2006**, 128, 3011–3018.
- (93) Bruijninx, P. C. a; Sadler, P. J. *Curr. Opin. Chem. Biol.* **2008**, 12, 197–206.
- (94) Yan, Y. K.; Melchart, M.; Habtemariam, A.; Sadler, P. J. *Chem. Commun.* **2005**, 4764–4776.
- (95) Jung, Y.; Lippard, S. J. *Chem. Rev.* **2007**, 107, 1387–1407.
- (96) Kaerberlein, T.; Lewis, K.; Epstein, S. S. *Science* **2002**, 296, 1127–1129.

- (97) Steele, H. L.; Jaeger, K.-E.; Daniel, R.; Streit, W. R. *J. Mol. Micr. Biot.* **2009**, *16*, 25–37.
- (98) Keasling, J. D. *Science* **2010**, *330*, 1355–1358.
- (99) Taubert, A.; Napoli, A.; Å, W. M. *Curr. Opin. Chem. Biol.* **2004**, *8*, 598–603.
- (100) Allen, T. M.; Cullis, P. R. *Science* **2004**, *303*, 1818–1822.
- (101) Tanner, P.; Baumann, P.; Enea, R.; Onaca, O.; Palivan, C.; Meier, W. *Acc. Chem. Res.* **2011**, *10*, 1039–1049.
- (102) Nikaido, H.; Vaara, M. *Microbiol. Rev.* **1985**, *49*, 1–32.
- (103) Pata, V.; Dan, N. *Biophys. J.* **2003**, *85*, 2111–2118.
- (104) Ben-Haim, N.; Broz, P.; Marsch, S.; Meier, W.; Hunziker, P. *Nano Lett.* **2008**, *8*, 1368–1373.
- (105) Bennett, B. D.; Kimball, E. H.; Gao, M.; Osterhout, R.; Van Dien, S. J.; Rabinowitz, J. D. *Nat. Chem. Biol.* **2009**, *5*, 593–599.
- (106) Köhler, V.; Wilson, Y. M.; Dürrenberger, M.; Ghislieri, D.; Churakova, E.; Quinto, T.; Knörr, L.; Häussinger, D.; Hollmann, F.; Turner, N. J.; Ward, T. R., *Nat. Chem.* **2012**, in press.
- (107) *Fundamentals of Crystallography*; Giacovazzo, C., Ed.; 1. ed.; Oxford Science Publication, 2000.
- (108) Bürgi, H. B.; Hauser, J.; Weber, T.; Neder, R. B. *Crystal Growth & Design* **2005**, *5*, 2073–2083.
- (109) Weber, T.; Estermann, M. A.; Bürgi, H. B. *Acta Cryst. B* **2001**, *57*, 579–590.

VIII Curriculum Vitae

Tillmann Heinisch

Personal Details

Date and Place of Birth: October 24th, 1982, Leipzig, Germany
Title: PhD
Nationality: German

Education

Feb. 2009 – Feb. 2013 PhD student in Chemistry and Structural Biology with Prof. Thomas R. Ward and Prof. Tilman Schirmer, Department of Chemistry and Biozentrum, University of Basel, Switzerland. Dissertation Title: *Structure-based design of artificial metalloproteins and beyond. (Magna cum laude)*

Oct. 2006 – Nov. 2008 Master of Science Degree in Chemistry/Structural Biology with Prof. Norbert Sträter, Biotechnological Biomedical Centre, University of Leipzig, Germany. Thesis Title: *Research on the synthesis of artificial metalloenzymes based on RNase S.*

Oct. 2005 - Aug. 2006 Bachelor of Science Degree in Chemistry with Prof. Dieter Sicker, Institute of Organic Chemistry, University of Leipzig, Germany. Thesis Title: *Isolation of the compounds nicotine, theobromine, capsaicine and galanthamine from natural sources.*

Oct. 2003 - Aug. 2005 Vordiplom Degree in Chemistry at the Technical University of Chemnitz, Germany.

